FUNDAMENTALS OF HYDROGEN INDUCED STRESS CRACKING IN DUPLEX STAINLESS STEELS

Thesis submitted for the degree of

Doctor of Philosophy

at the University of Leicester

by

Lisa Blanchard

Department of Engineering

University of Leicester

2018

To my parents,

ABSTRACT

Duplex stainless steels (DSSs) are widely used by oil and gas industry due to their good corrosion and mechanical properties, which made them suitable for subsea applications. In this environment the use of cathodic protection (CP), to prevent corrosion, generates hydrogen that can be absorbed at the metallic surfaces. Unfortunately, while this technique is useful and intended to prevent structural carbon-steel components from seawater corrosion, it can introduce atomic hydrogen to the DSS components (attached to the structural carbon steels), which are known to be susceptible to hydrogen embrittlement via hydrogen induced stress cracking (HISC). This phenomenon is recognised to occur once a critical level of stress and hydrogen concentrations are met in a susceptible microstructure.

To investigate the fundamentals of this mechanism, a multifaceted, comparative programme of microstructural characterisation, investigation of low temperature creep (LTC) and environmental testing was conducted on two DSSs of UNS S31803 grade: a rolled and seam welded pipe component and a hot-isostatically pressed (HIPed) can. Strain distribution was observed during LTC using digital image correlation technique; the relevance of fracture toughness testing methods to assess DSSs against HISC was investigated with the determination of microstructural factors influencing the resistance to HISC. Furthermore, the influence of residual stresses (induced by welding) was investigated on HISC thresholds, through tensile testing of specimens extracted from a pipe-to-flange welded component retrieved from 12 years of operations. The measurement of residual stresses was carried out by the neutron diffraction technique.

The microstructural homogeneity and directionality of the HIPed and wrought materials, respectively, were found to have a major influence on the accommodation of

stresses during LTC and resistance to HISC. Environmental testing showed the superior performance of the HIPed material. This testing programme also pointed out the complexity of interpreting the data obtained using the conventional fracture-toughness-based testing methodologies, with a fatigue pre-crack notch, to assess DSSs against HISC, particularly in terms of crack initiation. The presence of micro and macro-residual stresses was determined in the small-scale specimens extracted from the pipe-to-weld component; however; the macro-residual stress state did not explain the relatively better HISC performance of the cross-weld specimens, compared to that in the parent materials.

ACKNOWLEDGMENTS

I would like to express my greatest appreciation and sincere gratitude to Dr. Kasra Sotoudeh for his supervision and strong support throughout the 4 years of this PhD. I could not have completed this thesis without your encouragement, in-depth technical knowledge and unconditional enthusiasm on the topic. I would like to express my deep appreciation to Prof. Hongbiao Dong for his supervision and guidance.

TWI and TWI's client are deeply acknowledged for providing me the opportunity to get involved in two real cases of HISC failure investigations of DSS components retrieved from subsea. These concrete industrial cases provided considerable significance to this research project.

My thanks are extended to the TWI team and particularly to Shiladitya Paul, Philippa Moore, Menno Hoekstra, Simon Smith and Tyler London for their scientific expertise, invaluable advices and discussions. A special thanks to Michael Dodge, David Griffiths and Imran Bhamji for their notable contributions to the structure and technical content of this work, their patience with me and for pushing me to succeed. I would like to thanks Ashley Spencer, Lukas Suchomel, Jerry Godden and Stuart Page for the great help and training in the skills necessary to undertake my studies.

I would like to thanks Saurabh Kabra from ISIS, Rutherford Appleton Laboratory, for training me on ENGIN-X.

A special thanks to my friends and fellow research students: Marion Bourebrab, Dorothy Winful, Michael Walker, Somsubhro Chaudhuri, Cui Er Seow, and all the

IMPaCT team. I will look back on the innumerable chats, coffees breaks, sport sessions, laughs and trips with fond memories.

Words are not enough to acknowledge the unconditional support of my family, Maman, Papa, Simon et Fanny, merci! Thank you for always being there in the great and in the more challenging times.

Financially, this work was funded by TWI Ltd. and the Engineering and Physical Sciences Research Council (EPSRC) (Grant No: EP/L016206/1) in Innovative Metal Processing for financial support. I feel privileged to have had the opportunity to work on this project - thank you.

TABLE OF CONTENTS

LIST OF TABLES

LIST OF FIGURES

GLOSSARY

AFM	Atomic force microscopy
AOD	Argon Oxygen Decarburisation
BCC	Body-centred cubic
BSE	Backscattered electron
CCD	Charged-coupled devices
CP	Cathodic protection
CT	Computed tomography
CTOD	Crack tip opening displacement
DSS, (S)DSS	Duplex stainless steel, super duplex stainless steel
EBSD	Electron backscatter diffraction
EDM	Electro discharged machining
EDX	Energy dispersive X-Rays
EPFM	Elastic plastic fracture mechanics
FCC	Face- centred cubic
FIB	Focus ion beam
FPC	Fatigue pre-cracked
GTAW	Gas tungsten arc welding
HAB	High angle boundary
HIP	Hot isostatic pressed

HISC	Hydrogen induced stress cracking
KS	Kurdjumov-Sachs
LAB	Low angle boundary
LMO	Local misorientation
LTC	Low temperature creep
ND	Normal direction
OPS	Oxide polishing suspension
OR	Orientation relationship
PCT	Phase contrast tomography
PRE	Pitting equivalent number
RD	Rolling direction
RT	Room temperature
SCE	Silver chloride calomel electrode
SEM	Scanning electron microscopy
SENB	Single edge notched bend
SSRT	Slow strain rate testing
UNS	Unified numbering system
UTS	Ultimate tensile strength
TD	Transverse direction
TEM	Transmission electron microscopy
VOD	Vacuum Oxygen Decarburisation
XMT	X-ray micro-tomography
XRD	X-ray diffraction

Chapter 1.

INTRODUCTION

Duplex and super duplex stainless steels (S)DSSs are materials characterised by relatively high mechanical properties, good corrosion resistance and competitive prices compared to other corrosion resistant alloys. Consequently, those alloys are of particular interest for the oil and gas industry and specifically for subsea application. In these environments, duplex stainless steel components are connected to materials requiring a protection against seawater corrosion and hence, the use of cathodic protection (CP) is employed and successfully protects these parts. However, CP is also a main source of hydrogen and DSSs have been found susceptible to hydrogen induced stress cracking (HISC). This embrittlement mechanism is characterised by the combined effect of an appropriate hydrogen concentration and sufficient high stress in a susceptible microstructure and has been found responsible for major failures in service. Despite clear environmental and economic consequences of HISC failures, the fundamental micro-mechanisms of HISC remain largely unknown.

Guidelines for designing with DSSs, exposed to CP have been developing since the early failures; however, the current Standards or guidelines do not provide a standard test method for assessing DSSs against HISC, and those used for ranking the materials' performance with respect to HISC, do not take into account the effects of certain parameters, such as low-temperature creep, strain rate, residual stresses etc. Past research projects on this topic has shown the significant effects of a few of these parameters and the uncertainties associated with them. In some cases, materials' behaviour during environmental-mechanical testing could not be explained and established. There is, therefore, an academic and an industry need to understand the

materials' response to testing and service conditions, for valid assessments and evaluations to be made.

The current understanding of HISC, obtained from failure investigations and testing programmes carried out on DSS components, showed that manufacturing processes can define the microstructure (e.g. directionality of phases, austenite spacing, nitride precipitation etc.) and consequently the HISC resistance of DSSs. Hence, the resistance-to-HISC of a particular grade differs according to the manufacturing processes employed, e.g. hot isostatic pressing, forging, casting, etc. A manufacturing process widely used and controlled to manufacture DSS pipe product is rolling. This process generates DSS microstructures with high directionality. For components of more complex shapes, HIPed (hot isostatic pressed) manufacturing is employed, although certain size limitations are met. This production technique has improved and ensured high dimensional precision and superior mechanical properties of such products, compared to conventionally-produced components. Hence, HIPed products are increasingly employed in a wide range of applications, including subsea components. It is therefore important to understand these materials better through evaluating their resistance-to-HISC.

The present work was aimed at developing a more in-depth understanding of HISC and its micro-mechanisms, using the state-of-the-art experimental methods. Particularly, the focus of the project was placed on the effect and role of key microstructural parameters on the resistance-to-HISC of DSSs and on the evaluation of potential issues with testing methodologies currently used to qualify DSSs performance in hydrogen environment. The observations made could be used to improve the existing guidelines for assessing and designing with DSSs against HISC.

A multifaceted testing programme was pursued to study two fundamentally different DSS microstructures: a seam-welded (rolled) pipe and a HIPed material, with similar chemical composition. This programme included an in-depth material characterisation, the study of low-temperature creep (LTC) phenomenon, the evaluation of performance in hydrogen environment. Moreover, the impact and interaction residual stresses during small-scale HISC testing were investigated using a pipe-to-flange component retrieved from subsea after 12 years of operations.

This thesis comprises seven chapters; Chapter 1 provides an introduction to this thesis and its structure, followed by a literature survey reviewing the metallurgy of DSSs, the fundamentals of HISC in DSSs and the role of key parameters and the current HISC testing methodologies, Chapter 2. Chapter 3 presents the details of experimental techniques used throughout the programme.

An in-depth material characterisation, using a series of advanced techniques, was carried out and reported in Chapter 4. The microstructure characterisation included light and scanning electron microscopy (SEM), coupled with energy-dispersive X-ray (EDX) spectroscopy, and electron backscatter diffraction (EBSD) mapping, as appropriate, to quantitatively determine various microstructural parameters, such as austenite spacing, phase balance, grain boundary and misorientation properties etc. General mechanical properties of the alloys were determined by standard hardness and tensile testing methods.

Chapter 5 and 6 provides a comparative study of the HIPed and wrought materials behaviour with respect to LTC and HISC. Chapter 5 is an investigation of LTC, which is a time-dependent deformation phenomenon occurring in a range of materials, including stainless steels and particularly DSSs, at temperatures significantly lower than those conventionally considered for thermally-activated creep of stainless steels. This is considered rather important, as several studies have suggested LTC to be a prerequisite for HISC. This chapter attempts to observe the micro-mechanism(s) of this phenomenon and discusses its potential impact on the resistance-to-HISC. For this purpose, interrupted tensile testing, coupled with the digital image correlation (DIC) technique and EBSD mapping, were employed to determine strain distribution and microstructural changes during LTC.

Chapter 6 is a fracture-toughness-based testing programme studying various key microstructural, environmental and testing parameters, using extensive post-test fractographic and metallographic examinations, comparing the cracking behaviour of the two materials investigated. For tests carried out in air, the methods have proved to be relevant and useful for obtaining quantitative input (i.e. crack growth/extension via tearing) for engineering critical analysis (ECA). This study however, investigated the suitability of such methodologies in the context of environmental cracking, i.e. HISC in DSSs. The effect of displacement rate, hydrogen pre-charging and notch geometry of

single edge notched bend (SENB) specimens, were investigated, in terms the test output and interpretations associated with it. The comparison of the wrought and the HIPed materials cracking behaviour in air and in a hydrogen-charging environment allowed the determination of key microstructural features influencing the resistance-to-HISC.

Chapter 7 investigates the influence of residual stresses induced by welding, and their interactions with stresses developed by HISC testing, on the resistance-to-HISC a pipe-to-flange joint from a subsea component retrieved after 12 years of service. The assessment was carried out using neutron diffraction residual stress measurements and small-scale constant-load tensile testing of round plane-sided specimens, in a simulated seawater solution under cathodic protection. This investigation is the continuation of previous work carried out at TWI, and an attempt to address some unexpected observations made. The author is currently conducting further work on the HISC behaviour of the two materials used in this project, to further characterise the alloys' structures in 3D. This is carried out using phase-contrast X-ray micro-tomography technique at the Japan Synchrotron Radiation Research Institute (JASRI), with Prof. Toda and Dr. Hirayama from the University of Kyushu, Japan. The results will be linked to the rate of hydrogen permeation in the alloys, measured using a Devanathan and Stachurski electrochemical cell. The findings of these ongoing experiments will be published in a journal paper.

Chapter 2.

LITERATURE REVIEW

2.1 Duplex stainless steels

2.1.1 Development of duplex stainless steels

Duplex Stainless Steels (DSS) were invented in 1927 and commercialised in the early 30's. At that stage, they were mainly composed of Cr, Ni and Mo. These alloys offer enhanced mechanical properties relative to austenitic grades, particularly in relation to strength and hardness; furthermore they offer improved corrosion resistance, especially to stress corrosion cracking [1]. However, early in their development, the technology was not sufficiently advanced to allow control of the microstructure during the manufacturing processes and, as a consequence DSS did not achieve the required performance. In the 1970's, with the high demand for corrosion resistant alloys from the expanding oil and gas industry, DSS were further improved. This was achieved with the invention of AOD (Argon Oxygen Decarburisation) and VOD (Vacuum Oxygen Decarburisation). By controlling the amount of S, P, C, N and O, these processes allowed better control of the microstructure during manufacturing, ensuring optimal properties of the alloys [2]. The development of continuous casting has also had a significant influence on DSS development [3] and allowed significant cost savings to be made. Since then, work has been carried out to explore the influence of alloying elements (e.g. nitrogen impacts on austenite stability); this has solved the major welding issue namely conserving the dual phase microstructure, and led to the development of new grades: super duplex stainless steel (SDSS) and hyper duplex stainless steels (HDSS) alloys. These highly alloyed materials are suitable for corrosive environments.

The current applications for DSS are mainly in those industries requiring high strength materials able to withstand highly corrosive conditions, namely the chemical and petrochemical, oil and gas, marine transportation, power generation, food, and pulp and paper industries [4]. In the case of the oil and gas industry, most of the DSS parts are employed for subsea applications such as pipelines, manifold sections, valves, pumps, flanges.

2.1.2 Classification and designation

A wide range of duplex stainless steel compositions are now available, designed to meet different industrial needs. Their performance is ranked on the basis of the pitting resistance equivalent number (PRE_N) based on chromium, molybdenum and nitrogen contents, which are the key elements for corrosion resistance of DSS. The PRE_N is defined as:

$$PRE_N = \%Cr + 3.3\ \%Mo + 16\ \%N \text{ [4]}. \quad (1)$$

Four classes of DSS exist: the lean duplex stainless steels, with a PRE_N lower than 30 due to the low Ni content and the absence of molybdenum in their composition. These are the cheapest DSS alloys designed to replace austenitic alloys AISI 316 and 304 [2], mainly in the construction industry [5]. Standard duplex stainless steels have a PRE_N of between 32 and 39. Three sub-categories can be differentiated within the 'standard' classification:

- DSS with a PRE_N from 32 to 33, which are the low cost option and the most widely used, DSS with a PRE_N of 35 to 36, which show better strength and corrosion resistance than the alloys with lower PRE_N;
- Alloys with PRE_N of 38 to 39, which are 25Cr grades that have even higher corrosion resistance and better weldability due to the high N content.
- More highly alloyed, super duplex stainless steels (SDSS), with a PRE_N of 40 or greater (Cr content superior to 25%wt), have even higher corrosion resistance and are specifically designed for more severe environments. However, the high content of alloying element included in their composition promotes the precipitation of intermetallic phases. Hence their manufacturing conditions (heating rate, quench temperature, etc.) are restricted and have to be carefully controlled to avoid intermetallic precipitation.

The information presented in Table 2.1, was taken from J. Charles, "Structure and mechanical properties of DSS". In this table, standard UNS designations are shown in relation to the main alloying elements and PRE_N. Due to the wide composition range for a UNS designation, alloys under the same designation can have different PRE_N number. This makes the PRE_N a more efficient way to classify DSS than the UNS designation.

Table 2.1: Chemical analysis of some wrought DSS [3]**.**

Standard designation	**Cr**	**Ni**	**Mo**	**N**	**Cu**	**W**	**PRE_N**
UNS S32304	23	4	0.1	0.1	-	-	24
UNS S31803	22	5	2.8	0.15	-	-	32/33
	22.8	6	3.3	0.18	-	-	35/36
UNS S32550	25	6.5	3	0.22	1.5	-	38/39
	25	6.5	3	0.22	-		38/39
UNS S31260	25	7	3	0.16	0.5	0.3	37
UNS S32550	25	7	3.5	0.25	1.5	-	41
			3.8	0.28	-	-	41
UNS S32750	25	7					
	25	7	3	0.27	-	2	39
UNS S32760	25	7	3.5	0.24	0.7	0.7	40
	27	7.5	3.8	0.27	0.7	0.7	44
	25	7.5	4.0	0.27	1.7	1	42.5

2.1.3 Duplex stainless steels properties

2.1.3.1 Mechanical properties

DSS are composed of ideally 50 % austenite and 50 % ferrite. This dual phase microstructure confers to the alloy a combination of properties from the two phases. In a simplified approach, ferrite provides strength and tensile properties while austenite enhances toughness [6].

2.1.3.1.1 Tensile properties

The elongation at failure of DSS is intermediate between the elongation at failure of ferrite and austenite, Table 2.2. Hence, the ductility of DSS can be determined from a linear rule of mixtures based on the phase balance. However, this is not the case for the yield strength: DSSs exhibit a yield strength more than twice that of austenitic steels and almost the same as ferritic stainless steels. This non intuitive behaviour can be explained by the grain size which is finer in DSS compared to austenitic and ferritic alloys, and so, according to the Hall-Petch relationship, yield strength is higher than both constituent phases[6] and [7]. SDSS exhibit a higher proof strength and ultimate tensile strength than conventional DSS.

Those properties are affected by composition, Table 2.2, as well as number of factors within the material production, processing and fabrication. Cold and hot forming processes can induce anisotropy in the mechanical properties of DSSs [7]: properties are different depending on the direction of loading. The process of rolling described by J. Charles [3] produces an elongation of the grain structure parallel to the rolling direction and results in an increase in the difference between tensile properties transverse and parallel to the rolling direction as the plate thickness reduces. The proof strength and ultimate tensile strength properties in the transverse direction are higher than in the longitudinal direction [8], while, the elongation at fracture is lower in transverse than longitudinal direction [9]. This behaviour is believed to be due to the strong crystallographic texture induced by the rolling process. Cold working in comparison to hot working results in higher proof strength and ultimate tensile strength [8]. Moreover, the deformation of austenitic alloys is known to lead to the transformation of austenite to martensite [10] and [11]. This can similarly occur in the austenite phase of DSSs and lead to an increase in the ultimate tensile strength [4] and a reduction in toughness. This transformation has been observed in UNS S32304 [4] and

UNS S31803 [11] and in DSS having an unstable austenite phase with lower content of Mo, Ni, N.

2.1.3.1.2 Toughness

Fracture toughness testing is used to establish component safety by assessing its flaw tolerance. Hence, fracture toughness properties as well as factors affecting them are critical for materials used in service. Correlation between impact testing and resistance to cracking results have been established in DSS [12]. However, while impact testing is a time effective testing method, resistance to cracking provides more accurate and complete sets of result.

Fracture toughness testing applied to duplex stainless steels base material and welds have demonstrated high resistance to cracking of this material in air [13], [14], [15] with lower cracking resistance than austenitic but higher than fully ferritic alloys[4]. The transition temperature ductile to brittle of DSS is included in the range 0°C to -100°C [14], [16], [17].

Dhooge and Deleu[13] presented fracture toughness results for DSS UNS 31803 and UNS 32760 using CTOD (crack tip opening displacement) testing method. The study shows the high cracking resistance of both materials in air for temperature as low as -60°C. Further work on weldments of these materials demonstrated a loss of toughness compared to the base material, however, the resistance to cracking is still high down to -40°C [18] and fractography analysis does not exhibit brittle fracture mechanism down to -60°C [12],[19].

The toughness properties of DSS and SDSS are mostly governed by the austenite phase and fractography analysis of specimens tested showed of a mix mode of cracking, containing brittle and ductile features that result from the different properties of δ and γ phases. The crack appears to initiate in the ferrite phase, propagates by cleavage and stopped at the austenite phase or change the fracture mechanism from cleavage to a ductile shear mode [6]. The fraction of cleavage fracture increases as the temperature is reduced [16].

Due to the dependence of the resistance to cracking to phase arrangement, forming process induces anisotropy in toughness. Hence, toughness strongly depends on the

crack orientation [15]. Indeed, crack resistance is higher with the orientation taken perpendicular to the rolling direction than to the longitudinal direction, where the probability to be stopped by an austenite grain is lower[7], [20].

Table 2.2: Mechanical properties of austenitic, ferritic, duplex and super duplex stainless steels in different conditions, at RT. These data are retrieved from J.O. Nilsson, J. Charles and R. N. Gunn [7]**,** [2]**and** [4]**.**

Alloy	**UNS designation**	**Conditions**	**Yield strength 0.2%, MPa**	**UTS, MPa**	**Elongation, %**	**Impact toughness, J**
Ferritic	UNS S43000	Annealed*	205	450	20	-
	UNS S44700	Hot rolled**	500	630	18	
Austenitic	UNS S30400	Annealed	210	515-690	45	>300
	UNS S31603	Annealed	170	485	40	
	UNS S08904	Hot rolled	280	600	50	
DSS	UNS S32304	Hot rolled	450	650	35	
		Annealed	400	600	25	300
	UNS S31803	Annealed	450	680-880	25	250
		Hot rolled	510	730	32	
SDSS	UNS S32750	Annealed	550	800-1000	25	230
		Hot rolled	650	840	30	

* Annealing is performed between a range of 1050°C to 1100°C.
**Hot rolling is performed between a range of 1000°C to 1200°C.

2.1.3.2 Corrosion

DSS are widely used in harsh environments due to their superior corrosion resistance, specifically to localised corrosion, stress corrosion cracking and intergranular corrosion.

2.1.3.2.1 Localised corrosion

The resistance of DSS to localised corrosion is similar or indeed higher than that of austenitic stainless steels [21]. Localised corrosion in stainless steels, such as pitting and crevice corrosion, is initiated by a passive layer breakdown [4]. Hence, the localised corrosion resistance of stainless steels depends on the level of alloying elements that promote the formation and stabilisation of the passive film [21], [7]. The influence of these elements on the corrosion resistance of DSS is quantified by the PRE_N, equation (1).

The PRE_N is related to the critical pitting temperature (CPT) by a linear relationship i.e. as the PRE_N increases, the CPT also increases. However, despite being a useful ranking tool, the accuracy of the PRE_N is limited by the heterogeneity of the DSS microstructures; compositional partitioning of Cr, Mo and N varies between austenite to ferrite and so the two phases demonstrate different corrosion resistance. The austenite phase is the most affected by pitting corrosion, due to its low Cr content [21]. Another factor affecting the reliability of PRE_N is the effect of precipitates, such as σ, χ, carbides or nitrides; these can create regions depleted in Cr, N and Mo and promote localised corrosion [21]. Hence, the pitting corrosion is located close to the secondary phases, precipitates or grain boundaries due to the lower Cr, Mo and N in these area [22].

The pitting corrosion behaviour of DSS seems to differ from the one observed in single phase alloys characterised by the formation of narrow cavities in the material. In DSS, once initiation had occurs to Cr, N, Mo depleted areas, the propagation is characterised by the selective dissolution of the attacked phase [23], [24].

2.1.3.2.2 Stress corrosion cracking (SCC)

Stress corrosion cracking occurs under the joint action of plastic straining and a corrosive environment (e.g. sodium chloride, hydrogen sulphides)[25]. The susceptibility of a material to SCC is dependent on both its composition and microstructure [7].

The combination of ferrite and austenite in DSS has been shown to give rise to better SCC resistance than observed in fully ferritic or austenitic alloys [4], [7], [26] and [21]. This is due to the combination of mechanical and electrochemical properties of the two phases. Ferrite has a higher strength than the austenite and thus during the deformation of DSS, the austenite phase undergoes plastic straining while ferrite plays a "keying role" [26], and the ferrite acts as obstacle for the crack propagation. Furthermore, the electrochemical potential of ferrite is lower than that of austenite hence austenite is essentially cathodically protected by the ferrite. An increase in the ferrite content, up to 60 %, is found to increase SCC resistance of DSS [27]. However, above this level ferrite can be detrimental and in-service cracking of components has been attributed to a high ferrite content in the weld [22].

2.1.4 Physical metallurgy of duplex stainless steels

2.1.4.1 Equilibrium phases

The superior properties of duplex stainless steels previously discussed, results from their dual phase microstructure. These alloys are designed to have a nominal composition of 50 % ferrite (δ), and 50 % austenite (γ), through a combination of their composition and the thermal history of the alloy.

The main alloying elements of DSS are divided into ferrite stabilisers: Cr, Mo, Si, W, Ti, Nb, Al, V and austenite promoters: Ni, Mn, N, C, Cu, N, Co. Work by H.C. Campbell and R.D. Thomas[28] established the chromium equivalent parameter (Cr_{eq}), grouping ferrite stabilisers under an empirical coefficient:

$$Cr_{eq} = \%Cr + 1.5\ \%Mo + 2\ \%Nb \quad (2)$$

Similarly, A. L. Shaeffler introduced the nickel equivalent parameter combining austenite stabilising elements [29]:

$$Ni_{eq} = \%Ni + 0.5\ \%\ Mn + 30\ \%C \quad (3)$$

After further investigation of the role of elements and the value of coefficients, the Welding Research Council established, in 1992, the following relationships [30]:

$$Cr_{eq} = \%Cr + \%Mo + 0.7\ \%Nb \quad (4)$$

and Ni_{eq} = %Ni + 35 %C + 20 %N + 0.25 %Cu (5)

On the basis of these WRC equations, DSS generally have a Cr_{eq}/Ni_{eq} ratio of between 2 and 3.5.

The dual phase nature of DSSs is mainly a result of the alloying elements however thermal/processing history can also have an influence. Figure 1 presents a phase equilibrium diagram based on temperature and the WRC Cr_{eq}/Ni_{eq} ratio. This figure shows that DSSs solidify in δ-ferrite phase field and are initially composed of 100 % δ-ferrite. The duplex stainless steel solidification sequence is: Liquid → Liquid + δ → δ →δ + γ [31]. Once the composition reached 50 % ferrite and 50 % austenite, the alloy is quenched. In the case where the quenching temperature is close to the ferrite solvus, the alloy is mostly ferritic and vice-versa if the quenching temperature is too low. Southwick and Honeycomb[32] showed that ferrite decomposition into austenite is controlled by two mechanisms: volume diffusion and interface migration. While cooling, elemental partitioning occurs between the two phases, resulting in local concentrations of ferrite and austenite promoters [33]. The temperature range of solidification is approximately 1400°C to 1000°C.

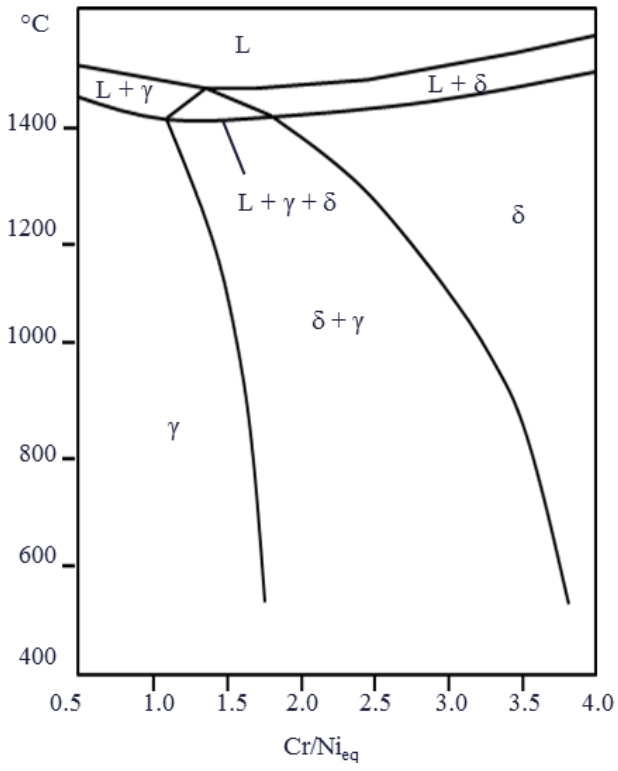

Figure 2.1: Phase diagram of duplex stainless steels according to Cr_{eq}/Ni_{eq} taken from WRC 1992. 2507, 52N and 2205 representing different duplex stainless steels grades [34]**.**

Austenite nucleates at ferrite grain boundaries [35] with preferential orientation relationship (OR): Kurdjumov-Sachs (K-S) and Nishiyama-Wassermann (N-W). The K-S relationship which is dominates, is defined as: {111}γ//{110}δ ,<110>γ//<111>δ, Figure 2.2, and N-W relationship is defined as: {111}γ//{110}δ ,<112>γ//<110>δ [36], [37]. Manufacturing processes which induce deformation of the material can alter these orientation relations.

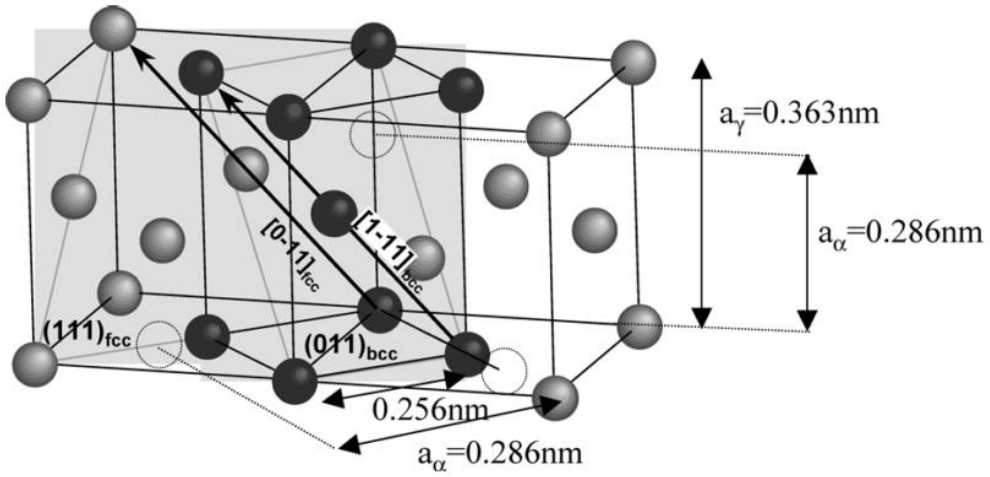

Figure 2.2: Schematic illustration of the Kurdjumov-Sachs OR according to [38]**.**

2.1.4.2 Other phases

During the solidification and subsequent cooling, other phases than γ and δ may precipitate which influence the resulting properties of the alloy. These will be discussed in the proceeding sections.

2.1.4.2.1 Carbides

Two main types of carbides, M_7C_3 and $M_{23}C_6$, with face centred cubic (FCC) lattice structures, can develop in DSSs. The 'M' is predominantly Cr but may contain Fe, Mo and Ni. Their formation originates from the supersaturation of C within the δ phase. Since C has higher solubility in austenite than in ferrite, if not enough time is given for C to diffuse in the γ, δ becomes supersaturated and carbide nucleation occurs. This effect is accentuated during cooling, as the solubility of C decreases in both phases with temperature [31]. In a fully ferritic matrix, M_7C_3 and $M_{23}C_6$ are the first precipitates to appear [39]. M_7C_3 precipitates first within a temperature range of 1050°C to 950°C whilst $M_{23}C_6$ precipitation occurs between 950°C and 650°C [40]. Before the transformation of ferrite into austenite, $M_{23}C_6$ carbides are located at δ/δ grain

boundaries. During ferrite decomposition, carbides nucleate and grow, following the eutectoid transformation sequence: $\delta \rightarrow \gamma + M_{23}C_6$ [41]. Consequently, carbides are located at δ/γ boundaries that are rich in Cr from the adjacent ferrite and C-rich from the adjacent austenite In the case of high carbon content DSS alloys, the γ and carbides grow in parallel. In the case of DSS alloys with a lower carbon content, as the carbides grow is limited [42], which reducing their pinning effect on the γ/δ front. In both cases, the $M_{23}C_6$ grows into the newly formed γ [43].

Carbides have a negative effect on DSS properties. Regarding corrosion resistance, carbide precipitation induces Cr depleted zones; this in turn increases the susceptibility to pitting corrosion. Carbides may, under certain conditions, reduce toughness properties and increase hardness properties[44]. This precipitation can be avoided by quenching from high temperature: 1050°C[4], however, with the low carbon content of the current DSSs, carbides precipitation is getting less of a concern.

2.1.4.2.2 Secondary austenite

Ferrite decomposition into primary austenite begins at elevated temperatures, and as the temperature decreases, this transformation is promoted. Hence, during manufacturing processes where the temperature is below δ solvus, such as, annealing or close to the fusion line during welding, new austenite grains can form. This newly formed austenite is known as secondary austenite, γ_2. The morphology and location of secondary austenite is temperature and time dependent. Three formation mechanisms can be distinguished.

- *T<650°C:* At this low temperature, the reaction is diffusionless, hence, γ_2 nucleates within the ferrite grain and has a similar composition. Correlation between this transformation and martensitic formation in steel can be made [7], [3]. The typical morphology of this newly reformed austenite is elongated plates within the ferrite grains.
- *650°C<T<850°C:* Above 650°C, the austenite adopts a Widmanstätten morphology and has a higher Ni content than the adjacent ferrite, indicating that diffusion is operating.
- *700°C<T<900°C:* Within this temperature range, a eutectoid transformation occurs: $\delta \rightarrow \sigma + \gamma_2$ at the δ/δ grain boundaries. The influence of secondary

austenite precipitation on duplex stainless steel properties is important in terms of corrosion resistance. The γ_2 has lower Cr and Mo content relative to primary γ and as a consequence its corrosion properties are lower, leading to a loss in pitting corrosion resistance [45].

2.1.4.2.3 Sigma (σ) phase

The most deleterious phase, regarding corrosion and toughness resistance, that can develop in DSS is σ-phase, the reason being that it occurs in larger amounts than other precipitates [45]. It precipitates in the temperature range between 600°C and 1000°C [33]. Sigma phase is composed of Fe, Cr and Mo and its precipitation is indirectly promoted by the addition of Ni [46] and N which stabilise the austenite and thereby promote the migration of Cr and Mo into the ferrite. It first precipitates at the triple points between ferrite, ferrite and primary austenite and along ferrite and austenite boundaries after longer annealing time [45]. It is formed via the eutectoid reaction: $\delta \rightarrow \gamma_2 + \sigma$ [46], where γ_2 is secondary austenite. The transformation of δ-ferrite into austenite leads to a depletion of Ni and enrichment in Cr and Mo at the δ/γ interface, promoting the formation of σ [47]. When the ageing time is prolonged, σ also precipitates within the ferrite grains. The precipitation of σ leads to a Cr-depleted zone, which in turn leads to a loss of corrosion resistance, particularly of the CPT, and affects the mechanical properties of the alloy [48]. The increase in the volume fraction of σ leads to a drastic reduction in the toughness [7], [49] and an increase in the tensile and yield strength [50]; as the annealing temperature increases the gain in tensile strength decreases [51]. The hardness is increased only after long incubation times [50]and is otherwise unaffected [49]. The precipitation of σ can occur after circa 10min or less at a temperature of 900°C, but its formation can be avoided by the use of fast cooling rates [40].

2.1.4.2.4 Chi (χ) phase

The precipitation of χ phase occurs within a temperature range of 700°C to 900°C and only after long time exposure. For this reason it is always present in a smaller amount than σ phase [7]. This intermetallic phase comprises mainly Cr and Mo and its bcc crystal structure ensures the continuity within the bcc δ ferrite matrix. As for σ phase, the precipitation of χ phase occurs at γ/δ interface boundaries and induces a reduction in toughness and pitting corrosion properties [4].

2.1.4.2.5 Nitrides

Nitrides, Cr_2N and CrN, are precipitates with an hexagonal crystallographic structure [2]. Two types of chromium nitrides exist: quenched-in and isothermal, depending on the heat treatment history of the alloy [52]. Quenched-in nitrides results from the super-saturation of N within the ferrite phase. Hence, their presence is enhanced by high/fast cooling rates from temperature above 1000°C, that inhibit the diffusion of N and thus restrict the formation of γ [53]. Their nucleation predominantly occurs within the ferrite grains, or at triple points, inclusions and dislocations and are thus termed intragranular nitrides. Inversely, isothermal chromium nitrides are intergranular and precipitate along δ/γ and δ/δ boundaries during isothermal treatments within a temperature range of 700 to 950°C [4]. They grow when the material is reheated. Nitrides are closely linked with the formation of secondary austenite when the alloy is reheated during processing to temperatures in excess of 900°C, acting as nucleation sites and providing a source of nitrogen as they subsequently dissolve. This mechanism is only valid at temperatures between 1000°C to 1100°C [53], [54] in which nitrides are able to dissolve and provide nitrogen but the dissolution rate is sufficiently low that they can still act as nucleation sites for secondary austenite. The precipitation of nitrides has a negative influence on corrosion properties as it creates Cr depleted zones promoting intergranular corrosion.

2.1.4.3 The influence of key alloying elements on phase formation

The chemical composition plays an essential role, in combination with the material processing, in determining the microstructure and hence properties of the DSS alloy. Below, each of the principal elements found in DSS is discussed, including their influence on corrosion resistance and mechanical properties.

2.1.4.3.1 Chromium

Chromium is a ferrite promoter. The binary Iron-Chromium phase diagram given in Figure 2.3 shows the restriction of the austenite formation as Cr content increases [55]. Chromium is one of the main elements contributing to the passive layer that forms on the alloy surface and protects it from corrosion. However, Cr also promotes the formation of embrittling phases and intermetallics, such as α', σ, intermetallic phases, χ and carbides, reducing ductility and toughness of DSS [4]. Furthermore, the formation of these secondary phases is directly linked to the creation of Cr depleted zones with an associated reduction in corrosion resistance.

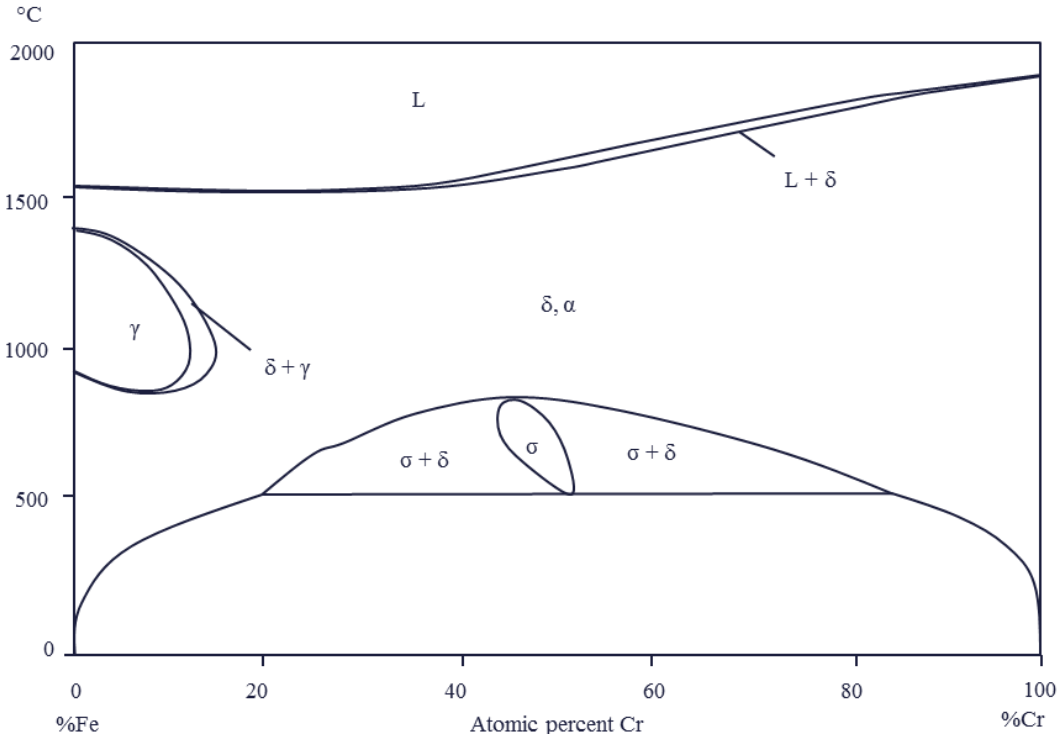

Figure 2.3: Iron-Chromium phase diagram, showing Cr influence on the austenite formation [56]**.**

2.1.4.3.2 Nickel

Nickel, is an austenite stabiliser, as can be seen in Figure 2.4, from which its addition can be seen to restrict the δ ferrite phase field. As in austenitic stainless steels, Ni strengthens the austenite phase by solid solution strengthening, without the formation of precipitates [31]. However, despite its strengthening and stabilising properties, the Ni content has to be controlled in relation to the Cr content to ensure an optimum phase balance and because of its negative effect on the corrosion properties of the alloy [4].

The addition of Ni decreases the C solubility in the austenite, promoting the formation of Cr-rich carbides and Cr depleted zones, promoting intergranular corrosion [55].

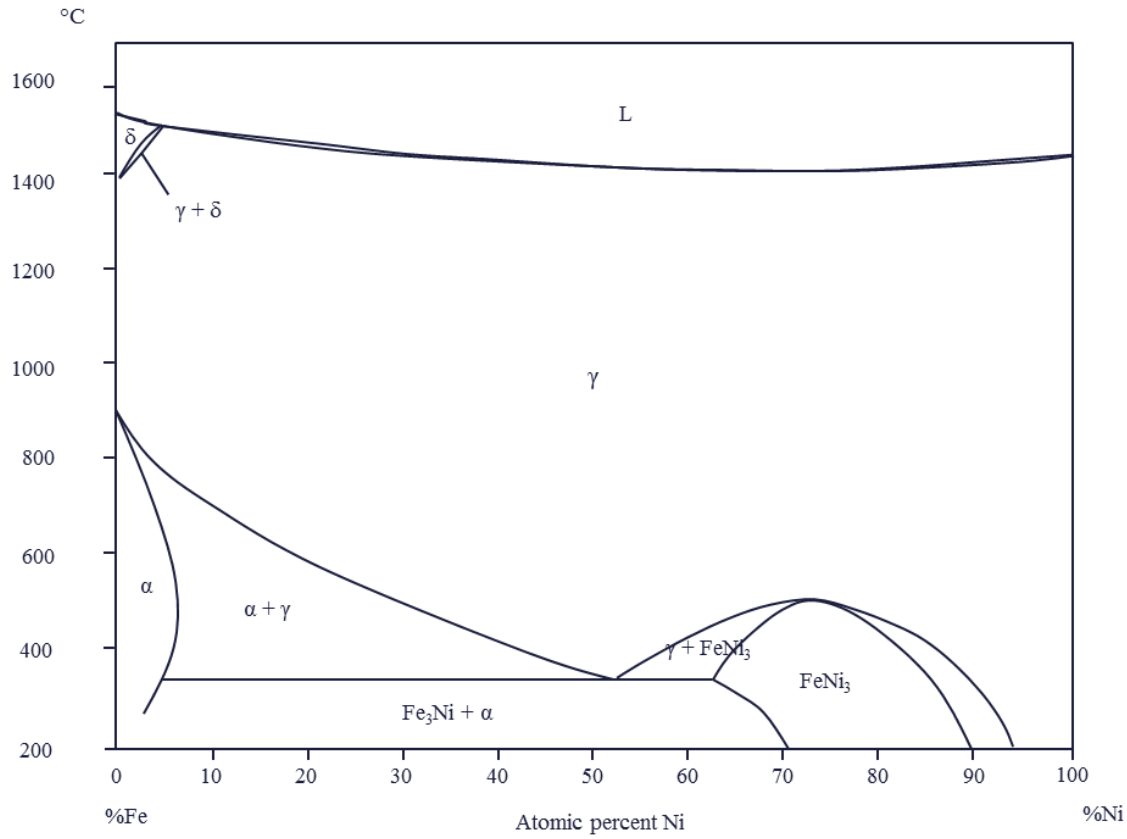

Figure 2.4: Phase diagram of Iron-Nickel, showing the promoting of austenite by Ni [56]**.**

2.1.4.3.3 Nitrogen

Nitrogen is present in two forms in DSS: as a solute and combined in the form of nitride precipitates. The typical total nitrogen content of DSS is within the range 0.08 to 0.35 wt%. Nitrogen is added to DSS to improve mechanical properties, corrosion resistance and austenite stabilisation [57]. The phase diagram Fe-Cr-N, given in Figure 2.5, illustrates the influence of nitrogen on the austenite stabilisation. A study carried out to look at the partitioning of nitrogen between the austenite and ferrite phases demonstrated that the profile matched that of Nickel, namely high in austenite and low in ferrite [58]. The fcc crystallographic structure of austenite contains more octahedral interstitial sites than the bcc ferrite and thus N has higher solubility in the austenite phase [31]. Nitrogen has a pronounced effect on the corrosion resistance of the DSS alloy. It plays a role in determining the intergranular corrosion resistance by delaying the formation of $M_{23}C_6$ [58], [55]. Nitrogen also acts in synergy with Mo, which

positively influence pitting corrosion resistance of DSS: N dissolves to form ammonium ions at the alloy surface which, by locally changing the pH, favours the formation of molybdate ions [59]. This synergistic process, not acting in single phase alloys, and easily occurring is DSS by the coexistence of the two phases with different compositions, is the main contributor to the superior pitting corrosion resistance of DSS relative austenitic stainless steels for a similar PRE [59]. Finally, N has a beneficial influence on mechanical properties through strengthening of the austenite, and retarding the precipitation of detrimental phases such as σ and χ [55].

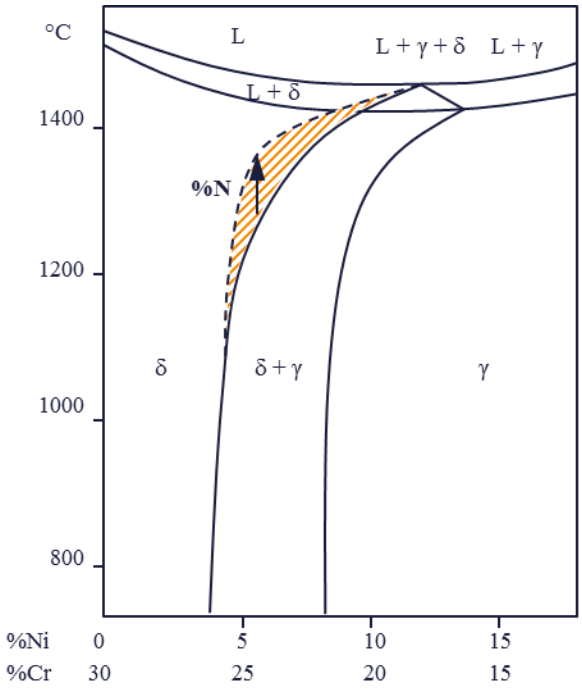

Figure 2.5: Schematic effect of nitrogen additions on the pseudo-binary Cr-Ni 68 Fe phase diagram [3]**. The hatched area shows the increase of the δ+γ area induced by the nitrogen addition.**

2.1.4.3.4 Molybdenum

Molybdenum is a ferrite stabiliser. The addition of Mo enhances the localised corrosion resistance of these alloys (pitting and crevice corrosion resistance) [4] [60], by playing a dual role within the passive layer. Firstly, Mo strengthens the re-passivation process by the formation of molybdate ions as the pits develop. The Mo also decreases the alloy corrosion rate by substitution for Cr and Fe ions at the metal/oxide interface [61], [4], [59]. The influence of Mo is reflected in the PREN equation which suggests that the effect of Mo is more beneficial than Cr for localised corrosion resistance of DSS [62].

However, by decreasing the solubility of C, the addition of Mo promotes $M_{23}C_6$ precipitation, which, in turn, reduces the intergranular corrosion resistance [55]. The addition of Mo also contributes to the formation of the detrimental intermetallic phases σ, χ and Laves phase and it enables their precipitation after long time exposure at elevated temperatures.

2.1.5 Manufacturing processes for DSSs

Manufacturing processes have a fundamental influence on DSS microstructures. The process most widely used for DSS components and pipeline is the forging process, which generates an anisotropic structure of austenite grains in a ferrite matrix. HIPed manufacturing, used for complex shape components, produces a homogeneous microstructure with equiaxed and evenly-distributed austenite and ferrite grains. This microstructure is obtained from atomised DSS powder packed into a canister to which high pressure and temperature are applied. The products obtained show high dimensional accuracy and superior mechanical properties than traditionally produced (forged/rolled) components and for this reason are becoming more widely used in subsea structures. Figure 2.6 gives an example of the microstructure obtained from a rolled DSS pipe and HIPed component.

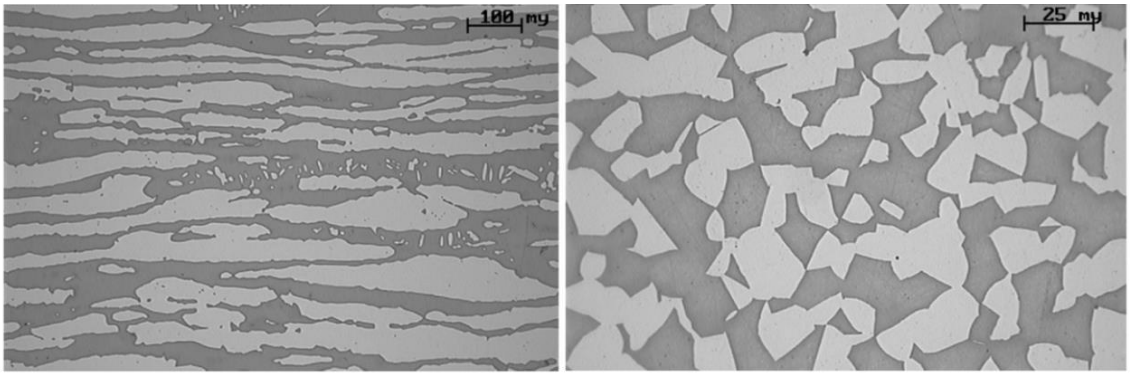

Figure 2.6: a) Forged and b) HIPed DSS microstructures [63]**.**

2.1.6 Micro-mechanical deformation mechanism in DSS alloy

The deformation mechanism of DSS is complex due to its dual-phase microstructure. This micro-mechanism has been studied using different characterisation techniques:

advanced microscopy (i.e. AFM, EBSD, TEM and digital image correlation [64][65]) as well as time of flight neutron and X-Ray diffraction [66] [67].

First of all, with a fcc crystallographic structure, the austenite phase is composed of 12 closely packed slip systems with a lower critical resolved shear stress than the ones of the bcc ferrite phase. In fully austenitic alloys, the low stacking fault energy (SFE) also enables twinning mechanisms to take place. Furthermore, the different thermal expansion coefficients of austenite and ferrite lead to the development of residual stresses in both phases during solidification and cooling. Tensile residual stresses are present in the austenite phase, compensated by compressive residual stresses in the ferrite phase [68].

As load is applied to the bulk material, strain increases at the interphase boundaries and in the austenite grains. Those plastically deform in a heterogeneous manner, depending on their orientation relative to the loading direction. This deformation occurs by slip mechanism and not by twinning as the SFE is high in the dual-phase microstructure [69]. This deformation induces dislocation piles-up against grains boundaries [67] and so the austenite phase is work hardens [66]. The orientation relationship between austenite and ferrite in DSSs is mainly K-S enabling the transfer of dislocations from austenite to ferrite [64]. However, in the case of a different orientation relationship between bcc ad fcc crystals which does not enable dislocations transfer at the interphase boundary, accumulation of stress/strain develops and leads to potential crack initiation sites. If the load is maintained, straining of ferrite finally occurs in a homogeneous manner.

2.2 Hydrogen induced stress cracking (HISC) in DDSs

2.2.1 Description of the context

2.2.1.1 HISC definition and challenges

Hydrogen induced stress cracking is an embrittlement mechanism requiring the coexistence of hydrogen, stress and a susceptible microstructure. However, the threshold level of hydrogen content, stress and precise microstructural requirements to induce cracking are interdependent. As a consequence, if the hydrogen level is very high, cracking will occur at a lower stress intensity and microstructure susceptibility thresholds: phase balance, presence of intermetallic in the microstructure, grain size. This interdependence is shown schematically in the following Figure 2.7.

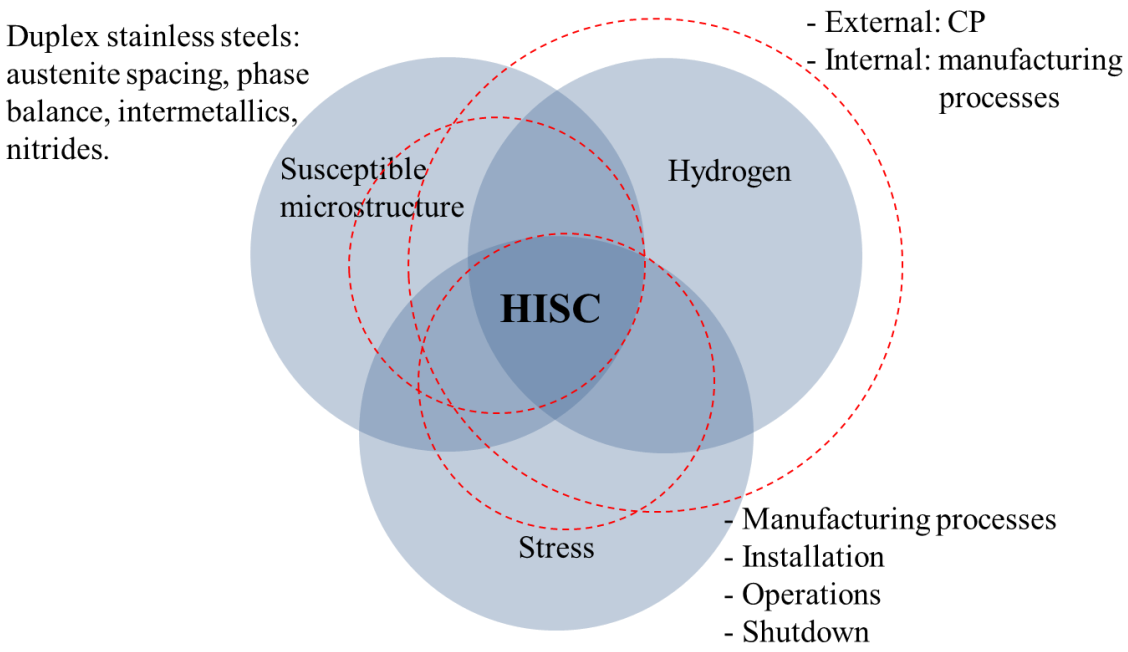

Figure 2.7: Scheme representing the requirements for HISC. Red dotted circles represent an increase of hydrogen content leading to a smaller stress level and less susceptible microstructure to induce HISC.

The high strength and corrosion resistance of DSS, discussed in the preceding sections, have made them ideal materials for use in subsea environments [70]. In the 70's, these alloys were widely used by the oil and gas industry in offshore structures. In 1989, the first case of SDSS and DSS failure occurred in the North Sea (Brae field), and the components were retrieved to the surface for investigation [71], [72]. The cause of

theses failures was attributed to the coexistence of hydrogen in the microstructure coupled with overload while handling the cold worked components leading to hydrogen induced stress cracking (HISC). The same mechanism of HISC is also reported to be the cause of DSS subsea bolt failures [73].

At that time, the susceptibility of DSS to hydrogen induced stress cracking was known [9] but a detailed understanding of the mechanism had still to be established. Hence, following these major failures, significant effort was directed towards investigating this embrittlement mechanism further in order to produce suitable guidelines for the use of DSS and SDSS alloys in subsea environment [74]. The research mainly focused on the design of subsea structures and it was found that only stresses above the material UTS generated embrittlement at cathodic potentials lower than -700 mV_{SCE} [75]. The industry also relied on the other DSS and SDSS components in service for almost 10 years under CP that did not suffer from hydrogen embrittlement. Following the very new failure experiences, design guidelines were developed, establishing stress limits[73].

However, despite these precautions, five major HISC failures of DSS components occurred between the end of the 90's and mid-2000 in the Norwegian and UK oil fields: Foinaven field, North Sea in 1996 (BP)[76], Scott field (Amerada Hess); Chevron Texaco-Conoco Britannia field (Conoco) in 1999 [Hydro technology and project, DNV No. 2004-3471], Garn West field (Shell)[77] and Balder (ExxonMobil) [78], ChevronTexaco Kuito Failure (Offshore West Africa). These catastrophic HISC failures led to further investigation in order to develop better guidelines for the use of DSS under cathodic protection, leading to the DNV Recommended Practise, in 2008 [79], but the fundamental mechanism is still not understood [80].

At the present time, HISC failures of DSS and SDSS components are still occurring, mainly due to unpredictable events, such as, a sudden temperature drop from shutdown, seabed movement inducing a high local stress concentration. At the same time, there is a requirement from the oil and gas companies that the guidelines are not excessively conservatives. For these reasons, a better understanding of the fundamental mechanism of HISC is needed.

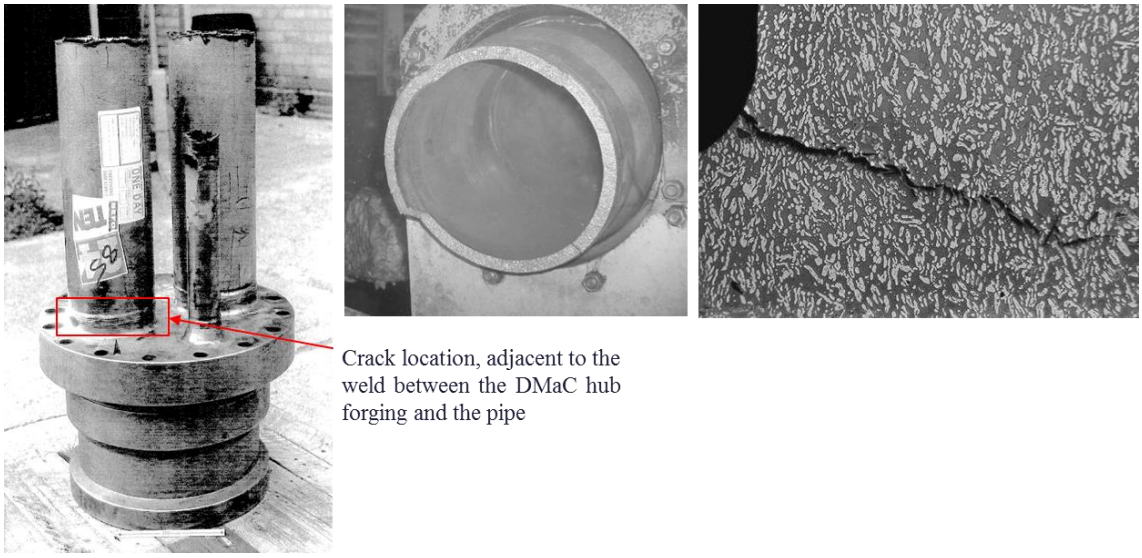

Figure 2.8: a) Foinaven failure [76]**, b) Garn west failure** [77]**, c) micrograph cross section outboard side of the hub,**[77]**.**

2.2.1.2 Hydrogen behaviour in DSS

Hydrogen ingress and embrittlement results from a series of processes involving: the transport of hydrogen to the metal surface, hydrogen adsorption at the metal surface and hydrogen absorption and transport within the metal lattice. In subsea environments, hydrogen occurs at the metal surface mainly as a result of the application of cathodic protection (CP). The cathodic current, induced by the coupling of zinc sacrificial anodes with the subsea installations and the application of a cathodic potential, is required to protect ferritic parts from seawater corrosion. However, these ferritic parts are connected to DSS components, and thus the CP leads to hydrogen generation over the entire surface of the structure.

Hydrogen adsorption can result from Van-der-Waals interactions: physisorption or chemisorption [81]. The latter is the adsorption mechanism of interest in the case of hydrogen-metal system. Hydrogen ingress, following adsorption, competes with two recombination processes: chemical recombination from two hydrogen atoms adsorbed, and electrochemical recombination of an adsorbed hydrogen atom and a proton. The propensity for of these mechanisms to take place, shown schematically in Figure 2.9 is influenced by the prevailing chemical environment, the nature of the metal surface and the stress state of the metal sorbent (apply, residual or both). After hydrogen being

adsorbed by the metal surface, it can be dissolved within the lattice. Absorption is defined by the rate of hydrogen entry into the material.

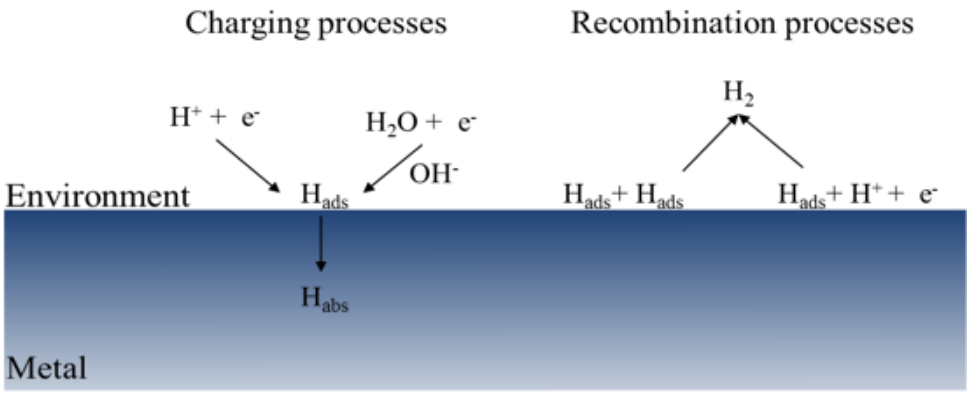

Figure 2.9: Scheme of the adsorption reaction taking place on the metal surface [82]**.**

Transport of hydrogen presents within the metal lattice is a combination of solubility and diffusion properties. In the particular case of DSSs, hydrogen transport is related to hydrogen behaviour within ferrite and austenite phases. Solubility is the relation between the hydrogen content and pressure, which is mainly determined by the crystallographic structure of the metal. Indeed, hydrogen is first located at the interstitial sites so their volume and density is determinant. In DSSs, due to the different crystallographic structures of ferrite and austenite, the solubility of hydrogen in austenite is much greater than in ferrite: $S_\delta \approx 0.70$ ppm and $S_\gamma \approx 70$ ppm [83], resulting from the higher number of tetragonal sites within the fcc lattice, Figure 2.10. The solubility can be increased by the presence of defects within the microstructure [84]: vacancies, triple-points, voids, dislocations, grains boundaries, interphase boundaries, dislocations [85], [86]and [87]. Those imperfections play the role of traps for immobile hydrogen and can be of two sorts: deep or irreversible [88]. The content of hydrogen atoms trapped at irreversible traps is termed residual hydrogen.

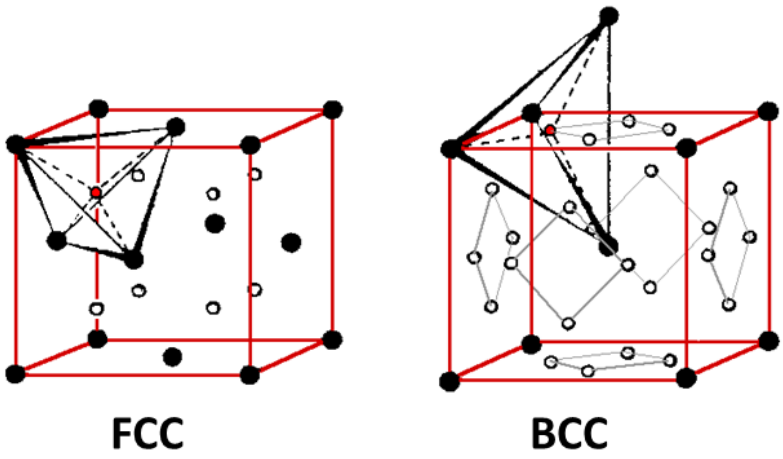

Figure 2.10: Tetragonal interstitial sites in fcc and bcc crystallographic structures [89]**.**

Hydrogen diffusion in metal is the migration of hydrogen atoms from an interstitial site to another. The term diffusible hydrogen refers to the sum of the interstitial hydrogen and the hydrogen presents at reversible traps in the microstructure[86]. The diffusion of hydrogen, D, in metals can be described by first Fick's law, which determines the flux of hydrogen atoms, J_x, according to the gradient of hydrogen concentration, ∇C:

$$J_x = -D(\nabla C)_t$$

In body centred cubic (bcc) structure, as ferrite, hydrogen diffusion coefficient is five orders of magnitude higher than that in the face centrered cubic (fcc) austenite: $D_\delta \approx 10^{-11}$ $m^2.s^{-1}$ and $D_\gamma \approx 10^{-16}$ $m^2.s^{-1}$. Hence, in DSSs hydrogen diffusion occurs mainly through the ferrite phase [8,9,10 and 11] and at room temperature, hydrogen diffusion coefficient established by permeation methods [93], is of the order of 10^{-14} $m^2.s^{-1}$ [94][95]. Hence, hydrogen transport in DSS is dependent of the tortuosity of the austenite-free path, which in turn is determined by phase percentage, phases distribution, phase orientation, grain size [96], etc. This explained that specimens extracted from the same component but according to different orientation plans can exhibit different diffusion coefficient values.

Another factor influencing transport and hydrogen distribution is the presence of internal and external stresses and strain [97],[98]. Difference in hydrogen behaviour between the two phases is enhanced by the residual stresses present within the material

after cooling. Indeed, divergence of thermal expansion coefficients resulting in compressive stresses in the ferrite and tensile stresses in austenite promotes hydrogen ingress and solubility within austenite compare to ferrite [99]. B.R.S. da Silva et al. [100] also demonstrated the increase of hydrogen apparent solubility with elastic stresses in DSS. Finite element analysis had been extensively used to model hydrogen diffusion and solubility according to the DSS microstructures and strain distribution [101], such as at the crack tip of fracture toughness specimens, [102], [103].

2.2.1.3 Analysis of HISC failures

The examination of the HISC fracture faces post-test revealed characteristics features [83], [74], [104], [75], such as a lack of necking and the presence of micro-cracks on the specimen surface close to the fracture edge [105] and [106]. This was also observed when comparing specimens strained under cathodic protection and specimens strained in air, Figure 2.11, [83] and [75]. This embrittlement effect is increased by decreasing the cathodic potential applied [75]. The influence of hydrogen is also evident on the fracture surface by a change in fracture morphology between the inner part of the specimen, with a characteristic ductile morphology of microvoid coalescence (mvc) and an outer band representative of the limit of hydrogen penetration within the sample [83][107]. In this outer, hydrogen-charged, band, the fracture morphology differs the between ferrite and austenite phases; the ferrite exhibits transgranular cleavage fracture [75] [105] while the austenite grains exhibits plastic deformation characterised by mvc (tearing) [108] and with a rougher surface appearance. [106]. Also, Figure 2.11 b), showing the side view of a HISC crack clearly shows that it propagates through the ferrite phase (dark) and get around the austenite grains. For this reason, the oil and gas industry uses austenite spacing as a mean of indicator for resistance-to-HISC of DSSs [109]. In the case of components with strong microstructure directionality the austenite spacing is measured according to the principal viewing direction. As an example, in the case of rolled materials, such as plate or pipe, the austenite spacing is measured perpendicular to the rolling direction.

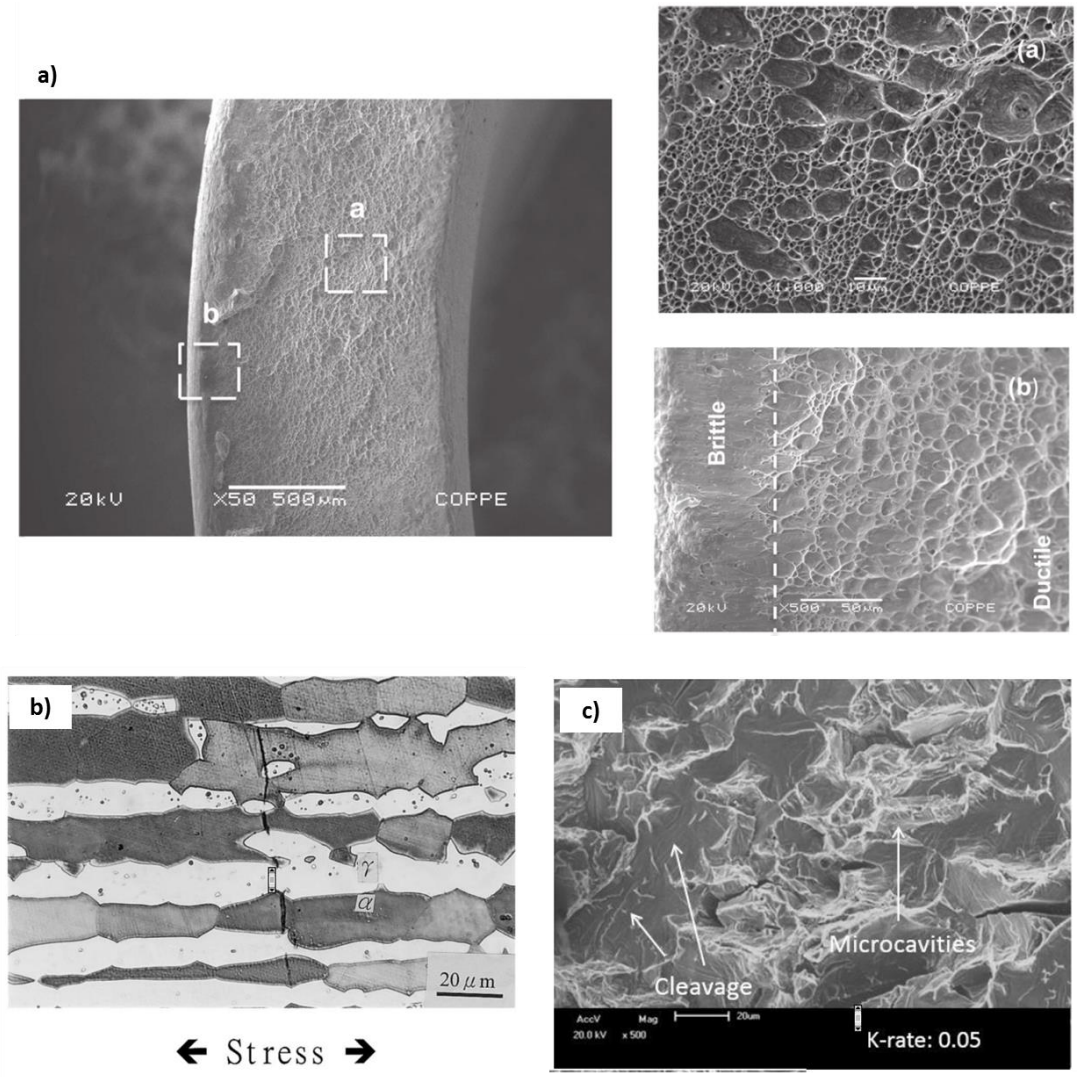

Fig. 8. Micrograph showing the internal crack in specimen B after SSRT in 26 wt% NaCl at an applied potential of −1500 mV (strain rate = 3×10^{-5} s^{-1}).

Figure 2.11: a) Fracture surface of a UNS S32750 tube tested under cathodic protection, different morphology between outer diameter exposed to hydrogen and the inner diameter[100]**; b) Internal HISC crack through ferrite phase in a UNS S32750 tested in CP** [96]**; c) fracture faces of UNS S32750 CTOD specimens tested under CP** [110]**.**

2.2.2 Mechanism of HISC in DSSs

2.2.2.1 Low temperature creep (LTC)

2.2.2.1.1 Introduction

LTC is observed in a wide number of pure metals and alloys. This phenomenon occurs at temperatures T < 0.25-0.3 Tm, where Tm is the melting temperature of the alloy, as the material undergoes a constant load test at load levels either above or below the yield

strength. Depending on the material, creep strains can be very low, from 0.1 % to 5 %. This low temperature phenomenon is often related to 'primary creep' as the first regime of high temperature creep, due to the similar behaviour of a decrease in strain rate with time, as seen in Figure 2.12.

The LTC phenomenon can be observed through the use of two static test methods, either load controlled or displacement controlled [111] and [112]. In the case of load controlled tests, as the specimen is held at a constant load level, LTC elongation is recorded. In the case of displacement controlled test, as the specimen is loaded to a constant strain level a decrease in load or stress relaxation is recorded [113], [114], [115] which is a consequence of LTC [111], [116]; in this case, LTC is observed indirectly.

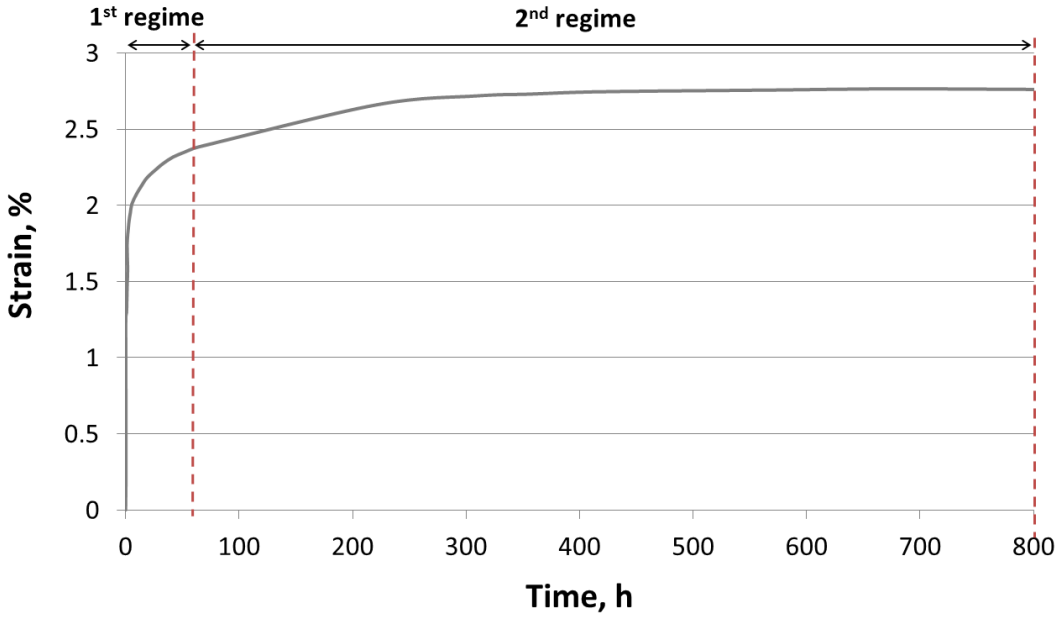

Figure 2.12: Strain development in a tensile specimen due to LTC at 98 % of the 0.2 % proof stress for a UNS S32760 [117].

2.2.2.1.2 LTC in DSS

Prior to the discussion of LTC in DSS, it is worth noting that DSS exhibit superplastic and creep behaviour at high temperatures [118], [119] and [120]. This behaviour is highly dependent on the applied strain rate and the microstructure. It is found that cold worked, refined and homogeneous microstructures exhibit higher degree of elongation than annealed and heterogeneous microstructures [118]. This behaviour is believed to

be due to dislocation slip[120], dynamic recrystallization and grain boundary and interphase boundary sliding at higher applied loads [118],[119].

Figure 2.12 shows the strain evolution vs time during constant load testing of a super duplex stainless steel (UNS S32760) at 98 % of the 0.2 % proof stress. The increase in strain at load levels below the yield stress proved the occurrence of LTC phenomenon in DSS. Two regimes can be distinguished: in the minutes following the application of the load, a strong increase in strain is detected, this is followed by a second phase where the rate of strain increase decreases until reaching a very slow strain rate through the remainder of the test [117].

Similarly to other alloys that undergo LTC, the resulting amount of plastic strain is proportional to the load applied. Figure 2.13 shows the effect of the applied load on the LTC behaviour of a DSS alloy of grade UNS S31803, as the load increases the amount of strain in also icreased.

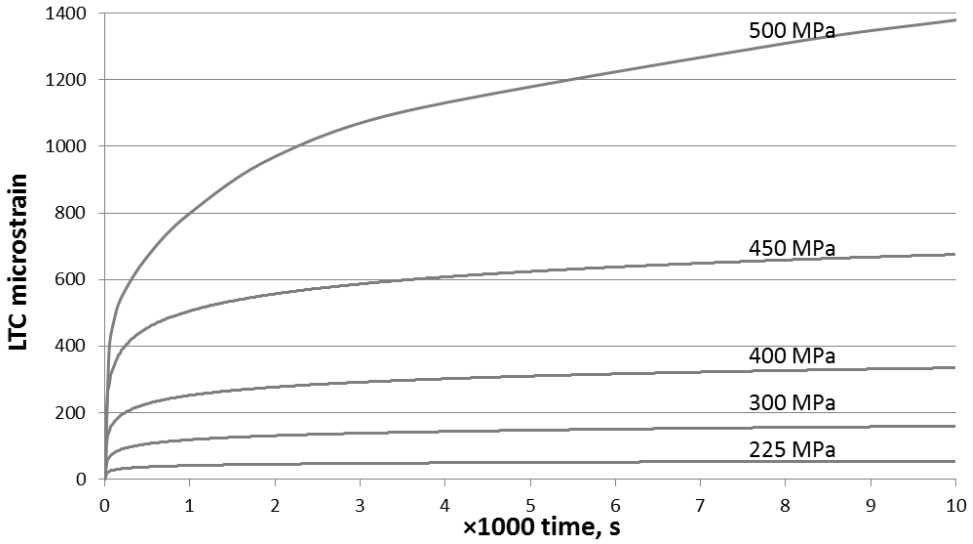

Figure 2.13: Influence of applied stress on LTC behaviour of DSS tested in constant load below the yield stress (525 MPa), data retrieved from [121]**.**

The fundamental mechanism of LTC in duplex stainless steels has yet to be established, however, despite its name, it is acknowledged that this phenomenon should not to be linked to high temperature creep deformation mechanisms [113]. U. H. Kivisakk [114] attributed LTC to the unequal stress distribution between the γ and δ phases while the material is under load. Figure 2.14 is a schematic representation of the stress

distribution between γ and δ in a DSS. In most DSS, γ is more ductile than δ. As a consequence, once stress is applied to the alloy, γ and δ experience different strain (ε_γ and ε_δ). However, in order to keep the material structure those strains tend toward ε, with $\varepsilon_\delta < \varepsilon < \varepsilon_\gamma$. Hence, δ experienced higher load than γ and deform plastically. This is supported by G. Chai and al. work [122], investigating the influence of alloying elements on the LTC micro-mechanism. The alloying elements within the material determine the phase strength and hence the micro-mechanism can vary for different DSS alloys. According to R. Francis [113] LTC behaviour is related to the mechanical properties of stainless steels that demonstrates a non-linear elastic behaviour.

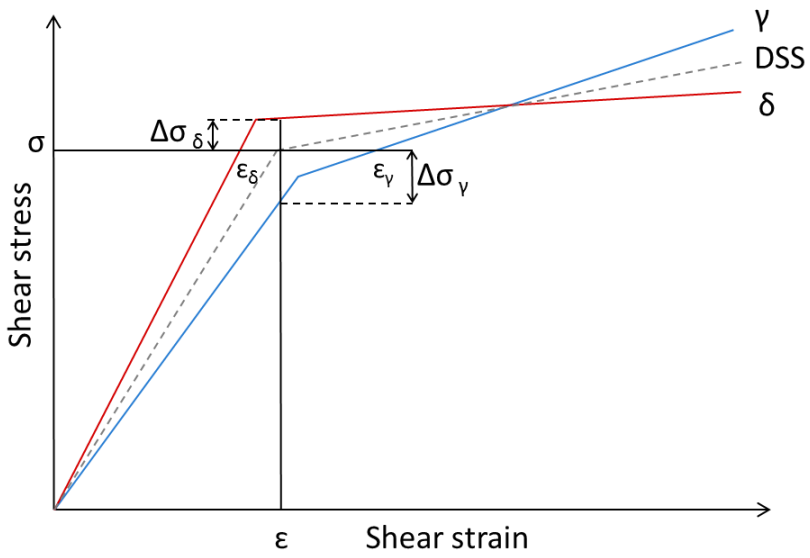

Figure 2.14: Schematic stress strain curve for a typical DSS (grey) with γ (blue) and δ (red) behaviour, retrieved from [114]

Assessment of the LTC behaviour of DSS is fundamental to understand the HISC mechanism for these grades. According to G. Chai and al., HISC results arises from the combination of hydrogen interaction with plastic loading and LTC. P.Woollin [117] distinguished HISC initiation and propagation and found that, crack initiation only occur in the presence of LTC, indicating that this phenomenon is a pre-requisite for HISC to occur.

2.2.2.2 HISC in DSS

Hydrogen embrittlement (HE) or hydrogen assisted cracking (HAC) has been an issue for many years across diverse industry sectors since it affects different metals and crystallographic structures. Many questions still remain to understand hydrogen embrittlement. Currently, three main mechanisms are discussed for single phase alloys, each of them being preponderant depending on the material and the fracture type. The AIDE (Adsorption Induced Dislocations Emission) is responsible of intergranular fracture; HEDE (Hydrogen Enhanced Decohesion) is present in brittle, intergranular fracture in very high strength material and HELP (Hydrogen Enhanced Local Plasticity) induced slip band structure is present in fcc materials such as Ni-based super alloys and austenitic stainless steels [123].

HISC occurs under the combined action of stress, hydrogen and a susceptible material. In the case of DSS the difficulty of establishing the HISC mechanism is increased by the dual phase structure involving complex hydrogen transport in the microstructure and as well as the heterogeneous distribution of stresses within the two phases while the material is under load.

A HISC crack initiates at the surface of the component [76] and [124], where the hydrogen concentration is highest. It is also observed that the crack initiates in the ferrite grains [117][106]. This could be related to the AIDE mechanism acting. More specifically, Y. Mukai and M. Murata [108] found that crack initiation was located at the ferrite grain boundaries or at the interphase boundaries and always led to the development of micro-cracking within the ferrite.

Failure investigations have shown that once a sharp crack is present at the surface of a component, the local accumulation of stress and hydrogen at the crack tip causes the crack to propagate by cleavage through the ferrite phase [104], [122], [125]. The progression of cracking is then stopped by the austenite grains, acting as obstacles[116], [108] and [122], although the smaller austenite grains, for example secondary austenite grains, are less efficient at stopping crack propagation [116].

The difference in crack propagation behaviour between the two phases is linked to their different properties in terms of hydrogen transport and mechanical response to loading. The entry of hydrogen in ferrite, due to its high diffusion coefficient, in conjunction

with cold creep, leads to cracking in the ferrite [116] [124] and [126]. Chai proposed that the HISC mechanism was influenced by the difference in the mechanical properties of ferrite and austenite. In most of the duplex stainless steels, austenite is the softer, more ductile, phase, hence, for the continuity of the system, when a load is applied to the material, the austenite experiences a lower load and the ferrite a higher load, than the total applied force. In the case where alloying elements increase the strength of the austenite, the ferrite work hardens when loaded, making it harder and more susceptible to cracking [124].

Once, the crack propagates through the ferrite and is stopped by the adjacent austenite, two scenarios can be identified for the continuation of cracking: the crack either follows the phase boundary and goes around the austenite [108], or the crack goes through the austenite. In the latter case, P. Woollin questioned whether this propagation was controlled by hydrogen ingress in the austenite or simply by mechanical loading. Oltra [125], proposed a sequence for the crack penetration in the austenite. His mechanism was based on studies of hydrogen behaviour in fcc metals, such as hydrogen in nickel alloys and austenitic stainless steels [127][128]. As the tip of the crack reaches the austenite, micro-cracking develops in the austenite phase following the {111} plane and this leads to hydrogen ingress into the austenite. Hydrogen ingress can induce dislocations generation and movement creating a local enhanced plasticity zone [127], which interacts with the previously hardened zone, creating dislocations pile ups [128]. A micro-crack advances when a critical stress and critical hydrogen concentration are reached. The crack path has a zig-zag shape, due to the fact that cracking is following {111} slip planes in the grains. The work by G. Chai supports the cracking mechanism in the austenite phase of DSS being related to the HELP mechanism in the austenite [124].

2.2.2.3 The factors influencing hydrogen induced stress cracking

2.2.2.3.1 Influence of the microstructure

Alloy microstructures result from the combined effects of composition, manufacturing route and fabrication process. In the following sections, the influence of precipitates, austenite spacing, grains orientation, pre-straining and the austenite to ferrite ratio on the HISC resistance of DSSs are reported.

2.2.2.3.1.1 Deleterious phases and intermetallic

As documented in the « Physical metallurgy of duplex stainless steels » section, precipitation of additional phases and intermetallics in DSSs leads to embrittlement and can also have a negative effect on their resistance-to-HISC. The most documented embrittlement phase is σ and, as reported by T. Cassagne [129] and K. Nakade [130] this phase and more specifically the σ/δ boundaries provide preferential sites for HISC initiation. Indeed, σ precipitation promotes the occurrence of secondary cracking and hence, drastically decreases resistance-to-HISC of DSSs.

G. Byrne et al. [131] investigated the influence of nitrides on HISC properties by performing SSRT on UNS S32760, see Table 2.1. Significant reductions in the stress to failure were found in comparison to nitride-free microstructures. On the basis of this work, the same authors explored the development of a new alloy: Zeron 100 AFP (Advanced Forged Process). Zeron 100 is a SDSS grade corresponding to the UNS S32760. The aim was to promote secondary austenite precipitation with Cr and N being dissolved from previously existing nitrides. The decrease in nitride content and increase in secondary austenite were designed to maximise the HISC resistance [132]. In the context of investigating DSS component failures, the work by M. Aursand et al. [133] looked at the influence of nitrides on the same SDSS grade, but in this instance employed SENT testing; the work showed that heat treated materials with lower nitride content exhibited a higher HISC resistance.

However, in both papers, the difficulty to quantitatively assess the nitride content is reported. Firstly, the volume fraction of nitrides in commercial alloys is low and the size of the individual nitride particles is in the order of 50nm[134] making observation by light microscopy or SEM difficult. Another challenge faced once quantifying nitrides by metallographic means is that different etchants reveal qualitatively the nitride content for a single material [135]. For these reasons, the authors can only quantitatively compare the nitride content in microstructures [136] and [133]. From their results, it is clear that higher nitride content leads to higher HISC embrittlement; however, a nitride content threshold for HISC to occur in duplex stainless steels has not yet been established.

2.2.2.3.1.2 Manufacturing processes

Manufacturing process affects two major features of the microstructures: the grain size, coarseness and the directionality, creating texture within the material. Those two features have been reported to play a significant role on the resistance-to-HISC of DSSs.

DSSs coarseness is commonly defined by its austenite spacing. DNV guidance qualifies a coarse DSSs microstructure if the austenite spacing is superior to 30µm [109]. Large austenite spacing have been reported to affect the resistance-to-HISC in two ways: crack propagation [76], [117], [116], [77], and hydrogen diffusion [124], [126]. Indeed, a HISC crack propagates through the ferrite phase and austenite grain acts as obstacles. The failure investigation carried out on a fitting from Foinaven in the North sea [116], [76] [77] revealed a coarse microstructure within the cracked pipe, leaving large areas of ferrite through which the crack could propagate, unhindered by austenite colonies. Woollin et al.[117], showed that, as austenite spacing increased, the strain to failure decreased and thus the resistance-to-HISC was reduced.

In the work carried out by G. Chai et al. [124], higher hydrogen diffusion coefficient was measured in the coarser microstructure, which is consistent with a coarse microstructure being more susceptible to HISC. Furthermore, grain boundaries are known to act as trapping sites for hydrogen and therefore, in fine grained microstructures, where the grain boundary area is higher, the time to reach critical hydrogen concentration for HISC to occur is increased. This finding is supported by P. Woollin investigation [137] , into the relationship between hydrogen content to austenite spacing; for the same applied charging potential the hydrogen concentration was higher in the coarser grained microstructure.

In view that different processes are employed to produce different materials/components determining austenite spacing, manufacturing route should be taken into account in the design of materials and structures against HISC [138]. T Cassagne [129] ranked the microstructure resulting from different manufacturing routes, according to their HISC susceptibility, in the following way: forging > rolled plates > HIP in decreasing order of susceptibility. And this is in agreement with G.O. Lauvstad [104] work on the higher resistance-to-HISC of HIPed components compare to forged ones.

In addition to the coarseness of the grain structure, the manufacturing process can results in orientation and texture of the microstructure. In other words, depending on the manufacturing route employed, the HISC resistance can vary with the loading direction and the direction of hydrogen ingress. W. Zheng and D. Hardie [9] investigated the HISC resistance of a 2205 DSS with a banded microstructure loaded in different directions relative to the rolling direction. Perpendicular to the rolling direction the susceptibility to embrittlement was lower than parallel to the rolling direction. This is explained by the probability that a growing crack is arrested by an austenite island is higher perpendicular to the rolling direction. Moreover, while the microstructural orientation influences the probability that a crack will be stopped, it also affects the hydrogen behaviour; A.Turnbull et al.[94] studied the effect of microstructural orientation on hydrogen diffusion and reported that the diffusion coefficient was higher if the hydrogen flux was parallel to the direction of elongated austenite. This is related to the complexity of the hydrogen path, this being lower in the longitudinal direction than in the transverse direction [95].

The microstructural homogeneity is therefore another factor of the manufacturing method that must be taken into account when designing DSS components against HISC.

2.2.2.3.1.3 Cold working

The cold work of DSS parts is, in many instances, unavoidable as it is a requirement of the manufacturing process. Moreover, as cold work increases the material strength, it can actually be perceived as advantageous by industry. However, P. Sentence [139] investigated a failure of a heavily cold worked DSS pipeline that failed in the Marathon's Brae field in the North sea. It was found that the pipeline contained a critically high hydrogen concentration. S.S Chen [140] investigated the influence of cold work on a 2205 DSS with and without hydrogen charging, using tensile tests and a permeation experiment. A.Elhoud [84] and al. studied the influence of a lower level of cold work on DSS properties in air and under cathodic charging. Displacement controlled tensile tests were performed on UNS S39274 DSS at a strain rate of 1mm.min-1. The results from both investigations are presented in Figure 2.15. Although the measure of the embrittlement is different, as reflected by the two scales, as well as differences in the materials and the charging methods adopted in the two studies, the main trend can still be distinguished; firstly, the data show that cold work induces a loss of ductility of DSS in the absence of hydrogen. In addition to a reduction

in the elongation to failure, S.S. Chen et al. [140] reported an increase of the UTS of the alloy and A. Elhoud et al. [84] reported an increase in the yield strength and a decrease in the extension to failure. The addition of hydrogen charging enhances the embrittlement phenomenon as can be seen from the Figure 2.15. The fracture surface analysis confirmed this finding [84]: the depth of embrittlement, within the typical HISC embrittlement zone around the surface of the sample, was increased following cold working and extensive ferrite cleavage and transgranular cracking were observed.

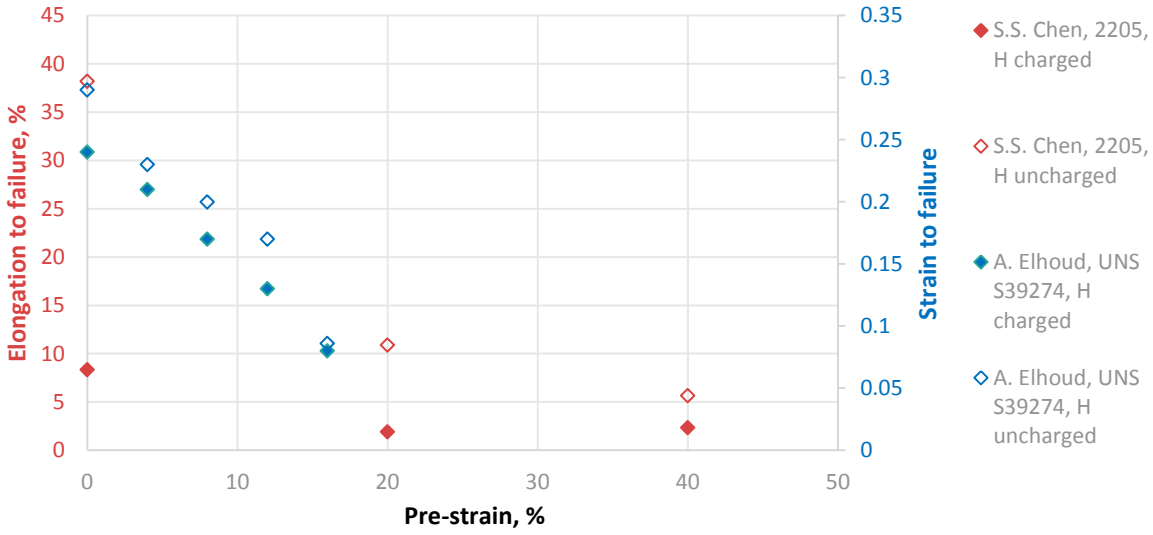

Figure 2.15: Cold work influence on DSS embrittlement with and without H pre-charging. Results from S.S Chen[140] **and A. Elhoud** [84]**.**

An explanation for this behaviour is linked by different authors [140], [84], [141], [142] to the hydrogen behaviour in deformed material. A. Elhoud attributes the decrease in HISC resistance with cold work to an increase in the solubility of H in the material enhanced by plastic deformation. Permeation experiments on cold work DSSs have demonstrated an increase compare with un deformed materials [140], [142]. Hydrogen permeation is a combination of hydrogen intake, hydrogen solubility and hydrogen diffusion.

Y. Huang [141] discusses that, by increasing the dislocation density, plastic straining increases the trapping sites, which lower diffusion coefficient in the heavily cold worked material. The increase in permeability is explained by higher hydrogen ingress into the material resulting from an increase number of active sites for hydrogen

generation at the contact of the deform surface: higher hydrogen adsorption of deformed materials. A.J Griffiths and A. Turnbull, however recorded greater total hydrogen content in the cold work material but with a higher diffusion coefficient, when studying UNS S31803 DSS at 80°C. The assumption is made here that cold worked materials could exhibit a lower concentration of trapped hydrogen and a less tortuous path for hydrogen to diffuse within the ferrite.

Finally, M. Aursand investigated cold worked DSS components that failed through HISC [133]. This work highlighted that even if cold work has been demonstrated to decrease HISC resistance of DSS, no specific guidelines have been developed to account for this other than through hardness testing, which, in most cases, is not able to detect local or superficial regions of increased susceptibility that have been exposed to high deformation.

2.2.2.3.1.4 Ferrite to austenite ratio

DSS are manufactured to ideally contain 50 % ferrite and 50 % austenite, however, when subjected to heat treatments or welding this ratio can change, either locally or through the entire microstructure. As the two phases have different mechanical properties and response to hydrogen ingress and diffusion, a change in the phase balance can lead to significant changes to the HISC resistance.

As reported by P. Olsson [83], Cun-Jan and Jargelius studied the influence of phase balance between 36 % and 70 % ferrite in a UNS S31803 on the HISC resistance. A significant increase in HISC susceptibility was observed with increasing ferrite content. A similar observation was reported by R. Francis et al.[73], about the work of D. Hutchings, in which a drop of 77 % in elongation ratio was measured with an increase in ferrite content from 50 % to 70 % in a UNS S32760 DSS; in this case the interruption of crack propagation by austenite grains was less probably due to the overall lower volume fraction of austenite.

Mukai et al. [73] investigated the change in HESCC (Hydrogen Embrittlement Stress Corrosion Cracking) resistance of DSS with ferrite contents varying from 40 % to 100 %. In this study 45 % ferrite was set as the critical ferrite content for HESCC. Above 60 % ferrite no further embrittlement is observed.

Commercial DSS are generally specified to have a δ/γ percentage between 40 and 60 %. P. Woollin et al. in his work [117], showed that this ratio is not critical, as the results indicated that with a microstructure containing between 40 and 67 % ferrite, the effect of phase balance was secondary to the influence of austenite spacing.

In conclusion, the microstructure, which is determined by the interaction of the composition, fabrication process and thermomechanical treatments, is principally responsible for defining the HISC resistance of DSS. However, between the different factors discussed in this section it is not possible to assign any ranking in their significance although, for commercial alloys, it has been found that a coarse 'banded' microstructure is particularly deleterious for HISC resistance[116].

2.2.2.3.2 Hydrogen

2.2.2.3.2.1 Source of hydrogen

Hydrogen can be present in the microstructure prior to operation, internal hydrogen, or ingress into the microstructure from the service conditions, external hydrogen. In both cases, increase in hydrogen content in the microstructure induced loss of ductility in DSS.

Following the failure of heavily cold work pipelines in the Brae field in the North Sea, Sentance [139] carried out a comparative study of the HISC susceptibility between cracked and un cracked components. From this work, a minimum hydrogen concentration of 15ppm was established for cracking to take place. The same grade of DSS was investigated by A.J. Griffiths and A. Turnbull [143] through permeation experiments and SSRT (slow train rate test) programme, conducted at 80°C. The threshold of total hydrogen concentration for cracking determined was significantly higher: between 100 and 250 ppm. Zackroczymski et al. [144], measured the hydrogen concentration in a UNS S31803 duplex stainless steel, by desorption technique, after mechanical testing. Significant decrease in ductility at a total hydrogen concentration of 26 wt%ppm, with an associated drop in the time to failure was measured.

There is a large disparity, reported in the literature, regarding the thresholds of hydrogen content to induce cracking. This highlights the influence of the charging conditions and microstructure on the cracking mechanism[9] and [83]. Also, the limitation to measurement of hydrogen concentrations and the establishment of

thresholds is that these do not provide information on local hydrogen distribution, which could be the cause of local embrittlement, leading to further cracking.

2.2.2.3.2.2 Charging conditions

A number of different methods for hydrogen charging exist. Thermal charging consists of heating the sample up to a temperature close to 300°C in a hydrogen atmosphere. The samples are then stored in liquid nitrogen to avoid hydrogen evolution prior to hydrogen measurement [9]. Although very efficient in introducing high hydrogen content in the material, this method is very severe and can lead to microstructural changes in the material due to the high temperature and pressures employed. This technique can be used to simulate H embrittlement from a welding process but it is not representative of the charging in a subsea environment. For the latter, a more representative option is the electrochemical charging. This technique consists of placing the material into a conductive solution and applying an electrical potential. In order to reproduce the in-service cathodic protection conditions, seawater (or a simulated seawater/NaCl solution) is generally used with an applied potential of between -600 mV_{SCE} to -1500 mV_{SCE} [117] [104]. This method also allows the study of other environmental variables such as sulphide concentration, pH, etc. by the addition of H_2S, H_2SO_4 to the solution [83], [143], [145]. An increase of hydrogen ingress in the microstructure can also be achived by the use of 'poisons' such as' As_2O_3, $NaAsO_2$, which hinder the hydrogen recombination reaction at the material surface [144], [146].

2.2.2.3.2.3 Influence of the applied cathodic potential

A. J. Griffiths and A. Turnbull [143] presented a relationship between hydrogen uptake, charging current density and applied potential during testing of DSS under CP conditions. As the potential decrease towards more negative values (i.e. increase in absolute value), the charging current increases, and the total hydrogen content in the material rises. This relationship between potential and hydrogen content was also shown by P. Woollin et al. [117], independently of the material investigated. Hence, as the applied cathodic potential is lowered, the embrittlement of the material increases [117], [145], [96], [73].

The following works [117], [75] on UNS S22760 and [108] on a SUS 329 J1 investigates the influence of cathodic protection potential by establishing strain thresholds for cracking, reduction area, and time to failures under constant load testing.

An agreement was found between these data on a cathodic potential threshold of -800 mV_{SCE} under which the material is severely embrittled. Figure 2.16 compares those results: the use of different testing methods and embrittlement assessments converge on a decrease of material performance between -800 mV_{SCE} and -900 mV_{SCE} applied potential. However, Tsai et al. [145] found a significant decrease in the strain to failure was reported towards the lower end of the applied potential: final elongation reductions from 44 % to 18 % between -1000 mV_{SCE} and -1500 mV_{SCE} respectively, which is less severe than found in the studies previously. These findings highlight the dependency between the DSS microstructure tested, the charging conditions and the test parameters.

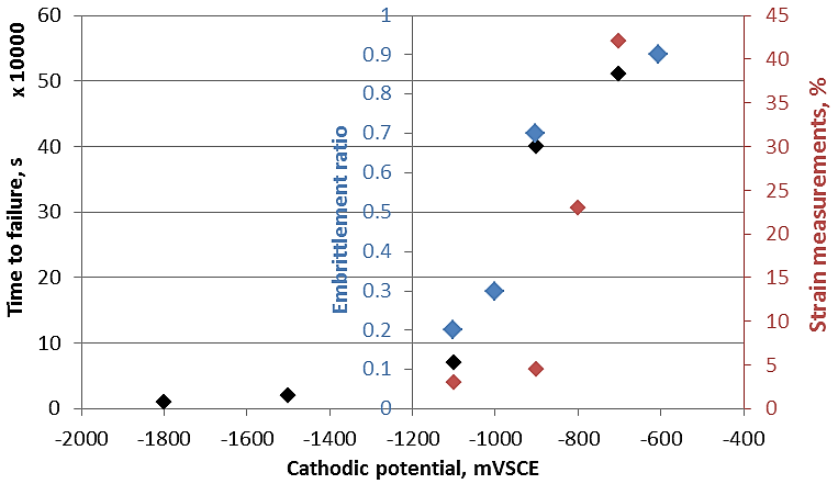

Figure 2.16: Graph showing the potential influence on embrittlement of an UNS S32760 and a SUS329J1. Embrittlement measured through strain threshold for crack initiation [117]**, the reduction area ratio** [75] **and time to failure** [108]**.**

2.2.2.3.2.4 Temperature

The temperature is another testing variable and this should be representative of the service conditions. In the case of subsea applications, there are three key temperatures; 4°C, the temperature of deep-sea water, 1000 feet, relevant to shut-in and assembly conditions; ambient temperature representative of the environment of the component prior to submersion and 80°C, the operating temperature.

Following the Foinaven failure in the North Sea, A. Bahrami and P. Woollin [137], identified existing gaps within the DNV RP F112 [79] 'Guidance for design of DSS against HISC' document. In this work, the influence of temperature was assessed by means of load controlled tests on UNS S32760 and UNS S32205. The results showed

that increasing the temperature from 20°C to 80°C increased the normalised stress threshold for HISC initiation and subsequent propagation of a crack. However, in the component tested at 80°C, the hydrogen content was found to be higher and more cracks were found to have initiated, though not propagated. Similar behaviour was observed in the results of SSRT tests reported by P. Olsson et al. [83], to look at the effect of temperature on HISC behaviour of a UNS S31803. A lower time to failure was recorded for the specimen tested at 20°C compared to the one at 80°C, but for this latter specimen the reduction of area compared to that reported for the tensile test in air, was larger, and, as seen in the work by A. Bahrami and P. Woollin, the H concentration was higher for the sample tested at 80°C for both the SSRT and load controlled tests. These results complicate the explanation of the influence of temperature on HISC resistance. F. Elshawesh et al. [147] investigated the temperature effect on HISC susceptibility for a UNS 31803/32205 duplex stainless steels. Displacement controlled tests were carried out at 22°C and 70°C under cathodic charging. Here as well, embrittlement was more severe at lower temperatures, with a reduction in elongation observed at room temperature compared to that at 70°C. This finding is supported by the work of A.J. Griffith and A. Turnbull [148], involving SSRT testing of a similar composition alloy at 80°C and 20°C. In this work, a significant drop in the plastic strain to failure was noticed between the test at 80°C and the one at 20°C. An increase in charging current density was also noticed with increased testing temperature.

However, in the case of investigating the influence of the temperature on pre-charging the higher temperatures are found to be more detrimental. J. Hsu et al.[149], carried out tensile testing of UNS 31803/32205 duplex stainless steel after pre-charging the specimens at 25°C, 45°C, 60°C and 80°C. In this case, specimens pre-charged at higher temperatures exhibited lower fracture strain and a larger embrittlement area.

These results are related to hydrogen behaviour in DSS. Permeation experiments showed that diffusion coefficients increased with temperature [85], leading to higher hydrogen ingress into the material [142]. This, in turn gave rise to a larger embrittlement zone, evident on fractography examination with increased pre-charging temperature [149]. Where the test itself was performed at higher temperature: 80°C compared to 20°C, a higher level of crack initiation was recorded by A. Turnbull and A.J Griffiths showing increased current density with increasing temperature. Moreover,

at 80°C, a more homogeneous distribution of hydrogen develops within the material than at 20°C, whereas at the lower temperature the hydrogen accumulates at the crack tip [129].

2.2.2.3.3 Stress

Stresses can be induced in the material at any point of the component life: fabrication (residual stresses), installation and operation and this in turn can promote HISC. As described in the paragraph on hydrogen transport in DSSs, internal and external stresses increases hydrogen concentration [97],[98] and once a critical amount of hydrogen and stress are combined HISC can occur.

2.3 Evaluation of resistance-to-HISC: testing methods

2.3.1 Introduction

In order to improve design against HISC, testing methods have been developed involving testing in environments that replicate as closely as possible the service conditions, but which can be carried out on a scale and in a time frame that makes them suitable for use in industry. In this case, the time, the type of loading, the defects such as buried defects, material homogeneity, are difficult to reproduce [83] and [111].

DSSs resistance-to-HISC depends widely on material microstructure, such as phase fraction, austenite spacing, austenite distribution, presence of deleterious phases; as well as the type of loading and the environmental factors [2], [88]. Different testing approaches can be used, the main ones being: tensile testing, fatigue testing and fracture toughness testing, each of them having different outcomes. In those three cases, the following parameters have to be considered: 1) the test control parameter: load, displacement or displacement rate; 2) the mode of loading, 3) the specimen type and geometry, 4) the environment. While tensile testing aimed to establish material performances and material ranking, fracture toughness is concerned with the structure integrity of a component, however, both methods are affected in the same way by these testing parameters. In the proceeding sections, the concepts of fracture mechanics are presented and followed by the influence of testing parameters on tensile testing and fracture toughness testing.

2.3.2 Fracture toughness testing

2.3.2.1 Introduction

Apart from the evaluation of material performance, fracture toughness testing aims to evaluate the structural integrity of a component, in the presence of flaws. Flaws in components are common and can be introduced during manufacturing, installation and operation for example by mechanical damage or corrosion. The presence of such defects induces local stress concentration, changes in the stress distribution and the potential for cracking during operation. Hence, fracture mechanics was developed to address this issue and to determine the resistance of a material to crack extension [150]. Fracture toughness is a widely-adopted industrial practice and the methods have proved to be relevant and useful for obtaining quantitative input (i.e. crack growth/extension via tearing) for engineering critical analysis (ECA), from tests carried out in air. Two main fracture toughness approaches exist, depending on the material investigated: linear elastic fracture mechanics (LEFM) for brittle materials, and elastic plastic fracture mechanics (EPFM) for more ductile materials.

2.3.2.2 Linear Elastic Fracture Mechanics (LEFM)

In the case of brittle materials, linear elastic approach is developed from the atomic level: material fracture is a rupture of the atomic bonding. The corresponding cohesive stress is σ_c :

$$\sigma_c = \sqrt{\frac{E\gamma_s}{x}} \tag{6}$$

With E: Young modulus; γ_s: surface energy and x_0: the equilibrium spacing of atoms. However, in practice, the applied stress in order to initiate material fracture is found to be well below the cohesive force. This finding highlights the significance presence of flaws and stress concentrators within materials.

The stress intensity factor, K, characterising the elastic deformation at the crack tip is introduced. The following equations are valid in the case of mode I of fracture. This value is dependent of the geometry of the crack and the body. From this component the stress and strain at the vicinity of the crack tip are:

$$\sigma_{ij} = \frac{K}{\sqrt{2\pi r}}\sigma_{ij}(\theta) \quad (7)$$

$$\varepsilon_{ij} = \frac{K}{\sqrt{2\pi r}}\varepsilon_{ij}(\theta) \quad (8)$$

K: intensity factor; σ_{ij}: stress singularity; ε_{ij}: strain singularity; r: radius of the investigated zone at the crack tip. These mathematical expressions are valid in plane stress and plane strain conditions, Figure 2.17, which are dependent on the geometry. Once a critical stress intensity factor, K_C, is reached the crack propagates. K_C is the fracture toughness of the material. The intensity factor can also be defined using an energy based approach:

$G = \frac{1-\nu^2}{E}K^2$, in plane strain conditions; (9)

$G = \frac{1}{E}K^2$, in plane stress conditions; (10)

where G is the rate of change of energy potential of the system. The crack advances once G reaches a critical energy value, G_C. This approach is only valid for material that does not undergo plastic deformation before cracking.

2.3.2.3 Elastic-Plastic Fracture Mechanics (EPFM)

This approach is an extension of the LEFM for elastic-plastic materials, such as DSSs. In this case, the crack tip of elastic-plastic materials undergoes deformation before cracking. This method is based on the J-integral and CTOD parameters.

Unlike in the elastic approach, in elastic-plastic (non-linear elastic) materials the fracture parameters are influenced by the plastic zone developing at the crack tip as stresses are applied. The shape of this plastic zone depends on the loading conditions defined in Figure 2.17.

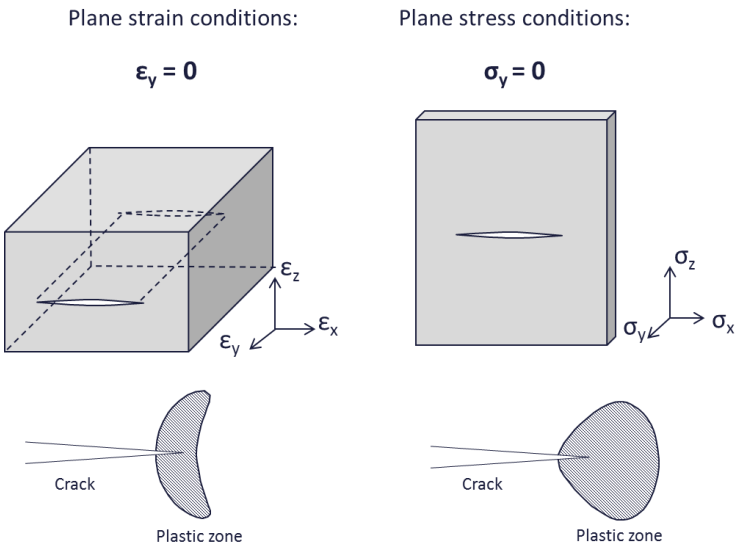

Figure 2.17: Plane strain and plane stress conditions.

In ductile materials, the crack tip can tear through the plastic zone in a stable ductile manner, absorbing energy and locally increasing the toughness at the crack tip. Figure 2.18 shows the tearing resistance, J-R curves obtained for DSS welds and representing the energy required for a stable crack to propagate where Δa is the crack advancement and J, the strain energy release rate for a more generalised LEFM for non-linear elastic materials. The first part of the curves, almost linear and steep, corresponds to the blunting of the crack tip, from which the crack initiates as the load increases.

The values of J depend on the specimen geometry, and are valid in the case where the plastic zone at the crack tip is small compare to the crack length. This path independent integral is defined by the following mathematical expression:

$$J = \int_{\Gamma} (W dy - t \frac{\partial u}{\partial x} ds) \tag{11}$$

With, Γ the contour surrounding the notch tip, ds is an element of arc length along Γ, u the displacement vector, t the traction vector, (x,y) Cartesian coordinates, and W the energy density defined as:

$$W = \int_0^{\varepsilon} \sigma_{ij} d\varepsilon_{ij} \tag{12}$$

σ represents the stresses, ε is the infinitesimal strain tensor and [151].

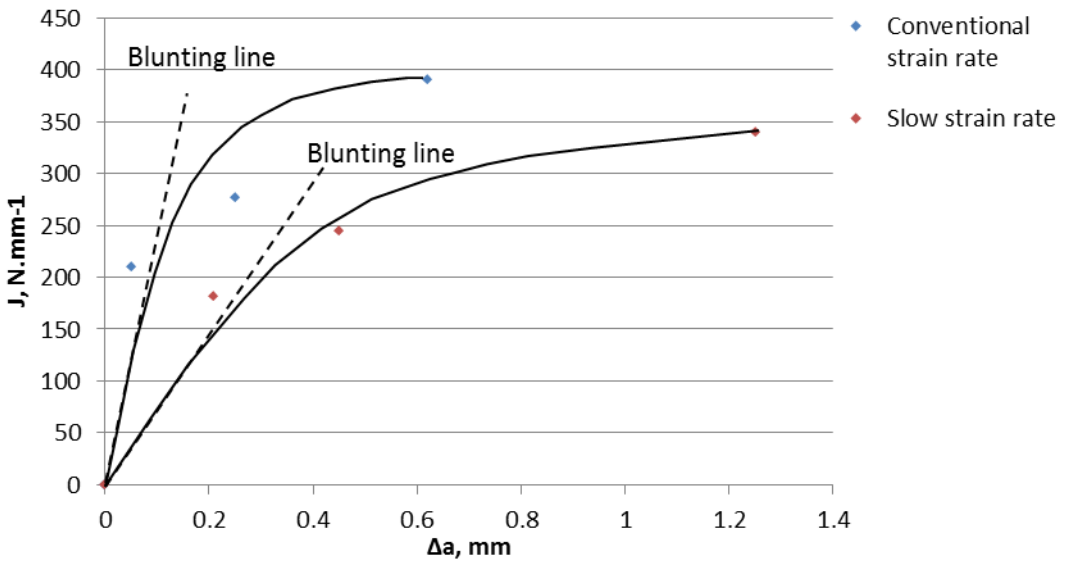

Figure 2.18: Resistance curves of a duplex stainless steel welds at two different strain rates [152]**.**

Another parameter commonly used in a resistance curve is the CTOD (Crack Tip Opening Displacement), δ_t. This parameter is defined by the opening displacement of the original crack tip or by the displacement at the intersection of a 90 vertex with the crack faces, Figure 2.19.

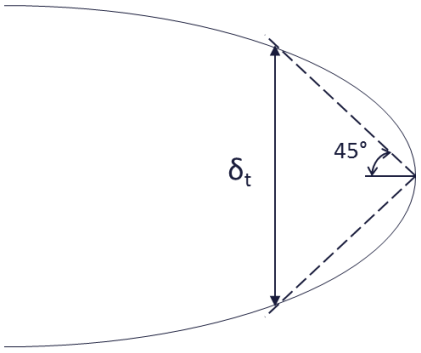

Figure 2.19: Scheme of the crack tip opening displacement, δ_t.

2.3.3 Testing parameters

2.3.3.1 Test control parameter

2.3.3.1.1 Constant load test

Constant load testing is a simple concept where samples are tested under a fixed, dead-weight load for a period of time, often while immersed in a potentially corrosive environment. During the test, the strain is measured and the time to failure is recorded. This method can be used in uniaxial tension, where the strain is measured with an extensometer, or in a bending configuration for the investigation of the material's resistance to environmental cracking, on notched or un-notched specimens [114]. In the case of HISC assessment, testing is carried out in a hydrogen-charging environment.

In addition to the environmental parameters (e.g. applied potential, temperature) constant load tests allow the effect of time and load to be studied, depending on the test procedure. In the case where the test is stopped before the sample failed, the determination of stress and strain thresholds for crack initiation and propagation can be made [117]. Conversely, if the test is not interrupted and time to failure is recorded, the influence of environment conditions and time can be assessed [108]. This test method is used in air to investigate low temperature creep phenomenon [117], [126], [153] as it does not allow the material to relax. Therefore, depending on the application targeted, the results can lead to conservatism [137].

2.3.3.1.2 Step loading testing

A step loaded approach, described by ASTM F1624 [154], was developed to reduce the testing time and material wastage associated with sequential constant load tests. The samples are held under a constant load for a predetermined time. In the case where the sample does not fail, the load is increased gradually and sustained until cracks are detected in the sample. Johnsen et al. [88] established a method that aimed to determine the critical load by step loading with only three specimens. In this configuration, it is recommended to carry out a test at the previously determined critical load directly. This step ensures that the results are not conservative due to the hydrogen diffusing during the step loading periods.

2.3.3.1.3 Constant strain test

In this static mode of loading [111], the specimens are slowly loaded to a defined elongation or crack tip opening displacement (CTOD) level in the case of notched specimens [104]. The specimens are then held for a given time and monitored for crack extension. Unlike load controlled tests, the displacement controlled method leads to relaxation of the material around the crack tip, and so can result in potentially non-conservative results [137]. Hence, this is a useful test method for ranking materials but it can be non-representative of the service conditions [104].

2.3.3.1.4 Constant strain rate test

The slow strain rate tensile (SSRT) test is an incremental loading test method described by standard practices [155] and [156]. This technique is the most commonly used for HISC testing and environmentally assisted cracking (EAC) [111]. A strain rate in a range of 1×10^{-6} s^{-1} to 4×10^{6} s^{-1} is typically applied to the sample [88], in an environment simulating service conditions (e.g. simulated seawater under cathodic protection), until the specimen fails. Depending on the type of sample used, smooth or notched, the data generated from the tests include the stress-strain curve of the tested material, along with the time to failure and embrittlement susceptibility, or fracture properties, respectively [111] and [88].

While effective to rank materials or establish the influence of environmental parameters in a short period of time [111], [88] and [88] the method is not generally considered suitable for qualification purposes. Indeed, the method is judged to be too severe as the sample is put under continuous strain and so, not representative of service conditions [111], [148]. Comparison of constant load and constant strain rate results on the same DSS component show that constant strain rate results are more conservative. Another factor contributing to the severity of the test is the constant cracking of the passive layer and exposure of free metal surface and facilitates hydrogen ingress [83] and [82].

2.3.3.1.5 Interrupted slow strain rate tests

Another approach is to interrupt the SSRT. This method is extremely time consuming but allows the determination of thresholds for crack initiation and propagation: as the test is intermediately stopped, crack advancement is detected using non-destructive examination [148]. However, during the interruption of the test, the material is able to

relax and so the results are conservative when compared with constant load test results [116].

2.3.3.2 Loading mode

For constant load, constant strain and constant strain rate tests, the most common way of applying load is either uniaxial tension or bending, depending on the service conditions to be replicate; in the case of single edge notched specimens, the tension (SENT) specimen is preferred by the pipeline industry to the bend specimen (SENB) as it is considered to better represent the loads on girth weld flaws under the axial stress of a pipe [88].

Depending on the aim of the environmental test; whether for ranking materials, or investigating the effect of metallurgical and environmental parameters or simulating service conditions for qualification purposes, the specimens shape can vary from smooth to notched and/or fatigue pre-cracked. Notched samples are used to simulate cracks or stress concentration at the component surface and so directly in contact with hydrogen.

Different notches can be used to represent different stress concentration factors [157] [78]: U-notch for geometrical change; V-notch representing weld-toe and fatigue pre-crack to simulate a surface crack. The stress intensity increases from the U-notch to the V- notch and the fatigue pre-crack is the most severe configuration [102]. In addition, hydrogen diffuses to the crack tip leading to high local concentration in this type of specimens compared to smooth specimens [158]. However, only fatigue pre-cracked specimens can be used for generating data for fracture mechanics calculations and the development of resistance curves.

2.3.3.3 Specimen size

The specimen size is another important factor that can influence the results of fracture mechanics tests. P. Woollin and al. [117] found that full scale specimens have lower resistance-to-HISC than small size specimens. This was attributed to the HISC mechanism being dependent on stress intensity. Indeed, in full thickness specimens, stress intensity can reach higher values than in small sub-size specimens where the

surface crack size is restricted. The size of the specimens is a factor that must be taken into account while ranking the HISC resistance of materials.

2.3.4 Testing methodology for the assessment of HISC in DSSs

Tensile methodologies aim to establish material performance and material ranking. The performance of such tests in environment is not an issue for data interpretation and the main concern with those testing methods in the case of DSS is the occurrence of LTC in this material that can lead to conservative or un-conservative results depending on the service conditions studied.

Fracture mechanics testing however, and specifically the development of resistance curves involve theory and equations only valid under particular conditions. Hence, the performance of fracture testing in environment can be a challenge. V. Olden[159] highlights the limitation of current fracture mechanics approaches to represent the full story of the complex mechanism taking place at the tip of the crack on a specimen under CP: stress and strain distribution as well as hydrogen diffusion and solubility. As an example, the displacement rate recommended by the standards [160], [161] and [162] is not suitable for hydrogen diffusion study [110].

In spite of this, understanding of the material behaviour in environment with the presence of flaws has to be assessed. Hence, testing methodologies based around standard fracture toughness testing, have been developed to evaluate the evolution of stress and strain at the crack tip [88]; to compare the resistance-to-HISC between HIPed and forged DSSs using SENB specimens loaded to a CTOD level for a period of time [104]; to evaluate the presence of environmental parameter [158]. In these cases the resistance curves are not always plotted and the use of other parameters such as, maximum crack advancement, crack mouth opening displacement (CMOD) measured with a clip gauge, maximum CTOD, are used to assess material resistance.

2.4 The objectives of this research

This work aimed to give a better understanding of HISC mechanism in DSSs by the mean of a multi-faceted approach. The objectives of this work were:

1) Providing observations of the LTC micro-mechanism in DSSs and relate it to its influence on the resistance-to-HISC;
2) Investigate the influence of residual stresses remaining in tensile specimens on their HISC thresholds;
3) Quantitatively evaluate the effect of key microstructural and environmental parameters on cracking resistance of DSSs to HISC;
4) Contribute to improving the existing guidelines for designing DSSs for use in subsea components;
5) Generate data on various microstructural and mechanical parameters of both HIP-consolidated and rolled DDSs.

Chapter 3.

EXPERIMENTAL METHODS

3.1 Introduction

This chapter presents the principles of the main techniques used in the following chapters. First, the functioning of electron backscatter diffraction (EBSD) and processing of the data will be discussed. This technique was used in the material characterisation chapter (Chapter 4) and in the study of LTC phenomenon (Chapter 5). The investigation of LTC also involved digital image correlation (DIC) mapping which is discussed here, together with its interpretation. Moreover, the principle of the neutron diffraction technique for the measurement of residual stresses in the pipe-to-flange joint (Chapter 7) is presented.

3.2 Electron backscatter diffraction (EBSD)

3.2.1 Principle

EBSD is a crystallographic technique based on the acquisition and indexing of diffraction patterns within the SEM. By collecting diffraction patterns from multiple points (i.e. mapping) it is possible to obtain crystallographic information on the structure and orientation of grains within a given specimen. Computer processing of the electron diffraction data enables identification of the phases and grain boundaries present and their distributions. It also provides information on the local and relative orientation of grains; the presence of preferred crystallographic orientations (i.e. texture) [163]. This technique is fully automated which allows analysis of thousands of data points, with the primary outcome presented in the form of orientation or phase maps of the scanned region.

Figure 3.1 shows the EBSD configuration and major steps to obtain crystallographic data. A highly-polished specimen is positioned in the SEM chamber and tilted to 70°. Detailed information on the sample preparation carried out for this study given in Chapter 4. The EBSD detector is comprised of a phosphor screen, which collect the scattered electrons. As they hit the screen electrons generate bands of bright light. The bands generated are collected by a CCD (charged-coupled devices) camera located behind the screen.

EBSD patterns are produced by scattering of the incident electron beam at the metal surface. The incident electrons are scattered by the sample, and those electrons which satisfy Bragg's law constructively superpose:

$$2sin\theta_{hkl}d_{hkl} = n\lambda_{hkl} \quad (13)$$

Where h,k and l are the miller indices of the crystallographic planes, and d_{hkl} the interplanar distance of the crystal lattice. This constructive interference generates diffraction cones, known as Kossel-cones, which projected onto a planar phosphor screen, forming the Kikuchi lines [163]. The spacing between Kikuchi lines is directly correlated with the interplanar distance of the crystal lattice, d_{hkl}. For each family of crystallographic planes a band is generated on the screen and the overlay of those lines is called a Kikuchi pattern.

The Kikuchi patterns are initially solved by locating the positions of the Kikuchi bands, using the Hough Transform, and subsequently identified by comparing them to the theoretical patterns for a particular crystallographic structure and orientation [164]. This step is entirely automated by the acquisition software. The interpretation of the patterns requires definition of a coordinate system for the specimen, and its position relative to that of the phosphor screen [165].

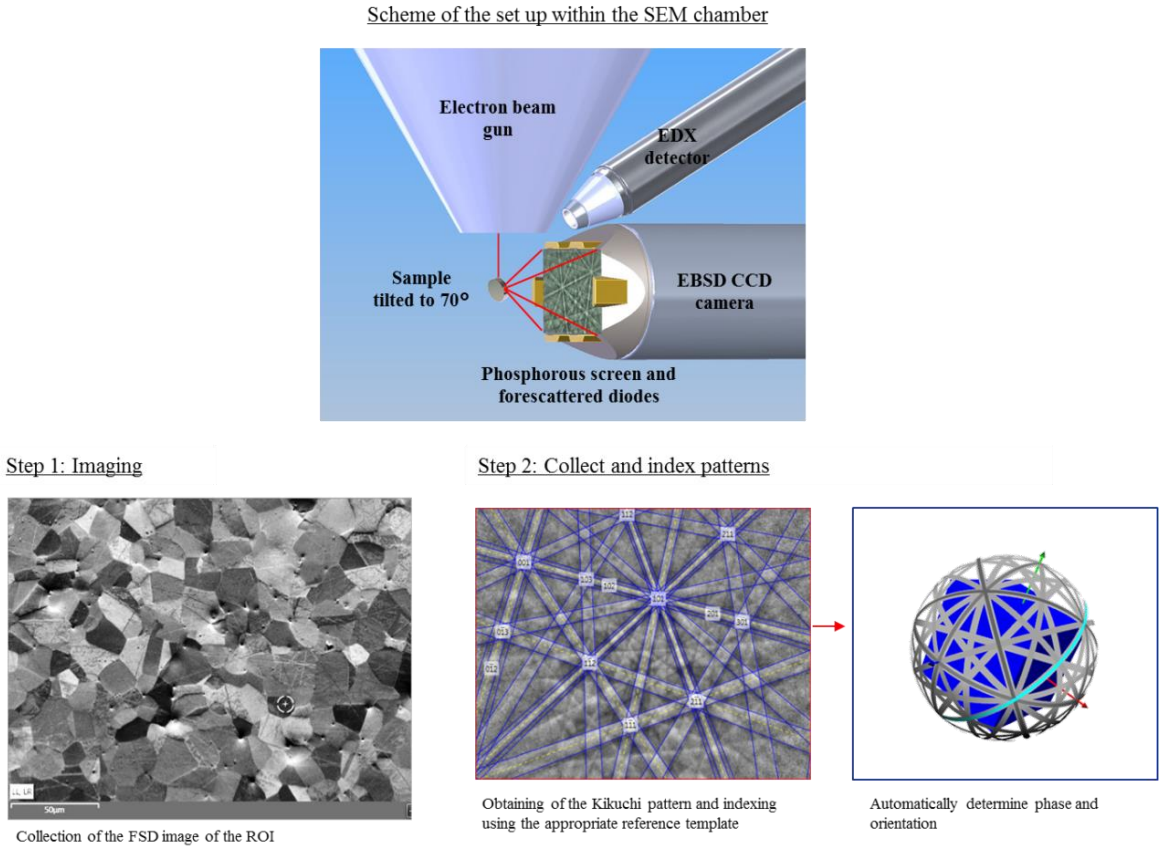

Figure 3.1: EBSD mapping steps, courtesy of TWI.

Different representation of the EBSP data is adopted to enable detailed phase, microstructural and texture analyses:

- Phase maps: represent the phase distribution within the scanned area, with each phase assigned a different colour in the resultant map. In this work, this representation was used to differentiate between fcc (i.e. austenite), and bcc (i.e. delta ferrite) crystallographic structures.
- Euler maps: are generated on the basis of the Euler angles ($\phi1$, Φ, $\phi2$), which are used to give the relative orientation of two coordinates system[163]. Applied to a real material, these angles are used to relate the specimen coordinate (rolling direction, RD, normal direction, ND, transverse direction, TD to the crystal coordinate [166];
- Orientation maps: are widely used to characterise materials in which high levels of symmetry are involved or when the specification of only a single axis is required. Orientation maps capture this characteristic by the use of colour coded maps in which, each colour shade corresponds to the crystallographic orientation of the grain that is parallel to a reference direction. The reference direction is defined by the user. In the case of a rolled material, the reference direction commonly used is the rolling direction.
- Local misorientation maps (LMO): These representations are based on the relative difference in orientation between a single measurement point and its nearest neighbouring measurement points [163]. These maps allow identification of a particular degree of misorientation over the scanned area, which can be used to determine differences in orientation between grain boundaries, grains, and their substructure.

3.2.2 Optimisation of EBSP data and EBSD settings

The reliability of the EBSD data can be improved by increasing the quality and sharpness of the EBSP, the resolution of their acquisition by the CCD camera and the accuracy of their indexing. The quality of the EBSPs can be improved by high quality specimen surface preparation and optimisation of the beam parameters such as, increasing the beam voltage and the aperture, which results in increasing the interaction volume. The parameters of the CCD camera used to record the patterns can also be optimised. The binning mode (1×1, 2×2, 4×4, 8×8, 10×10) defines the number of

pixels from the obtained image that are combined in one pixel of the final image. A low binning mode results in long acquisition time but enhances the final image quality [163]. The binning mode 2×2 was chosen in this study. The gain, determines the intensity of the output signal but its increase also induces noisier images. The indexing of the pattern is defined by the number of Kikuchi bands that have to be detected to assign the pattern. A parameter indicating the quality of the indexing is the mean angular deviation (MAD) which is the average misfit angle between the obtained Kikuchi bands and the standard ones [167]. The refinement of the EBSD map is also determined by the number and size of measurement points i.e. the step size.

3.3 Digital image correlation (DIC)

3.3.1 Principle

The DIC method is a displacement mapping technique developed in 1980 at the University of South Carolina [168] and significantly improved since. It is based on the measurement of the displacements occurring at a sample surface, by comparing images of the region of interest (ROI) before, during and after deformation. The image is sub-divided into subsets, and displacement is tracked in each of these subsets. The number of subsets, for a given area, and their spacing determine the spatial resolution of the measurements. The displacement in the subsets is tracked using features, speckles, or other markers that provide contrast in the image. Each subset contains a number of these features enabling to track its 2 dimensional (or 3 dimensional) displacement from one stage to another, Figure 3.2.

Those displacements are measured and used to calculate strains using the following equations for 2D displacements:

$$\varepsilon_{xx} = \frac{du}{dx} \tag{14}$$

$$\varepsilon_{yy} = \frac{dv}{dy} \tag{15}$$

$$\varepsilon_{xy} = \frac{du}{dy} + \frac{dv}{dx} \tag{16}$$

With ε_{xx} and ε_{yy} the local strains in the x and y directions respectively; u and v the displacement vectors and ε_{xy} the in plane shear strain.

In the present work, the as-polished surface of the wrought and the HIPed specimens were not displaying distinctive features to be tracked, so an artificial pattern was deposited. To ensure reliable DIC analyses, the pattern's speckles have to fulfil the following requirements: they have to be of similar size, distinguishable among each other and randomly distributed, and more importantly, they must follow the movement of the underlying surface [169].

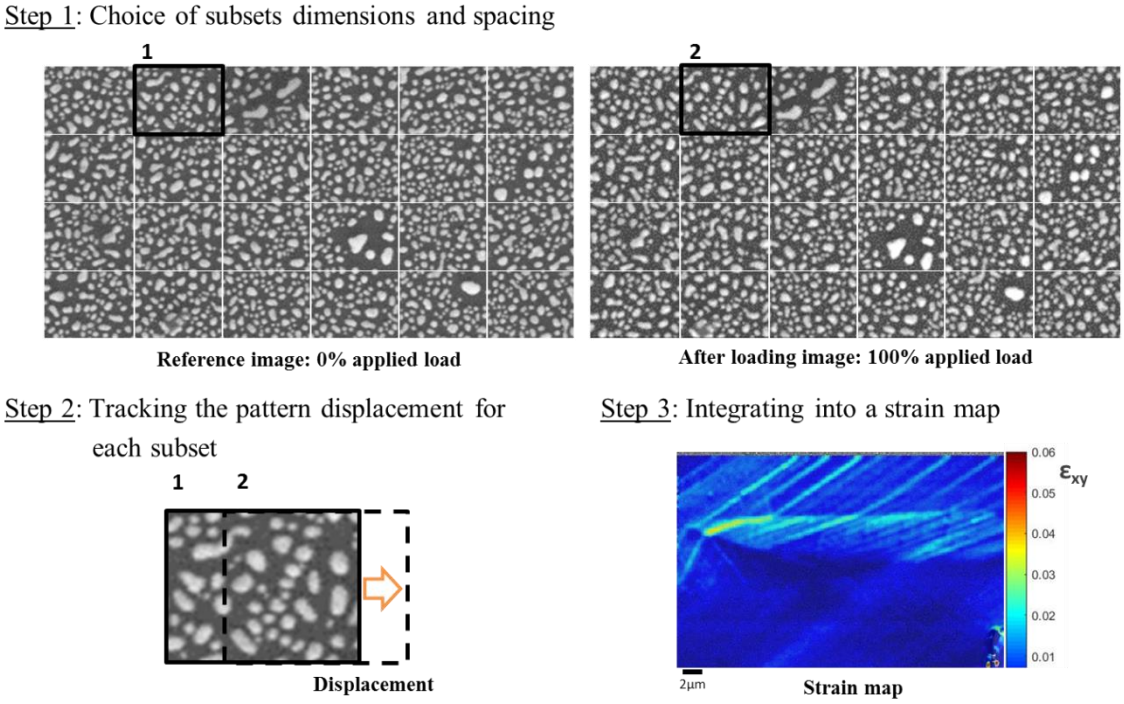

Figure 3.2: Pattern tracking for DIC analysis and image treatment procedure to obtain strain map.

3.3.2 Interpretation of the DIC map

3.3.2.1 Description of a resulting DIC map

After processing the DIC data, the resulting strain map reveals different features. The most commonly observed are strain localisations [170],[171],[64] and deformation bands[172], [173]. The interpretation of these features requires relating the generated map with the underlying microstructure. This is made by overlaying them with SEM images or EBSD maps of the ROI, obtained before the deposition of the DIC pattern.

The regions of strain localisation (e.g. grain boundaries) are readily identified with the overlay. However, the identification of the deformation bands, recognised as slip traces [174], [175], require further analysis.

3.3.2.2 Identification of the activated slip system during deformation of DSSs

As described in the literature review, DSSs deform by slip mechanism. A slip system is characterised by a crystallographic slip plane and a crystallographic slip direction. For every grain in the material, different slip systems can be activated during deformation. The slip system with the highest probability to be activated during loading is the one having the highest ratio between the applied stress and resolved shear stress on the slip plane. This ratio is defined as the Schmid factor, Figure 3.3.

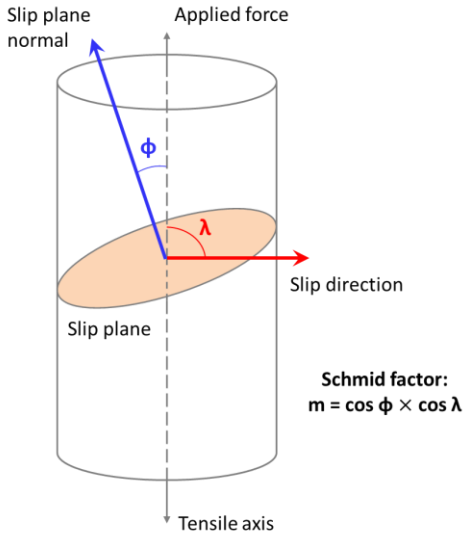

Figure 3.3: Illustration of the Schmid factor product adapted from [176].

As a material deform by slip, the intersection between the slip planes and the material surface generates slip traces. Slip traces are observable on DIC maps and are characterised by a trace angle, θ, which is the angle between the slip trace and the loading direction, Figure 3.4. The methodology described below shows how to identify which slip system was activated using the trace angle and the EBSD data of the ROI.

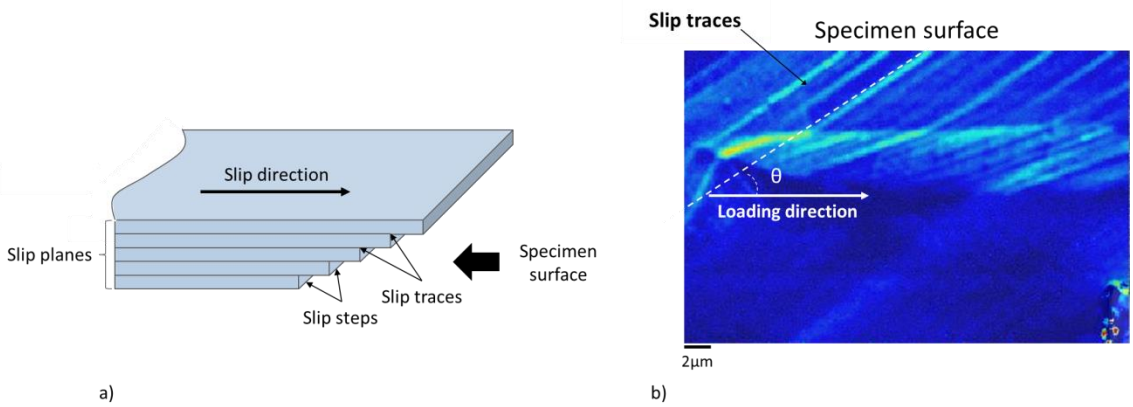

Figure 3.4: a) Schematic representation of the formation of slip traces at a specimen surface [177]**, b) DIC map in which a slip trace was identified using the trace angle, θ.**

The slip systems are dependent on the plane with highest atomic density of the crystallographic structure. In the case of fcc materials, there are four planes of type {111} each of which can be activated in three directions <1-10>, which means 12 active slip systems. In the case of bcc materials, the slip system are {110} <-111>; {211} <-111> and {321} <-111> which represents a total of 48 active slip systems.

The University of Sheffield developed a tool: Crystal Mathematical Tool, which take as input the Euler angles of a grain, and calculates, for every theoretical slip system, the trace angle, with respect to the loading direction, generated and the Schmid factor associated for this slip system. Hence, for each grain, all the slip systems, defined as a crystallographic plane and a crystallographic direction, are transposed into the sample space using the Euler angles of the grain assessed. This calculated angle is compared to the one measured on the DIC map.

Slip traces analysis for austenite is fairly straight forward because of the limited possible slip systems. However, for ferrite, some of the calculated slip trace angles can be very close, which makes it difficult to identify the active slip system in the experimental data. Hence, following the same reasoning as the one developed by M. Marinelli et al [178] in an investigation on fatigue properties of DSSs, an order of priority was used to identify the most likely slip plane; {110} <-111>, being the most likely, followed by {211} <-111> and finally {321} <-111>. Once the slip plane was determined, the slip direction was identified by the one having the highest Schmid factor.

3.3.2.3 Identification of K-S OR

Once the slip systems activated are established, the OR between ferrite and austenite, can be identified. As described in the literature review, K-S OR is commonly found between fcc and bcc crystal structure and hence can be present at phase boundaries in DSSs[37]. This OR is defined as {111}γ//{110}δ ,<110>γ//<111>δ. The presence of this particular OR in the obtained DIC maps was examined following T. Zhai methodology [179].

The orientation of a deformed crystal can be defined in the sample coordinate by two angles: ψ and θ, where ψ is the angle between the slip plane and the loading direction and θ is the angle between the slip trace and the loading direction, visible at the specimen surface, Figure 3.4. A schematic representation of those two angles is given in Figure 3.5. Using ψ and θ, the relationship between two neighbour crystals is defined by α, the twist angle and β, the tilt angle:

$$\alpha = \psi_1 - \psi_2 \tag{17}$$

$$\beta = \theta_1 - \theta_2 \tag{18}$$

The twist angle, α, is determined using the following equation:

$$\psi = \arctan(-\frac{N_1}{N_2}) \tag{19}$$

Where, N: [N_1, N_2, N_3] is the normal vector of the slip plane activated within the sample system coordinates. This vector was identified previously, using Crystal Mathematical Tool. The tilt angle, β, was determined from the measurement of the trace angles θ_1 and θ_2 of the two adjacent grains. The measurements were made by image analysis of the DIC map using ImageJ software. The K-S orientation relationship (OR) was attributed to a phase boundary satisfying α < 10° and β < 5°.

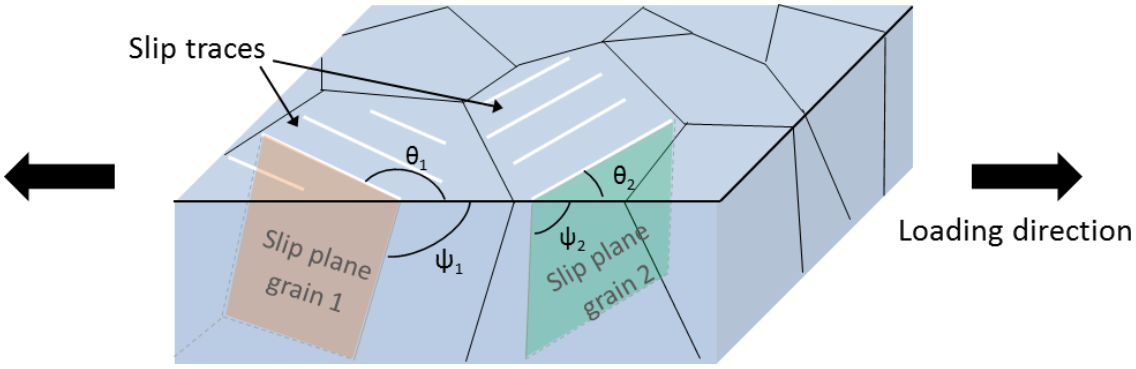

Figure 3.5: Illustration of θ and ψ angles, defining the orientation of deformed grains in the sample space.

3.4 Residual stresses measurements using neutron diffraction

3.4.1 Introduction

The residual stresses within a material can be quantified using many different techniques, including: the contour method, hole drilling, synchrotron X-ray diffraction (XRD) and neutron diffraction. XRD and neutron diffraction are both very expensive techniques but can give more accurate data in a non-destructive way as derived from the measurement of atomic spacing in the material. Neutrons have a large penetration depth into steels compare to X-rays, allowing the measurement of average lattice parameter of the bulk material [180].

3.4.2 Engin-X

The residual stress measurements were carried out using neutron diffraction on the Engin-X beamline at ISIS, Rutherford Appleton Laboratory, in Harwell, UK. Neutrons are generated by a spallation phenomenon where highly accelerated particles (protons,) hit a heavy nuclei metallic target [181] and are scattered in the different beamlines. An aerial view of Engin-X beamline set up is given in Figure 3.6. Neutrons travel through the incident beam slits before interacting with the target sample volume, from which they are diffracted. Two times of flight detectors are used to simultaneously record the diffraction data generated for two orthogonal strain components. Hence, the instrument allows the measurement of two strain directions at the same time (e.g. radial and hoop). The sample is rotated by 90° in order to perform measurements in the third strain direction (e.g. longitudinal). The interaction volume of the beam, known as the ‘gauge

volume', is bound by the beam slits and by the use of converging collimators, which are located in front of each bank of detectors.

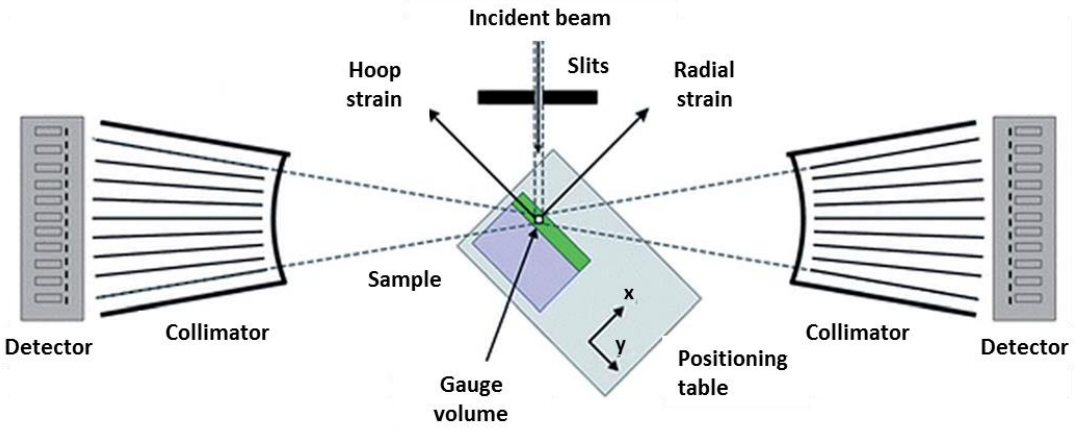

Figure 3.6: Illustration of Engin-X configuration, adapted from [182]**.**

3.4.3 Principle

The output from the beamline detectors is the neutron time of flight, t_{hkl}. The extraction of the average lattice parameters, d_{hkl}, of the gauge volume studied from those data is made by the use of Bragg's law:

$$d_{hkl} = \frac{\lambda_{hkl}}{2sin\theta_{hkl}} = \frac{ht_{hkl}}{2m_n Lsin\theta_{hkl}} \quad (20)$$

where h, k and l are the crystallographic planes, λ_{hkl} is the neutron wavelength of the diffracted neutron, θ_{hkl} is the angle of diffraction, h is the Planck constant, m_n the neutron mass and L is the neutron path length. The determination of the lattice parameters from the neutron diffraction time-of-flight spectra was made using the Pawley refinement method [183]. This peak fitting methodology, on the opposite of the Rietveld method, also widely used to fit of neutron diffraction spectra, takes into account the intensity of the peaks. This important difference allows reducing peak correlation, and so uncertainties in the resulting lattice spacing, when two peaks overlap which is often the case in diffraction spectra of a two phases alloy. From those data, the relative strain, ε_{hkl}, is calculated for each measurement point, using the following equation:

$$\varepsilon_{hkl} = \frac{d_{hkl} - d_{0,hkl}}{d_{0,hkl}} \quad (21)$$

where $d_{0,\,hkl}$ is the stress-free interplanar spacing. As this parameter is used as reference for the calculation of all the strains, its evaluation is critical [184]. Different measurement approaches exist and in the present work, the use of small cubes, extracted from the material, were used. This technique is based on the assumption that cutting into the material results in relieving it from any constraint of the surrounding macroscopic stress field.

Once the strains are established, the stresses in the three directions can be calculated according to Hooke's law:

$$\sigma_i = \frac{E}{(1+\nu)(1-2\nu)} \left((1-\nu)\varepsilon_i + \nu(\varepsilon_j + \varepsilon_k)\right) \quad (22)$$

Where i,j and k, the three main directions, E is the Young modulus and ν the Poisson's ratio of the material.

3.4.4 Quantification of the uncertainties

During neutron diffraction experiments, uncertainties can be introduced from a number of sources, which can have an impact on the lattice parameter measured. These uncertainties include: the beam alignment and its calibration, the setup of the sample on the stage and the data analysis (i.e. refinement method). Among them, only the uncertainties induced during Pawley refinement method are quantified. Hence, to avoid estimation errors it was decided to take into account only these refinement uncertainties. In this work, the experimental uncertainties, $u(x_i)$, were derived using an error propagation method of the form [185]:

$$u^2(\varepsilon_i) = \sum_{i=1}^{N} \left(\frac{\partial \varepsilon}{\partial x_i}\right)^2 u^2(x_i) \quad (23)$$

Where x_i is any potential error contributor, if the equation (21) is substituted in the equation (23):

$$u(\varepsilon_i) = \frac{d_i}{d_0}\sqrt{\frac{u^2(d_i)}{{d_i}^2} + \frac{u^2(d_0)}{{d_0}^2}} \tag{24}$$

In the same way,

$$u^2(\sigma_i) = \sum_{i,j=1}^{N} (\frac{\partial \sigma_i}{\partial \varepsilon_j})^2 u^2(\varepsilon_j) \tag{25}$$

And hence, by substituting equation (22) in (25):

$$u(\sigma_i) = \sqrt{\left(\frac{E}{1+\nu}u(\varepsilon_i)\right)^2 + \left(\frac{\nu E}{(1+\nu)(1-2\nu)}\right)^2 (u^2(\varepsilon_i) + u^2(\varepsilon_j) + u^2(\varepsilon_k))} \tag{26}$$

Chapter 4.

MATERIAL CHARACTERISATION

4.1 Introduction

In order to get a better understanding of HISC in DSSs, this work proposed to compare the response of two fundamentally different DSSs microstructures: conventionally manufactured and hot isostatically pressed (HIPed) products, to different aspects of this embrittlement mechanism. The two materials have the same nominal duplex stainless steel grade alloy, UNS S31803, but different microstructures. Samples were a pipe component made from a seam welded rolled plate and a HIPed can, hereafter referred to as wrought and HIPed materials, or M1 and M2 respectively.

A complementary study was also carried out on the influence of residual stresses in small scale tensile specimens on the resistance-to-HISC. The component for this work was a SDSS pipe to flange component, retrieved from service after 12 years of operation. The pipe, made of UNS S32760 grade was connected by girth weld to a UNS S32750 forged flange on one end. Those two sets of materials were fully characterised and the results are described below.

4.2 Characterisation of the wrought (M1) and the HIPed (M2) materials

4.2.1 Chemical composition

The chemical compositions of the two samples are listed in Table 4.1. Concentrations were measured using optical emission spectrometry (OES). The diffusible hydrogen

was measured by the hot extraction method, using gas carrier analysis at 400°C, in a Bruker G4 Phoenix hydrogen analyser. The residual hydrogen and nitrogen contents were measured by the melt extraction method, using gas fusion analysis, in an ELTRA ONH 2000 analyser. The hot melt extraction method allows the determination of the total amount of hydrogen content up to the melting point and hence, includes the trapped hydrogen [186], compare to the hot extraction method. The nominal composition of UNS S31803 is given in Table 4.1 with the nominal composition of UNS S31803 for comparison, and the diffusible and residual hydrogen measurements are given in Table 4.2.

Table 4.1: Chemical composition of the wrought (M1) and HIPed (M2) materials, measured by OES, and the nominal specifications for UNS S31803.

Material	Elements present (wt.%)								
	C	**Si**	**Mn**	**P**	**S**	**Cr**	**Mo**	**Ni**	**N**
M1	0.022	0.32	1.77	0.028	0.002	22.0	2.48	5.1	0.16
M2	0.034	0.73	1.13	0.021	0.004	22.1	2.91	5.2	0.19
UNS S31803	0.030 max	1.00 max	2.00 max	0.03 max	0.02 max	22-23	3.0-3.5	4.5-6.5	0.14-0.2

Table 4.2: Hydrogen contents for the wrought (M1) and the HIPed (M2) materials

Material	Diffusible hydrogen, ppm	Residual hydrogen, ppm
M1	<0.1	3
M2	<0.1	2

4.2.2 Microstructural characterisation

4.2.2.1 Sample preparation

Metallographic cross-sections were extracted in the three principle directions (i.e. the rolling, transverse and normal directions) from the pipe material, Figure 4.1. Only one

direction was studied for the HIPed material as the microstructure was highly uniform within the can. The cross-sections were hot-mounted in conductive Bakelite using a Buehler Simplimet XPS1 hot mounting press. This involved a heating step to 180°C for 7 minutes, with the application of 220 bar pressure and cooling down for 7 minutes. The samples were prepared using standard metallographic techniques for microstructural characterisation. The samples were manually ground using 60 to 2500 grit SiC abrasive paper and subsequently polished using soft, synthetic cloths and diamond paste of 3 μm, 1 μm and 0.25 μm, diluted in lubricant.

To perform light microscopy, the samples were subsequently etched electrolytically, in a 40 % KOH solution at 6 V for 3 seconds. This etching procedure revealed the grain boundaries and differentiates between the austenite and ferrite phases. Additional polishing was conducted using an ATM Saphir 560 automatic polisher to prepare the specimens for scanning electron microscopy (SEM). The specimens were polished using a 50 % OPU suspension in deionised water, for 10 minutes and an applied load of 25 N. The use of OPU resulted in some light etching of the polished specimens, which facilitated SEM examination of the microstructure in the secondary electron (SE) and, backscattered electron (BSE) imaging modes, as well as energy-dispersive X-rays (EDX) spectroscopy, and electron backscatter diffraction (EBSD) mapping.

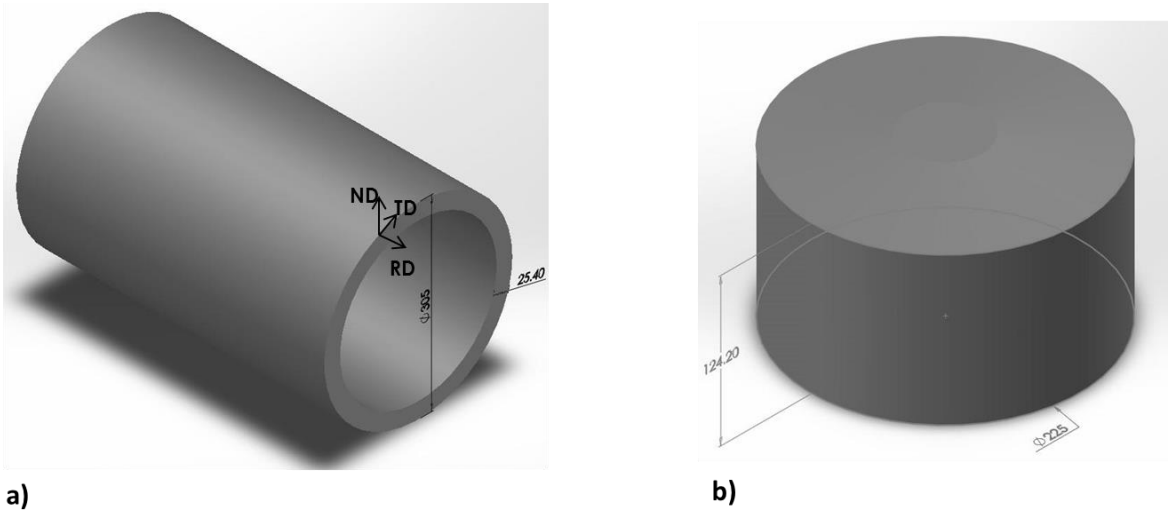

Figure 4.1: Schemes of a) the wrought material (M1) with the rolling, transverse and normal (RD, TD and ND) directions, respectively, and b) the HIPed material (M2).

4.2.2.2 Light microscopy and assessment of key microstructural parameters

The 3D microstructural representation of the M1 and M2, given in Figure 4.3 and Figure 4.4, respectively, was obtained by imaging using Olympus BX41M light microscope and Photoshop software. The light microscopic images were used to measure the ferrite-austenite phase balance, also known as ferrite content, and the austenite spacing of the alloys, with their methodologies described below.

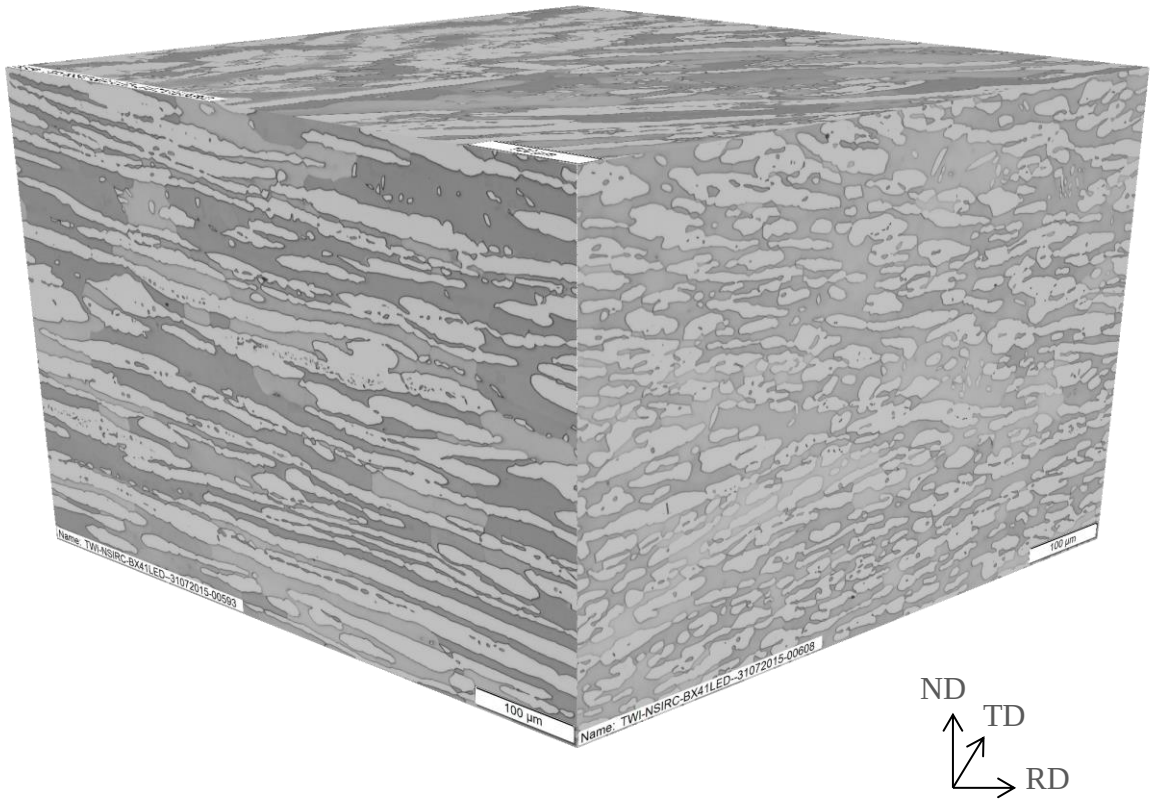

Figure 4.2: 3D microstructural representation of the wrought material (M1). Etched electrolytically in 40 %KOH solution, at 6 V for 3 s, scale bar 200 µm.

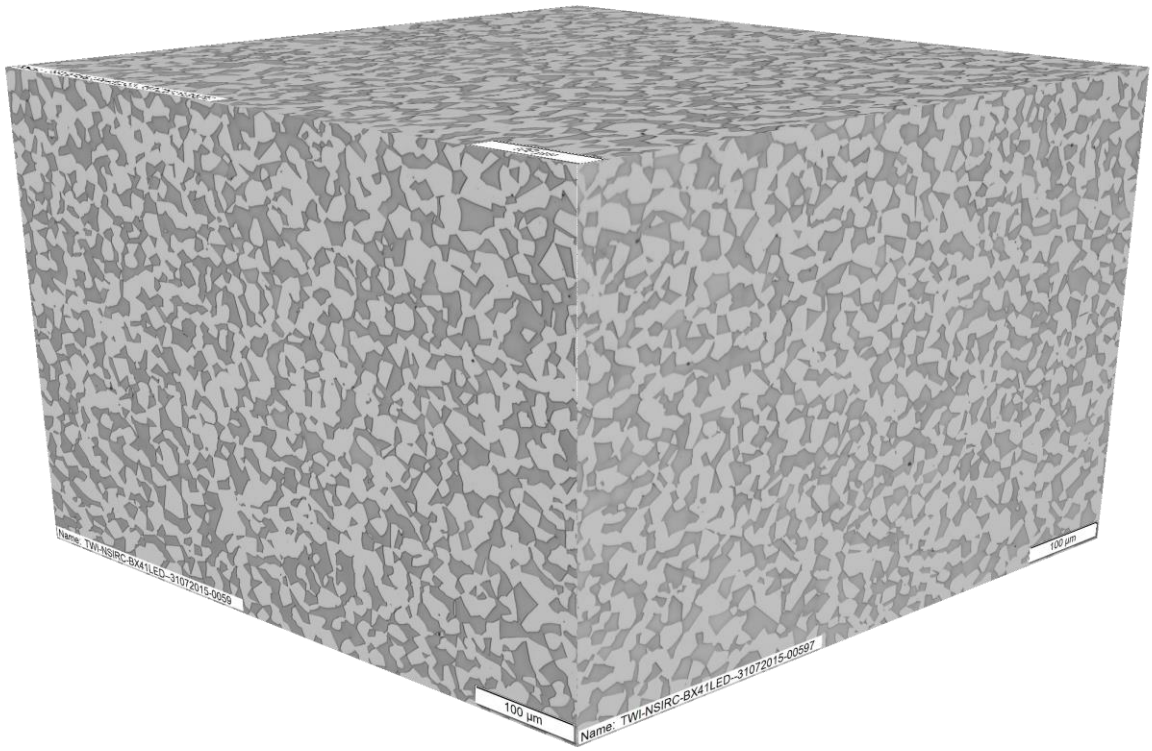

Figure 4.3: 3D microstructural representation of the HIPed material (M2) Etched electrolytically in 40 %KOH solution, at 6 V for 3 s, scale bar 100 µm.

4.2.2.2.1 Phase balance between ferrite and austenite

The phase balance in the two materials were measured using manual point counting, based on the point intercept method guidelines given in ASTM E562: 2011. For each material, 32 fields were examined at a final screen magnification of 2000× (corresponding to a microscope magnification of 500×), using a 25-points grid superimposed on the images. The average ferrite content, standard deviation and the 95 % confidence interval are given in Table 4.3 for the wrought (M1) and HIPed material (M2).

Table 4.3: Phase balance and average austenite spacing measurements of the wrought material (M1), in 3 main directions, and the HIPed material (M2).

Material	M1			M2
	M1ND	M1TD	M1RD	
Average ferrite content in %	50.38	49.25	51.13	40.63
Standard deviation %δ	26.59	13.51	16.84	14.22
95%CI	10.18	5.17	6.45	5.44
Austenite spacing, µm	17.91	9.75	11.36	10.73
%RA	17.3	12.7	8	10.4

4.2.2.2.2 Austenite spacing

The average austenite spacing was determined manually using the linear intercept method, in accordance with ASTM E112: 2012 [187]. For each direction 10 random fields were examined, this ensures that the statistical reliability of the results met the requirements of relevant guidelines, i.e. DNV-RP-F112 [109]. For each field, the minimum requirement of 50 intercepts was met. This ensured the use of an appropriate magnification and so, the obtaining of micrographs representative of the microstructure. In the case of the wrought material (M1), the three major planes were examined. For the two planes parallel to the normal direction, the austenite spacing was measured in the through-thickness direction. For the plane perpendicular to the normal direction, the measurements were taken perpendicularly to the rolling direction. Due to the homogeneous microstructure of the HIPed material (M2), only one representative direction/plane was considered to measure the average austenite spacing. The results and their relative accuracy (% RA) are given in the Table 4.3.

The analysis of the microstructures showed that the wrought material (M1) exhibited a ribbon-like microstructure of elongated austenite grains, along the pipe rolling direction, within a ferrite matrix. The HIPed material (M2) revealed a microstructure of homogeneously-distributed, equiaxed austenite and ferrite grains.

The austenite spacing of the wrought material (M1) along the through-thickness direction (the direction in which HISC is expected), and the grain size of M2 were similar and measured to be approximately 10 μm.

4.2.2.3 Scanning electron microscopy

SEM imaging, EDX analysis were performed in a Zeiss Sigma FEG-SEM with the AZtec Software by Oxford Instruments. The parameters used for imaging and EDX analysis were a beam-voltage of 20 keV, 30 μm aperture and 10 mm working distance. SEM images of the two microstructures are given in Figure 4.4, with the associated EDX spectra for both materials. SEM and EDX analysis of the two materials did not reveal any deleterious phases, i.e. sigma phase, in the two microstructures. The EDX spectra of the two materials, Figure 4.4, showed that ferrite and austenite have different chemical compositions: Mn and Cr contents were higher and Ni content lower in the ferrite than those in the austenite.

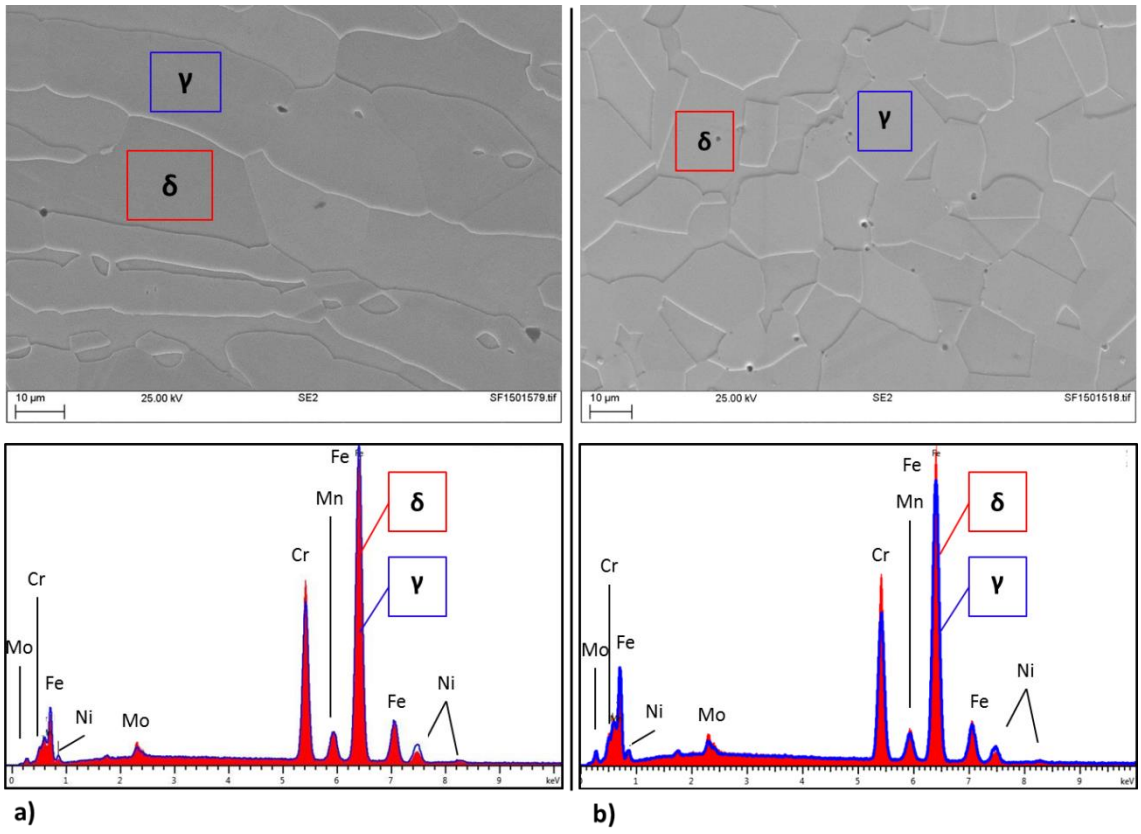

Figure 4.4: SEM images and associated EDX spectra taken within the austenite and ferrite grains of a) the wrought material (M1) and b) the HIPed material (M2).

4.2.2.4 EBSD

EBSD mapping was also carried out in the Zeiss Sigma FEG-SEM, equipped with the Aztec acquisition Software by Oxford Instruments. The beam parameters used were a voltage of 30 keV and an aperture of 120 μm. The binning mode was 2×2, with a gain of 4. The Kikuchi patterns used to index ferrite and austenite phases were generated using the following data: [188] and [189] for ferrite and austenite, respectively; the minimum number of Kikuchi bands identified by pattern to be assigned was 8; this lead to an average MAD value of 0.5° over the scanned area. The processing of the data was done in Channel5 software.

The phase maps representing the austenite and ferrite distribution in M1 and M2 are given in Figure 4.5.

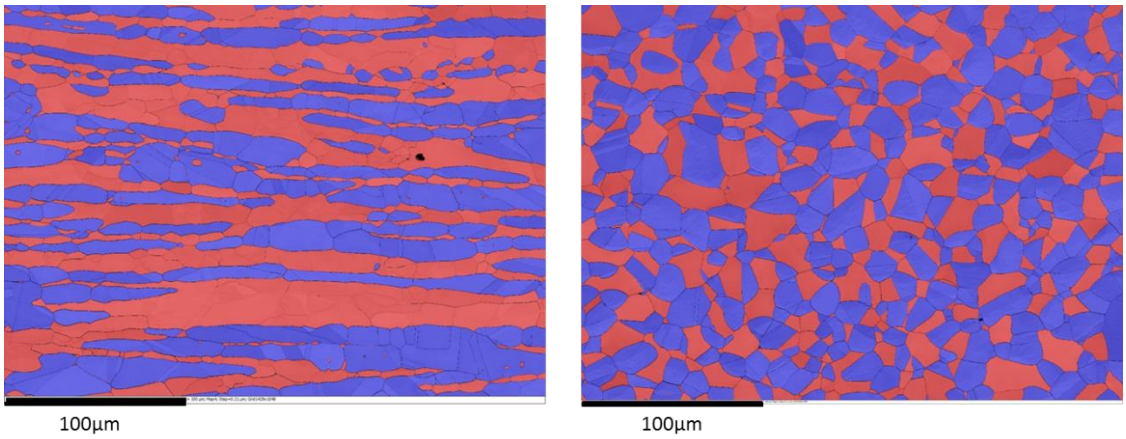

Figure 4.5: Phase maps: δ ferrite in red and γ austenite in blue, for a) the wrought (M1) and b) the HIPed (M2) materials. The scale bar is 100 µm; the specimens were etched by OPU (10 min, 25 N, in diluted OPU).

Figure 4.6 gives the orientation maps for the wrought and the HIPed material with respect to the reference direction, which correspond to the rolling direction, in the case of the wrought material and the horizontal direction in the case of the HIPed material. The step size was 0.21 μm, as for all the EBSD maps in this work. This was chosen as a compromise between a high quality resulting map with a suitable mapping time.

EBSD mapping highlighted the microstructural differences between the two materials which are induced by the different manufacturing processes employed, Figure 4.5 and Figure 4.6.

In the case of the wrought material, the orientation maps showed that the ferrite grains are majority of green and pink shades, indicating that, in this area, they have a preferred crystallographic orientation parallel to the rolling direction. This is not the case for the austenite grains which showed homogeneous repartition of shades, indicting various crystallographic orientations parallel to the rolling direction. In the case of the HIPed material, both phases displayed random crystallographic orientations [190].

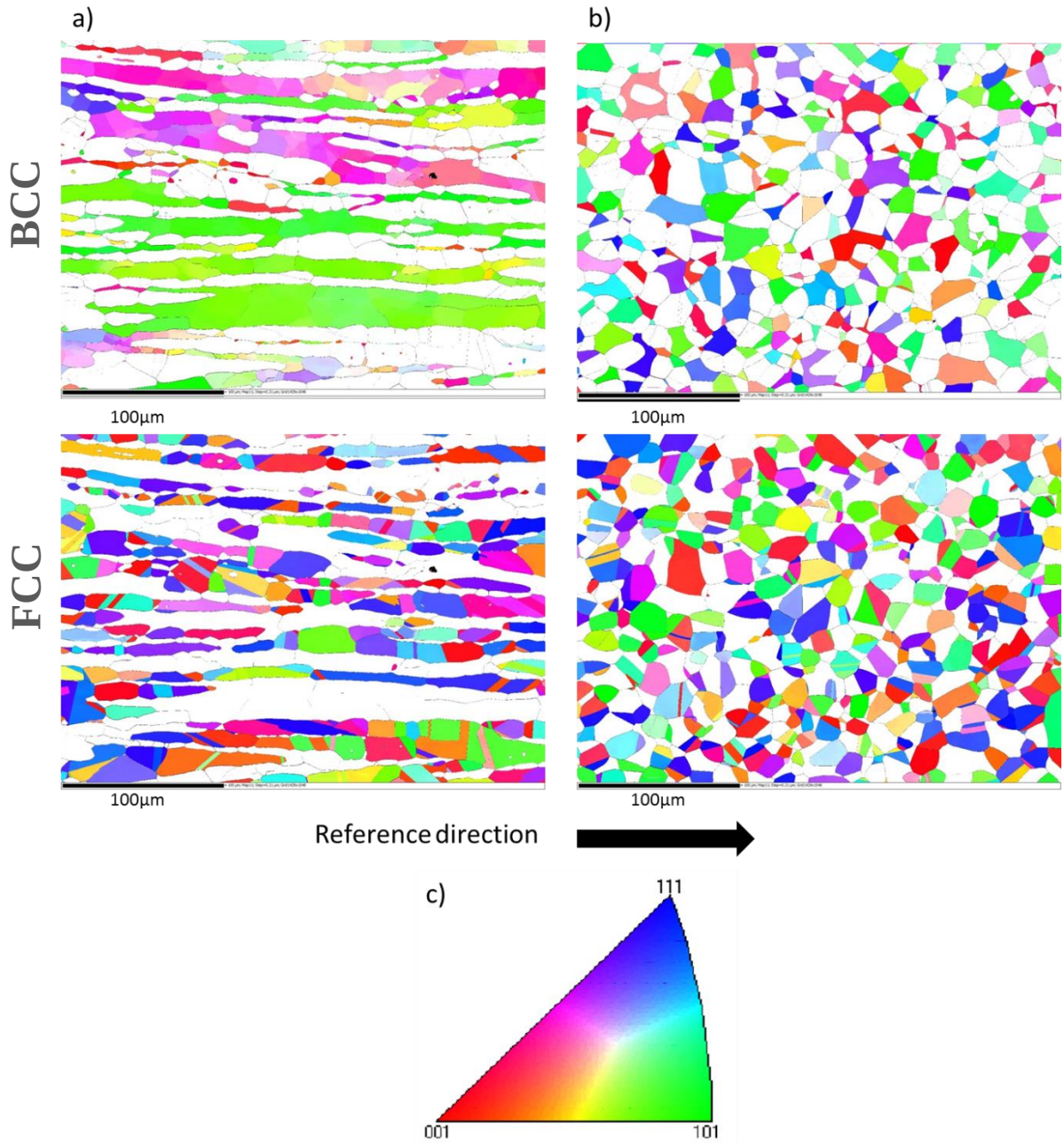

Figure 4.6: Orientation maps of the ferrite, bcc and the austenite, fcc, phases in the case of a)the wrought and the b)HIPed materials, according to the reference direction; c) Orientation map legend for austenite and ferrite.

4.2.3 Mechanical properties

4.2.3.1 Tensile properties

The room temperature tensile properties of M1 and M2 were measured in accordance with ASTM A370: 2015 [191]. In the case of the wrought material, three samples were extracted parallel to the longitudinal direction: one was located as close as possible to the outer diameter (M1-OD), one at mid-thickness (M1-MT) and one as close as possible to the inner diameter (M1-ID) of the pipe. The results are given in the Table 4.4. Macrographs from the fracture faces of M1-OD and M2, after room-temperature tensile testing, were taken using a camera and are given in Figure 4.7.

Table 4.4: Tensile properties of the wrought material (M1) measured using specimens extracted adjacent to the inner, mid-thickness and outer diameter, and of the HIPed material (M2).

Material	0.2% offset yield stress, MPa	UTS, MPa
M1-OD	562	737
M1-MT	515	725
M1-ID	569	733
M2	540	795
Typical UNS S31803	448	621

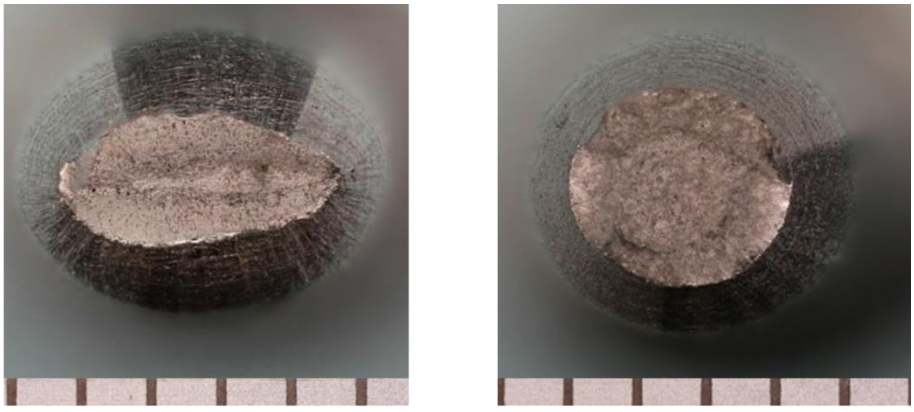

Figure 4.7: Macrographs of the fracture faces of the tensile specimen, a) M1OD and b) M2, tested at room temperature.

It was noticed that the HIPed material (M2) had a higher UTS than the wrought material (M1). This latter exhibited a range of mechanical properties across the thickness. For the rest of the work, the 0.2 % offset yield stress of this material was represented by the data obtained from the testing of the M1-MT specimen, which fell between the values obtained from the specimen extracted adjacent to the two the OD and ID, i.e. M1-OD and M1-ID.

4.2.3.2 Hardness

Vickers macro-hardness of both materials was measured using a 10 kg load. The results are given in Table 4.5 and showed that the average macro-hardness values were slightly higher in the wrought than in the HIPed material.

Furthermore, Vickers micro-hardness testing was carried out in order to determine the hardness of the austenite and ferrite phases in each material. Micro-hardness measurements were made using a 100 g load for the wrought material (M1), the typical indent size was 25*25μm. However, a smaller load of 25 g was chosen for the HIPed material (M2), due to its smaller grain size distribution. This ensured that the measurement indent was fully within the target grains, with a typical indent size of 10*10μm.

Comparison between those measurements showed that, the average hardness of the austenite was higher than that in the ferrite in the case of the wrought material (M1), and the opposite was observed for the HIPed material (M2).

Table 4.5: Macro and micro-hardness measurements for wrought and HIPed materials.

M1			**M2**		
Macro-hardness, HV, 10 kg	**Austenite micro-hardness, HV, 100 g**	**Ferrite, micro-hardness, HV, 100 g**	**Macro-hardness, HV, 10 kg**	**Austenite micro-hardness, HV, 25 g**	**Ferrite, micro-hardness, HV, 25 g**
248	253	243	237	251	262
249	253	201	237	256	281
254	281	235	236	245	281
253	268	265	240	281	262
257	251	251	234	235	268
257			233		
253			237		
248			253		
Averages					
252	**261**	**239**	**238**	**253**	**270**

4.3 SDSS flange-to-pipe material after 12 years of subsea service

The current study is concerned with the HISC testing of the materials involved in a joint between a DSS pipe and flange, and the interpretation of the results obtained. Microstructural characterisation of the materials from this welded component was performed in a previous study on the assessment of the residual stress of this joint [192]. Therefore, the materials properties generated in that work are merely reported in the following section. The results reported were obtained using the same experimental methodologies described earlier in the paragraph 4.2.2.1 of the current chapter.

4.3.1 Description of the component

The component investigated in this work was a superduplex stainless steel (SDSS) component composed of a girth weld between a UNS S32750 forged flange, and UNS SS32760 pipe, Figure 4.9. This joint was part of a SDSS gooseneck, retrieved after 12 years of subsea service.

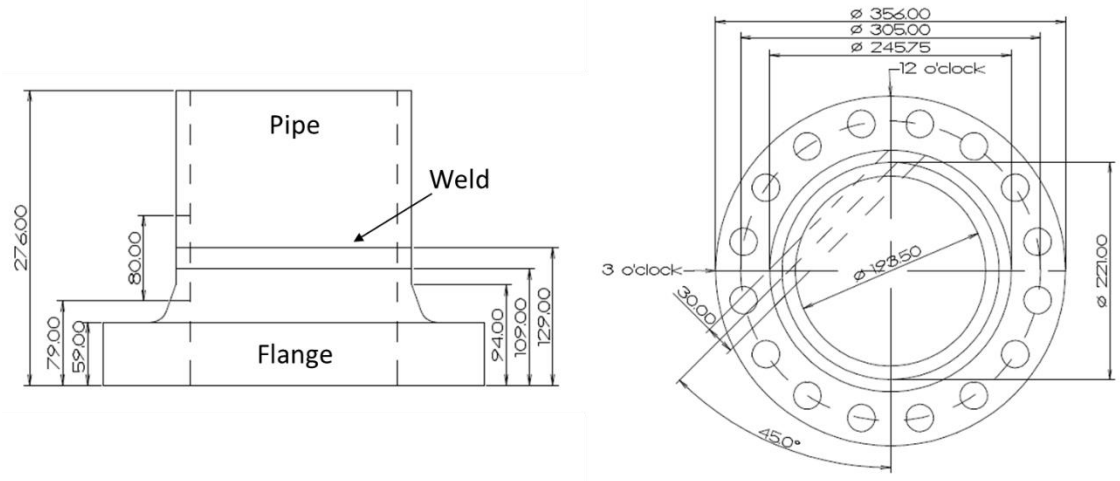

Figure 4.8: Drawing of the flange to pipe component [192]**.**

4.3.2 Chemical composition

The chemical compositions of the pipe, weld and flange materials are given in Table 4.6. The nominal chemical compositions of the UNS S32760 and the UNS S32750 were also included for comparison.

Table 4.6: Chemical composition results from the parent and weld materials. The nominal chemical composition of UNS S32760 and UNS S32750 are also added [192].

Material	Elements present (wt.%)								
	C	**Si**	**Mn**	**P**	**S**	**Cr**	**Mo**	**Ni**	**N**
Pipe	0.032	0.540	0.720	0.019	0.009	25.1	3.560	7.000	0.270
Weld	0.014	0.390	0.680	0.029	0.004	25.0	3.860	8.800	0.210
Flange	0.014	0.300	0.320	0.021	<0.021	24.9	3.800	6.800	0.283
UNS S32760	0.030	1.0	1.0	0.030	0.010	24.0-26.0	3.0-4.0	6.0-8.0	0.2-0.3
UNS S32750	0.030	0.8	1.2	0.035	0.020	24.0-26.0	3.0-5.0	6.0-8.0	0.24-0.32

4.3.3 Microstructure

A macrograph of the through thickness of the pipe-to-flange joint is given in Figure 4.9, with the 11 locations in which the ferrite-austenite phase balance was measured. The phase balance measurements are given in Table 4.7.

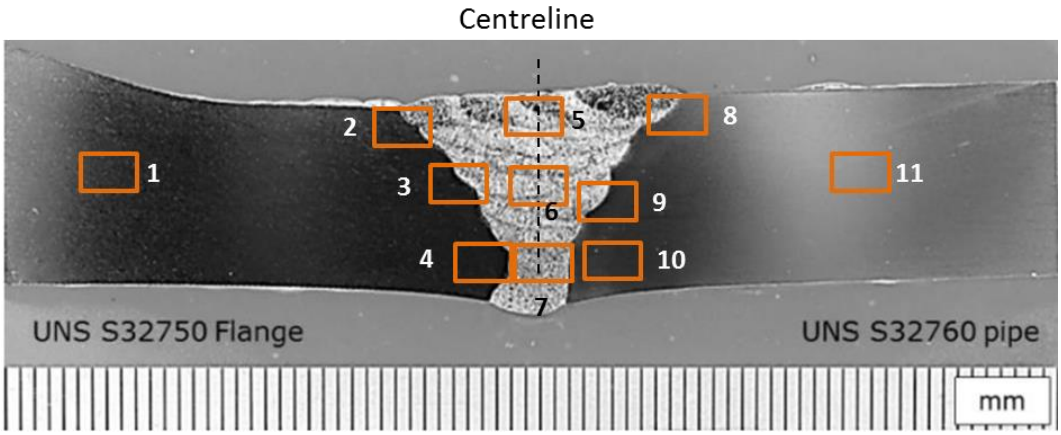

Figure 4.9: Macrograph of the pipe to flange joint [192].

Table 4.7: Measurements of the ferrite to austenite phase balance at the 11 locations on the flange to pipe through thickness [192]**.**

	Location of the measurement area										
	1	**2**	**3**	**4**	**5**	**6**	**7**	**8**	**9**	**10**	**11**
Average ferrite content in %	48.0	57.0	57.3	58.0	49.2	38.8	43.3	52.0	51.0	53.4	47.1

EBSD mapping of the interfaces flange to weld and weld to pipe, through thickness, was performed. The resulting phase maps are given in Figure 4.10. It was observed that the pipe material had a very fine microstructure with austenite grains elongated and parallel to the rolling direction. The flange microstructure was coarser microstructure.

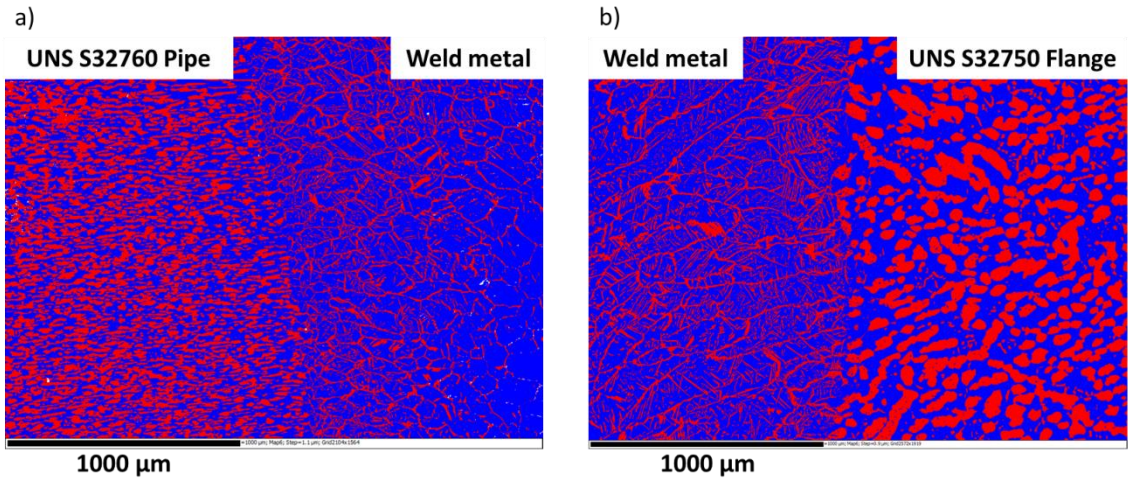

Figure 4.10: EBSD phase map of the interfaces a) flange to weld metal and b) weld metal to pipe. Ferrite phase is in blue and austenite in red shade [192]**.**

Using the EBSD technique, the average of the ferrite grain size was determined, in the through thickness direction (i.e. transverse direction) and tangent to the weld (i.e. from the cap surface). The results are given in the Table 4.8. The measurement of the average phase grain size takes into account the grains anisotropy in two dimensions compare to conventional phase spacing which only takes into account grain spacing according to

one direction. However, if this method is easily carry out using EBDS it would be extremely time consuming to obtain manually, which is not the case for phase spacing. Conventionally, austenite spacing is mostly used compared to ferrite spacing however, give similar information on the material.

Table 4.8: Average of the ferrite grain size determined by EBSD at different locations of the weld interface [192]**.**

		Flange to weld interface		**Weld to pipe interface**	
		Flange	**Weld**	**Weld**	**Pipe**
Transverse	**Avg. Ferrite grain size, μm^2**	180	208	227	196
Tangential	**Avg. Ferrite grain size, μm^2**	50	67	160	93

4.3.4 Mechanical properties

4.3.4.1 Tensile properties

The mechanical properties of the two parent materials were determined at 4°C through tensile testing, in accordance to ASTM A370-15. Two specimens from each material were tested and the average 0.2 % offset yield stress and UTS values given in Table 4.9.

Table 4.9: Tensile properties of the pipe and flange parent material tested at 4°C [192]**.**

Material	0.2 % offset yield stress, MPa	UTS, MPa
Pipe	666	936
Flange	619	822

4.3.4.2 Hardness

Vickers micro-hardness testing, using a 300 g load and a fine indentation spacing of 0.4 mm, was employed to plot the results in the form of a map across the weld, Figure 4.11.

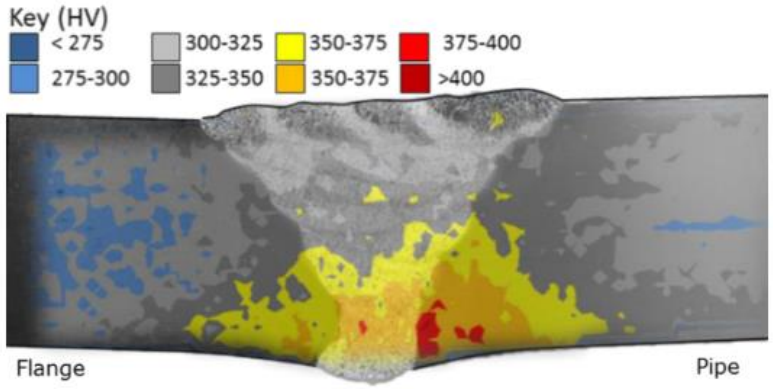

Figure 4.11: Micro-hardness map overlaid with the macrograph of the weld [192]**.**

4.4 Summary

Microstructure characterisation and mechanical performance were carried out on a conventionally manufactured and HIPed DSS samples. These results will be used in chapters 5 and 6, which compare the response of these two materials, to different aspects of HISC mechanism. A complementary study was also carried out on the influence of residual stresses in small scale tensile specimens on the resistance-to-HISC by examining a SDSS pipe to flange component retrieved from service after 12 years of operation. These material characterisation results will be used for the analysis in Chapter 7.

Chapter 5.

LOW TEMPERATURE CREEP AND ITS EFFECT ON HISC IN DSSS

5.1 Introduction

As discussed in the literature review, DSSs are materials that undergo low temperature creep when subjected to a constant load. The macroscopic behaviour of LTC of DSSs was observed and discussed by many investigators [114], [117], [113], [122] but its microscopic mechanism is still not established. In service conditions, DSSs components can be found in constant load configuration and after the investigation of HISC failures, conclusions on LTC being a prerequisite for HISC to occur were drawn [193] and [122]. Hence, it is crucial to understand this phenomenon, as well as its interaction with hydrogen and its potential influence on the HISC mechanism.

The work presented in this chapter is an attempt to develop a better understanding of the micro-mechanism of LTC and its link with HISC in DSSs, by comparing the responses of the wrought and the HIPed materials (which were characterised in Chapter 4).

The work studied the mechanical response and microstructural changes, in terms of the evolution of strains and misorientations, in the two alloys during testing. The development of strains within the two microstructures was studied by coupling constant load testing and digital image correlation (DIC) of the EBSD maps obtained, after each step of loading, from the tested specimens. While DIC is a powerful tool, high-resolution analysis of large areas can be very time consuming using this technique. Therefore, initially focus was placed on studying the development of strains during

LTC, using DIC coupled with incremental step-loading tensile tests, within an area encompassing only a few austenite and ferrite grains. Additional testing using single step-loading tensile tests followed by EBSD mapping was performed to enable to confirm the DIC observations, using a larger area.

DIC is a technique allowing the observation of microscopic behaviour during deformation [169]. The principles of this method were presented in Chapter 3. The experimental methodology adopted here involved three major steps:

1) the preparation of the specimen (which comprised machining, metallographic preparation and deposition of a marker on the centre of the specimen to locate the ROI);
2) the EBSD mapping of the ROI;
3) the performance of DIC (which involved switching between tensile testing and SEM imaging; and the processing of the DIC data).

The data generated via EBSD were used to map local misorientation (LMOs) and the angle-boundary. LMOs allow the identification of a particular degree of misorientation over the scanned area, which can then be related to plastic strain [194], [195], [196].

5.2 Experimental methodology

5.2.1 Specimens preparation

Four flat, dog-bone-shaped tensile specimens, with the geometry shown in Figure 5.1, were extracted from each material, using electro-discharged machining (EDM). The as-machined thickness of the specimens was 2 mm. Taking into account an austenite spacing of 10 μm, this thickness ensured a minimum of 100 ferrite and austenite layers, and therefore the specimen was deemed representative of the bulk material. In the case of M1, the wider side of the gauge length was along the rolling and radial directions, and sampled the pipe's through-thickness microstructure, Figure 5.1. This choice of orientation aimed to replicate the loading conditions that would be experienced by the pipe in service, and allowed tracking of the austenite and ferrite phases and their boundaries during testing.

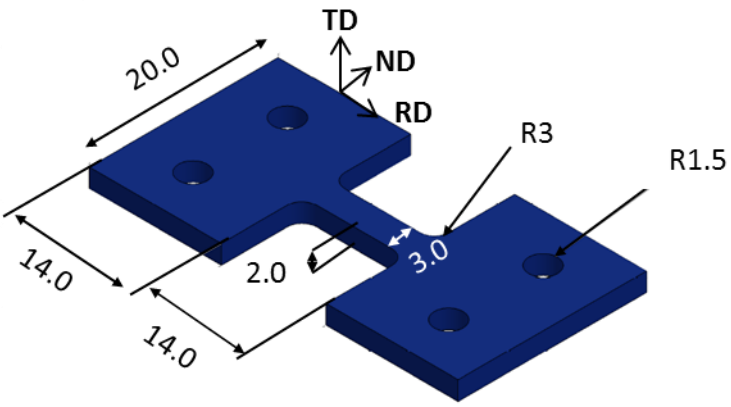

a)

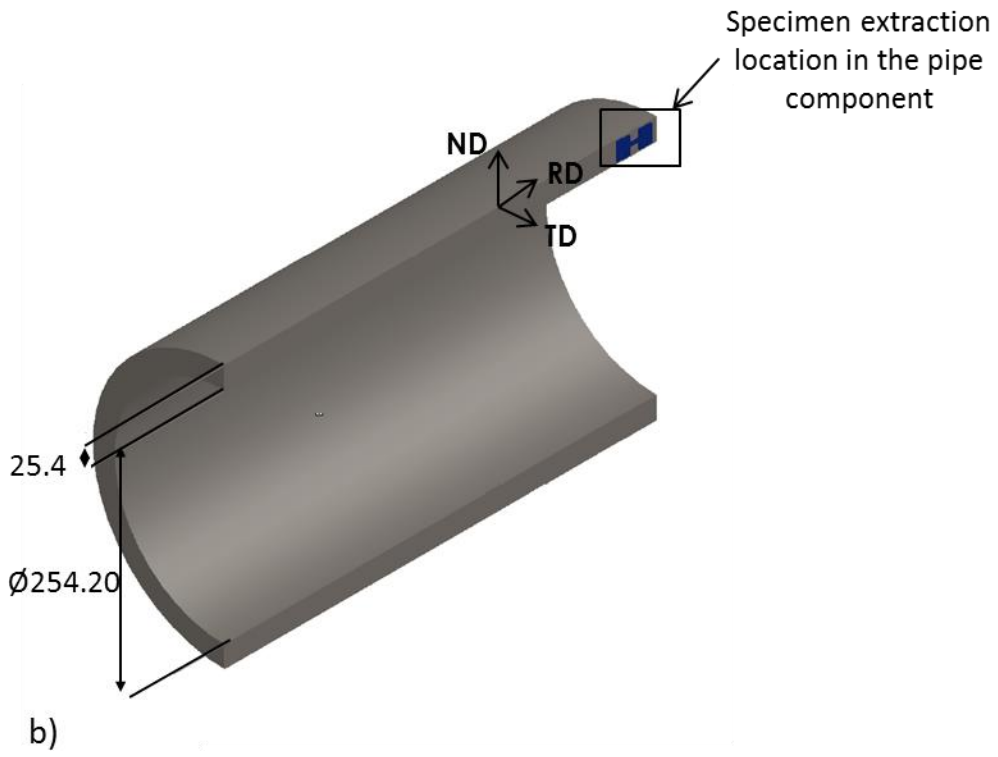

b)

Figure 5.1: Showing the a) dimensions in mm and, b) location of the specimens extracted from the pipe material (M1).

After machining, both sides of the specimens were manually ground using 60 to 1200-grit SiC abrasive paper, to remove any hydrogen which could have penetrated into the material during EDM [197], [198].

As described in Chapter 3, to be able to interpret the DIC outcome and link it to the underlying microstructure, EBSD mapping of the ROI is required to be carried out prior to the deposition of the DIC pattern. As such, one side of the two samples used for DIC were metallographically prepared using the same methodology described in Chapter 4 and enabling. This was carried out using a purpose-made sample holder. The size of the sample holder was determined such that it could be fit into the automatic polisher in order to perform the last polishing step. The addition of an aluminium ring around the holder ensured that the specimens stayed as flat as possible during manual grinding process, Figure 5.2a. This preparation step reduced the specimen thickness slightly; hence, the dimensions of the specimens were measured and recorded before testing.

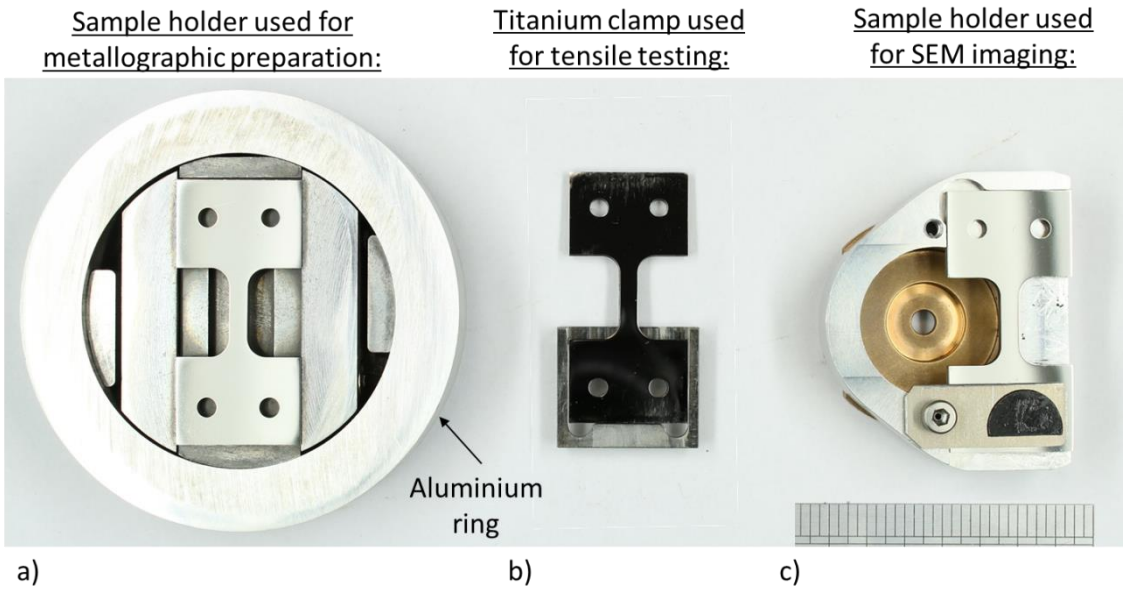

Figure 5.2: Showing the sample holders used for a) metallographic preparation; b) positioning in the tensile machine and c) positioning in the SEM chamber.

In order to track the ROI, a marker was deposited on the metallographically-prepared surfaces. This was achieved by Pt deposition in a focused ion beam (FIB) microscope. The size of the marker was approximately 1 μm × 5 μm, and ~ 2 μm in thickness and was positioned in the centre of the gauge length.

5.2.2 EBSD mapping

EBSD mapping of the ROI was performed using parameters similar to those described in the Chapter 4. The EBSD maps were used at a later stage to relate the DIC maps to microstructural features (i.e. by overlaying the two maps). The marker, visible in the

EBSD and DIC maps, was used to align the two images. Furthermore, the data on the grain orientations were used to determine the slip system activated during LTC and the relative orientation between the austenite and ferrite. This was achieved by the methodology described in the Chapter 3.

5.2.3 Deposition of the DIC pattern

Deposition of the DIC pattern was made by gold remodelling method enabling to obtained DIC maps with a submicron spatial resolution [199]. In order to generate an optimal remodelling DIC pattern, i.e. speckles of similar size, distinguishable among each other and randomly distributed [169], the surface preparation of the specimen, the thickness of the gold layer[200] and the environmental conditions for remodelling have to be optimized. Di Gioacchino [199] investigated these conditions for stainless steel alloys and those were the ones followed in this study. A gold layer was deposited on the metallographically-prepared surface of the specimens, using an Edward S150B sputter coater instrument. Sputtering time was 2.5 minutes in an argon pressure of 103 atm. The gold remodelling was conducted in water vapour environment. As schematically shown in Figure 5.3, the specimen was placed on a hot plate at 280°C, next to a beaker filled with distilled boiling water; the set was covered by a glass cap to protect the specimen's surface, and to prevent the vapour from escaping. Duration of 3 hours was considered to generate a sufficiently-fine gold pattern.

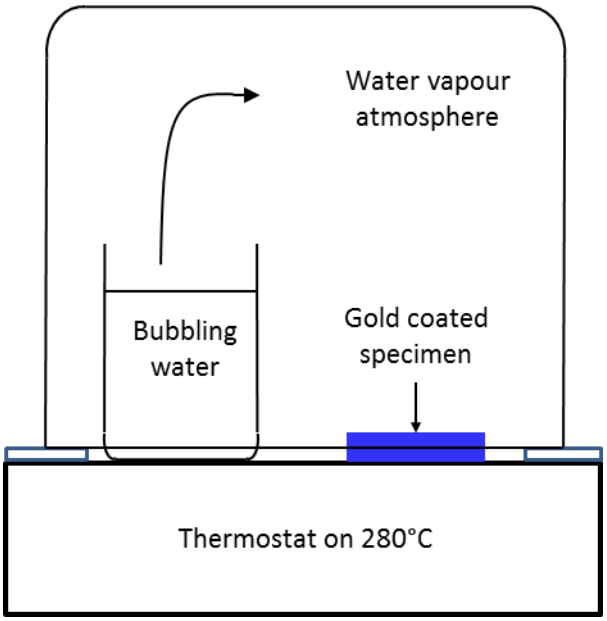

Figure 5.3: Schematically presenting the set-up of the gold remodelling process.

5.2.4 DIC imaging and data processing

Imaging of the DIC deposited pattern at every load levels was performed in a Zeiss Sigma FEG-SEM. Four SEM images of 26.1 × 37.6 μm^2, were taken at each load step, giving a total analysed area of approximately 50.1 × 73.3 μm^2, which correspond to 4068×5871 px^2. DIC analysis was carried out using the open source Ncorr 2D-DIC MatLABs software. Circular subsets were used, with a radius of 12 pixels and spacing of 8 pixels, allowing a degree of overlap. For each subset, the software calculated the displacement of the pattern's speckles between the loading step and the pattern before loading. Those displacements were converted into strains. The resulting DIC maps displayed the in plane shear strains, ε_{xy}:

$$\varepsilon_{xy} = \frac{du}{dy} + \frac{dv}{dx} \tag{27}$$

With u and v the displacement vectors in the x and y direction respectively. The regions seeing significant tensile strain were highlighted by yellow, orange and red colours. The four obtained strain maps, from the four regions were montaged using the Pt marker as a reference, using Gimp software.

5.2.5 Mechanical testing

5.2.5.1 Incremental Step-loading test procedure for DIC

Tensile tests was carried out, on a series of specimens loaded to certain load targets, not exceeding the materials'100 % 0.2 % proof stress. The width and the thickness of the specimens' gauge length were measured, prior to testing, at five different points, using a Vernier calliper. The values obtained were averaged to be used for determining the target load levels needed to be applied during testing. Testing was performed in an Instron tensile testing machine frame, a titanium clamp fitting the specimen geometry, Figure 5.2b), was used to ensure straight positioning of the specimen. The specimens were first loaded to 50 % of their 0.2 % proof stress ($\sigma_{y,0.2\ \%}$), 515 MPa and 540 MPa for M1 and M2 respectively, using a displacement rate of 0.02 $mm.s^{-1}$. The load was applied for 24 hours. Previous work on LTC in DSSs [117] showed that after a couple of hours the strain rate during LTC decreases significantly, hence 24 hours was sufficient to capture the major strain development. The specimens were subsequently unloaded, with SEM imaging performed on the ROI. Each specimen was then loaded to

60 %$\sigma_{y,0.2\ \%}$; 70 %$\sigma_{y,0.2\ \%}$; 80 %$\sigma_{y,0.2\ \%}$; 90 %$\sigma_{y,0.2\ \%}$; 100 %$\sigma_{y,0.2\ \%}$ and kept for 24 hours. At all imaging stages, the position of the specimens with respect to the microscope lens and working distance was consistently maintained using the same paramters, and the sample holder showns earlier in Figure 2.

Before the first loading, SEM images of the ROI with the DIC pattern were taken and the imaging parameters (i.e. beam voltage, aperture, magnification, noise reduction, image resolution: 3072 × 2304) were recorded.

5.2.5.2 Single loading test and EBSD mapping

Two specimens, of similar geometry to those used previously, were extracted from M1 and M2 and loaded to 90 %$\sigma_{y,0.2\ \%}$ for 24 hours using the same loading procedures described above. The sample surfaces were metallographically prepared and EBSD mapping was performed on the centre of the gauge length specimen, using the same parameters described in Chapter 3. The data were processed using HKL Channel5 software to generate phase, LMOs and angle boundary maps. The LMOs maps give the average LMOs for a misorientation below the sub-grain angle threshold, chosen as 5° in this work and consists of measuring the average misorientation between one pixel and its surrounding pixels, in this case 5, (i.e. the filter size was chosen as 5×5) and to assign the mean value to this pixel. For each of the LMOs maps generated the related histograms for the ferrite and austenite phases were extracted, using a binning of 0.05°. In the angle boundary maps, the low angles boundaries (LABSs, red lines), were defined by an angle superior to 2° and the high angle boundaries (HABSs, black lines) by an angle superior to 10°. The austenite-to-ferrite phase boundaries (blue lines) were also included. For each map, the related histograms for the ferrite and austenite phases were plotted, using a binning 0.05°.

5.3 Results and observations

5.3.1 Incremental step-loading and DIC

Figure 5.4 displays the crosshead-displacement curves of the tensile machine according to the time, recorded during testing at a load level of 100 %$\sigma_{y,0.2\ \%}$ of the two materials. These two graphs clearly demonstrate the occurrence of LTC in the two materials and

were consistent with previous observations of LTC in DSSs [117], [201],[126]. It was also observed that the HIPed material exhibited a superior elongation compared to that in the wrought material.

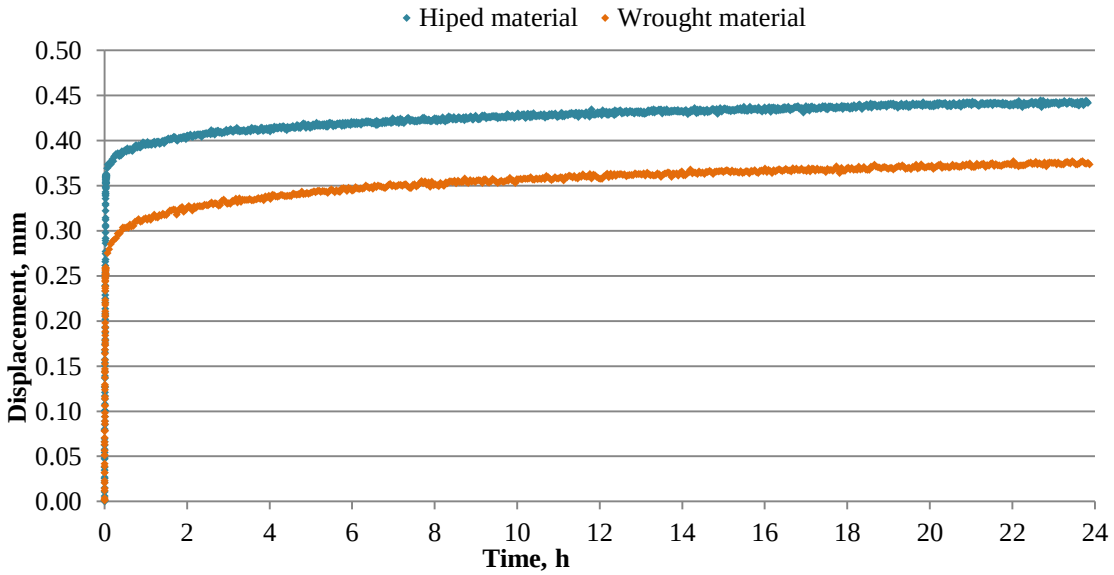

Figure 5.4: Displacement curves obtained after performing constant load testing to 100 %$\sigma_{Y,0.2\ \%}$ for 24 h on the wrought (orange line) and the HIPed (blue line) materials.

Figure 5.5 and Figure 5.7 display the DIC results obtained at each loading steps for M1 and M2 materials, respectively, with EBSD phase map (ferrite is in red and austenite phase in blue) and the orientation map overlaid. Those data were collected after each step of loading.

In the case of M1, Figure 5.5, the DIC results did not indicate any significant amount of plastic deformation, in terms of the development strain within the microstructure, below 70 %$\sigma_{y,0.2\ \%}$, and only some background noise was evident in the strain map. At 70 %$\sigma_{y,0.2\ \%}$, development of linear traces within the austenite grains, as well as straining at phase boundaries was apparent. Those linear features were assumed to be slip traces. At 80 %$\sigma_{y,0.2\ \%}$, the slip traces displayed a higher intensity. The image was also less noisy, new linear features parallel to the previous ones had formed, and similar new features also appeared within some of the ferrite grains. At 90 %$\sigma_{y,0.2\ \%}$, and 100 %$\sigma_{y,0.2\ \%}$, straining was intensified and also developed locally in some ferrite area, resulting in a heterogeneous distribution of strains within the ferrite matrix. At

100 %$\sigma_{y,0.2\,\%}$, the maximum local strain measured by the DIC analysis was identified to be located at a phase boundary.

The last image of the set shown in Figure 5.5 and Figure 5.7, is the DIC result superimposed on the orientation map (rather than the phase map). It can be seen that the angle of the slip traces within the austenite grains was dependent on the grain orientation.

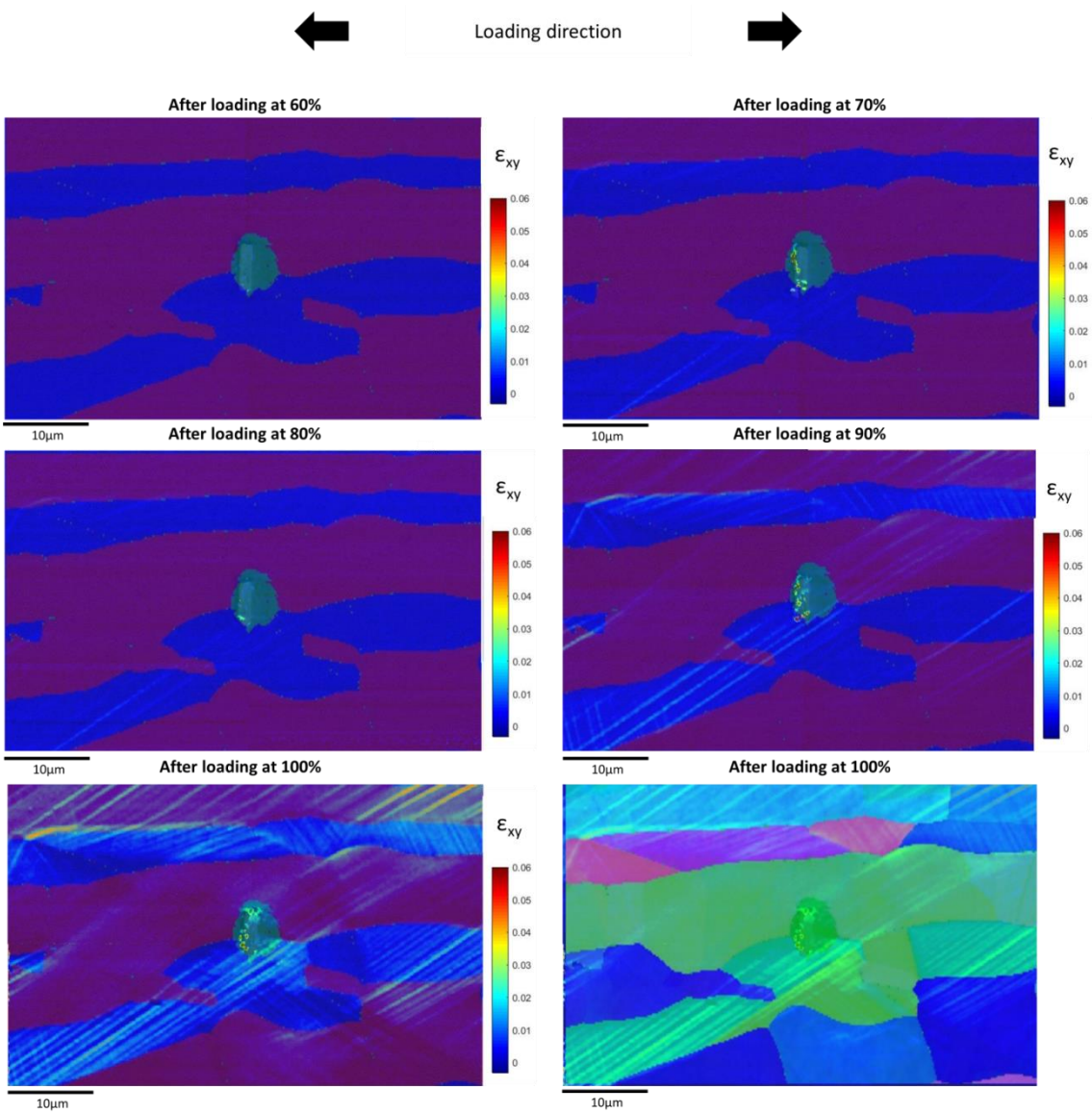

a)

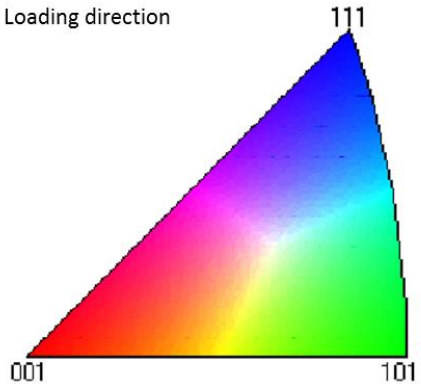

b)

Figure 5.5: a) EBSD phase maps at each loading step, overlaid with the DIC results obtained and orientation map, for M1, with b) orientation map legend for austenite and ferrite according to the loading direction.

In order to get a better understanding of the slip behaviour and strain localisation in the microstructure, the active slip systems were identified as well as the location in which the K-S OR between austenite and ferrite was fulfilled.

Figure 5.6 presents these results where the major deforming grains are numbered. In the case where the K-S orientation was fulfilled the slip traces drawn-out from the austenite grains to the ferrite grains. This was observed between the austenite grain 1(1_γ) and the ferrite grain 2 (2_γ) as well as between the austenite grain 6 (6γ) and the ferrite grain 3 (3_δ). At other phase boundaries where the K-S OR was not fulfilled, the slip traces generated within the austenite grains did not propagate in the neighbour ferrite (i.e. $2_\gamma/1_\delta$; $3_\gamma/5_\delta$; $4_\gamma/1_\delta$); however, an increase in the local strain level was observed.

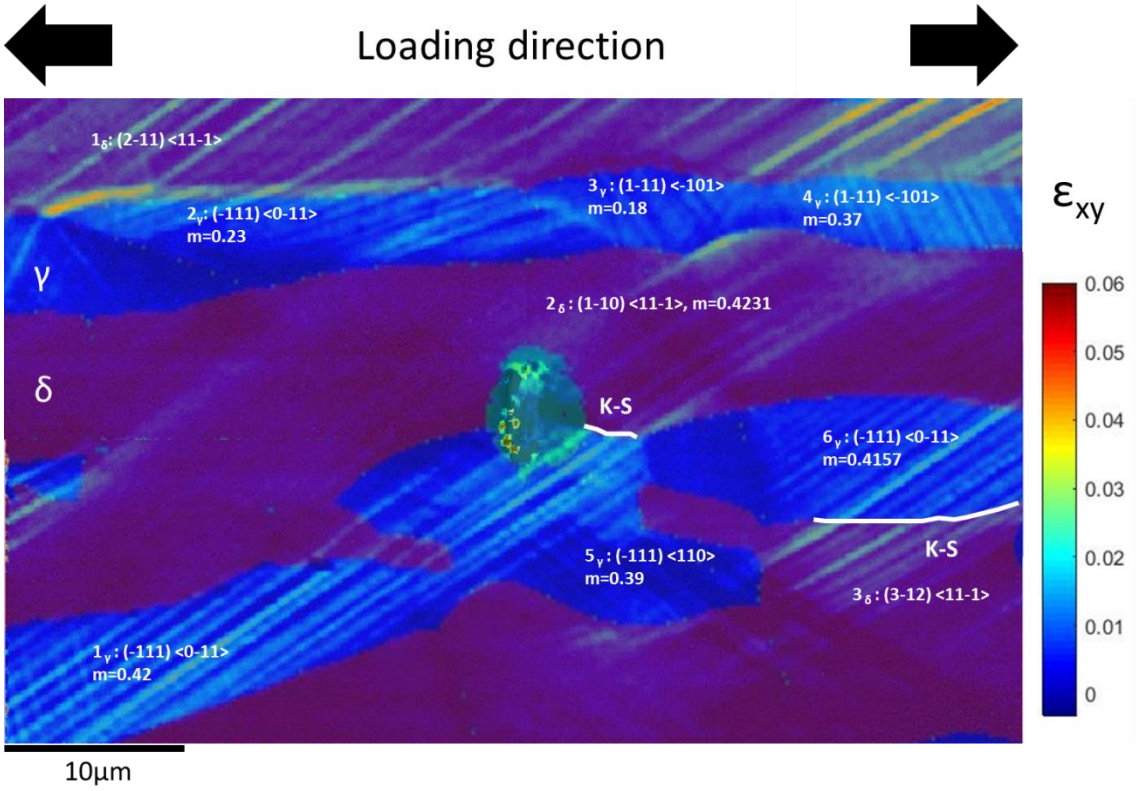

Figure 5.6: DIC results after 100 %σy,0.2 % applied load overlaid with the EBSD phase map for M1 and the identification of the slip system activated, their corresponding Schmid factors (m) and location of K-S OR.

Figure 5.7 and Figure 5.8 displayed the DIC maps obtained from the HIPed material. During this experiment slight alteration of the pattern occurred during loading, this resulted in some additional noise on the DIC map. The results showed the development of strain in the austenite grains, from the second loading step, i.e. 60 %σy,0.2 %. At 70 %σy,0.2 the development of new slip traces developed, and at 80 %σy,0.2 % no changes were observed. At 90 %σy,0.2 %, the development of strain in the austenite displayed higher intensity as well as development of new slip lines in the ferrite grains. Some austenite grains showed multiple active slip systems. At the last loading step, 100 %σy,0.2 %, new lines developed within the austenite grains and with a higher intensity. Figure 5.8 is the EBSD phase map obtained after loading to 100 %σy,0.2 %and overlaid with the associated DIC results, in which the slip systems activated were identified. Unlike M1, little extension of slip traces from the austenite grains to the ferrite grains was observable.

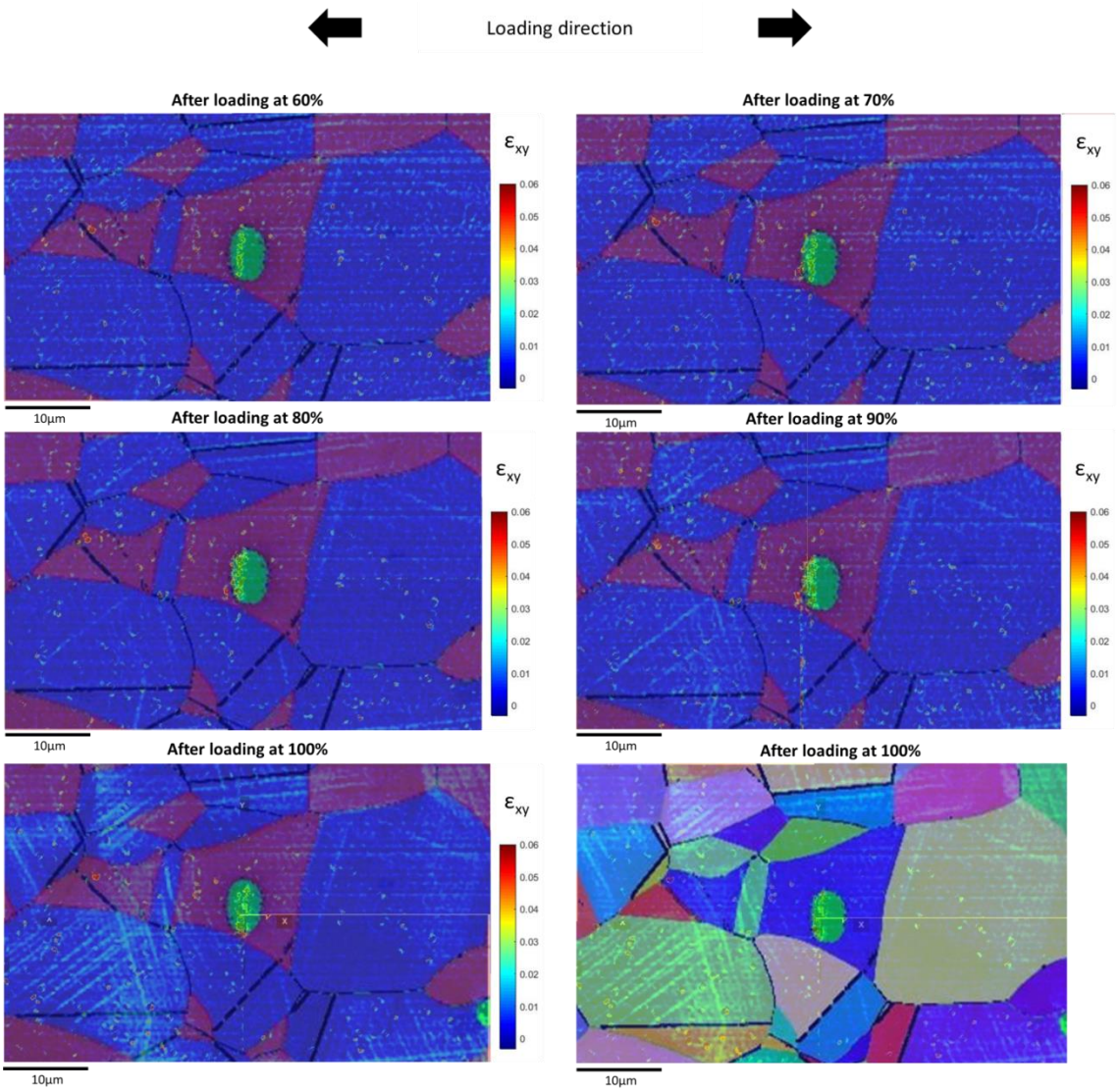

a)

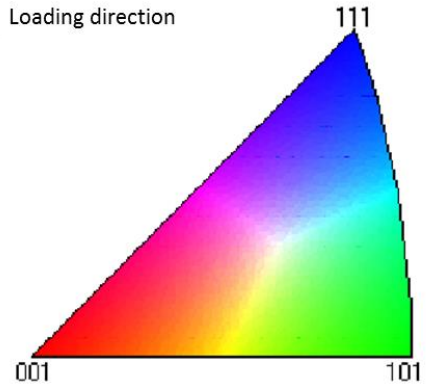

b)

Figure 5.7: Overlaid of the DIC results obtained at every load level with the EBSD phase maps and the orientation map, for M2 with b) orientation map legend for austenite and ferrite according to the loading direction.

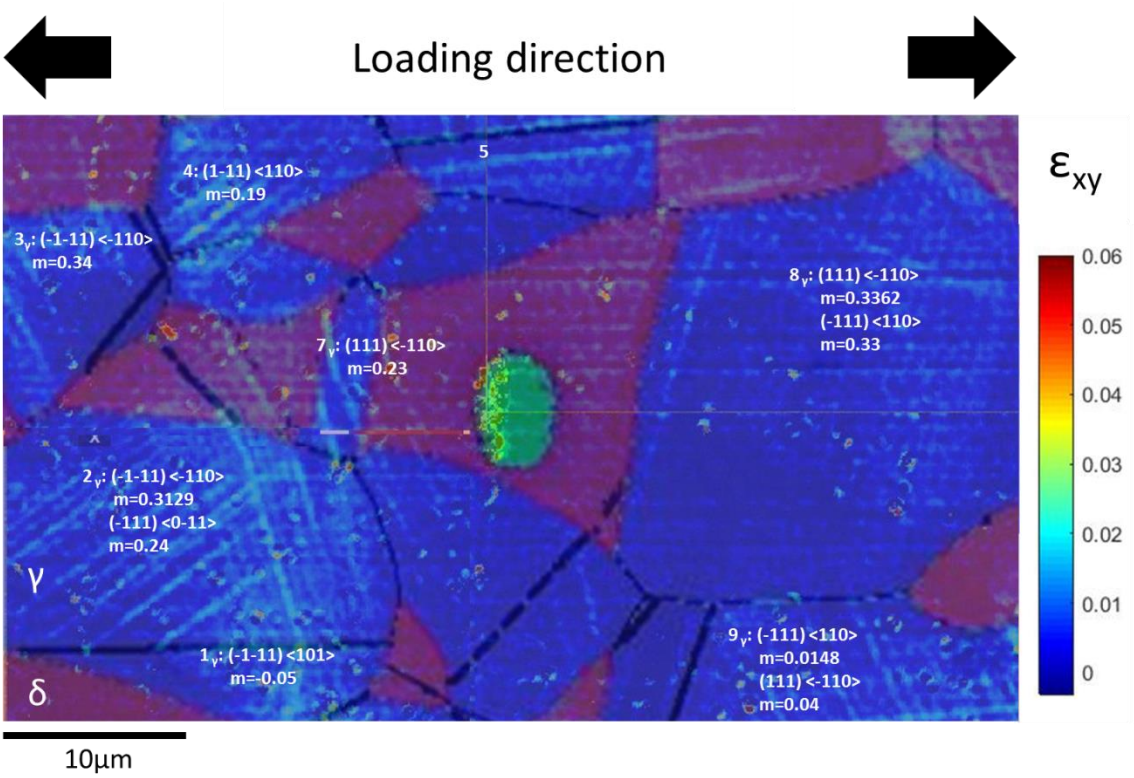

Figure 5.8: DIC results after 100 %$\sigma_{0.2}$ applied load overlaid with the EBSD phase map for M2 and the identification of the slip system activated with their corresponding Schmid factors (m).

5.3.2 Single step loading and EBSD mapping

The DIC findings revealed the localised mechanical response of the austenite and ferrite to loading during LTC; however, observations and interpretations were only limited to the small ROI investigated. In order to verify and obtain a more comprehensive understanding of the DIC observations, additional EBSD mapping was carried out on samples, from the two materials, loaded straight to 90 % $\sigma_{y,0.2\ \%,}$ for 24 hours. A larger field of view, encompassing a large number of grains and grain boundaries, was adopted to map the microstructure. This enabled further statistical analysis of the evolution of misorientations across the most highly stressed section of the specimens, i.e. the gauge length.

Figure 5.9 shows the result of the phase map, and associated LMOs and boundary angles maps for the wrought material. In the LMOs map, the higher degree of misorientation, highlighted in bright green, was associated with plastic straining. In the as-received condition (before loading), the material exhibited a degree of local misorientation, homogeneously distributed in the ferrite grains. This was consistent

with the previous work [202], and is thought to be due to the different thermal expansion coefficients of austenite and ferrite inducing residual stresses during solidification [68]. The LMOs map of the specimen loaded to 90 %$\sigma_{y,0.2\ \%}$ displayed higher level of local misorientation within some ferrite grains. The associated graphs,

Figure 5.11, showed an increase of misorientation angles in the specimen deformed compared to the one in as-received conditions for austenite and ferrite. The changes observed in the misorientation angles were very small (i.e. < 0.1°); however, for the level of strain levers dealt with here, i.e. up to 1 % at 90 % loading, this is thought to be significant. This behaviour was consistent with previous work on the deformation of DSSs [202] and indicates the development of plastic straining in the two phases for this material.

The angle boundary maps are displayed in Figure 5.10 with the associated histograms for austenite and ferrite in Figure 5.12 and Figure 5.13 respectively, before and after loading. The location of LABs was matching the location of the LMOs. In the case of the austenite phase, the histogram displayed two major peaks: one below 10° (LABS) and one at 60°. The peak at 60° corresponded to the primary recrystallization twin in austenite [203] and no changes of this peak were observed after loading, Figure 5.12c). However, slight decrease of the LABs peak was observed after loading. This observation was consistent with the LMOs and DIC results, indicating that straining is mainly accommodated within the austenite grains, and without much contribution from their twin boundaries. In the case of the ferrite phase, only one peak was observed in the histogram, in the LABs range, and an increase of the LABs population was seen after loading.

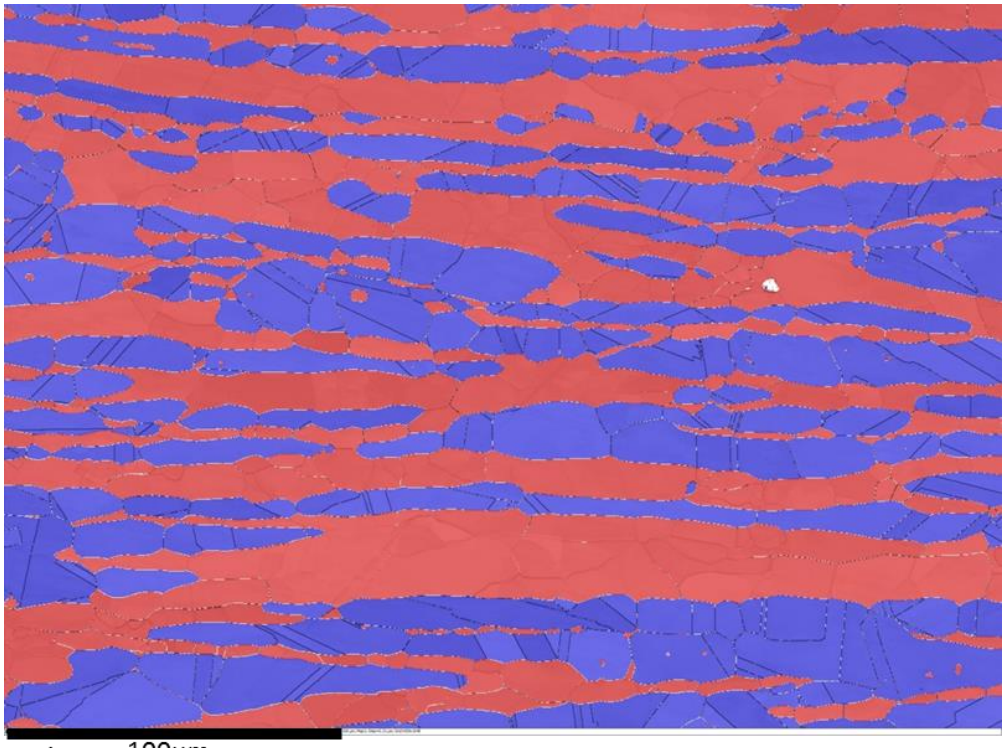

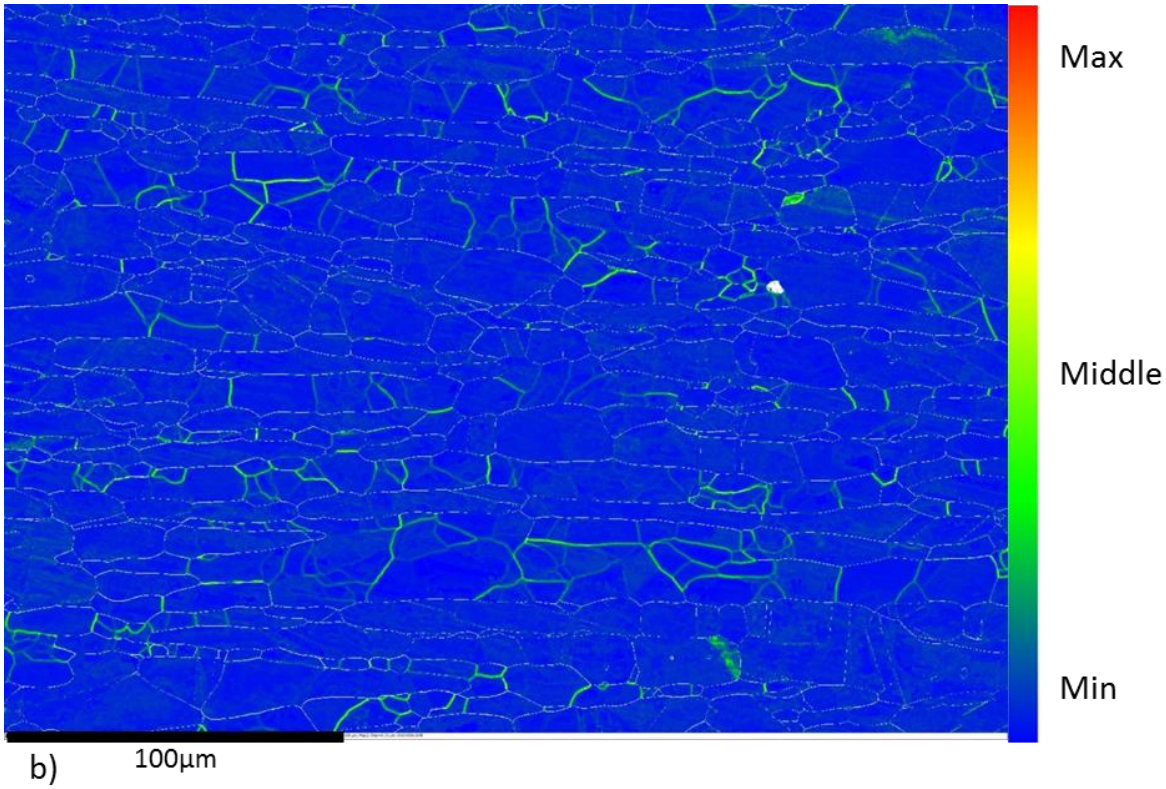

Figure 5.9 (continued): a) Phase map and associated b) LMOs map for the wrought material in as-received conditions.

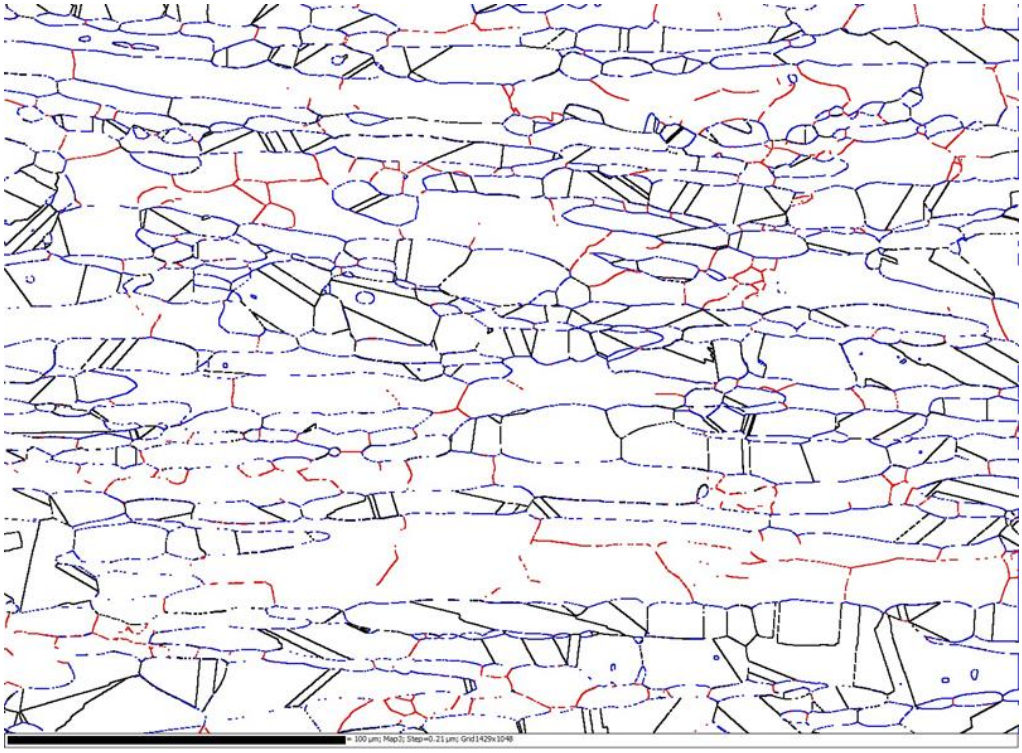

Figure 5.9: c) angle boundary map for the wrought material in as-received conditions.

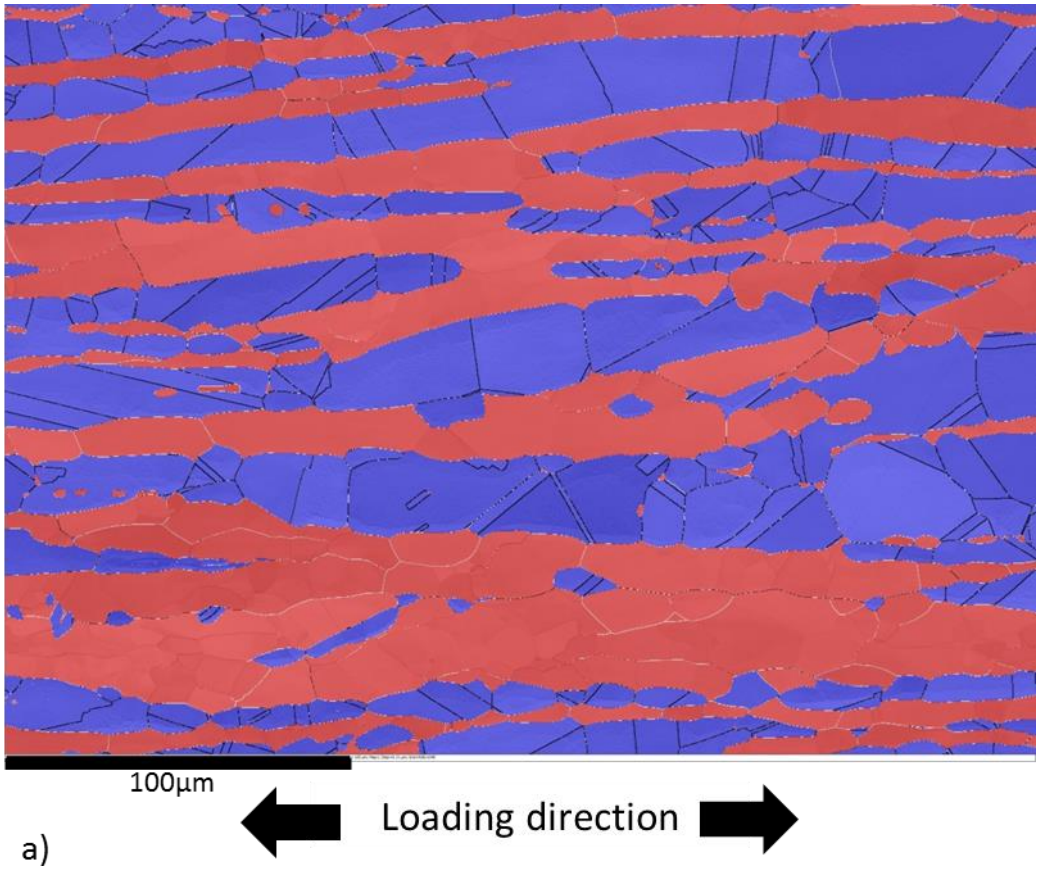

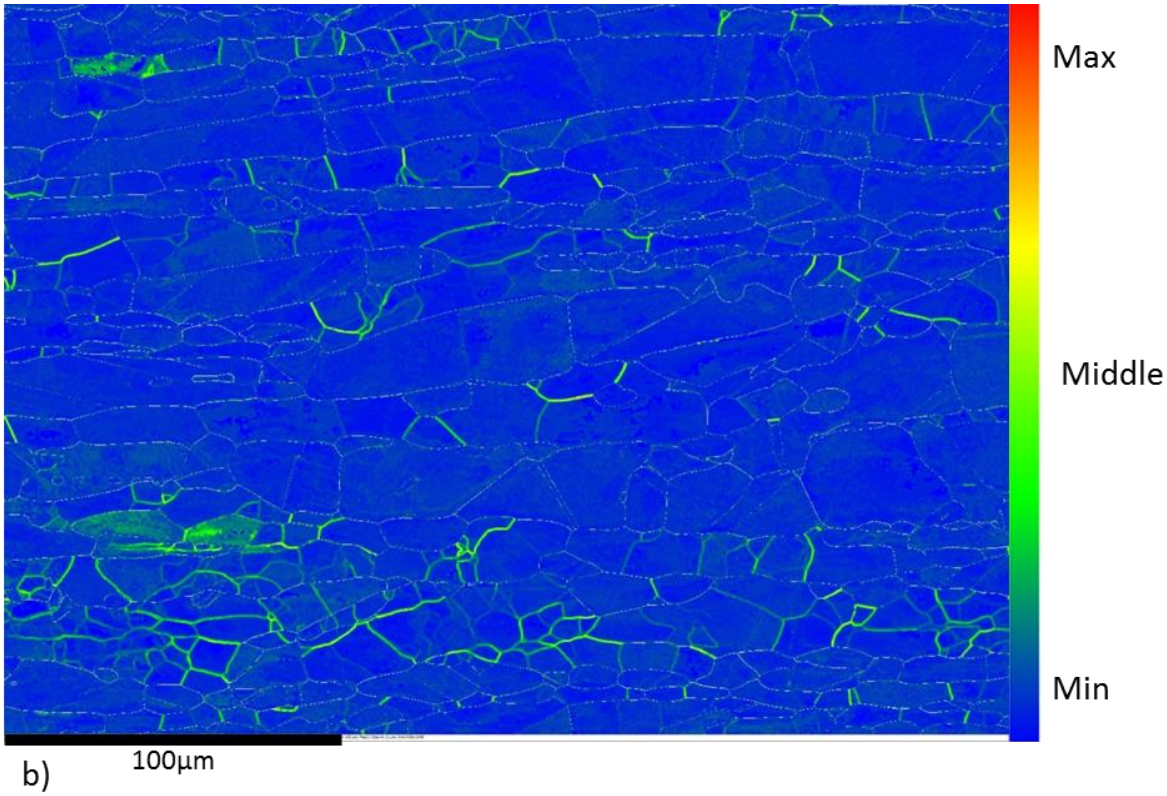

Figure 5.10 (continued): a) Phase map and associated b) LMOs map for the wrought material after loading to 90%$\sigma_{y,0.2\ \%}$ for 24 hours.

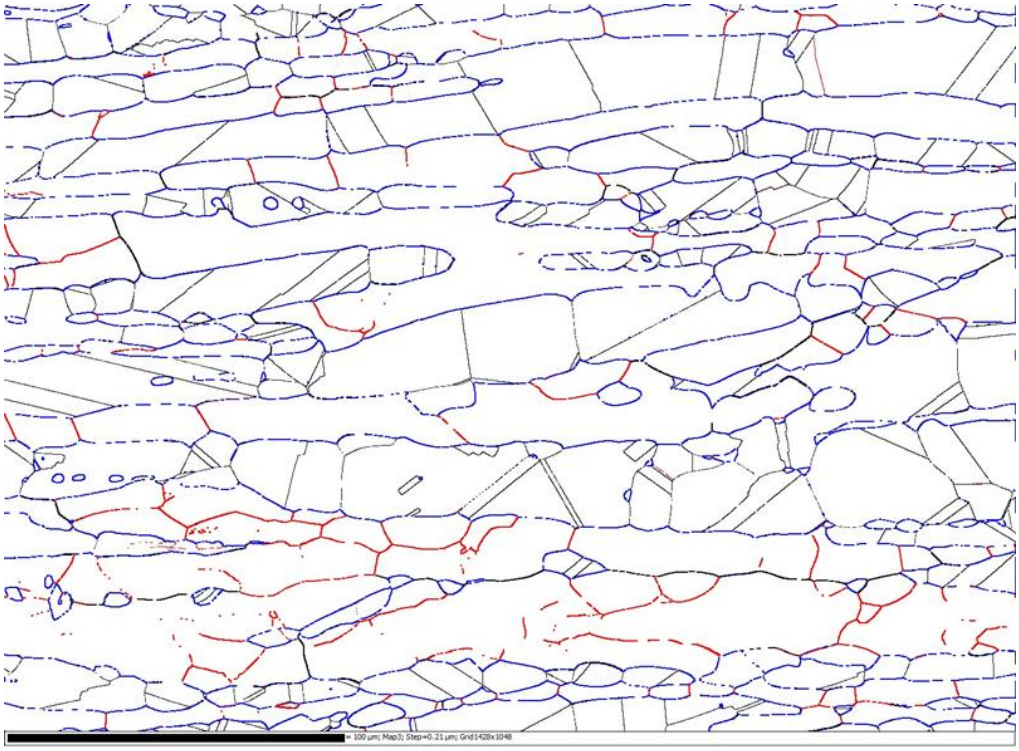

Figure 5.10: c) angle boundary map for the wrought material after loading to 90 %$\sigma_{y,0.2\ \%}$ for 24 hours.

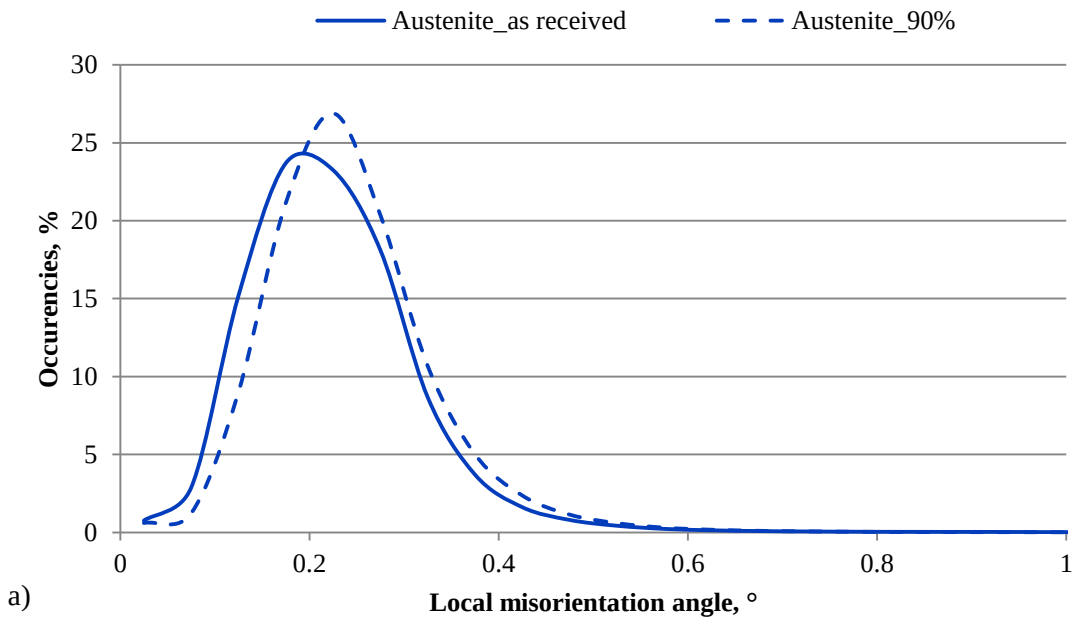

a)

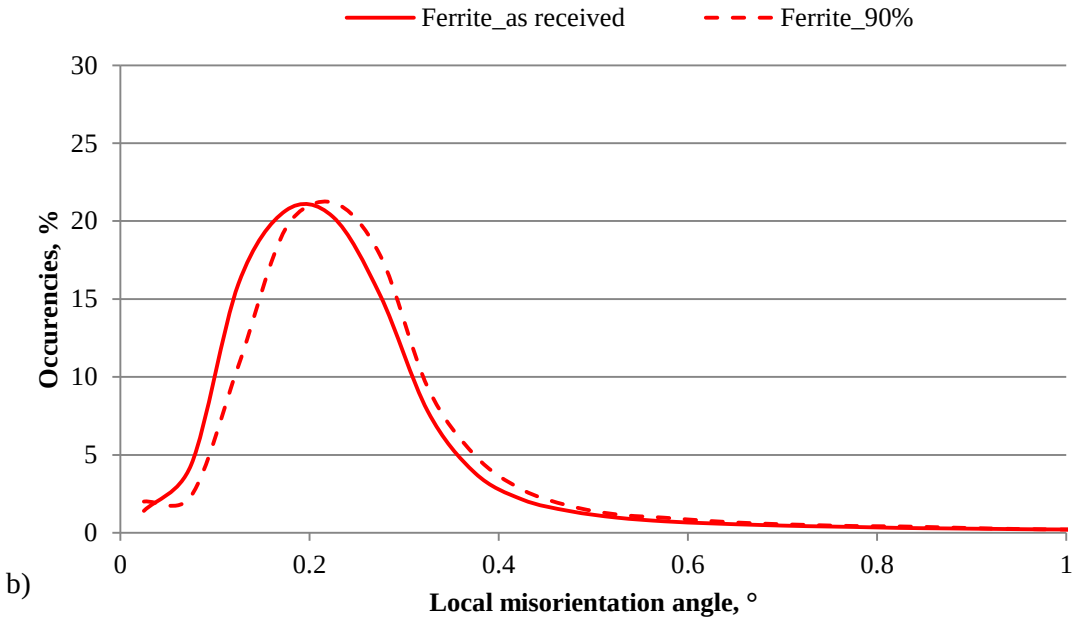

b)

Figure 5.11: Histograms associated with LMOs maps of the wrought material for a) austenite and b) ferrite phases in as as-received conditions (plain line) and after loading to 90 %$\sigma_{y,0.2\ \%}$ for 24 hours (dotted line).

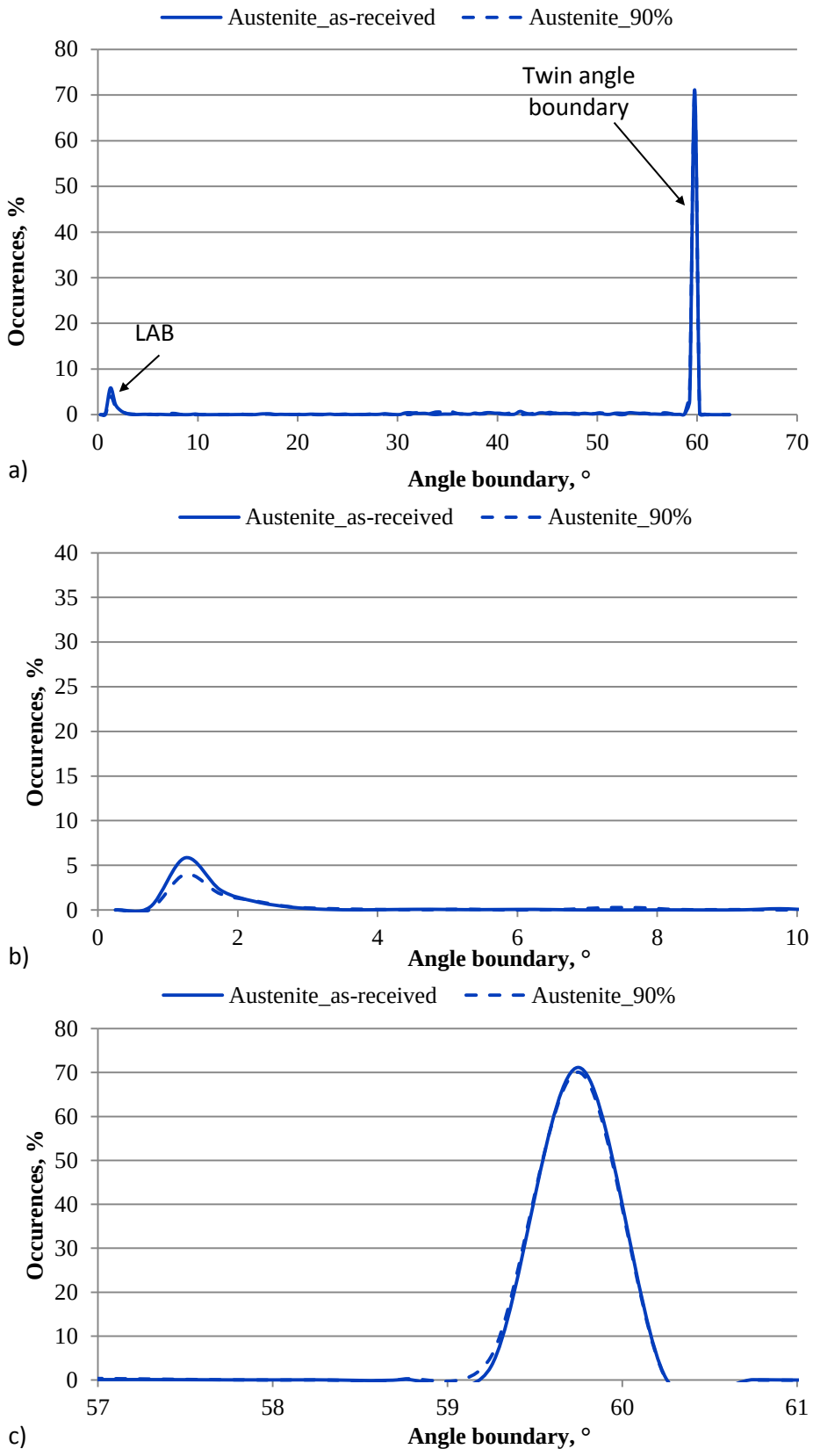

Figure 5.12: Histograms associated with the angle boundary maps in the case of the wrought material for the austenite phase, a) all range of angles, and magnification on the b) LABS and c) twin peak.

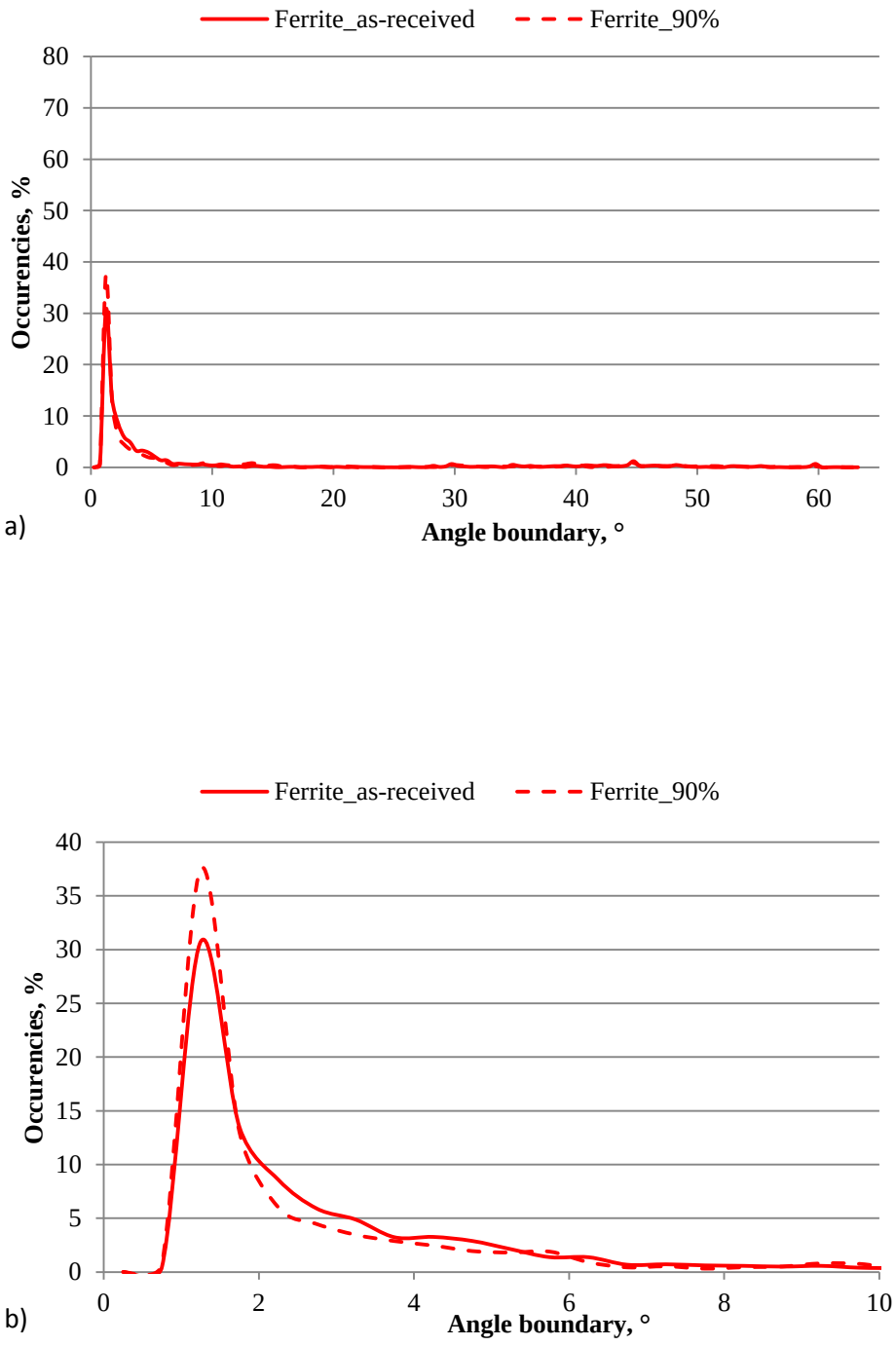

Figure 5.13: Histograms associated with the angle boundary maps in the case of the wrought material for the ferrite phase, a) all range of angles, and magnification on the b) LABS.

Figure 5.14 shows the phase map and the associated LMOs maps and angle boundary results for the HIPed material. The LMOs showed that in as-received conditions, almost no high misorientations were observable. After 90 $\%\sigma_{y,0.2\ \%}$ of loading, the specimen exhibited some local misorientation at the boundaries within ferrite and austenite phases. However, compared to M1, this was much lower. The graphs shown in Figure 5.16, confirmed this observation: a small change in the misorientation angle was observed for the austenite, but no changes was observed in the ferrite between the as-received condition and the specimens loaded to 90 $\%\sigma_{y,0.2\ \%}$.

According to the angle boundary maps, a very few LABSs were present in the as-received conditions and their population only slightly increased after loading. In the case of the austenite a similar histogram shape to that of the wrought material was obtained, with two major peaks: one for the LABSs and one for the twin boundaries. After loading an increase in the LABS population was observed. In the case of the ferrite phase, the angle boundary histogram showed more variation than in the case of the wrought material and the density of LABS was much lower in the HIPed than in the wrought material: 17 % against 38 %, respectively in as-received conditions. After loading, no changes in the population of LABSs were observable.

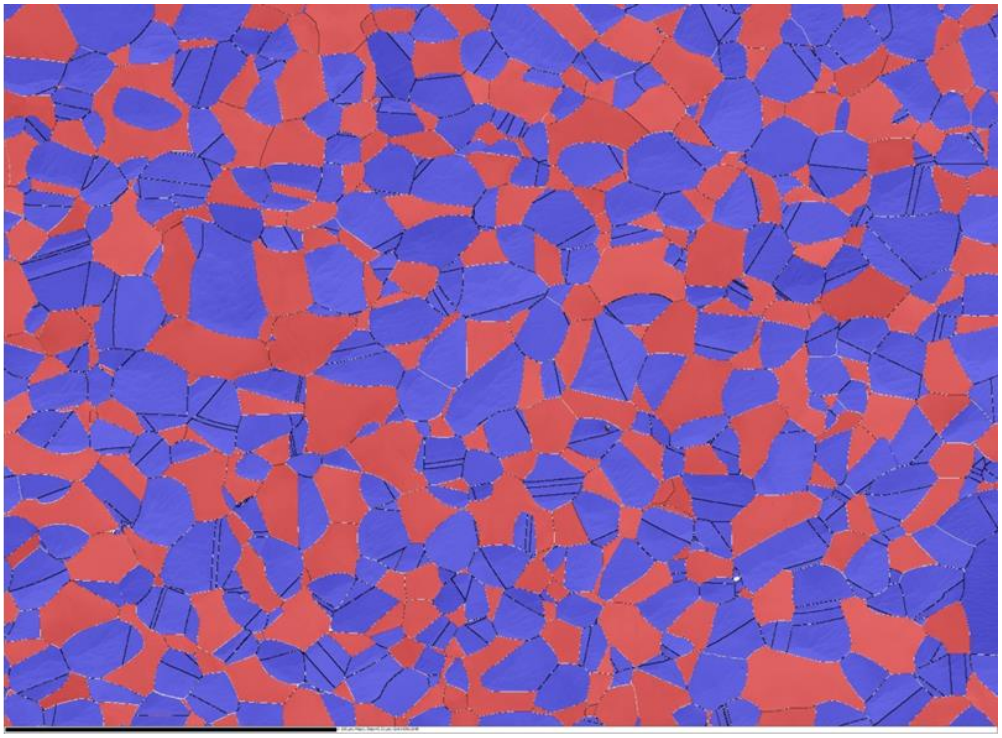

Figure 5.14 (continued): a) Phase map for the HIPed material in as-received conditions.

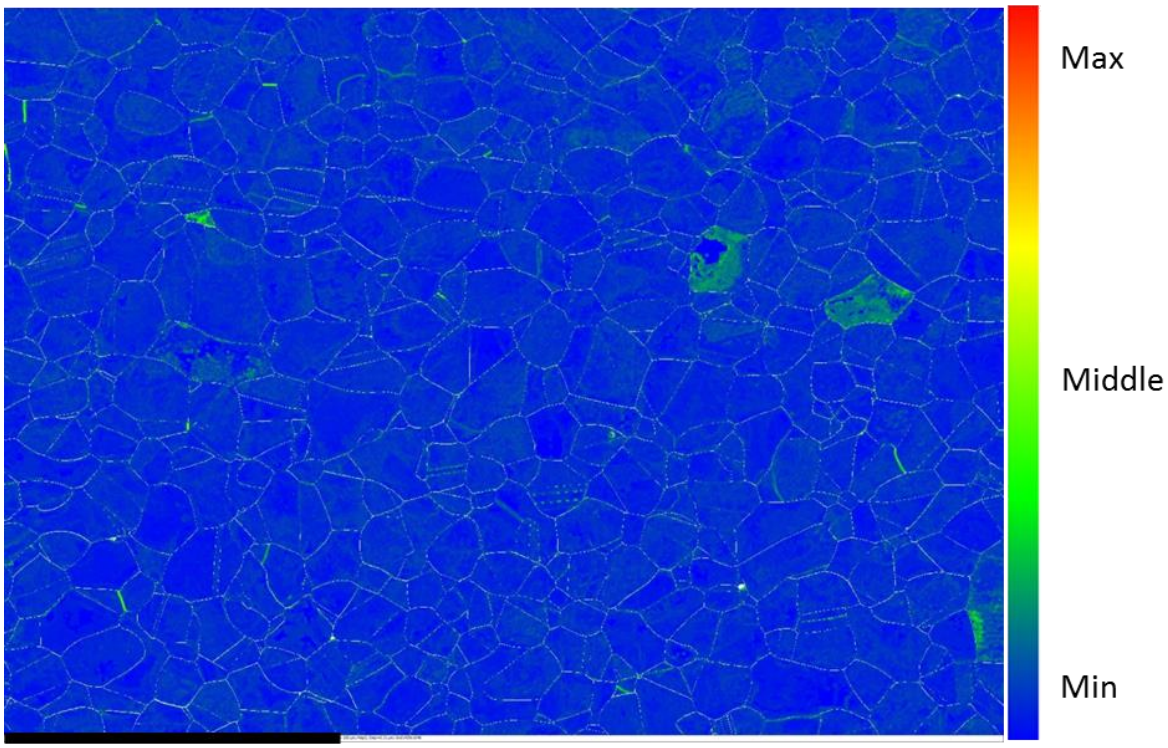

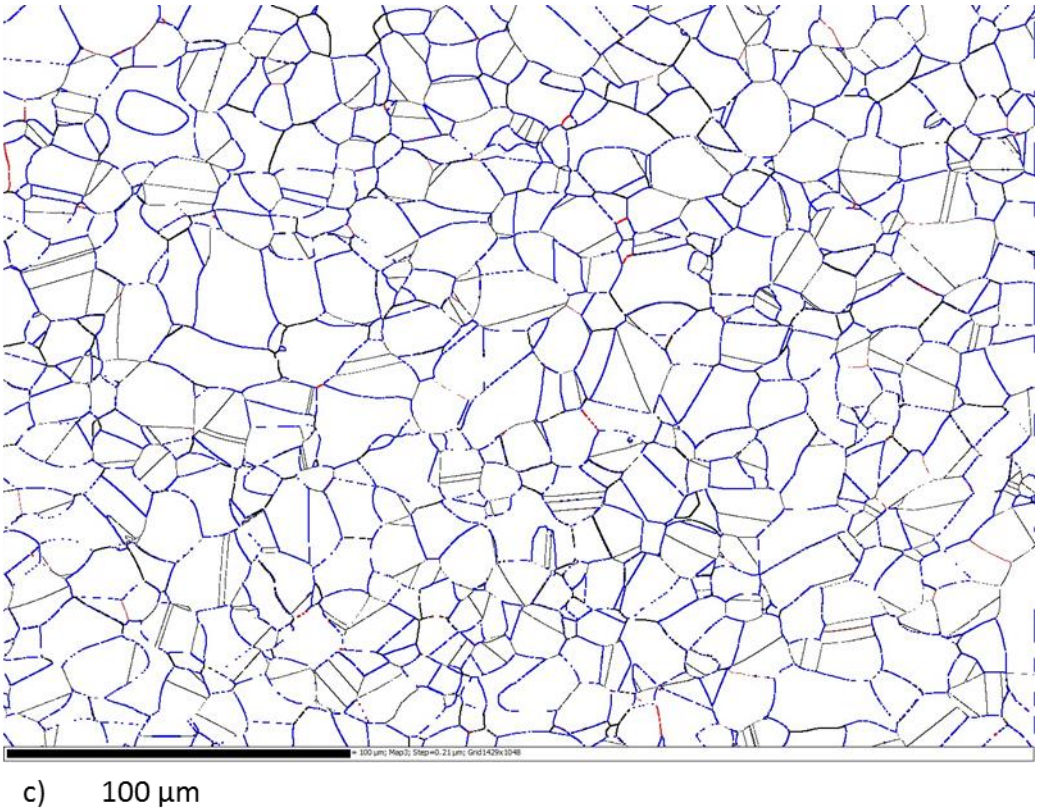

Figure 5.14: b) LMOs and c) angle boundary maps for the HIPed material in as-received conditions.

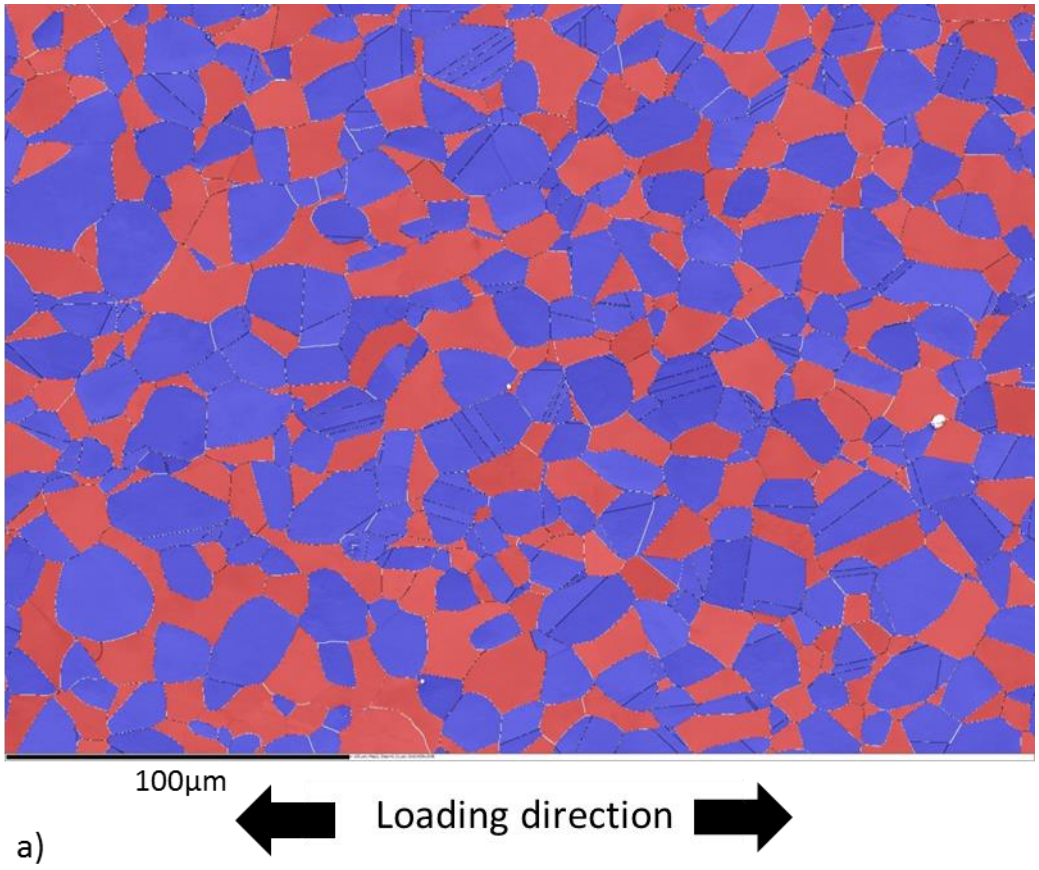

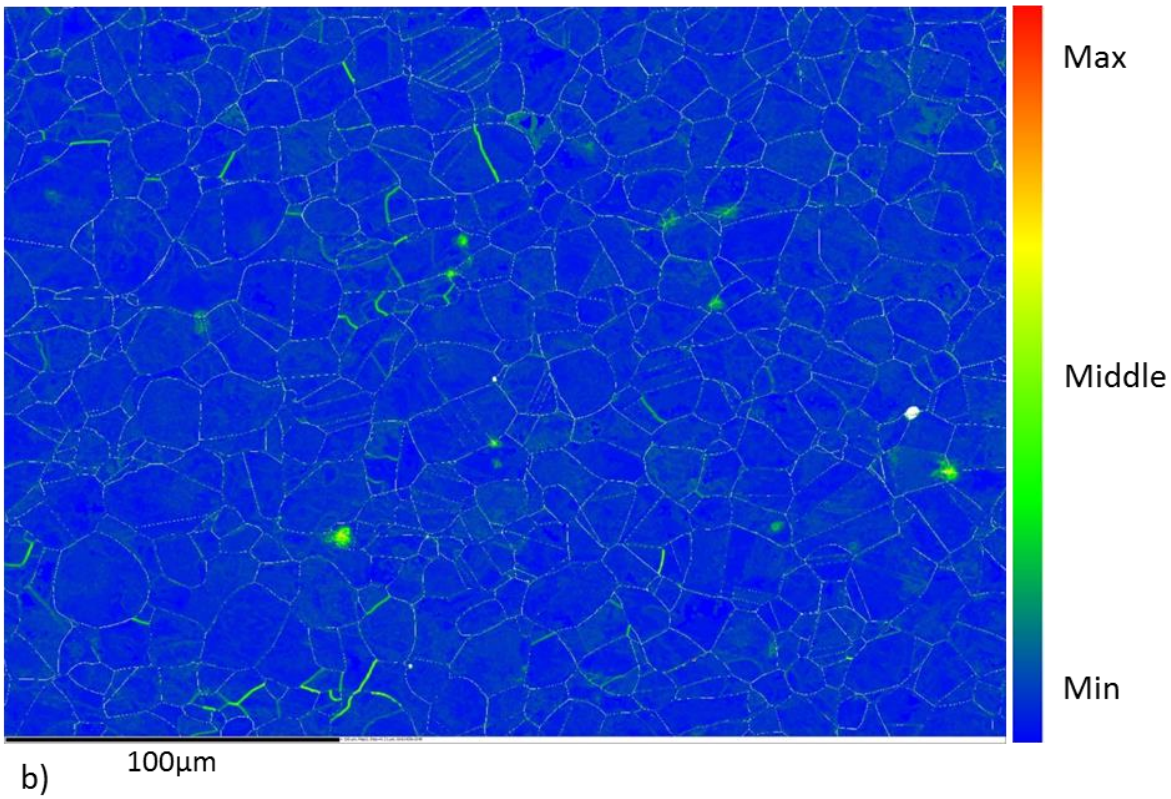

Figure 5.15 (continued): a) Phase map and associated b) LMOs for the HIPed material and b) after loading to 90 %$\sigma_{y,0.2\ \%}$ for 24 hours.

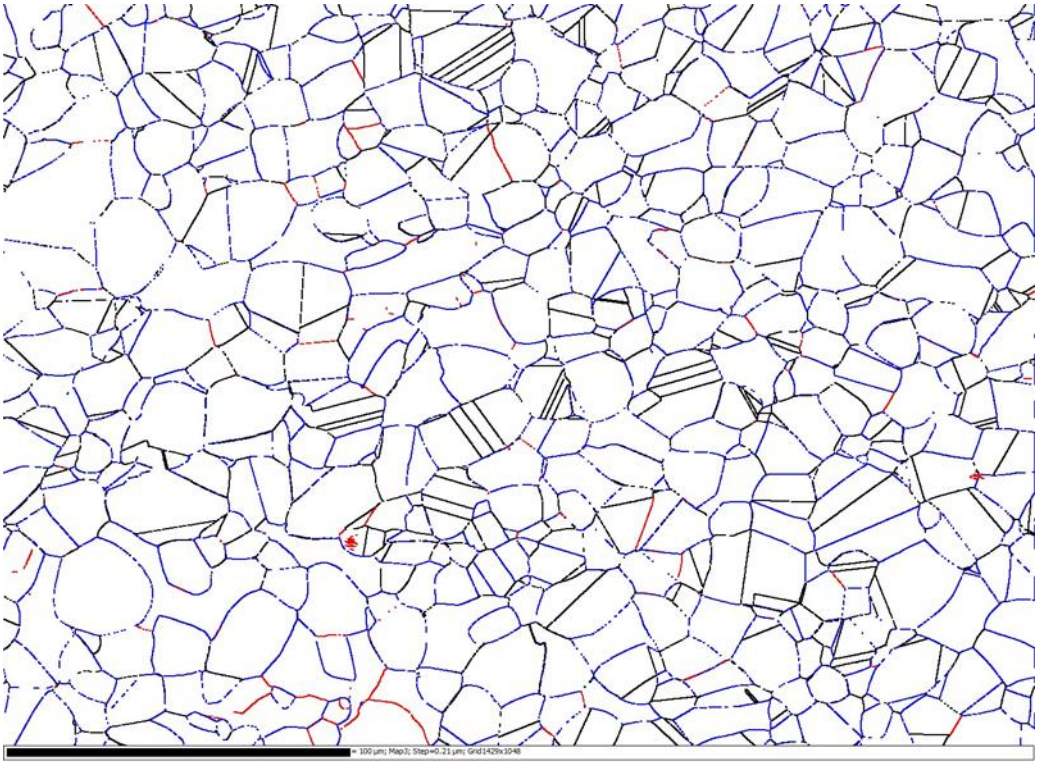

Figure 5.15: c) angle boundary map for the HIPed material and b) after loading to 90 %$\sigma_{y,0.2\ \%}$ for 24 hours.

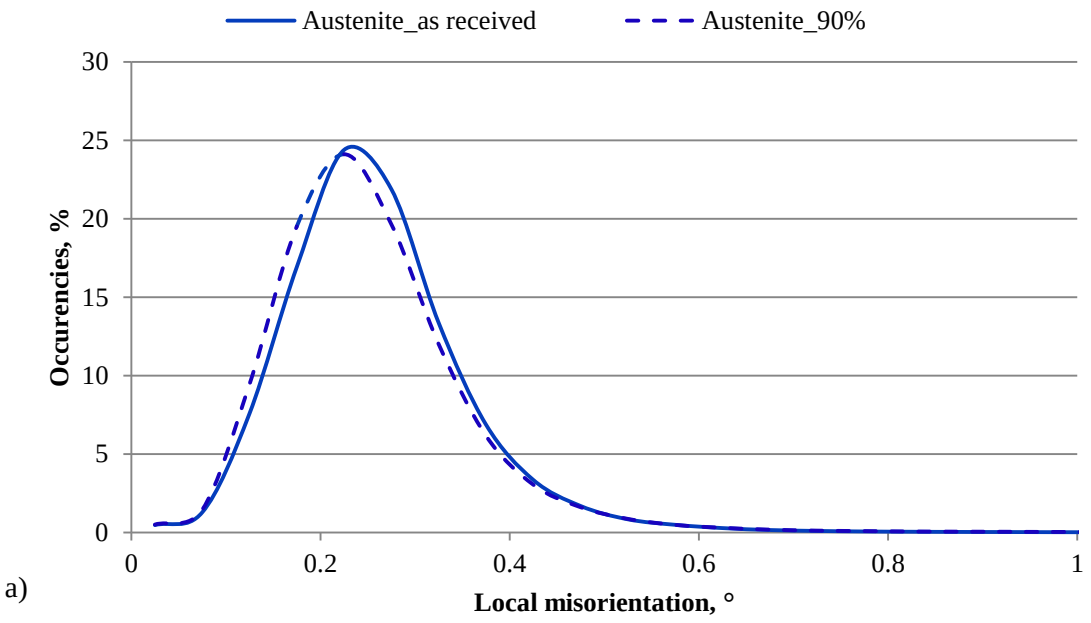

a)

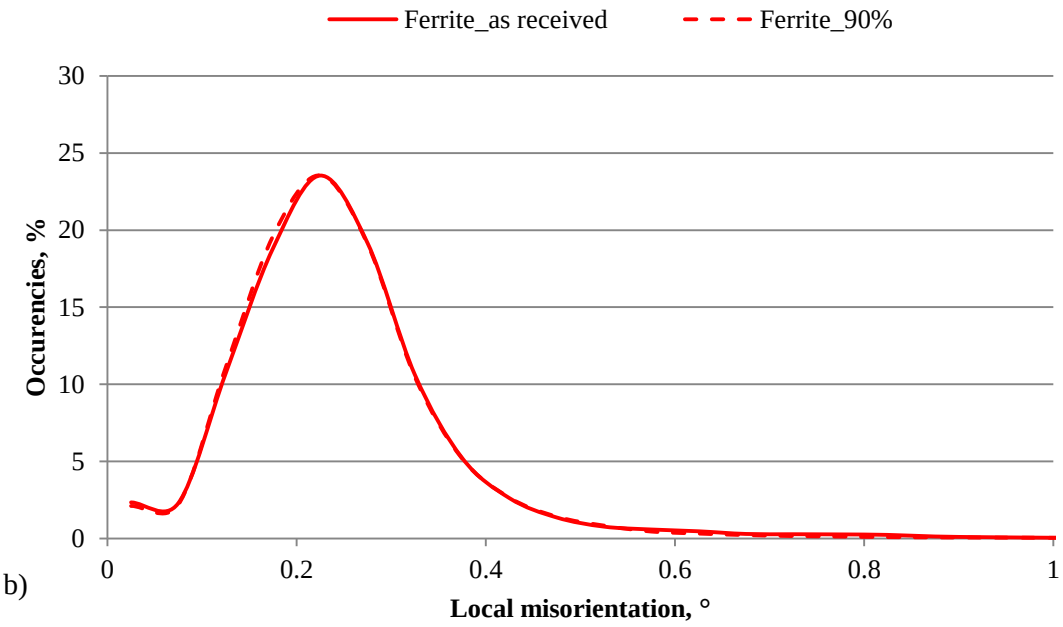

b)

Figure 5.16: LMOs graphs of M2 for the a) austenite and b) ferrite phases in as as-received conditions (plain line) and after loading to 90 %$\sigma_{y,0.2\ \%}$ for 24h (dotted line).

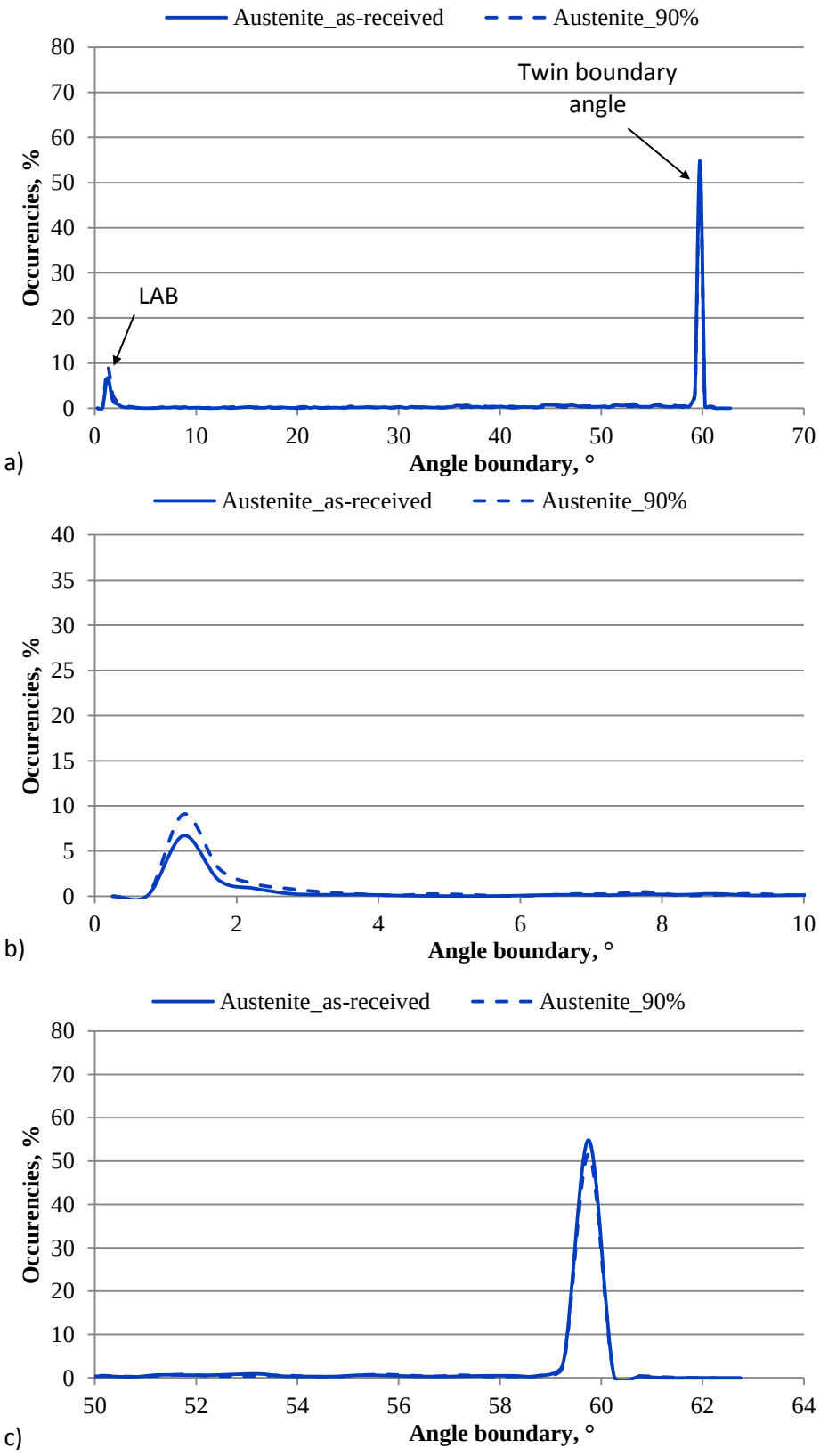

Figure 5.17: Histograms associated with the angle boundary maps in the case of the HIPed material for the austenite phase, a) all range of angles, and magnification on the b) LABSs and c) twin peak.

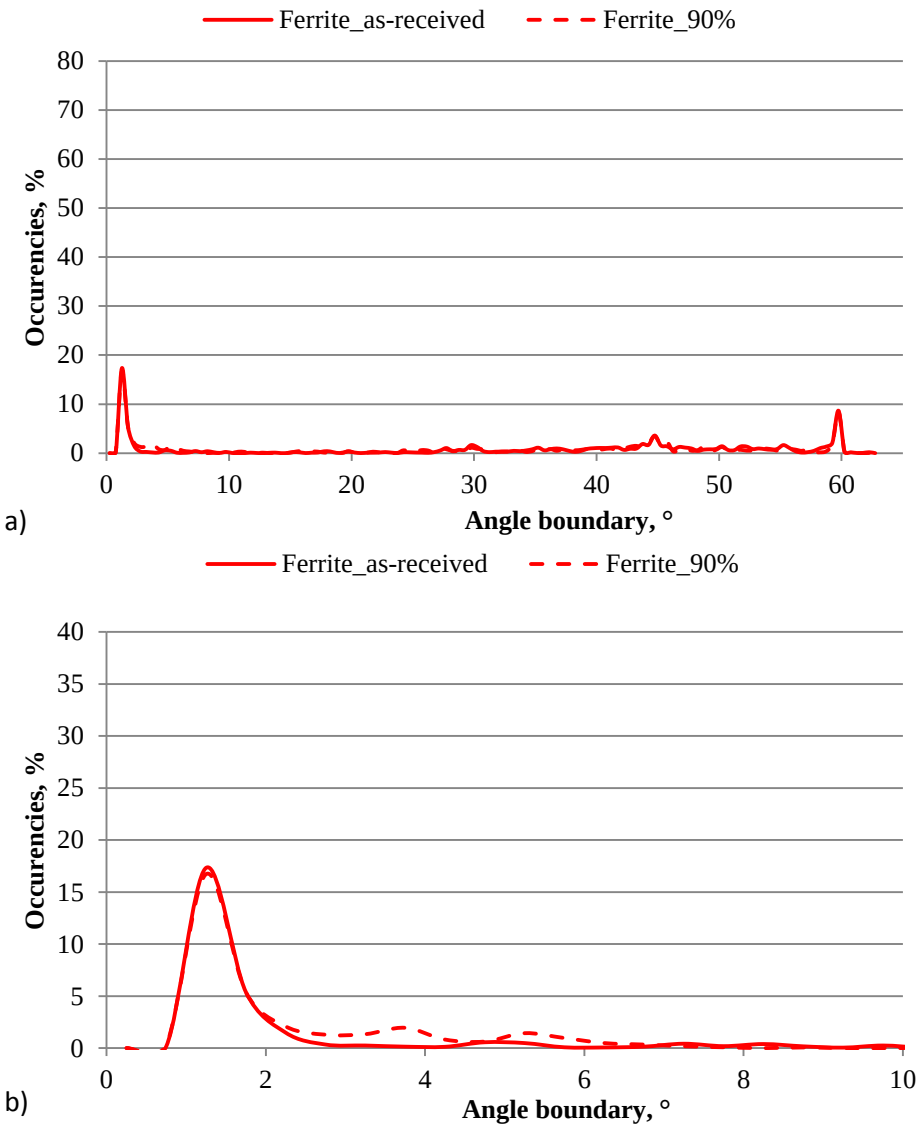

Figure 5.18: Histograms displaying the angles boundaries in the case of the HIPed material for the ferrite phase, a) all range of angles, and magnification on the b) LABS.

5.4 Discussion

5.4.1 LTC behaviour in DSSs

LTC phenomenon is defined as a material experiencing plastic deformation while subjected to constant load [126]. This phenomenon has been observed in a wide range of metals, and its dependence on the level of the load applied has systematically been reported [204], [205]. An important number of studies have looked at LTC in austenitic stainless steels [112], [206], [207], [208]. In the case of DSSs, LTC was also been observed and reported [117], [126], but the mechanism, such as load partitioning between the two phases and deformation mechanism are not yet established.

LTC phenomenon in wrought and HIPed DSS materials was investigated using DIC and ESBD mapping techniques. The displacement curves and DIC results showed that plastic deformation takes place in DSSs subjected to a constant load and that this deformation was dependent on the load level applied. These observations are consistent with the LTC definition given by U. Kivisakk [126] and confirmed the occurrence of this phenomenon in the two microstructures investigated.

The DIC results obtained for the wrought and the HIPed materials (Figure 5.5 and Figure 5.7), showed that deformation started within the austenite grains by slip and, only in the case of the wrought material, extended further into the ferrite, at higher load levels. This observation was consistent with the LMOs and angle boundary results exhibiting a shift in misorientation and variation in LABs population, respectively, in the austenite phase of the two materials after having experienced LTC; and only the ferrite phase of the wrought material displayed variation in misorientation and significant increase in LABS population. This deformation sequence was consistent with DSSs micro-deformation mechanisms, presented in the literature review, and the study of stress and strain partitioning between phases during loading [64], [65], [68] and [67]. The observations suggest that, below the yield strength of the material, plastic strain of the austenite phase is primarily responsible for the LTC behaviour of DSSs. This is consistent with the displacement curves, Figure 5.4, showing that the HIPed material elongated more than the wrought material, as it had a higher fraction of austenite (i.e. . ~ 60 %) compared to that of (i.e. ~ 50 %) in the wrought material (see Chapter 4 for the phase balance measurements and details).

In the case of the wrought material, as the austenite grains were deforming, for example at a load level equal to 90 %$\sigma_{y,0.2\ \%}$, slip traces tended to travel across into to the neighbouring ferrite grains, where K-S OR was satisfied between the two phases. This observation was consistent with tensile studies [209], fatigue studies [170], [178]and TEM observation [210] on the deformation mechanism of duplex stainless steels. In the case where the interphase boundaries did not comply with the K-S OR, an increase in strain, at the grain boundary was observable, which was also in accordance with the observation of surface deformation of DSSs during fatigue testing [170], [178].

5.4.2 Comparison of LTC behaviour of the wrought and the HIPed materials

For the wrought material, the LMOs and angle boundary results showed that straining had developed within the two phases, after loading to 90 $\%\sigma_{y,0.2\ \%}$. This was consistent with the DIC analysis showing that, for the same load level, all the austenite grains had experienced slipping and slip traces had also developed within some areas of the ferrite matrix. DIC results also showed heterogeneous distribution of strain within the ferrite, with areas displaying slip bands next to undeformed areas. This was consistent with the angle boundary maps, obtained after loading, and exhibiting high concentration of LABs concentrated in some of the ferrite grains. This was thought to be related to the deformation of the austenite grains, which occurred in various directions, due to its random crystallographic orientation, as described in Chapter 4. This deformation induced multiple directions of stresses on the surrounding ferrite matrix. This was consistent with the El Bartelli et al. observation [170], on the fatigue deformation in a DSS rolled alloy, showing that ferrite is subjected to a triaxial stress state by the deformation of the surrounding austenite grains having a random crystallographic orientation. In addition, at locations where K-S OR was fulfilled between the two phases, slip was transferred from the austenite to the ferrite. This promotes heterogeneous areas of stresses within the ferrite grains, which is consistent with C. Ornek work [64], and lead to the development of strain localisation at the grain boundaries, were slip cannot transfer from austenite to ferrite.

For the HIPed material, M2, results were significantly different. The angle boundary results displayed higher variation of angles population compare to the wrought material which reflect to the higher homogeneity of this material. After 90 $\%\sigma_{y,0.2\ \%}$ of loading, the LMOs and angle boundary results displayed slight changes in misorientation in the austenite phase but the ferrite phase does not seems to be affected by loading. This is in agreement with the DIC results in which, at the same load level, some of the austenite grains experienced slip but the only one ferrite grains in the area exhibited a slip band. Furthermore, strain localisation at the grain boundaries was not evident.

The DIC results suggested that, if LTC behaviour in the two materials is similar and follow the mechanism proposed previously i.e. austenite is responsible for LTC, the two materials for the same corresponding load level are at different stages. In the case of the wrought material, all the austenite grains of the ROI had deformed, inducing

heterogeneous strain and stresses distribution in the adjacent ferrite. In the HIPed material, for a similar load level, not all the austenite grains had deformed and hence, deformation of ferrite had still not begun.

In the context of HISC, it is well-known that hydrogen diffused to highly strain region in the microstructure [97]. Hence, in the case of the wrought material, LTC inducing heterogeneous strain distribution in ferrite could lead to area of higher local hydrogen concentration and HISC. However, in the case of the HIPed material, strain concentration was not observed and LTC allow the material to accommodate the load applied.

5.5 Conclusion

The present work investigated LTC in a HIPed and wrought DSS microstructures. The use of DIC analysis and EBSD mapping provided an insight on the microscopic mechanism of this phenomenon:

- Primarily, austenite is the phase responsible for LTC behaviour of DSS, with straining predominantly accommodated in this phase;

- In the case of the wrought material, the deformation of austenite during LTC induced heterogeneous distribution of stresses in adjacent ferrite grains which is thought to be detrimental for the resistance-to-HISC of this material;

- The HIPed material exhibited homogeneous deformation of the austenite during constant load testing and did not exhibited any significant local stress concentration;

- Strain localisation and the development of slip, from the austenite to ferrite grains, were observed to occur at lower load/stress levels in the wrought material compared to that in the HIPed material. The fundamental differences between the two alloys, in terms of the morphology of their phases in accommodating deformation, is thought to be responsible for the reduced capacity of the wrought material for sustaining enhanced, uniform straining. This, combined with the fact that hydrogen can diffuse and move around much

faster within the large, elongated bcc ferrite, could explain the lower resistance-to-HISC observed in the wrought material with an unisotropic microstructure.

- Unlike the commonly held view that LTC is a pre-requisite for HISC, the observations made here suggest that LTC is an inherent response of DSSs to loading, with its extent being a function of DSSs' microstructural parameters, such as the size, fraction, and directionality (and potentially, connectivity) of the phases. It was observed that the HIPed material with a higher fraction of austenite and a more homogenous microstructure, showed a larger LTC elongation, and a superior resistance-to-HISC, i.e. a higher load/stress HISC threshold compared to that in the wrought material.

5.6 Recommendations for future work

In order to further the current work, the following is proposed:

- Performing in-situ DIC analysis, i.e. performing tensile testing in a SEM such that strains can be observed without unloading the specimens;

- The use of more sophisticated methods, such as EBSD, to accurately record straining with time during tensile testing, given the small values of strains developed by LTC;

- 3D modelling of stresses induced in ferrite due to deformation of austenite for wrought (i.e. ferrite matrix) and HIPed microstructures and their relationship with stress-induced hydrogen diffusion;

Perform DIC analysis during LTC testing of hydrogen pre-charged specimens to develop an understanding of the strain partitioning between austenite and ferrite in the presence of hydrogen. This requires the use of a different DIC pattern (to that used in this work) which does not involve heating of pre-charged specimens. As otherwise, this will lead to the diffusion of hydrogen out of the material. An alternative to this technique could be the use of an ultra-fine grid, deposited with a FIB microscope, as a pattern.

Chapter 6.

ENVIRONMENTAL TESTING OF THE WROUGHT AND THE HIPED DSSS

6.1 Introduction

In this chapter, an environmental fracture-toughness based comparison, between the resistance-to-HISC of the wrought and HIPed materials, is presented. Fracture toughness based test methodologies are commonly used to rank a wide range of materials with respect to resistance to cracking in air; however, there are no established guidelines on how to conduct a fracture mechanics evaluation in a hydrogen-charging environment, such that test data can be well understood and used, directly, in a design or fitness-for-service assessment.

Furthermore, as discussed in Chapter 1, HIPed DSS components are increasingly employed in a wide range of applications, including subsea oil and gas production equipment and it is therefore important and highly desirable to understand these materials better and evaluate their performance in terms of both crack initiation and propagation, using test methods, which simulate relevant service conditions.

Using the data generated, a comparison between the resistances to HISC of HIPed and conventionally-manufactured wrought microstructures has been established and the significance of the key test method parameters and microstructural properties are investigated.

This study is entirely based on fracture toughness testing, a widely-adopted industrial practice to evaluate resistance to cracking; and the methods have proved to be relevant

and useful for obtaining quantitative input (i.e. crack growth/extension via tearing) for engineering critical analysis (ECA), from tests carried out in air. Such approaches have also been extended to testing in embrittling environments, in an attempt to estimate materials' resistance to cracking, and specify maximum tolerable flaw sizes in the simulated environment. This study aims to investigate the suitability of using this methodology in the context of evaluating the resistance-to-HISC of DSSs, this embrittlement mechanism being a combination of a local critical amount of stress and hydrogen content in the complex microstructure of DSSs. The testing part of this study was performed by the fracture mechanics technician team of TWI.

The basic microstructural and mechanical properties of the two alloys used (i.e. M1 and M2) are given in Chapter 4. Together with the comparison of their cracking behaviour, in air and in a hydrogen-charging environment, i.e. a 3.5 % NaCl solution (simulating seawater) under CP, the effect of applied displacement rate, hydrogen pre-charging time and the effect of stress concentration, through adopting two different notch geometries of SENBs, , are discussed in terms of the test output and interpretations associated with it. The work presented here also addresses some of the inherent challenges, issues and shortcomings faced when such tests are employed to evaluate resistance-to-HISC of (S)DSSs.

6.2 Experimental methodology

6.2.1 Specimen preparation

SENB blanks of 12.3×12.3×60 mm^3 were extracted from M1 material, in the longitudinal direction adjacent to the OD, using a band saw, and was subsequently ground back to 12×12×60 ± 0.1 mm^3 square specimens, Figure 6.1. The blanks extracted from M2 were 12.3×12.3×60 mm^3 and taken in the longitudinal direction of the can, using electro-discharged machining (EDM). The blanks were then ground back to produce 12×12×60 ± 0.1 mm^3 specimens.

Following TWI experience, the specimens were chosen not to include side grooves. Side grooves can help the development of a straight, even ductile tearing crack front,

but also generate a complex stress distribution near the edges, promoting hydrogen ingress from the specimen's sides, and were therefore avoided in this study.

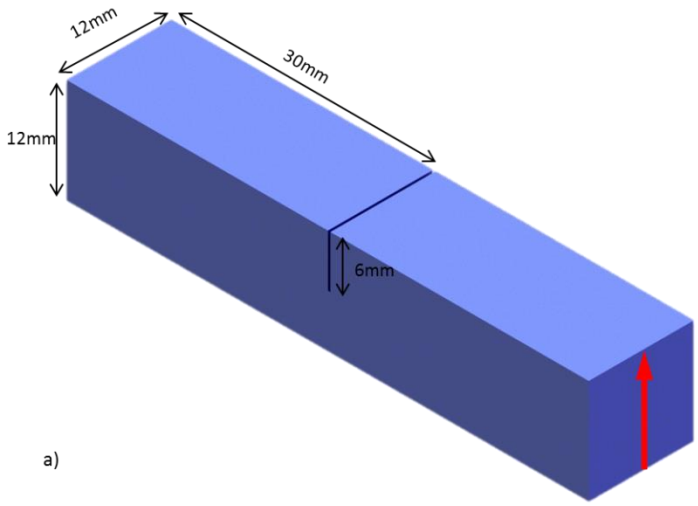

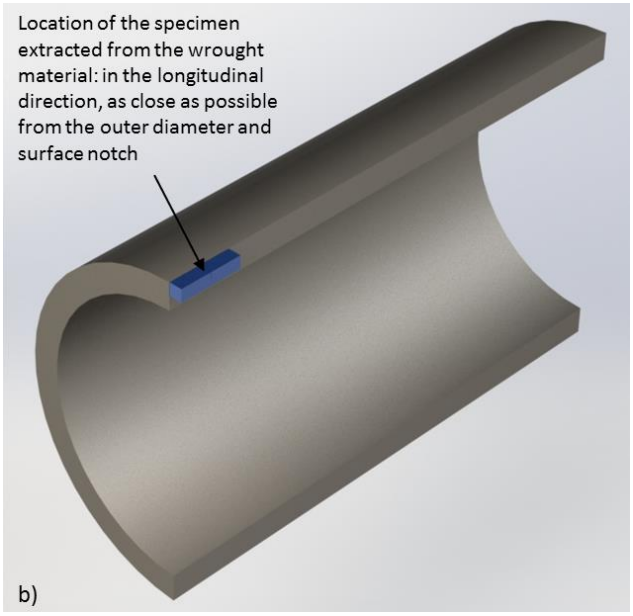

Figure 6.1: a) Scheme of the SENB specimen geometry, the red arrow indicates the location of the outer diameter for the specimens extracted from M1 and b) location of the extraction of the specimen in M1.

The initial crack length was measured on both sides of the specimen before testing, and a nominal initial notch depth to specimen width ratio (a_0/W) of 0.5 was used. The fatigue pre-cracked specimens were prepared in accordance with BS 7448-4. The actual a_0/W achieved was confirmed after testing once the measurements of the fatigue pre-crack length could be made from the fracture faces.

6.2.2 Testing procedure

Fracture toughness testing, following the unloading compliance procedure of BS7448-Part 4 was conducted at room temperature. The SENB specimens were tested in a three-point bending configuration, and instrumented using two clip gauges positioned on knife edges at different heights above the specimen notch mouth to determine the crack mouth opening displacement during the test. Once the specimen was in position, ten elastic unloadings were performed at 0.1 mm.min^{-1} displacement rate to determine the specimen compliance before the start of the test. The specimens were then increasingly loaded, into the plastic regime, while regular partial unloadings were carried out throughout the test to generate data in terms of J resistance curves (J R-curves), where J-integral or J which is the path-independent strain energy around the crack, in Nmm^{-1}, is plotted against the crack extension (in mm) measured or determined during the test.

The rate of testing is usually described by the stress intensity factor (K) rate, or K rate. This is the change in the elastic K during the initial elastic loading of the test. It takes into account both the crosshead displacement speed, the size of the specimen, and its crack length, and is calculated using the following equation:

$$K_{rate} = \frac{F_t * S * f\left(\frac{a_0}{W}\right)}{(B * B_N)^{0.5} * W^{1,5}} \quad (28)$$

The mathematical expression of $f\left(\frac{a_0}{W}\right)$ is defined in the BS 7448 standard for 3 point bending test specimens. F_t is the slope of the unloading curve of the load applied versus time in the initial loading of the test. In the case of this work, the specimen geometries were identical and differences between the calculated K-rates for specimens tested at a same cross-head displacement exist. This comes from the fitting of the slope and experimental inaccuracies. It is usually specified in MPa$\sqrt{m}$.s^{-1}, but sometimes units of Nmm$^{-1.5}$s^{-1} are given.

6.2.3 Influence of testing parameters

6.2.3.1 General

The relevance of fracture toughness methods and testing parameters, which were principally designed and developed to evaluate the performance of materials in air, is investigated here for testing DSSs in hydrogen-charging environments. The

displacement rate, which controls the duration of the test and so, the time given for hydrogen to diffuse into the material, together with the effect of hydrogen pre-charging duration prior to testing, have also been investigated. The influence of the notch geometry, which defines the stress concentration in the specimen, as well as its role in obtaining data on crack initiation and therefore HISC assessment has been studied and discussed. Table 1.1 gives a summary of the testing parameters, including the duration of pre-charging.

6.2.3.2 Displacement rate

A set of two samples, extracted from M1 and M2 were tested in air at a cross-head displacements rate of: 0.3 $mm.min^{-1}$, which gave K-rates of 1.059 and 1.089 $MPa.m^{1/2}.s^{-1}$, respectively. Those values were within the K-rate interval recommended by the BS7448-Part 4 standard, i.e. 0.5 to 3.0 $MPa.m^{1/2}.s^{-1}$. The other specimens were tested at a slower cross-head displacement rate of 0.0003 $mm.min^{-1}$, with the corresponding K-rates being in the range of 0.0008 to 0.0012 $MPa.m^{1/2}.s^{-1}$. In addition to M2, a specimen was tested at the slowest crosshead displacement allowed by the machine: 0.3×10^{-6} $mm.min^{-1}$, the corresponding K-rate was 0.00019 $MPa.m^{1/2}.s^{-1}$.

6.2.3.3 Hydrogen pre-charging duration prior to testing

Hydrogen pre-charging defines the starting near-surface conditions in terms of hydrogen concentration at the beginning of the test. Two main reasons for investigating the influence of this factor in the context of evaluating DSSs in environment are as follows:

- Environmental testing was aimed at stimulating the oil and gas subsea service conditions; hence, hydrogen charging methods for testing, including hydrogen pre-charging, should be carefully designed in order to suit this goal.
- Study of common mechanisms put forward for HISC, highlights the importance of crack initiation and so, the surface condition at the start of the test is critical.

Three specimens were extracted from each of the two materials (i.e. M1 and M2), hydrogen pre-charged for 3 hours, 72 hours and 504 hours, respectively, and tested in air at 0.0003 $mm.min^{-1}$. Hydrogen pre-charging consisted of immersing the specimens into a 3.5 % NaCl solution, with the application of a cathodic potential of -1100 mV_{SCE}

(to simulate subsea CP conditions). Moreover, one additional specimen was extracted from each material, hydrogen pre-charged for 72 hours, and tested under CP at 0.0003 mm.min^{-1} displacement rate, with the results compared to those obtained from the pre-charged specimens tested in air.

6.2.3.4 Notch geometry

Two notch geometries with different stress concentration factors were used: (i) fatigue pre-cracked (FPC), a requirement of standard fracture toughness-based methods and conventionally very conservative; and (ii) electro-discharged machined (EDM), and deemed to be more representative of real flaws and geometries, facilitating a study of crack initiation. The schematics and photographs of the two notches are shown in Figure 6.2. The EDM notches were made using a 0.25 mm diameter wire, inducing a 0.3 mm-wide notch. In all cases, no side grooving and an initial notch depth to specimen width ratio (a_0/W) of 0.5 was applied.

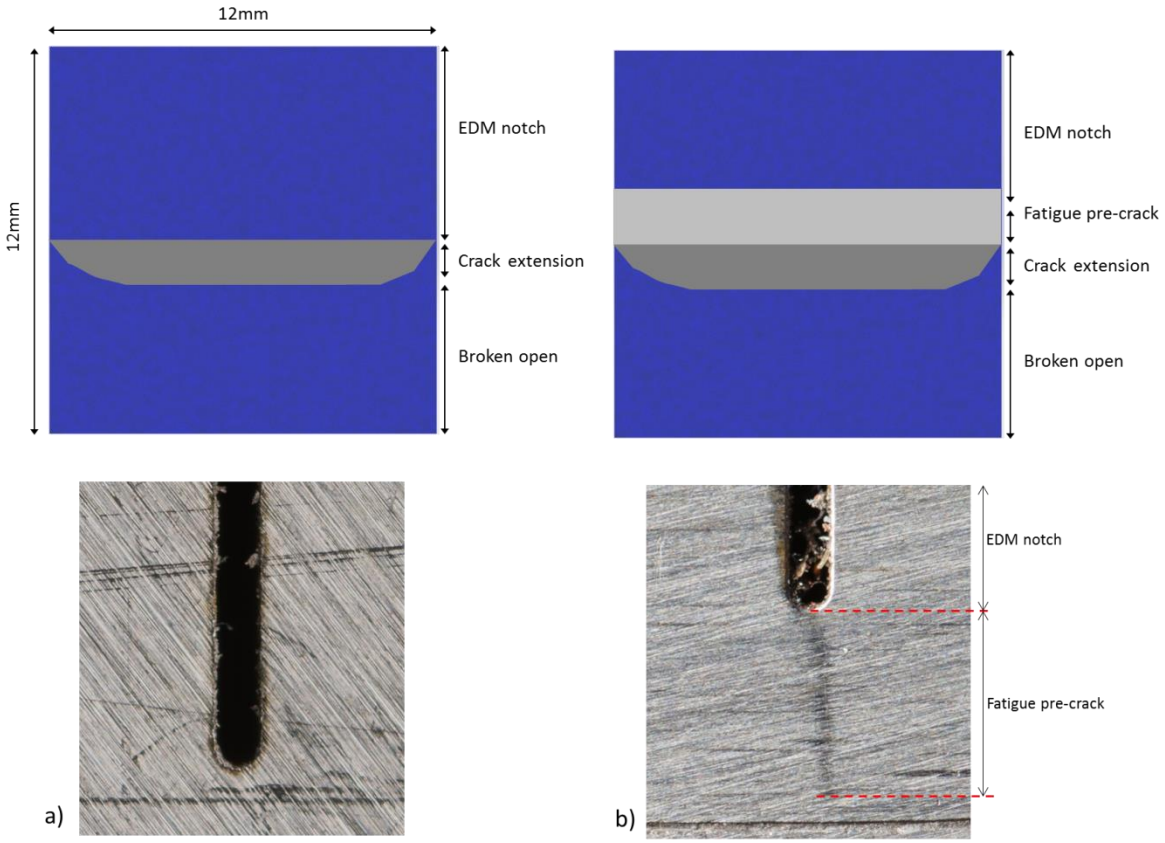

Figure 6.2: Schematic and photograph of the two notch geometries tested: a) EDM and b) FPC

Table 6.1: Summary of the testing parameters

Material	Displacement rate, mm.min^{-1}	Testing conditions		Notch geometry
		Hydrogen pre-charging time, h	Testing environment	
M1	0.3	/	Air	EDM
	0.0003	/	Air	EDM
	0.0003	3	Air	EDM
	0.0003	72	Air	EDM
	0.0003	504	Air	EDM
	0.0003	72	CP	EDM
	0.0003	/	Air	FPC
	0.0003	72	CP	FPC
M2	0.3	/	Air	EDM
	0.0003	/	Air	EDM
	0.3×10^{-6}	/	Air	EDM
	0.0003	3	Air	EDM
	0.0003	72	Air	EDM
	0.0003	504	Air	EDM
	0.0003	72	CP	EDM
	0.0003	/	Air	FPC
	0.0003	72	CP	FPC

6.2.4 Post-test analysis

After testing, the specimens were unloaded and heat-tinted at 320°C for ten minutes. This oxidises and helps to distinguish the crack extension developed during testing from the fracture surface when the specimen is broken open for examination. The depth of the crack initiation, a_0 (effectively the dimension of the initial fatigue pre-crack or EDM notch) and the crack end were measured using the 9-points measurement method described in the BS7448-Part 4 standard and subsequent fractography, carried out using light and scanning microscopy. The initial and final crack lengths measured from the fracture face were used to validate the initial and final crack lengths estimated from the unloading compliance technique, based on requirements in BS 7448-4. Following

fractography observation, one side of the specimens was cut in the longitudinal direction, perpendicular to the crack propagation and the side was metallographically prepared and etched in 40 % KOH aiming to observe the shape of the main crack as well as the presence of any secondary cracks propagating perpendicular to the main cracking direction. Side views of the crack propagation were investigated, the specimens were sectioned in three parts in length and the side of each part (specimen sides and specimen middle) were metallographically prepared and etched in 40 % KOH, allowing optical microscopy to be performed. Details of the cutting are given in Figure 6.3.

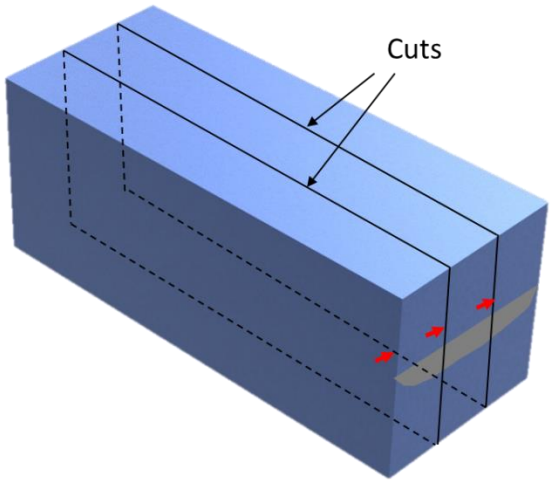

Figure 6.3: Scheme of the specimen broken open and the location of the cuts made to observe the side view of the crack. The red arrows represent the face metallographically prepared.

6.2.5 Generation of unloading compliance data and plotting methods of resistance curves

The crack extension curves are based on plotting J (fracture toughness defined as the path independent strain energy around the crack, also called J-integral, with units of Nmm^{-1}) against the estimates of crack extension derived from the unloading compliance technique. Although the experimental fracture toughness test procedures are similar for the three main standards i.e. ASTM E1820-15a, ISO 12135 and BS 7448-Part 4, the procedures and calculations they described to generate tearing resistance curves (R-curves), however, are different. In the tests reported here, the crack extension is not by stable ductile tearing but is affected by hydrogen-related cracking mechanisms. Therefore the procedures given in these Standards can only be applied as they relate to the environmental crack extension curves in this work.

6.2.6 Methodology to obtain unloading compliance data

6.2.6.1 Nomenclature

a = *crack length*	J_{pl} = *plastic part of J*
a_0 = *initial crack length measured using 9-points method*	S = *specimen span, distance between the specimen supports.*
$a_{0,\,est}$ = *initial crack length calculated*	V_1 = *notch opening displacement on the clip 1*
A_{pl} = *area under force versus displacement*	V_2 = *notch opening displacement on the clip 2*
b = *remaining ligament*	W = *specimen width*
B = *specimen thickness*	z_1 = *distance between the notch opening gauge measurement 1 to the surface of the specimen*
B_e = *specimen net section thickness*	z_2 = *distance between the notch opening gauge measurement 2 to the surface of the specimen*
B_N = *specimen net*	γ_{pl} , η_{pl} = *geometry factors*
E = *Young's modulus*	Δa = *crack growth*
J_{el} = *elastic part of J*	v = *Poisson's ratio*

6.2.6.2 Methodology

The unloading compliance method enables to plot the crack growth against J curve of a material in the particular orientation with a single specimen. This method is based on the assumption that the material compliance, i.e. the slope of the elastic unloading, decreases as the crack develops. For each unloading, the compliance is measured which can then be related to a crack length, Δa, and hence prediction of crack extension during the test. In the three standards: ASTM E1820-15a, ISO 12135 and BS 7448-Part 4, the experimental methods follow the same procedures; however, the way of calculating the crack advancement and J from the measured compliance are particular to the standard applied, although similar. Table 6.2 and Table 6.3 show the main calculations of the three Standards to construct the J versus Δa curves for a SENB specimen in a 3 points

bending configuration, with B the specimen thickness, B_N the specimen net section thickness, W the specimen's width and J_{el} and J_{pl} the elastic and plastic part of J respectively.

The first distinction between the BS 7448-Part 4, and the two others Standards is the application of rotation correction, reflected into z_{corr} and C_{corr} factors in ASTM and ISO, respectively. During the test, the compliance can be extracted from crack opening displacement determined by the clip gauges positioned on the specimens, as seen in Figure 6.4. In those cases, as the load is applied, the specimen rotates and an angle (θ) forms which affects the clip gauge measurements and hence the calculation of the compliance [211]. Hence, a rotation correction is applied ensuring the measurement of a valid compliance.

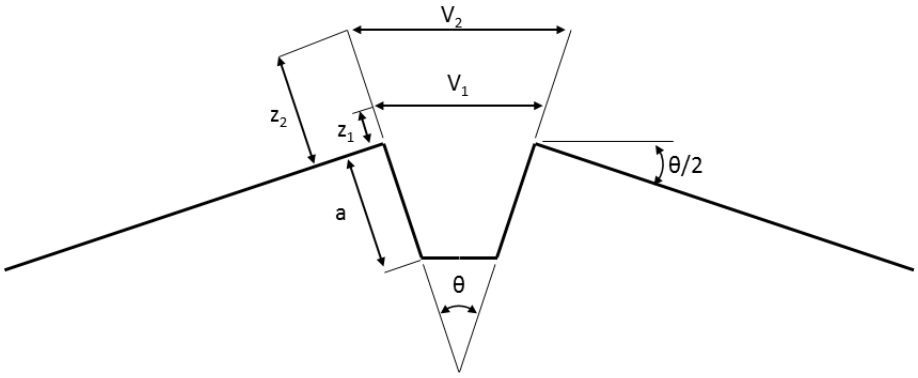

Figure 6.4: Location of the two clip gauges measuring displacements V_1 and V_2 for the determination of the crack mouth opening displacement, and the load line displacement.

Table 6.2: Mathematical equations applied for the calculation of the crack growth in the case of the BS 7448, ISO12135 and ASTM E1815a.

BS 7448	**ISO 12135**	**ASTM E1815a**
$\Delta a = a - a_0(*)$		
$\frac{a}{W} = 0.999748 - 3.9504u + 2.9821\,u^2 - 3.21408\,u^3 + 51.51564u^4 - 113.031\,u^5$		
$u_{corr} = \frac{1}{\left[\frac{4B_e W E' C_{corr}}{S.\,z_{corr}}\right]^{0.5} + 1}$	$u = \frac{1}{\left[\frac{4B_e W \lambda E C}{S}\right]^{0.5} + 1}$	$u_i = \frac{1}{\left[\frac{4B_e W E C_i}{S}\right]^{0.5} + 1}$
$B_e = B - \frac{(B - B_N)^2}{B}$		
$z_{corr} = 1 + \frac{z_1}{0.8\,a_0 + 0.2W}$ $Q = \left(\frac{S}{4}\frac{V_1 - V_2}{z_2 - z_1}\right)$ $D = 1 - 0.665\,(\frac{Q}{2W})$ $C_{corr} = \frac{C}{D}$	$\lambda = \frac{g_3(\frac{a_0}{W})}{g_3(\frac{a_{0,est}}{W})}$	
$E' = \frac{E}{(1 - \nu^2)}$	$g_3\left(\frac{a}{W}\right) = 6\left(\frac{a}{W}\right)\left(0.76 - 2.28\frac{a}{W} + 3.87\left(\frac{a}{W}\right)^2 - 2.04\left(\frac{a}{W}\right)^3 + \frac{0.66}{\left(1 - \frac{a}{W}\right)^2}\right)$	

(*) a_0 is measured on the specimen fracture face by the 9-points method

Table 6.3: Mathematical equations applied for the calculation of J in the case of the BS 7448, ISO12135 and ASTM E1815a.

BS 7448	**ISO 12135**	**ASTM E1815a**
$J = J_{el} + J_{pl}$		
$J_{el} = \left[\frac{F}{(BB_N W)^{0.5}} g_2\left(\frac{a_0}{W}\right)\right]^2 \cdot \frac{1-\nu^2}{E}$	$J_{el} = \left[\frac{F}{(BB_N W)^{0.5}} g_2\left(\frac{a_0}{W}\right)\right]^2 \cdot \frac{1-\nu^2}{E}$	$J_{el(i)} = \frac{K_{(i)}^2(1-\nu^2)}{E}$
$J_{pl} = \frac{2U_p}{B_N(W-a_0)}\left[1 - \frac{\Delta a}{2(W-a_0)}\right]$	$J_{pl} = \frac{1.9U_p}{B_N(W-a_0)}\left[1 - \frac{\Delta a}{2(W-a_0)}\right]$	$J_{pl(i)} = \left[J_{pl(i-1)} + \left(\frac{n_{pl(i-1)}}{b_{(i-1)}}\right)\left(\frac{A_{pl(i)} - A_{pl(i-1)}}{B_N}\right)\right] \times \left[1 - \gamma_{pl(i-1)}\left(\frac{a_{(i)} - a_{(i-1)}}{b_{(i-1)}}\right)\right]$

Secondly, the BS 7448-Part 4 standard uses the expression E' instead of E for the crack advancement calculation [TWI report 325/1986] and [212]. The effect of the rotation correction and the constant E' is given in Figure 6.5. It can be seen that using E instead of E' only translates the curve toward the left; and, the application of the rotation correction change significantly the value of the crack growth for a given J, due to the and hence has to be applied consistently in a comparison study.

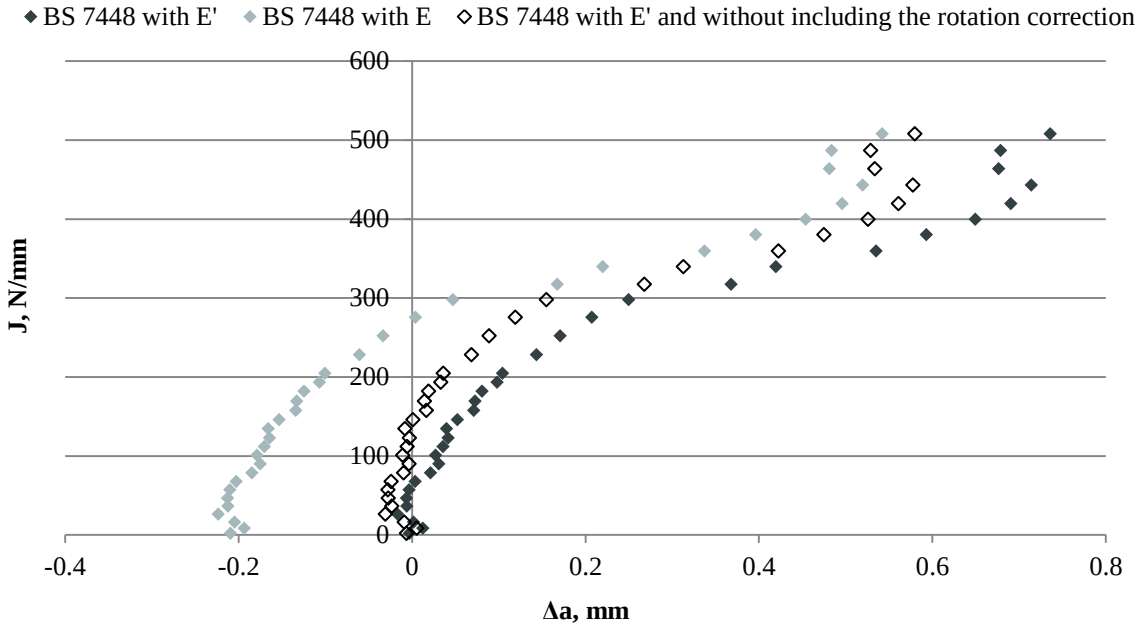

Figure 6.5: Influence of the rotation correction and E' rather than E in the BS 7448 Part 4 equation.

The rest of the crack growth calculations are very close between the three Standards; however, only the ISO 12135 includes a correction on a_0 measured in the Annexe H. This correction aims to eliminate an artefact of the unloading compliance method leading to "negative" crack growth on the resistance curve.

With respect to the calculation of J, each standard has its own singularities. In the case of the ASTM E1820, J is calculated in an incremental manner. Hence, J and the crack growth are based on the values of the previous step [213], which is not the case for the ISO 12135 and the BS 7448-Part 4 in whose J and crack growth are calculated independently of the previous steps. Figure 6.6 and Figure 6.7 compare the resistance curves obtained using the three standard calculation methodologies in the case of M1 tested in air at room temperature and M1 tested in air at room temperature after 3 hours of hydrogen pre-charging, respectively. For consistency, all include the application of the rotation correction and the use of E'. As expected from the mathematical expressions, differences in J and crack advancement values were observed. The application of the Annexe H of the ISO 12135 standard also allow the obtaining of more sensible curves as "negative" crack growth is eliminated, Figure 6.6.

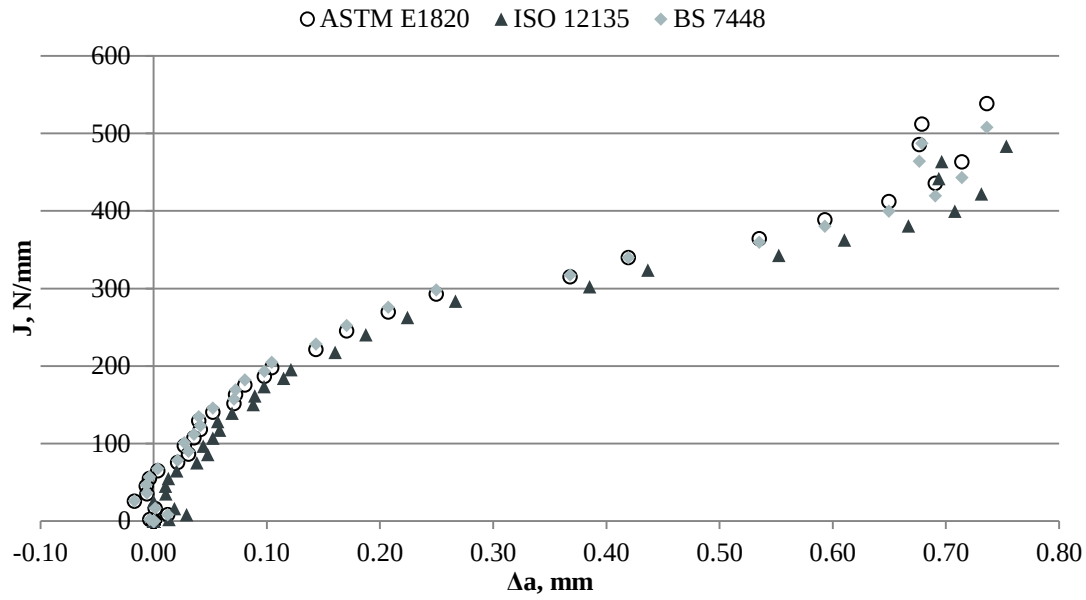

Figure 6.6: Comparison of the J-Δa crack extension curves calculated using the ASTM E1820, ISO 12135 and BS7448-Part 4 for an unloading compliance test on M1, in air.

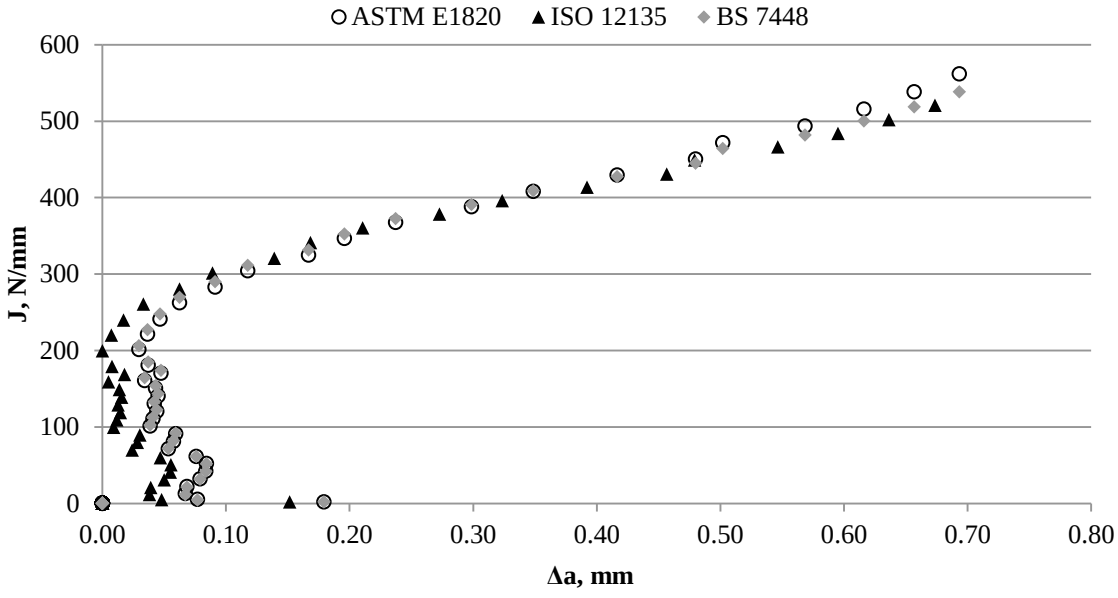

Figure 6.7: Comparison of the J-Δa crack extension curves calculated using the ASTM E1820, ISO 12135 and BS7448-Part 4 for an unloading compliance test on M1, in air after 3 hours of hydrogen pre-charging.

6.2.7 Description of the methodology used in this study

The analysis of HISC failures have proved that crack initiation is critical to understand HISC in DSSs. Hence, the resistance curves had to be designed to suit this requirement and ensured that the beginnings of crack extension curves were comparable and can be understood and exploited. For this reason, the ISO 12135 standard was found to be the most adequate, as it allowed the elimination of the testing method artefacts (negative crack growth) affecting the start of the curve. The mathematical expressions used for the rest of the study are given in Table 6.4.

Table 6.4: Mathematical expressions used in the study for the calculation of the J resistance curves.

<table>
<tr><th>Calculation of crack growth, Δa</th><th>Calculation of J</th></tr>
<tr><td>$\Delta a = a - a_0(*)$</td><td rowspan="2">$J = J_{el} + J_{pl}$</td></tr>
<tr><td>$\frac{a}{W} = 0.999748 - 3.9504u + 2.9821\,u^2 - 3.21408\,u^3 + 51.51564u^4 - 113.031\,u^5$</td></tr>
<tr><td rowspan="2">$u = \frac{1}{\left[\frac{4B_e W\lambda E' C_{corr}}{S.z_{corr}}\right]^{0.5} + 1}$</td><td>$J_{el} = \left[\frac{F}{(BB_N W)^{0.5}} g_2(\frac{a_0}{W})\right]^2 . \frac{1-\nu^2}{E}$</td></tr>
<tr><td>$J_{pl} = \frac{1.9U_p}{B_N(W-a_0)}\left[1 - \frac{\Delta a}{2(W-a_0)}\right]$</td></tr>
</table>

(*) In the case of negative crack growth, a_0 is corrected according to the Annexe H of the ISO 12135.

At the end of the test, once the specimen was broken open, the final crack length was measured using the nine-point average method recommended by the BS-7448 Part 4. This method consists of measuring the final crack length using a traveling microscope at nine equally spaced locations on the specimen fracture face. A weighted average is

calculated from those measurements: the measurements taken on the sides are averaged and added to the seven others. This average value was compared with the final crack length measured by the compliance method. The maximum error obtained from this comparison was of 11 %, which corresponds 0.782 mm on those specimens.

6.3 Results and discussion

6.3.1 Influence of the applied cross-head displacement rate

Figure 6.8 is showing a comparison of the crack extension curves generated for three specimens extracted from M1. Two of them were tested in air, at the crosshead displacement rate of 0.3 $mm.min^{-1}$ and 0.0003 $mm.min^{-1}$. The third specimen was tested at 0.0003 $mm.min^{-1}$ under CP. The curve of the specimen tested in air, and at high strain rate exhibited frequent oscillations between negative and positive crack growth, throughout the test. The macrograph of the fracture face, given in Figure 6.9, showed that no crack had propagated in this specimen. Hence, the J-curve of the specimen tested at high strain rate did not characterise its resistance to crack propagation but blunting. This is thought to be due to the high resistance to cracking of this material, which resulted in significant bending and slight displacement (e.g. slippage) of the specimen relative to the rollers during testing, generating such erroneous data points. Figure 6.10, showed the fracture morphology of the notches and, as expected from the fracture face, the specimen tested at standard displacement rate exhibited ductile behaviour, characteristic of plastic deformation.

The crack resistance curve of the specimen tested at low displacement rate, 0.0003 $mm.min^{-1}$, was very steady and the fracture toughness values were much lower than the specimen tested at higher cross-head displacement rate. The macrograph of the fracture face, Figure 6.8, showed that crack had propagated, and the edges of the specimens were deformed indicating a degree of ductility within the material. The crack morphology observed in the SEM, Figure 6.10, was consistent with mixed modes of cracking and comprised ductile and brittle areas. Embrittlement of the ferrite phase was observed, indicated by characteristic cleavage facets while the austenite phase presented a ductile mode of cracking.

Figure 6.8 also displayed the J-resistance curve obtained for M1 tested under CP at slow displacement rate. The fracture toughness values were lower than the ones obtained with the specimens tested in air, which is characteristic of hydrogen embrittlement. The macrograph of the fracture face illustrated the embrittlement caused by the presence of hydrogen with the absence of edge deformation of the specimen. The shape of the crack was wavy and irregular. The analysis of the crack morphology in the SEM, Figure 6.10, supported the occurrence of HISC in the specimen with the strong embrittlement of the ferrite characterised by facets and the presence of brittle secondary cracks propagating through this phase, perpendicularly to the main crack direction.

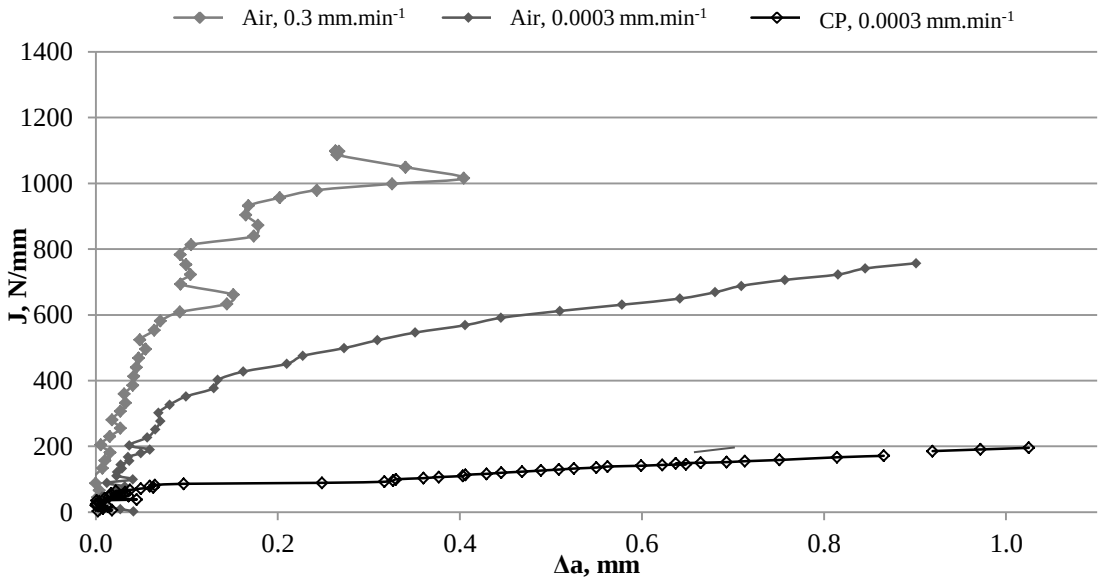

Figure 6.8: Comparison of the J resistance curves for the wrought material (M1) tested at 0.3 mm.min^{-1} and 0.0003 mm.min^{-1} cross-head displacement rate, in air and at 0.0003 mm.min^{-1} under CP.

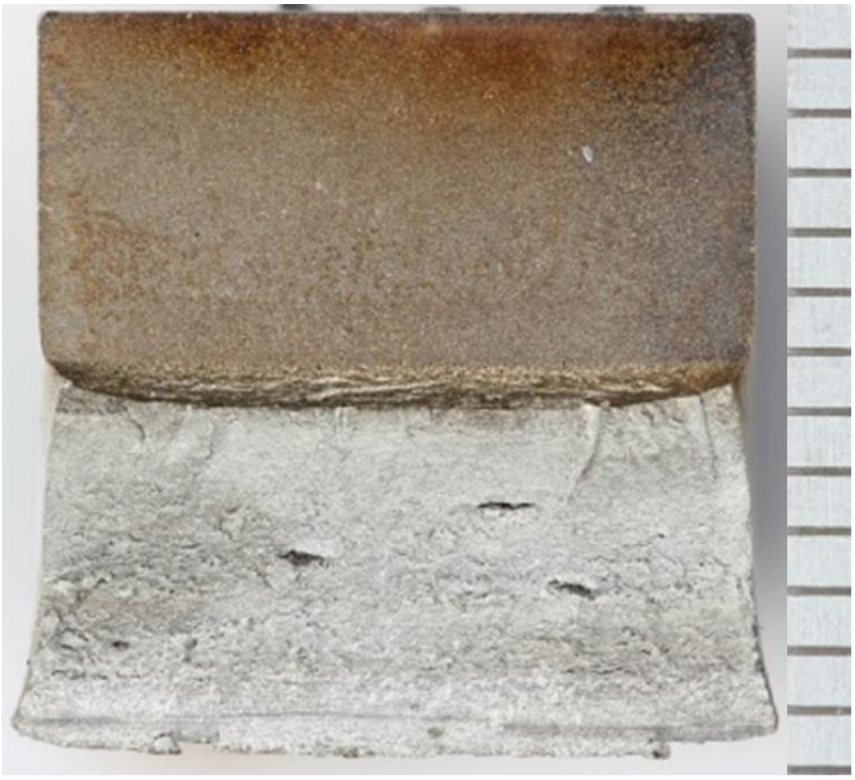

a) Material: M1 Test conditions: Air Displacement rate: 0.3mm.min^{-1}

b) Material: M1 Test conditions: Air Displacement rate: 0.0003mm.min^{-1}

Figure 6.9 (continued): Fracture faces of the specimens extracted from M1 tested at a) 0.3 mm.min^{-1} and b) 0.0003 mm.min^{-1} displacement, in air.

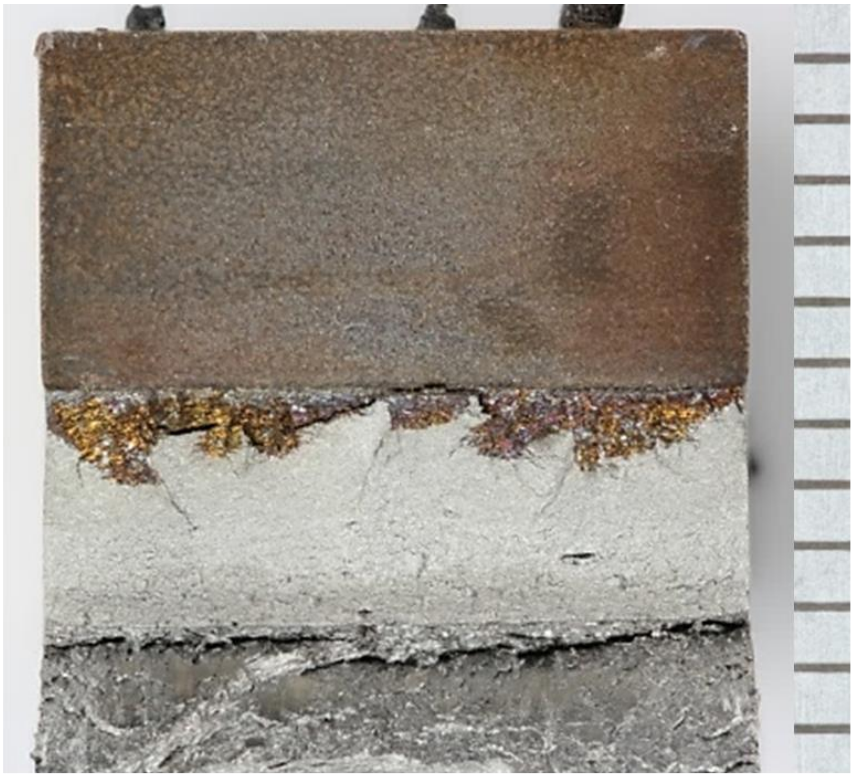

c) Material: M1 Test conditions: CP Displacement rate: 0.0003mm.min^{-1}

Figure 6.9: Fracture faces of the specimens extracted from the wrought material (M1) tested at at 0.0003 mm.min^{-1} displacement under CP.

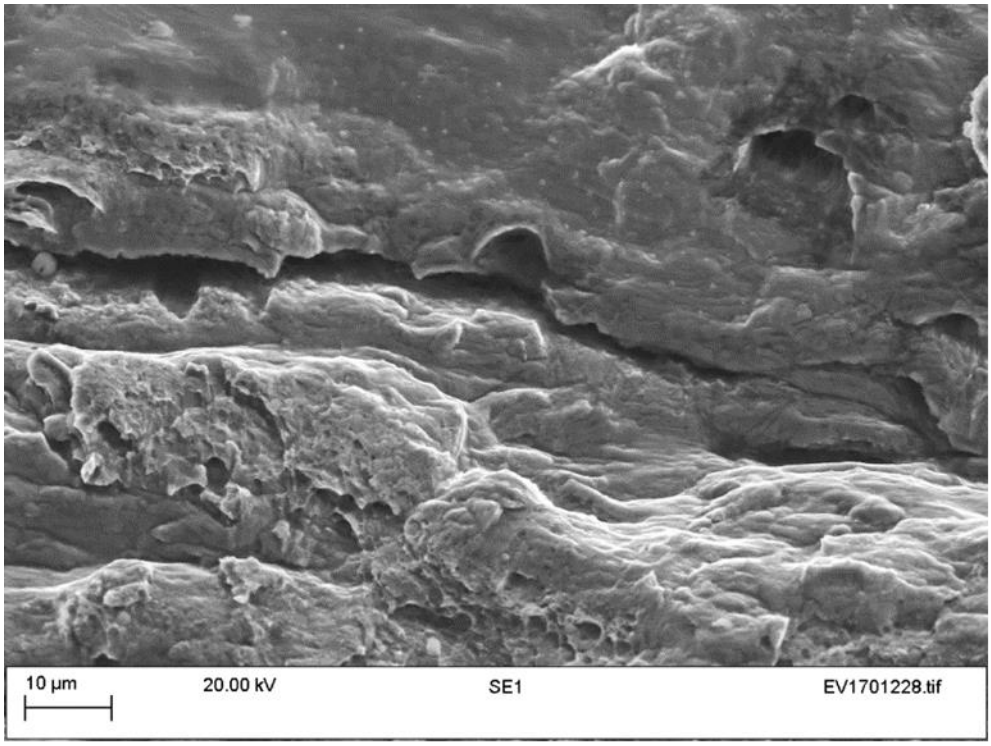

a) Material: M1 Test conditions: Air Displacement rate: 0.3mm.min^{-1}

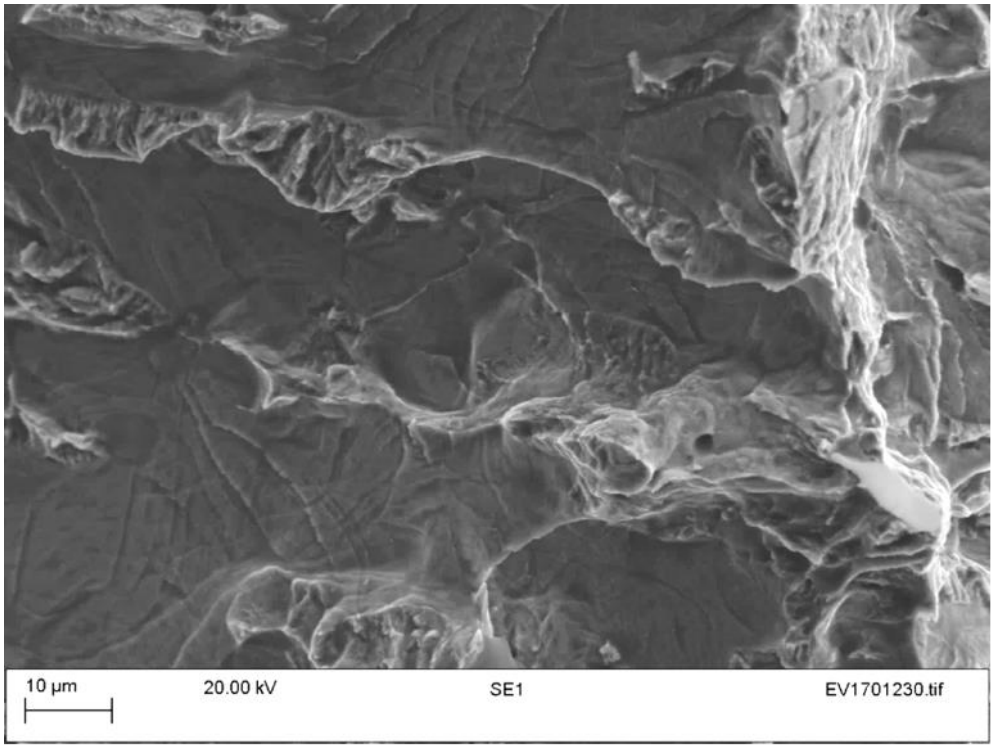

b) Material: M1 Test conditions: Air Displacement rate: 0.0003mm.min^{-1}

Figure 6.10 (continued): SEM images of the fracture face of the specimens extracted from M1 tested at a) 0.3 mm.min^{-1} and b) 0.0003 mm.min^{-1} displacement, in air.

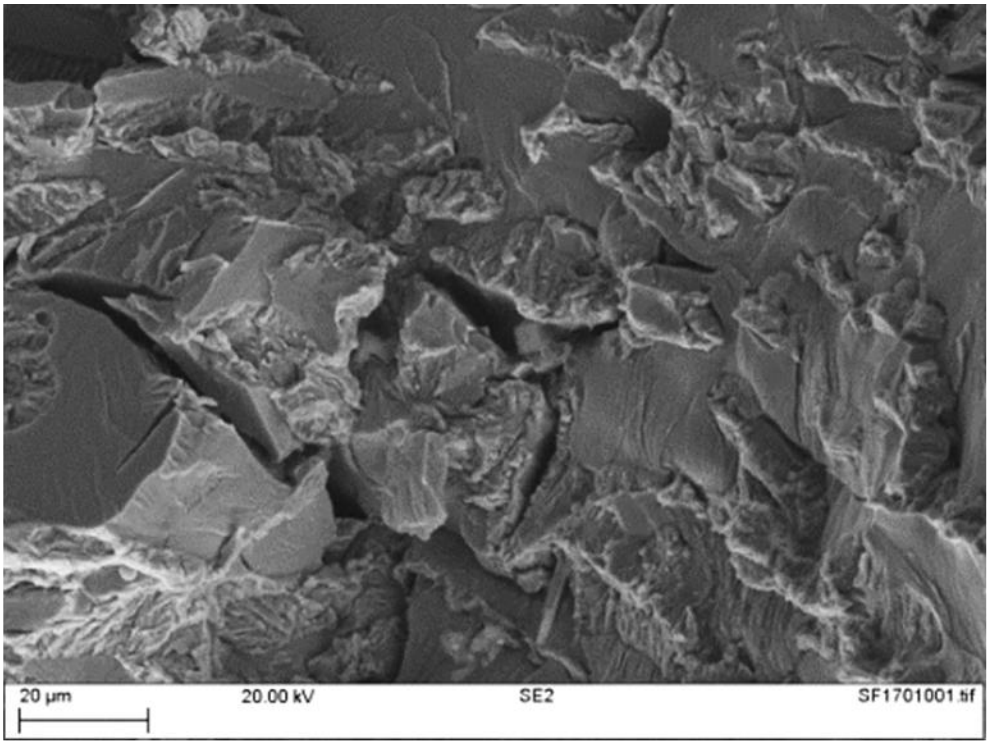

Figure 6.10: SEM images of the fracture face of the specimens extracted from M1 tested at 0.0003 mm.min^{-1} displacement under CP.

Figure 6.11, is a comparison of the J-resistance curves obtained for M2. Specimens were tested at a displacement rate of 0.3 mm.min^{-1} and 0.0003 mm.min^{-1}. The curve of the specimen tested at slow strain rate under CP is also included. The crack extension curves generated at 0.3 mm.min^{-1} exhibited a similar behaviour to that of M1, with oscillations in crack advancement. The macrograph of these specimen's fracture faces, Figure 6.12, did not show the propagation of a crack but mostly bending and tearing at the specimen notch. The fracture morphology also indicated a high degree of ductility, Figure 6.12. A specimen was also tested, in air, at the lowest displacement rate allowed by the machine capacity: 0.3×10^{-6} mm.min^{-1}. As for the previous results obtained with M2, the resistance curve displayed in Figure 6.11 was very messy, however its general trend exhibited slightly lower toughness values than those obtained from the specimen tested in air a higher displacement rate. The macrograph of the fracture faces, Figure 6.12, showed that the crack propagated in a very ductile manner, the SEM images were consistent with this observation, exhibiting micro voids coalescence, typical of ductile tearing behaviour.

The resistance curve of the specimen tested at slow strain rate and in CP conditions exhibited lower values than all the M2 specimens tested. The macrograph of the fracture face showed the propagation of a brittle crack. Furthermore, the analysis of the crack propagation morphology indicated the embrittlement of the specimen with the presence of secondary cracks and facets in the ferrite phase.

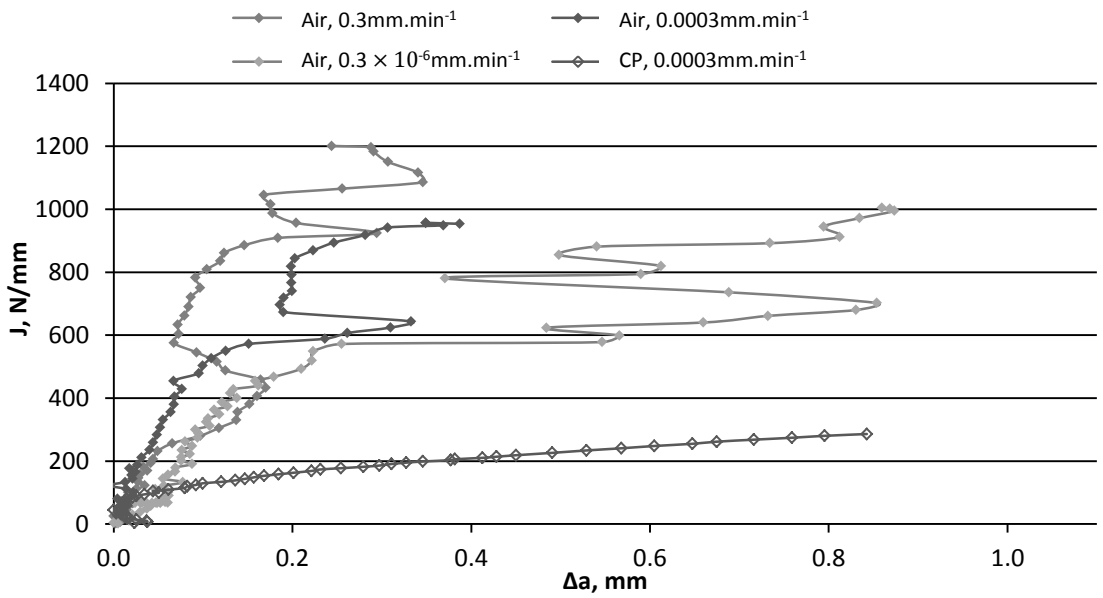

Figure 6.11: Comparison of the J resistance curves for the HIPed material tested at 0.3 mm.min^{-1} and 0.0003 mm.min^{-1} displacement, in air and at 0.0003 mm.min^{-1} displacement under CP.

a) Material: M2 Test conditions: Air Displacement rate: 0.3mm.min^{-1}

b) Material: M2 Test conditions: Air Displacement rate: 0.0003mm.min^{-1}

Figure 6.12 (continued): Fracture faces of the specimen extracted from the M2 and tested at a) 0.3 mm.min^{-1} and b) 0.0003 mm.min^{-1} displacement, in air.

c) Material: M2 Test conditions: Air Displacement rate: 0.3×10^{-6} mm.min^{-1}

d) Material: M2 Test conditions: CP Displacement rate: 0.0003mm.min^{-1}

Figure 6.12: Fracture faces of the specimen extracted from the M2 and tested at c) 3×10^{-6} mm.min^{-1} displacement rate, in air and at d) 0.0003 mm.min^{-1} displacement rate under CP.

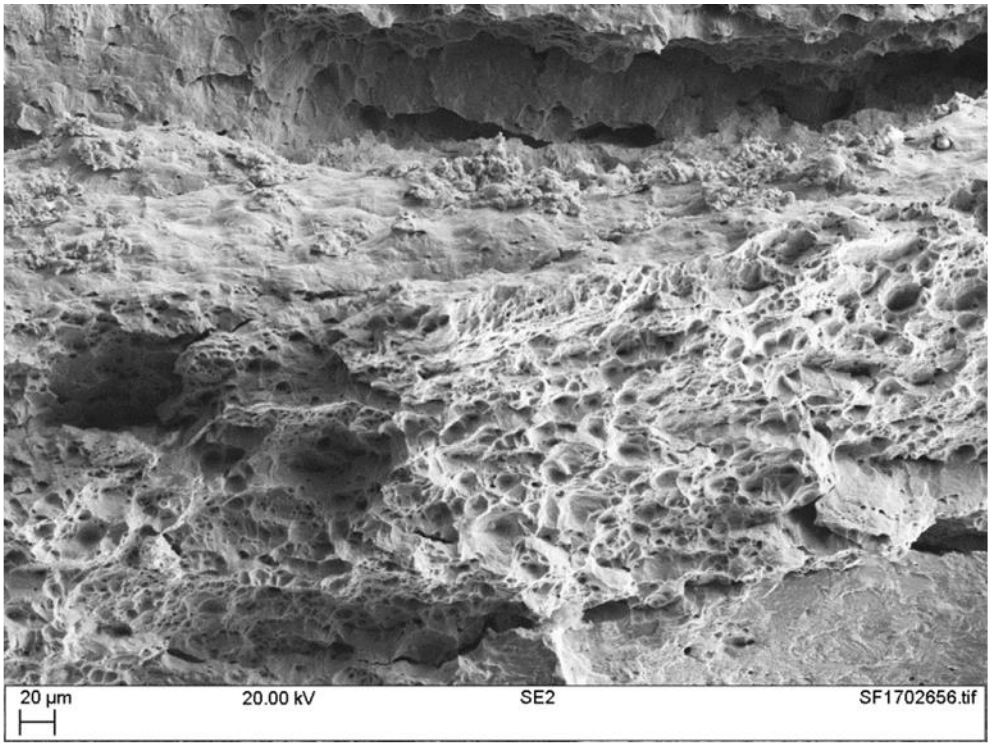

a) Material: M2 Test conditions: Air Displacement rate: 0.3mm.min^{-1}

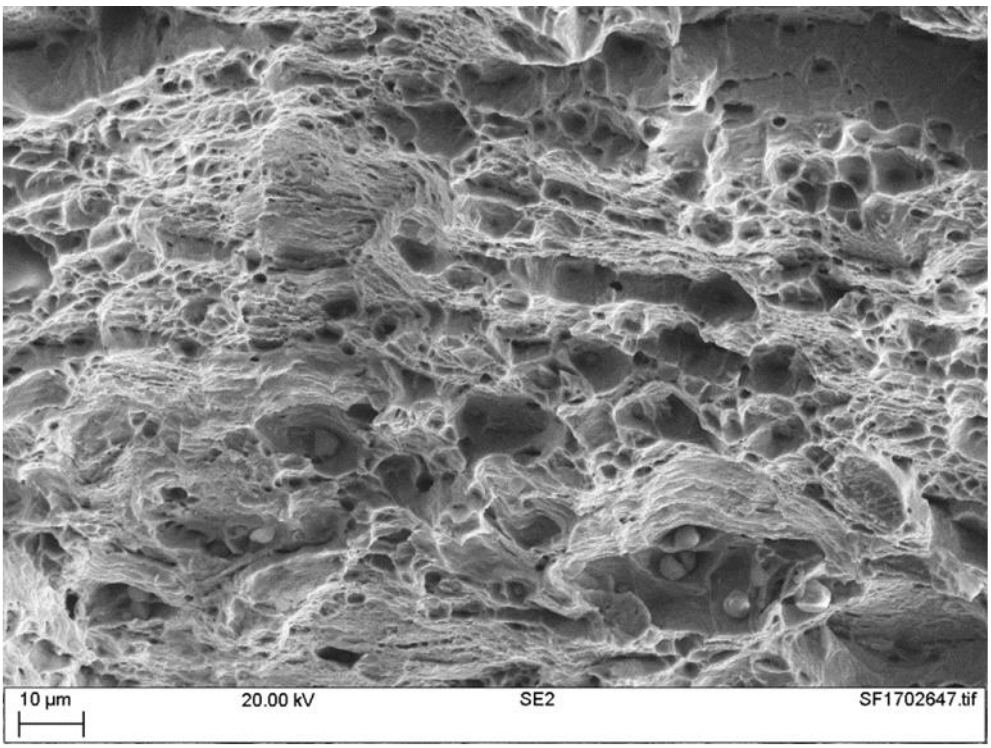

b) Material: M2 Test conditions: Air Displacement rate: 0.0003mm.min^{-1}

Figure 6.13 (continued): SEM images of the fracture face of the specimens extracted from M2 tested at a) 0.3 mm.min^{-1} and b) 0.0003 mm.min^{-1} displacement rate, in air.

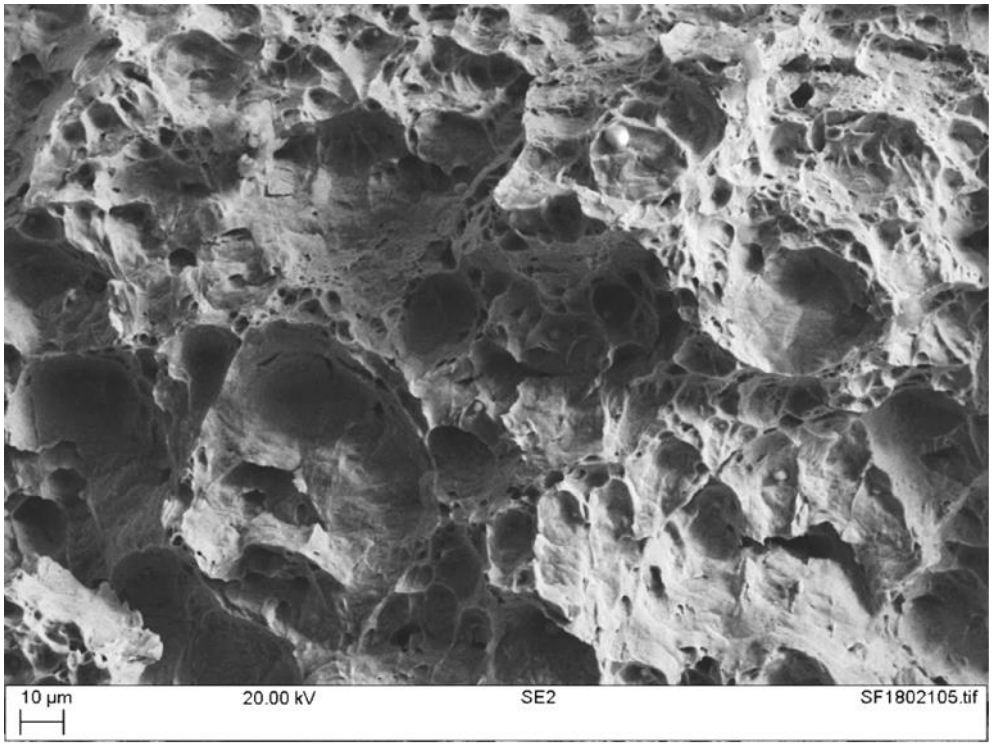

c) Material: M2 Test conditions: Air Displacement rate: 0.3×10^{-6} mm.min^{-1}

d) Material: M2 Test conditions: CP Displacement rate: 0.0003mm.min^{-1}

Figure 6.13: SEM images of the fracture face of the specimens extracted from M2 tested at c) 0.0003 mm.min^{-1} displacement rate in air and at d) 3×10^{-6} mm.min^{-1} displacement rate under CP.

The results obtained for the two materials tested at the displacement rate recommended by the standard: 0.3 $mm.min^{-1}$ attested of the high toughness properties of DSSs in air. However, in the case of the wrought material, it was shown that displacement rate had an impact on its cracking resistance. The decrease of toughness performance and the development of brittle cracking at slow displacement rate was consistent with the literature [152]. T. Depover et al. [214] and A. Scheid [110] also observed the detrimental effect of applying slow displacement rates for testing hydrogen embrittlement susceptible materials: dual phase alloys and SDSSs, and research projects at TWI[152] have shown the existence of a displacement rate below which the toughness properties are lower but stables for DSS materials.

In Chapter 3 on material characterisation, it was seen that, 2-3 ppm of hydrogen were present in the as-received materials and the crack morphology analysis showed typical hydrogen embrittlement feature of DSSs, similar to that observed on the specimen tested under CP conditions. An explanation for this observation was on the basis of the competition between the displacement rate applied and the diffusion rate of hydrogen in the material for a given stress concentration [97], [215], [102] and [216]. In the case of M1, 0.0003 $mm.min^{-1}$ was a displacement rate slow enough to enable the redistribution of hydrogen at the crack tip and induced HISC. However, the existing guidelines for designing with DSSs against HISC, do not provide displacement rate values to perform testing and engineering critical assessment (ECA) have not been developed in particular for those materials.

In the case of M2 no influence of the displacement rate was observed in air, the crack extension curves showed very similar behaviours and SEM analysis of the fracture faces did not show any loss of ductility compare to M1. Embrittlement only occurred at slow strain rate on the specimen tested under CP. Following the reasoning given for M1, this result showed that hydrogen diffusion in this material was lower, and therefore,, for the same displacement rate applied in air, the hydrogen did not had the time to redistribute in the highly stressed regions and induce HISC. Indeed, it was demonstrated in several works that the hydrogen diffusion in DSSs occurs mainly through the ferrite phase, [85], [92]and [217] due to a hydrogen diffusion coefficient being five orders of magnitude higher than that in the austenite and the solubility close to hundred times lower than in the austenite [83]. Hence, the different in the size and

distribution of ferrite and austenite grains within the two materials can be an important parameter, as described in Chapter 3, could explain their different hydrogen diffusion coefficients.

Records of crack propagation, i.e. data generated for $\Delta a > \sim 0.2$ mm, obtained by this method of testing using slow strain rates, are fairly uniform and consistent, as the curves are somewhat linear, and do not show any odd points or abnormal tendencies. Hence, the investigation on the influence of hydrogen pre-charging, notch geometry and environment were performed at the crosshead displacement of 0.0003 $mm.min^{-1}$.

6.3.2 The influence of hydrogen pre-charging and its duration prior testing

A comparison of the J vs Δa curves obtained for the specimens M1-3h, M1-72h and M1-504h, hydrogen pre-charged for 3 hours, 72 hours and 504 hours, respectively and tested in air are presented in Figure 6.14. The J vs Δa curves of M1 specimens tested in air and under CP with 3 days of hydrogen pre-charging were also added. It was observed that the very early part of the curves (i.e. $\Delta a < 0.1$ mm, representing crack initiation) of the M1-72h and M1-504h specimens overlapped, whilst that of the M1-3h specimen showed higher toughness values. As expected, the curve for the specimen tested in CP was placed lower than all other curves during crack propagation (i.e. $\Delta a > 0.1$ mm), but at the early stage of cracking (i.e. $\Delta a < 0.1$ mm), the M1-72h and M1-504h curves were fairly close to the specimen tested in CP. In contrast, the initiation of the M1-3h curve was almost overlapping with the curve of the specimen tested in air.

Macrographs of the crack faces for the three hydrogen pre-charged specimens, together with the specimens tested in air and under CP are shown in Figure 6.15. The slow displacement rate applied ensured that cracks had propagated in all the specimens. M1-3h and the specimen tested in air both exhibits crack "tunnelling": the crack was deeper in the middle of the specimen and quasi inexistent at the specimen edges, where deformation was observed. However, cracking in M1-504h, initiated equally from the entire width of the specimen and no deformation was observed from the specimen edges, i.e. no blunting. In the case of the sample M1-72h, deformation was noticed from the specimen edges; however, the crack also developed at one edge. M1-72h and M1-504h both developed a wavy and irregular crack, but this behaviour was not as

noticeable than in the case of M1 specimen hydrogen pre-charged for 72 hours and tested under CP, Figure 6.15.

Figure 6.16 gives the cracks morphology details. The location where those images where taken in the crack is given by the number in the corner of each micrograph, which refers to the numbers on the corresponding macrograph of the crack. M1-3h showed a mixed mode of cracking with ductile areas (location 1) and areas displaying brittle features (i.e. facets, cleavage) in the ferrite phase and tearing of the austenite. This was very similar to the specimen M1 tested in air without pre-charging, Figure 6.10. The specimen M1-72h also displayed a mixed mode of cracking (location 4 and 5); however, very brittle areas were observed on the specimen side. Similar observations were made on M1-504h, the side of the specimen exhibiting very brittle areas and a mixed mode of fracture, as the crack propagated.

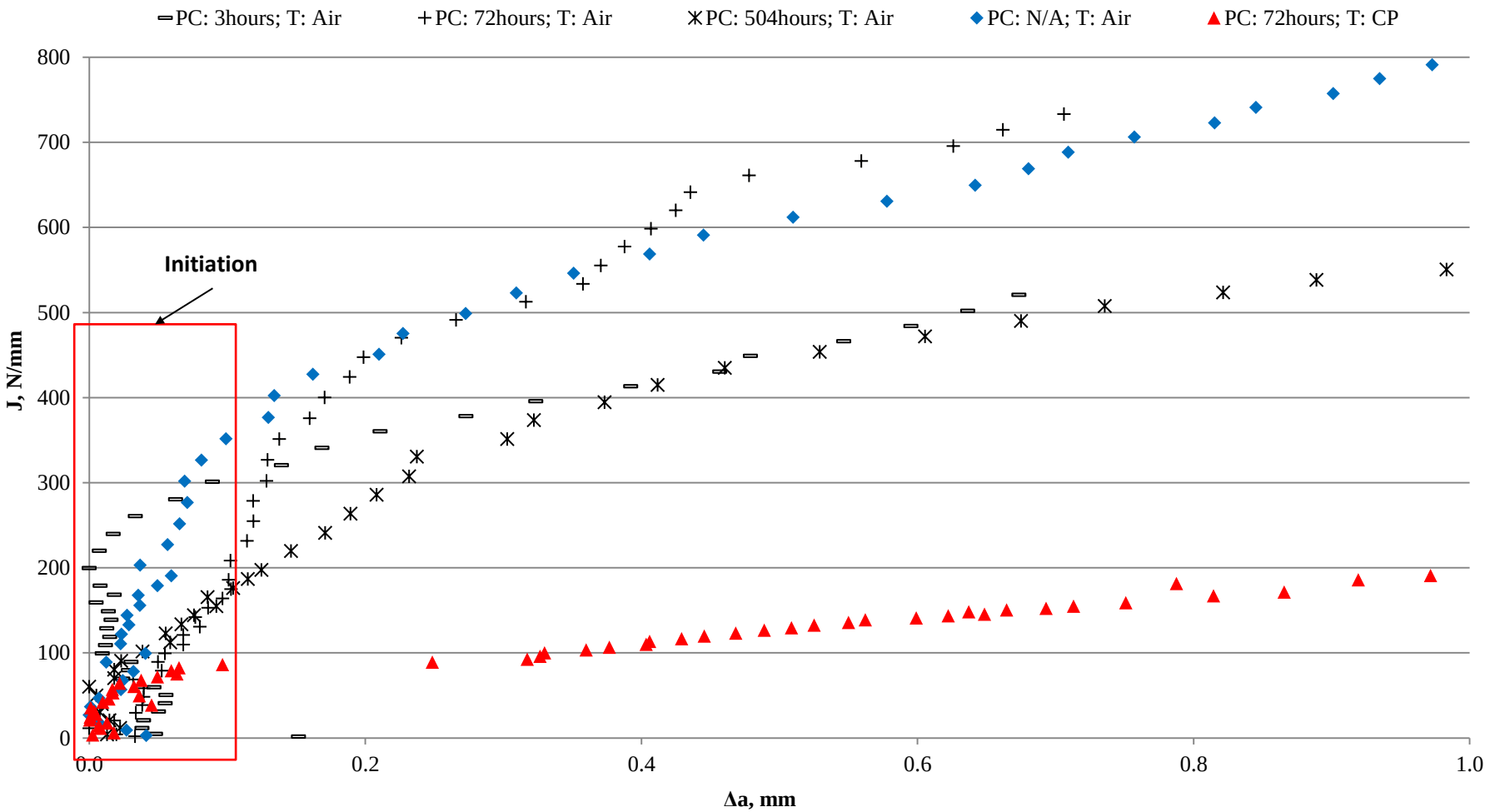

Figure 6.14: Comparison of the J resistance curves for wrought material (M1) tested in air at 0.0003 mm.min^{-1} displacement after 3 different pre-charging times: 3, 72 and 504 hours as well as in air and CP conditions. PC: Pre-charging time, T: testing conditions

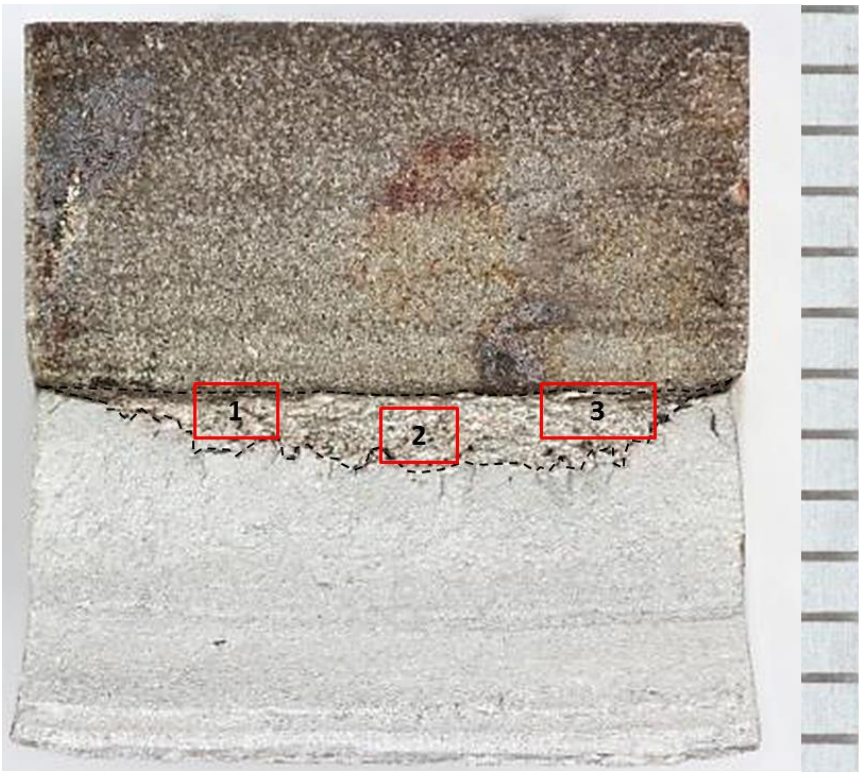

a) Material: M1 PC: 3h; T: Air Displacement rate: 0.0003mm.min^{-1}

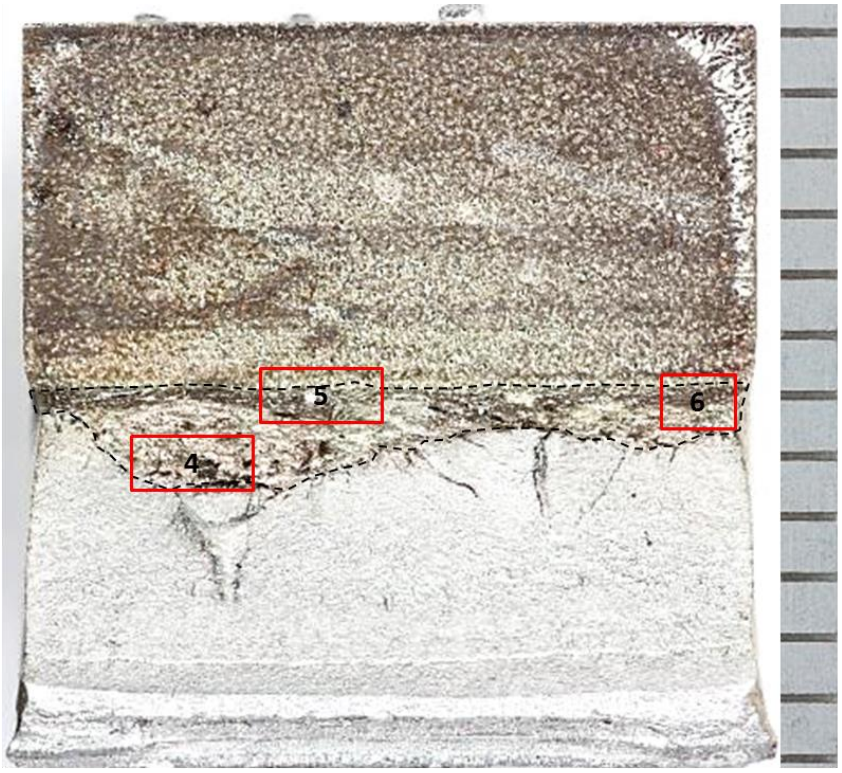

b) Material: M1 PC: 72h; T: Air Displacement rate: 0.0003mm.min^{-1}

Figure 6.15 (continued): Macrographs of the crack propagation in M1 specimens, hydrogen pre-charged for a) 3 and b) 72 hours and tested in air.

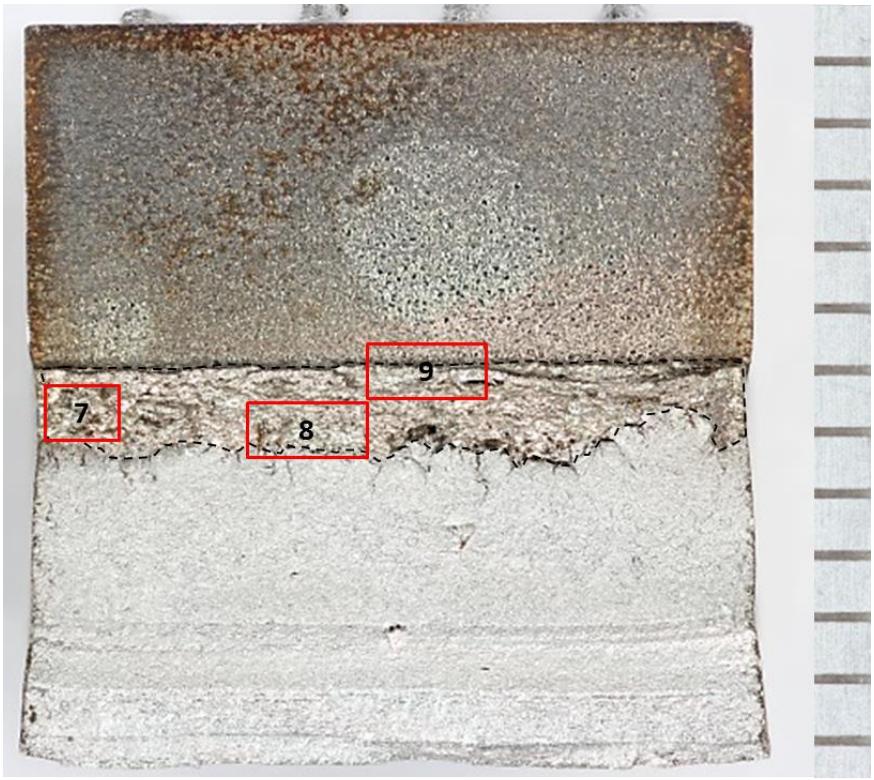

c) Material: M1 PC: 504h; T: Air Displacement rate: 0.0003mm.min^{-1}

Figure 6.15: Macrographs of the crack propagation in M1 specimens, hydrogen pre-charged for c) 504 hours and the specimen tested in air.

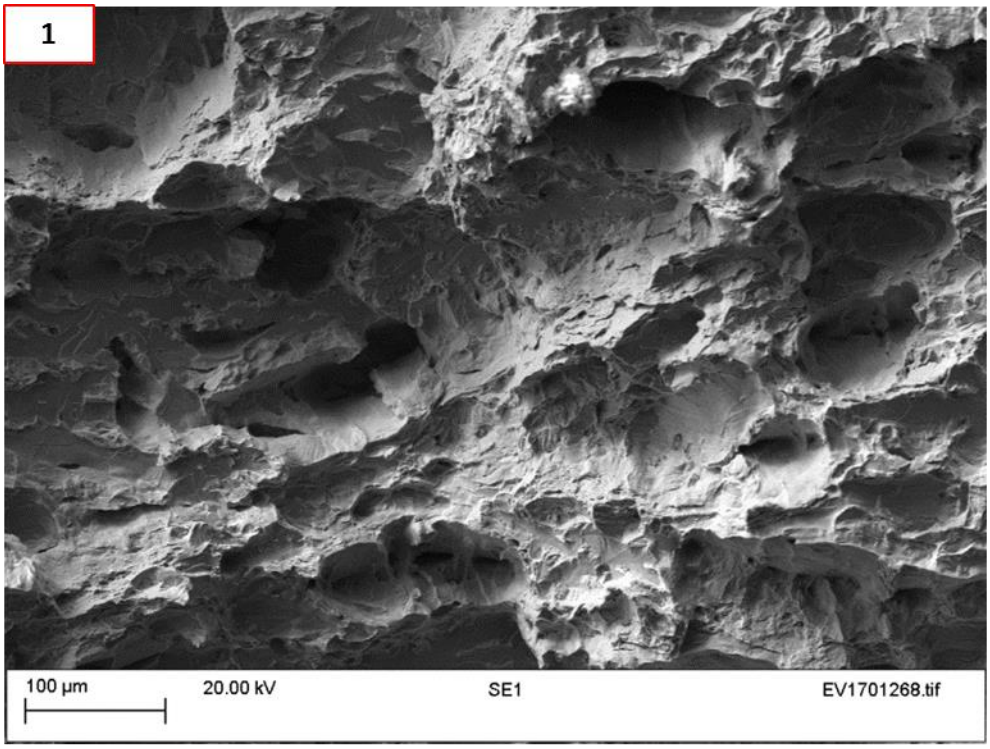

a) Material: M1 PC: 3h; T: Air Displacement rate: 0.0003mm.min^{-1}

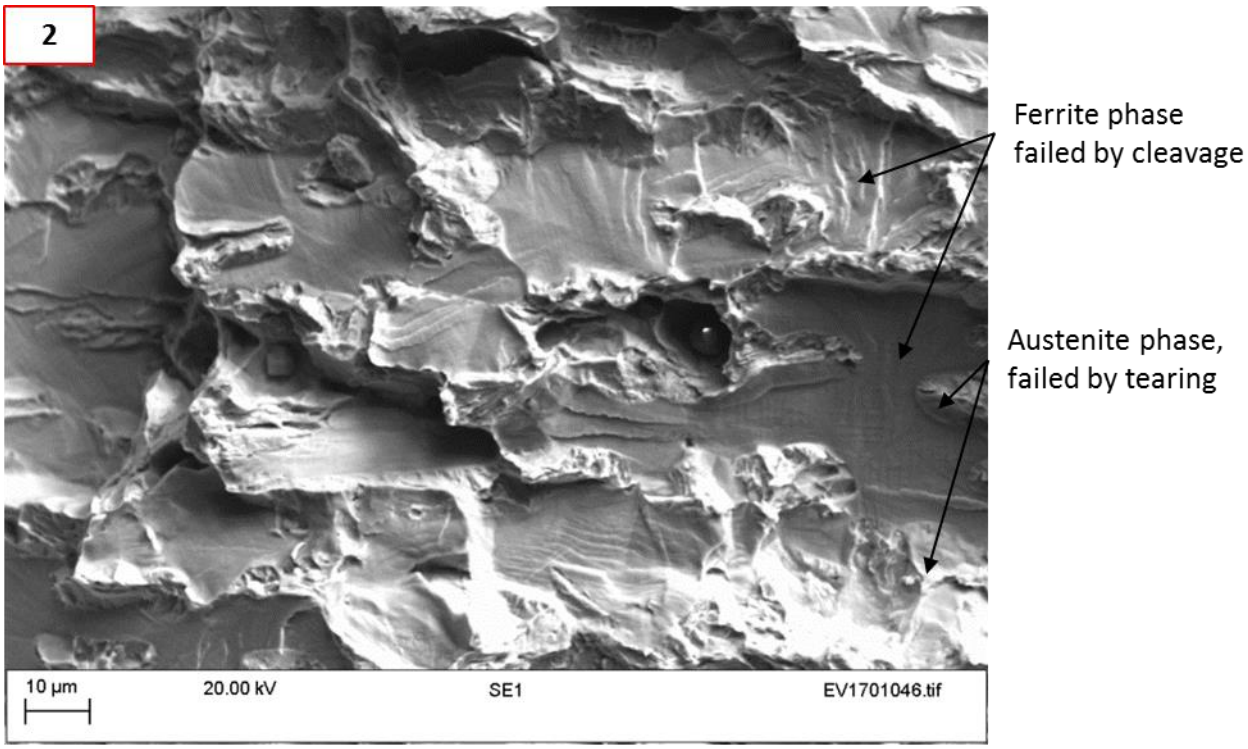

b) Material: M1 PC: 3h; T: Air Displacement rate: 0.0003mm.min^{-1}

Figure 6.16 (continued): SEM images of the crack morphology for M1 specimens, hydrogen pre-charged for 3 h, and tested in air. The number a) 1 and b) 2 are related to the area indicated on the macrograph, Figure 1.15.

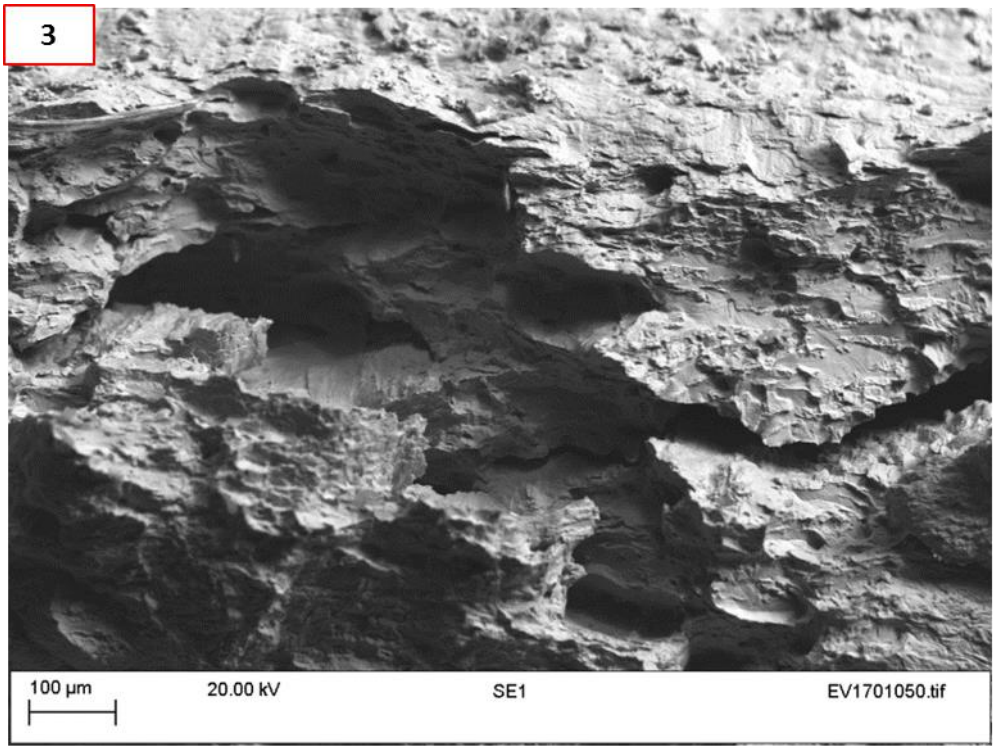

c) Material: M1 PC: 3h; T: Air Displacement rate: 0.0003mm.min^{-1}

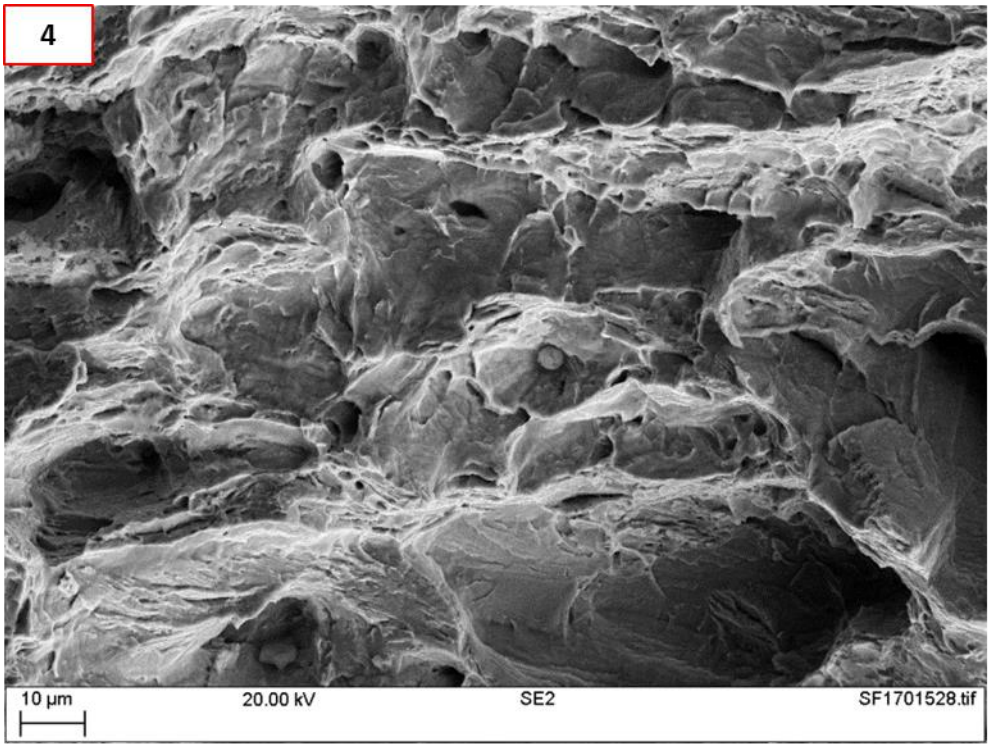

d) Material: M1 PC: 72h; T: Air Displacement rate: 0.0003mm.min^{-1}

Figure 6.16 (continued): SEM images of the crack morphology for M1 specimens, hydrogen pre-charged for c) 3 h and d) 72 h and tested in air. The number 3 and 4 are related to the area indicated on the macrograph, Figure 1.15.

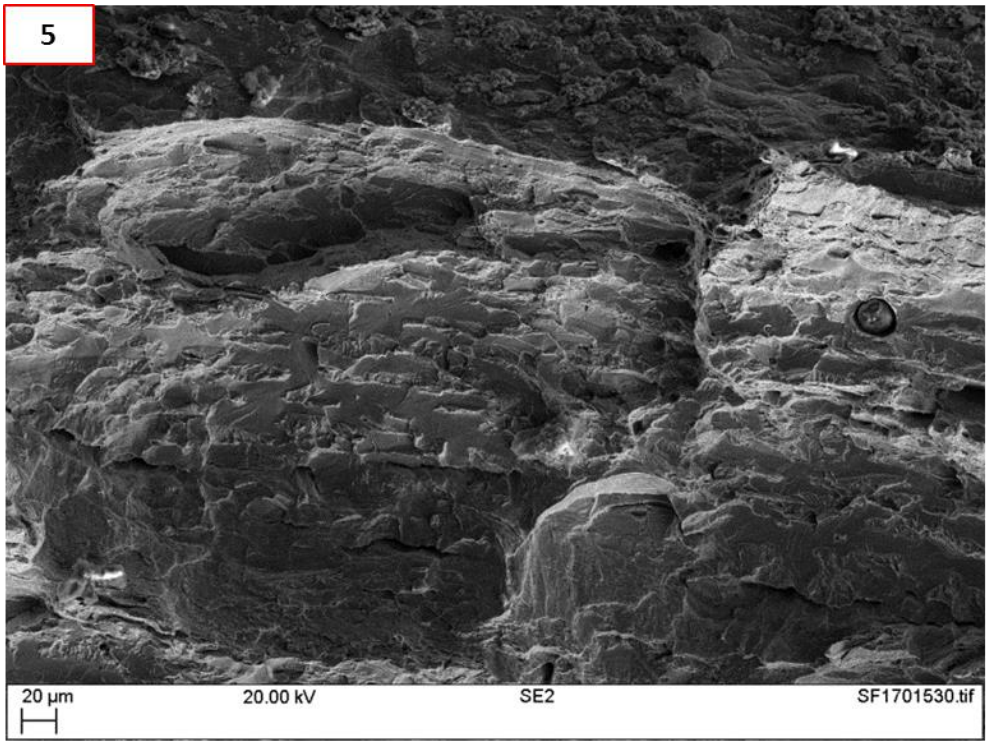

e) Material: M1 PC: 72h; T: Air Displacement rate: 0.0003mm.min^{-1}

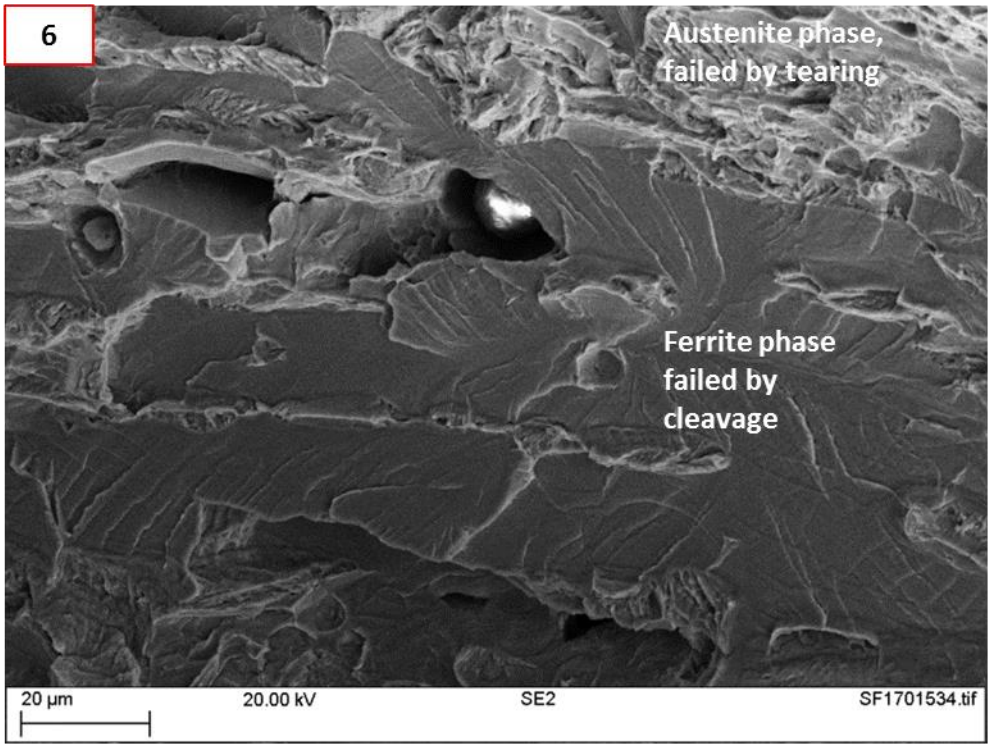

f) Material: M1 PC: 72h; T: Air Displacement rate: 0.0003mm.min^{-1}

Figure 6.16 (continued): SEM images of the crack morphology for M1 specimens, hydrogen pre-charged for 72 h and tested in air. The number f) 6 and g) 5 are related to the area indicated on the macrograph, Figure 1.15.

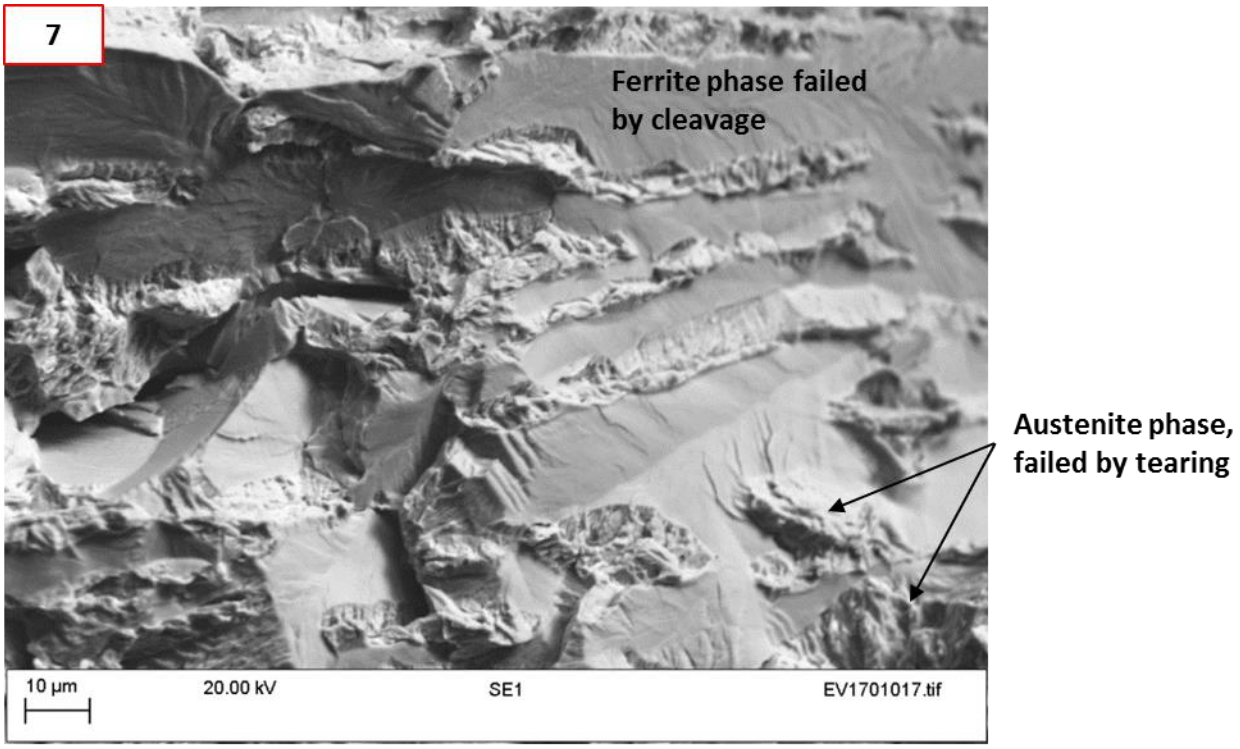

g) Material: M1 PC: 504h; T: Air Displacement rate: 0.0003mm.min^{-1}

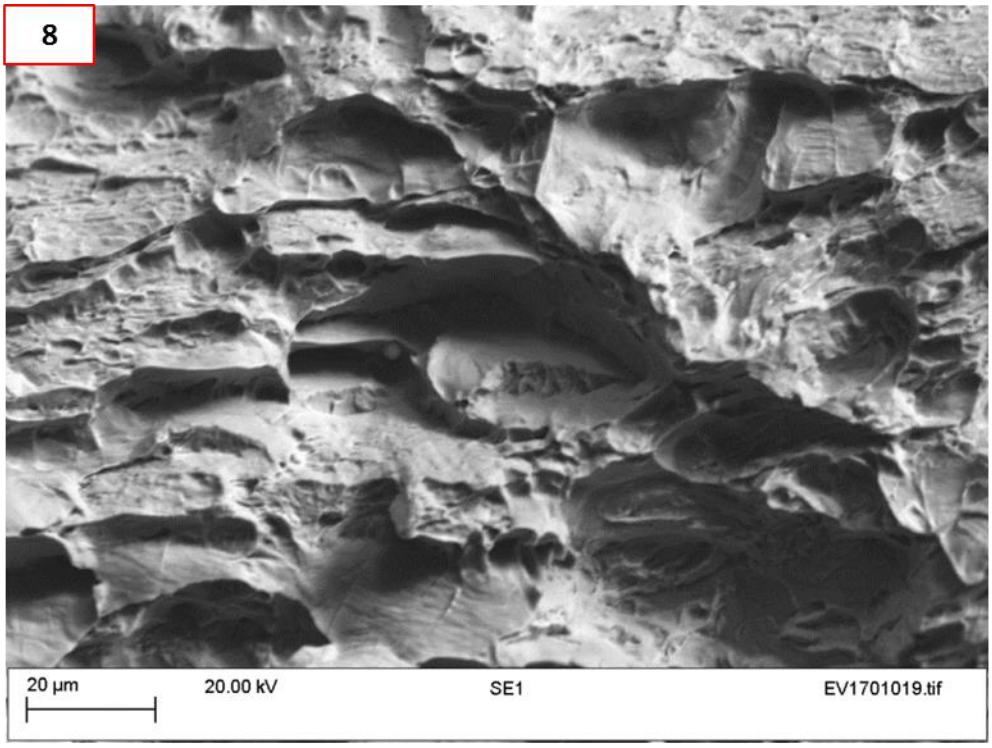

h) Material: M1 PC: 504h; T: Air Displacement rate: 0.0003mm.min^{-1}

Figure 6.16 (continued): SEM images of the crack morphology for M1 specimens, hydrogen pre-charged for 504 h and tested in air. The number g) 7 and h) 8 are related to the area indicated on the macrograph, Figure 1.15.

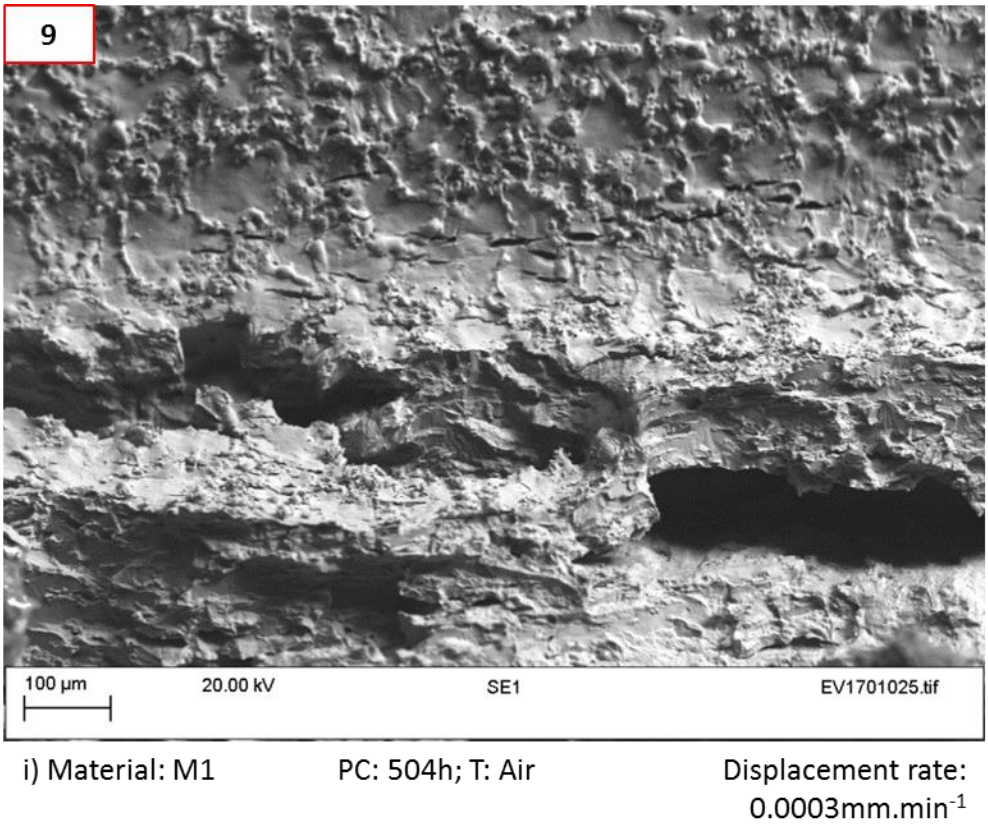

Figure 6.16: SEM images of the crack morphology for M1, hydrogen pre-charged for 504 h and tested in air. The number 9, in the corner is related to the location where the image was taken, see Figure 1.15.

Figure 6.17, represents the crack extension curves obtained for M2 after 3 hours (M2-3h), 72 hours (M2-72h) and 504 hours (M2-504h) of hydrogen pre-charging before testing in air. M1, the early part (i.e. initiation) of those three curves overlapped with the one of the specimen tested in air. However, differences in terms of fracture morphologies were apparent on the macrographs obtained from the fracture faces of the specimens, Figure 6.18. M2-3h displayed crack tunnelling which was similar to the specimen tested in air without pre-charging, but the specimens M2-72h and M2-504h exhibited a small zone of cracking on the sides. SEM observation of those areas displayed facets and ferrite cleavage, Figure 6.19. The rest of the crack was similar to the one in air with a lot of ductility characterised by the presence of micro-voids coalescence.

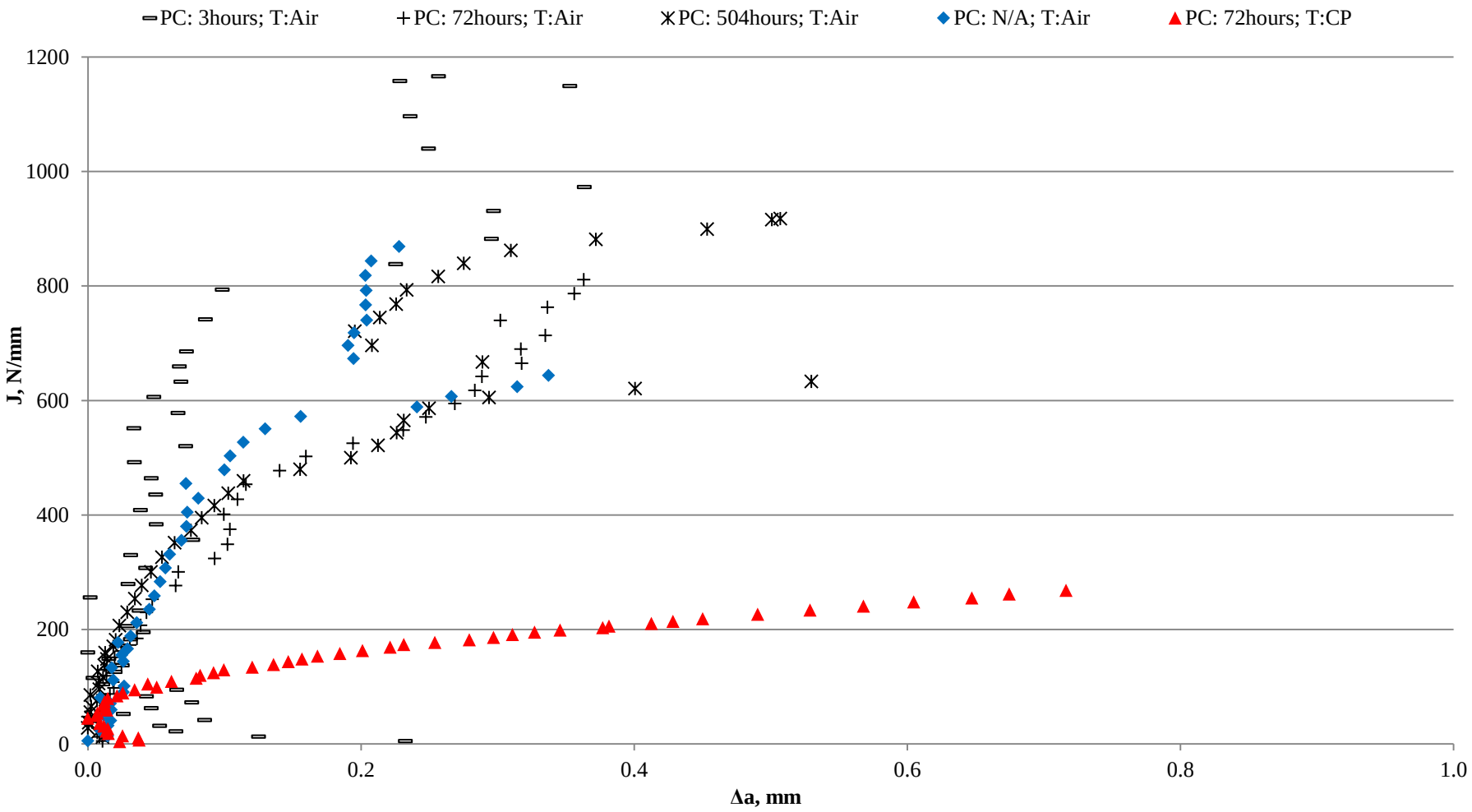

Figure 6.17: Comparison of the resistance curves for the HIPed material tested in air at 0.0003 mm.min^{-1} displacement after 3 different pre-charging times: 3, 72 and 504 hours as well as in air and CP conditions.

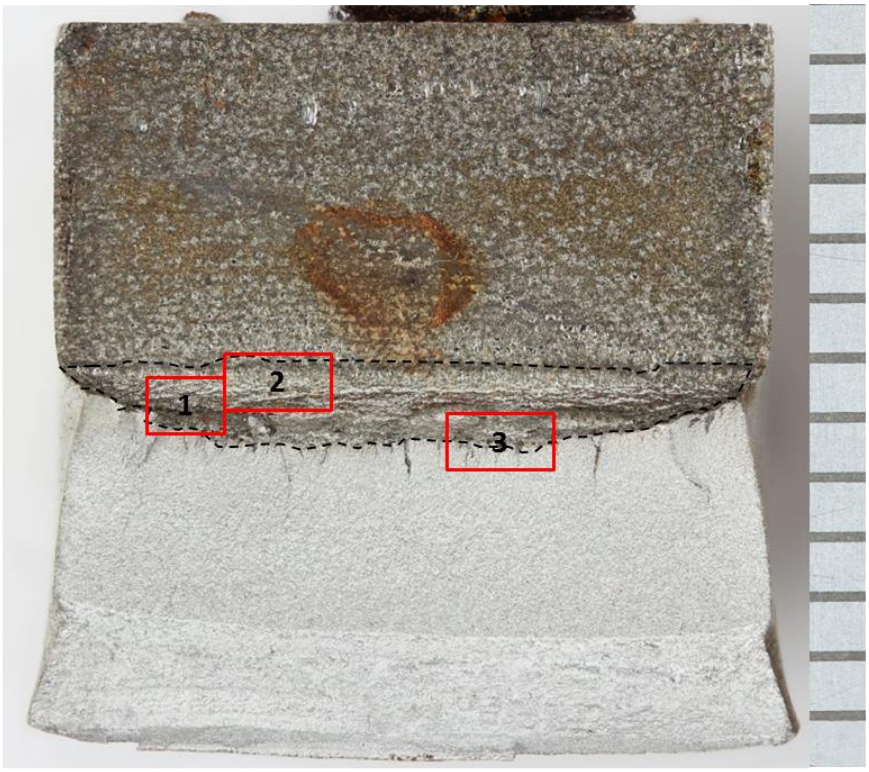

a) Material: M2 PC: 3h; T: Air Displacement rate: 0.0003mm.min^{-1}

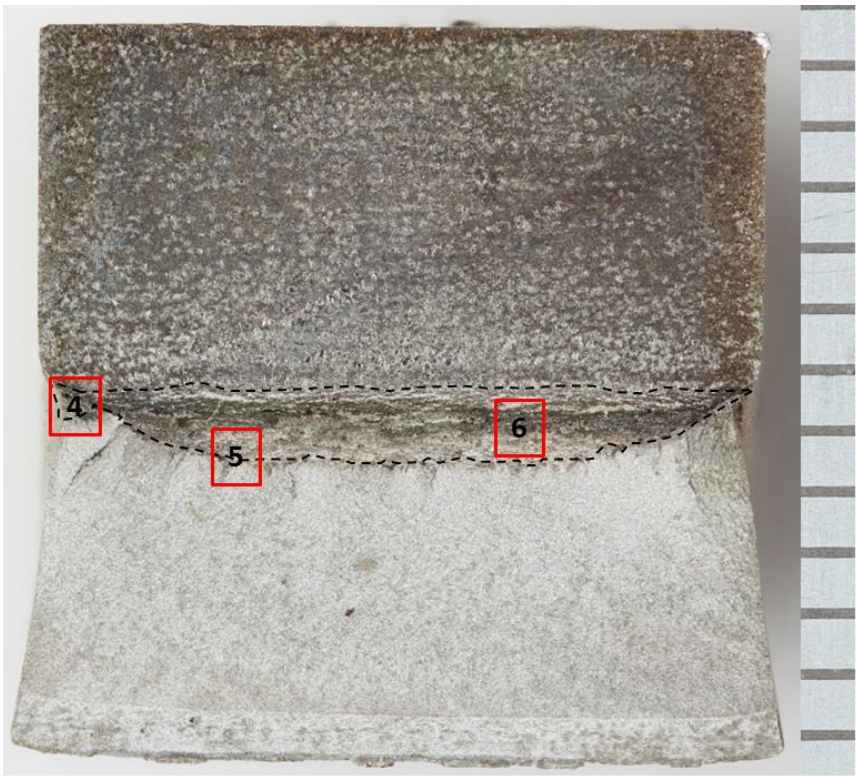

b) Material: M2 PC: 72h; T: Air Displacement rate: 0.0003mm.min^{-1}

Figure 6.18 (continued): Macrographs of the crack propagation in M2 specimens, hydrogen pre-charged for a) 3 and b) 72 h and tested in air.

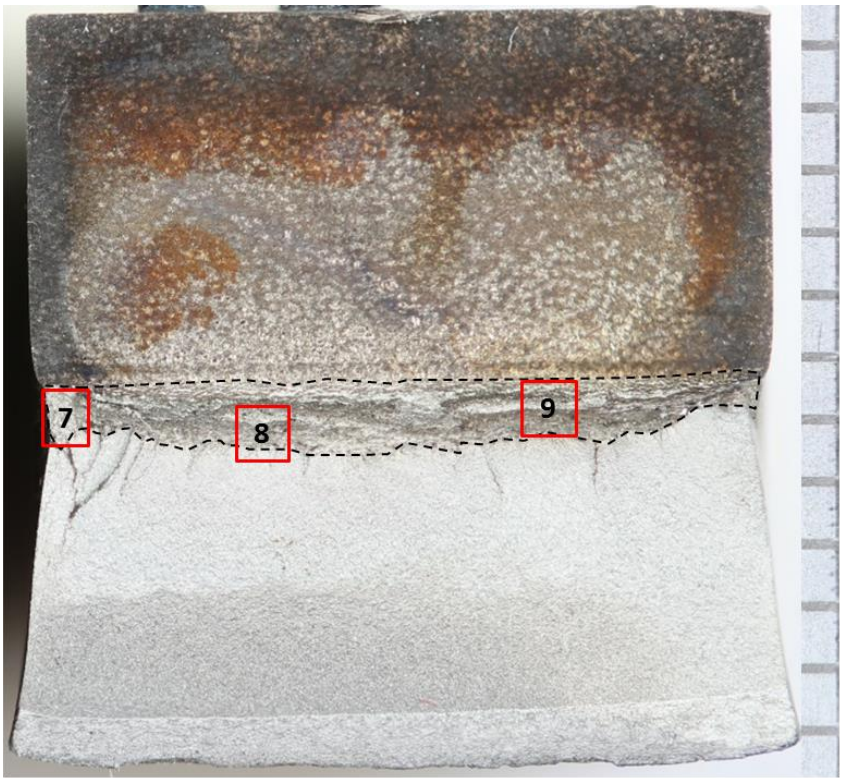

Figure 6.18: Macrographs of the crack propagation in M2 specimens, hydrogen pre-charged for c) 504 h and tested in air.

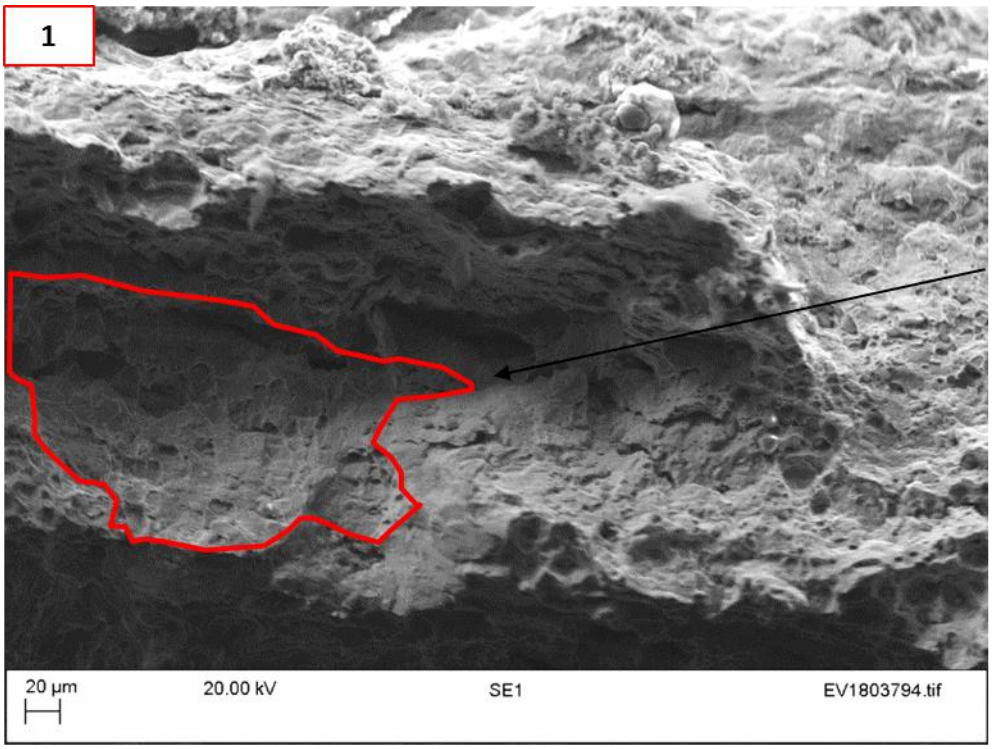

a) Material: M2 PC: 3h; T: Air Displacement rate: 0.0003mm.min^{-1}

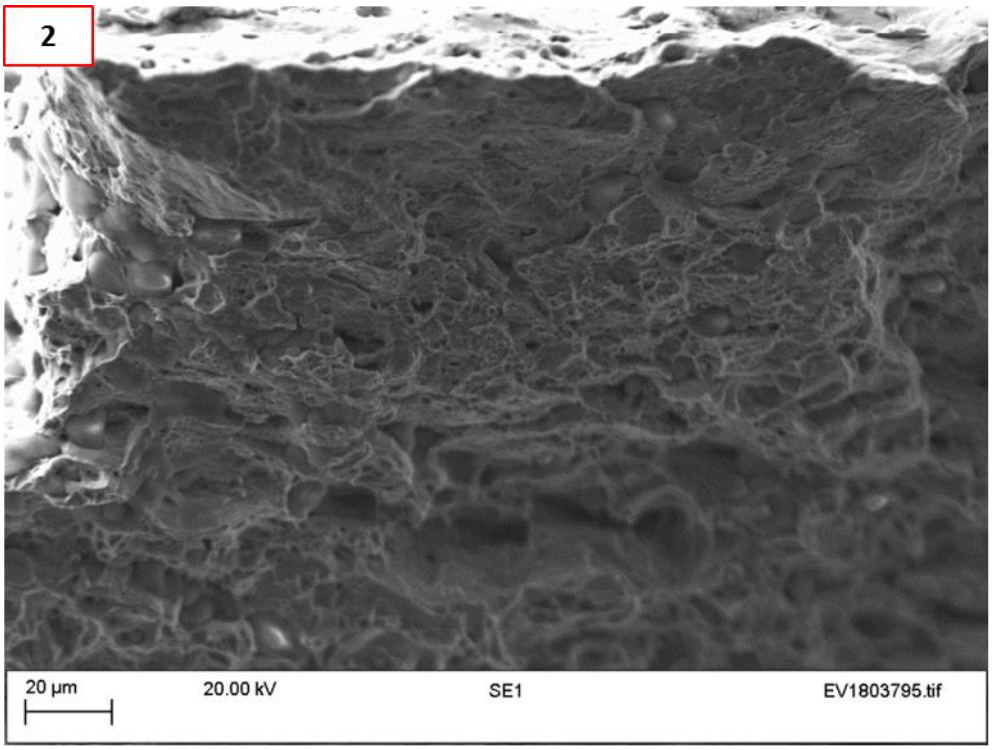

b) Material: M2 PC: 3h; T: Air Displacement rate: 0.0003mm.min^{-1}

Figure 6.19 (continued): SEM images of the crack morphology for M2 specimens pre-charged (PC) for 3 h and tested(T) in air. The number a) 1 and b) 2 are related to the area indicated on the macrograph, Figure 6.18.

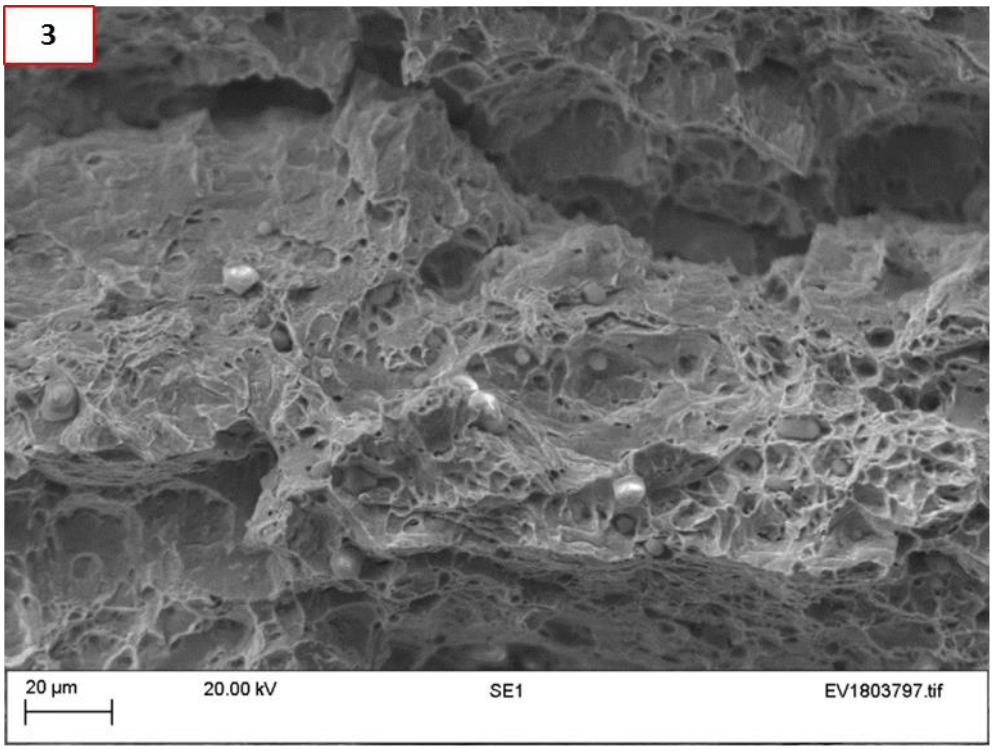

c) Material: M2 PC: 3h; T: Air Displacement rate: 0.0003mm.min^{-1}

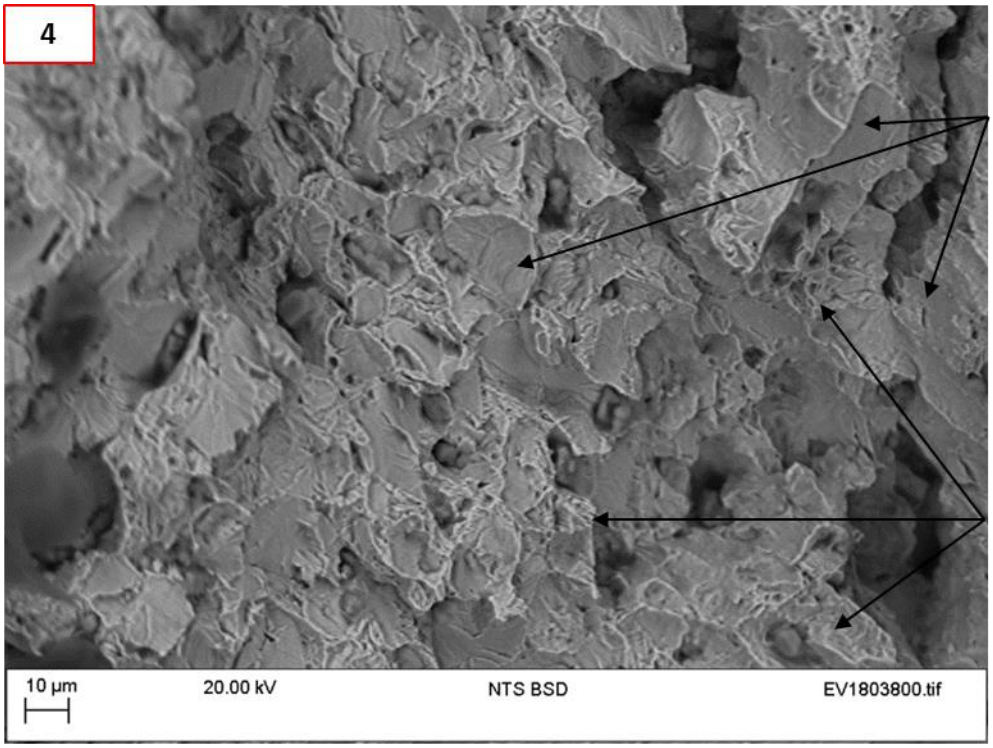

d) Material: M2 PC: 72h; T: Air Displacement rate: 0.0003mm.min^{-1}

Figure 6.19 (continued): SEM images of the crack morphology for M2 specimens pre-charged (PC) for c) 3 h and d) 72 h tested (T) in air. The numbers in the corner are related to the area were the images were taken. See macrograph, Figure 6.18.

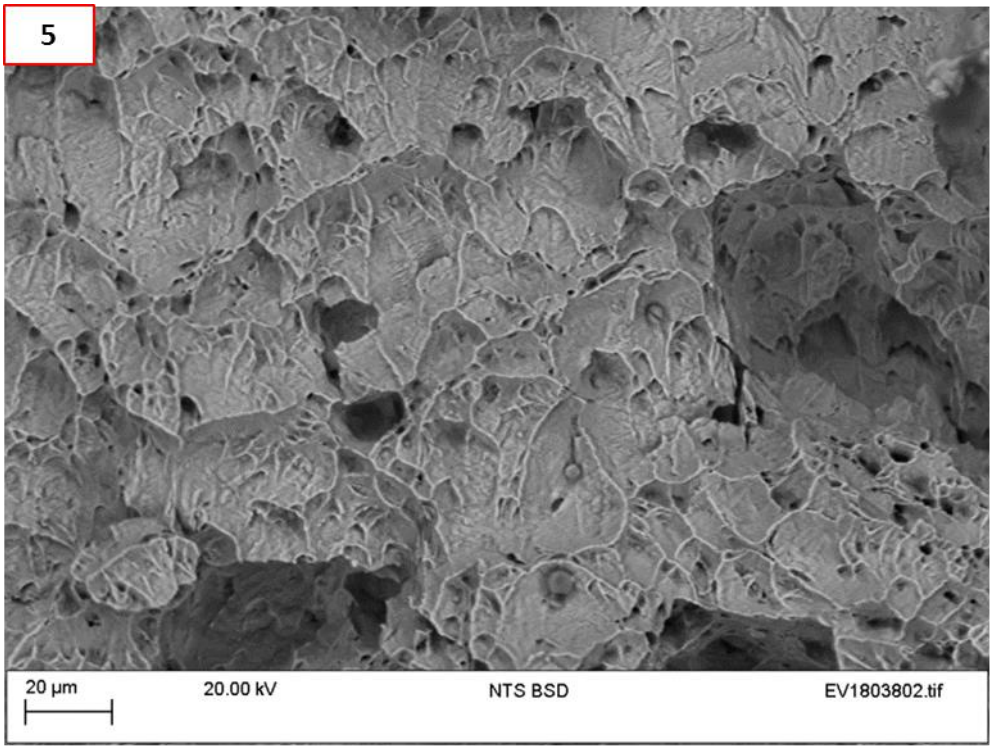

e) Material: M2 PC: 72h; T: Air Displacement rate: 0.0003mm.min^{-1}

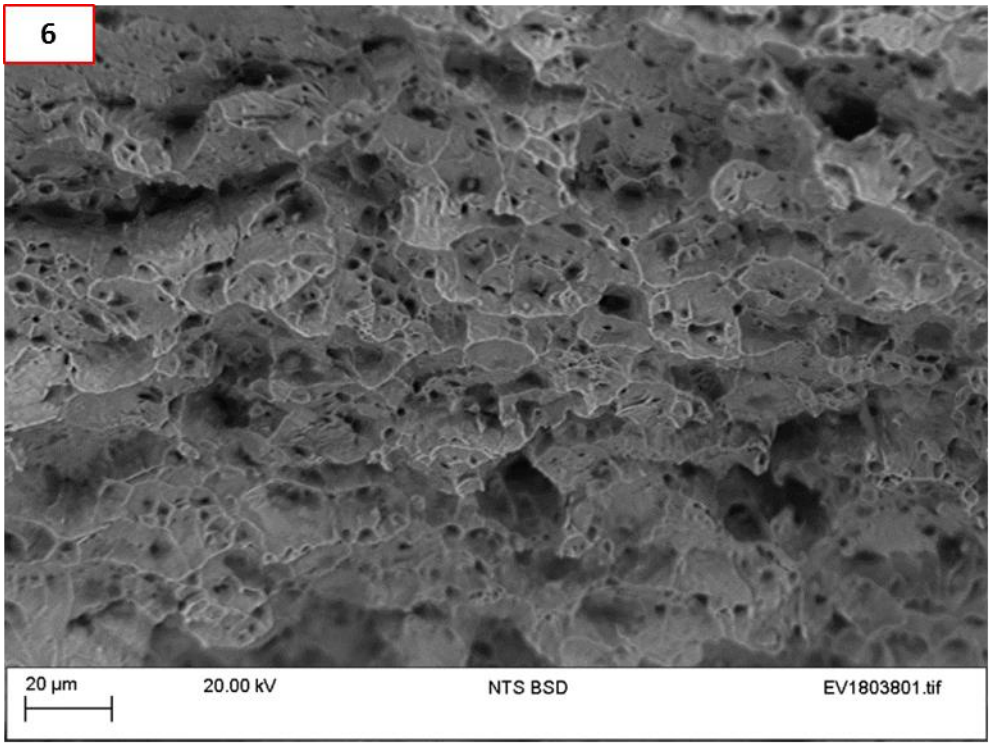

f) Material: M2 PC: 72h; T: Air Displacement rate: 0.0003mm.min^{-1}

Figure 6.19 (continued): SEM images of the crack morphology for M2 specimens pre-charged (PC) for 72 h and tested(T) in air. The number e) 5 and f) 6 are related to the area indicated on the macrograph, Figure 6.18. In both images failure by mvc was observed.

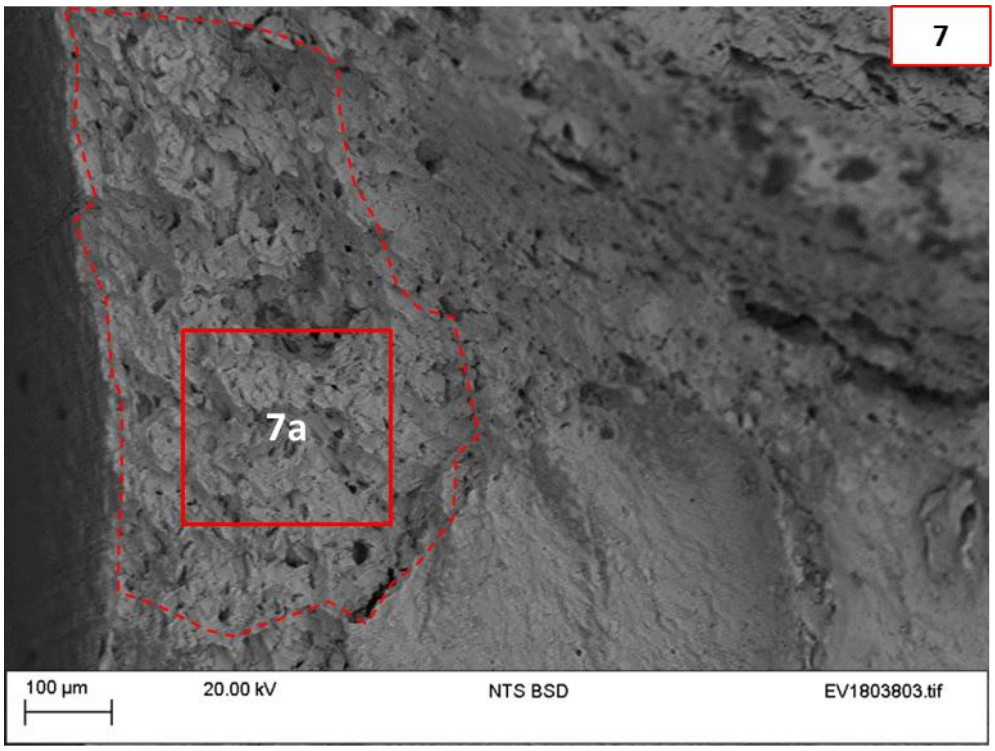

g) Material: M2 PC: 504h; T: Air Displacement rate: 0.0003mm.min^{-1}

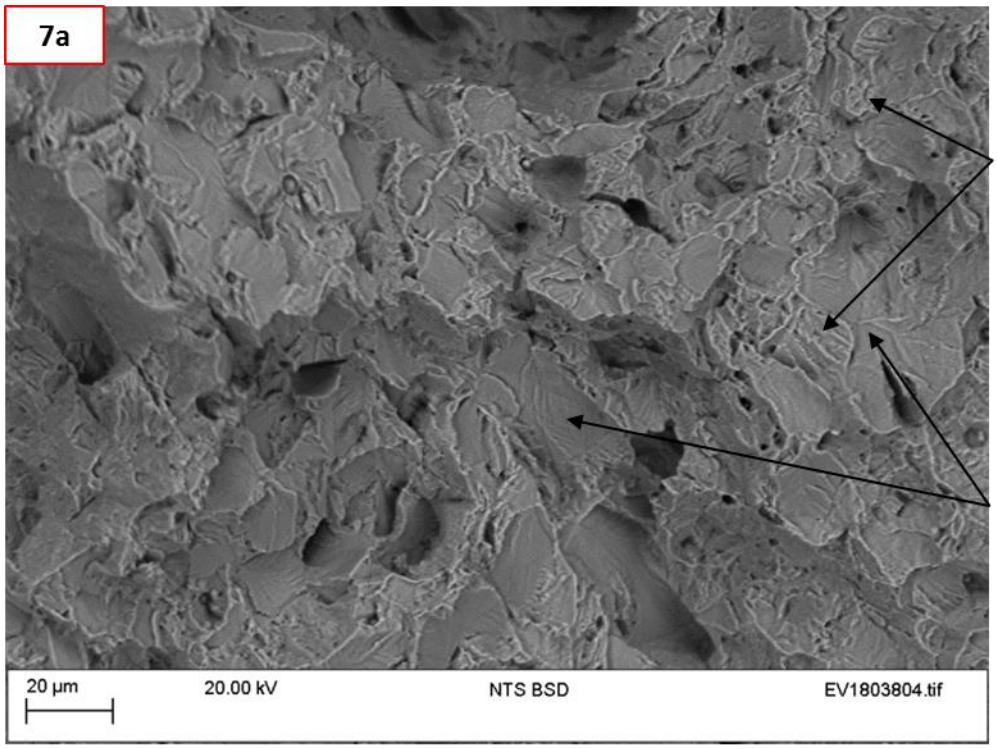

h) Material: M2 PC: 504h; T: Air Displacement rate: 0.0003mm.min^{-1}

Figure 6.19 (continued): SEM images of the crack morphology for M2 specimens pre-charged (PC) for 504 h and tested (T) in air. The number g) 7 and h) 7a are related to the area indicated on the macrograph, Figure 6.18. Embrittlement of the ferrite was observed.

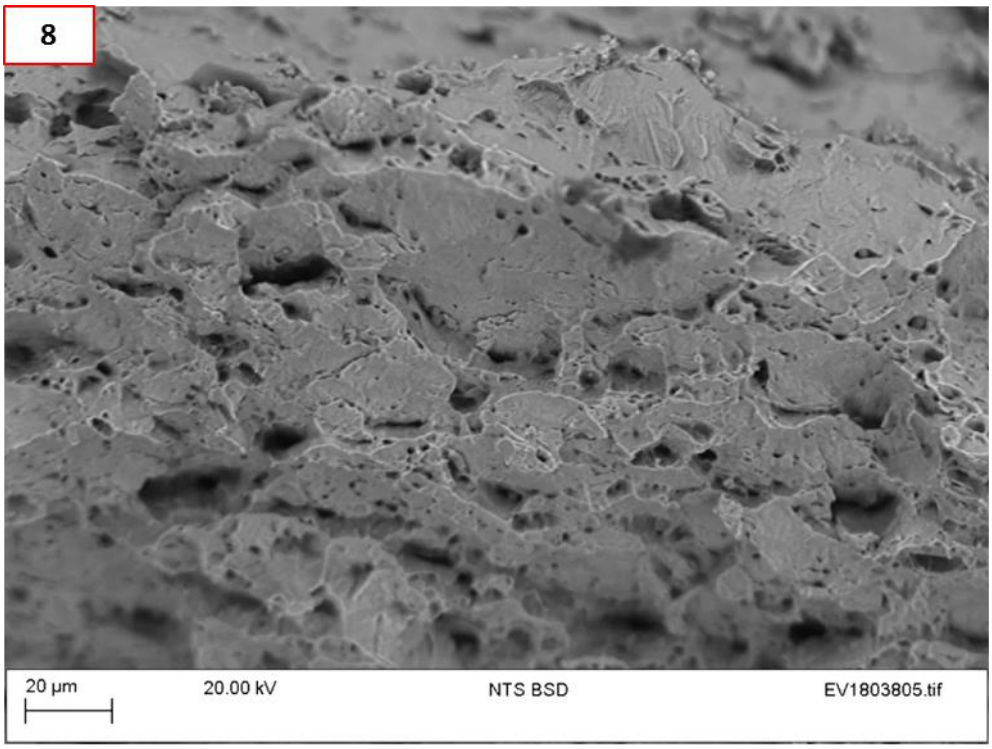

i) Material: M2 PC: 504h; T: Air Displacement rate: 0.0003mm.min^{-1}

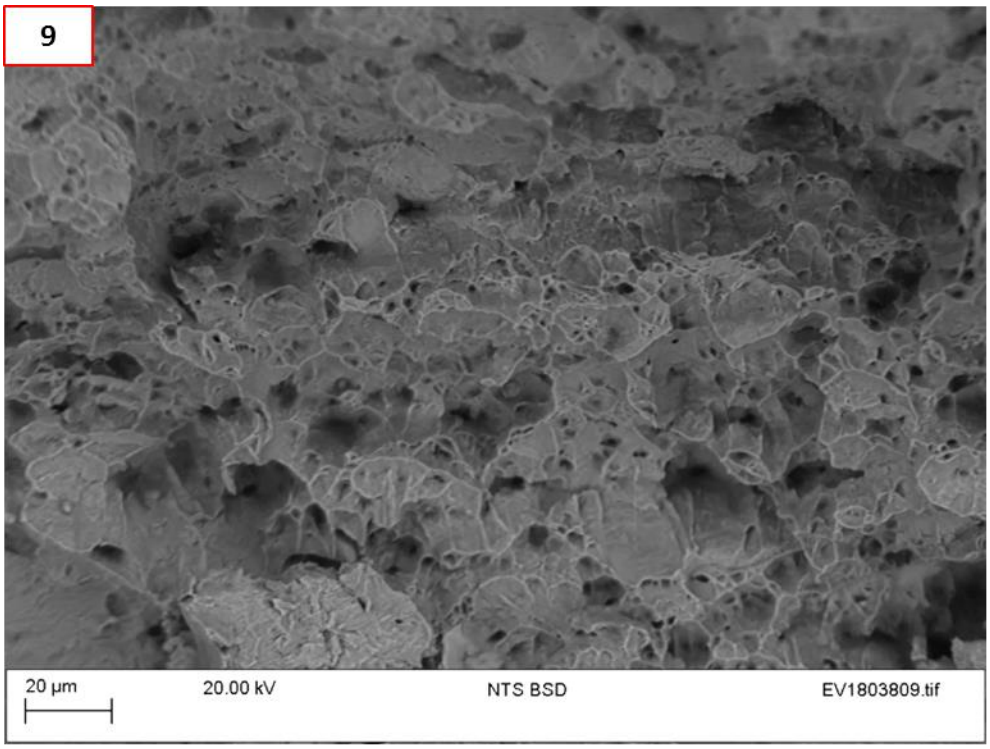

j) Material: M2 PC: 504h; T: Air Displacement rate: 0.0003mm.min^{-1}

Figure 6.19: SEM images of the crack morphology for M2 specimens pre-charged (PC) for 504 h and tested in air. The numbers in the corner of each image: i)8 and j)9 are the location where the image was taken, see Figure 6.18, mvc were observed in both locations.

In the literature, no agreement was found on the effects of pre-charging prior testing in environment. In the case of DSSs, hydrogen diffusion is very slow and the influence and importance of pre-charging was not always observed [218], [219], [110]. However, some authors have demonstrated the embrittlement effect of this first step in DSS [220] [116].

In the present study, the results showed the influence of hydrogen pre-charging on the two materials where features characteristic of hydrogen embrittlement were observable on the specimen sides. This was explained by the presence of hydrogen at the surface of the specimen after pre-charging, and the performance of the test at a very slow strain rate of testing, allowing hydrogen to promote cracking as soon as stress a sufficiently high load/stress is experienced. This embrittlement effect was more pronounced for the wrought material (M1) as it was visible on the J vs Δa curves and more obvious on the fracture faces than for the HIPed material (M2). This is thought to be due to higher hydrogen transfer in this type of microstructure.

The results obtained from the effect of hydrogen pre-charging and its duration, determined the optimum pre-charging duration for the specimens dealt with in this study to be 3 days. It is deemed that this pre-charging duration can ensure that a sufficient amount of hydrogen would be available within the material neighbouring the crack, to allow a valid environmental assessment of an 'embrittled material'., and that the presence of hydrogen at the specimen surface as comparable to real conditions in which DSSs are exposed to CP [88].

Another reason of using pre-charging prior testing was to ensure the consistency of the specimen surface state and crack tip before testing, allowing higher reproducibility of the testing conditions [221].

6.3.3 The influence of the notch geometry on the resistance to cracking

6.3.3.1 Introduction

This part of the work aimed to investigate the influence of EDM or FPC notch geometry of the SENB specimens for two main reasons:

1) The notch geometry has an influence on redistributing stresses and hydrogen concentration within the specimen. Indeed, the redistribution of hydrogen (present within the material or coming from external sources) with hydrostatic stresses and strains applied to the material has been reported by various researchers, and the modelling of hydrogen diffusion and solubility at and adjacent to a crack tip has been extensively developed [97], [98], [215], [102], [103]. Furthermore, B.R.S. da Silva et al. also demonstrated the increase of apparent hydrogen solubility with elastic stresses in DSS [100].
2) Furthermore, EDM and FPC notch geometries have fundamentally different outcomes. While EDM notch is not a crack and can give an insight on the conditions for HISC to initiate from a blunt geometry, FPC will only measure the crack extension.

6.3.3.2 Investigation of resistance-to-cracking behaviour of DSSs as a function of the notch geometry

A comparative study on the resistance-to-cracking behaviour of two DSSs the M1 and M2 materials with different microstructures, and as a function of two different notch geometries was conducted and has been discussed below. The crack extension curved from M1 and M2 specimens, with EDM and FPC notched (detailed earlier in Section 6.2.3.4), and tested in air and under CP, are presented in Figure 6.20 and Figure 6.21 respectively. In each graph, the effect of the different notch geometries is compared. General appearances of the fracture faces from the EDM and FPC notched specimens are given in Figure 6.22 and Figure 6.23 respectively.

Both the M1 and M2 materials, with and without an FPC notch, showed a significant resistance to cracking in air, as can be seen by their steep rising curves; this effect was much more pronounced in M2. However, when the two materials were tested under CP, their performances in terms of fracture toughness values suffered significant reductions. The curves showed significant lack of resistance at the early stage of the test , i.e. $\Delta a <$ 0.1 mm, and that, in addition to the curves having lower values of J for environmental compared to air testing, the slope of the curves was also lower, i.e. flatter curves. Irrespective of the test environment, the performances of the EDM-notched test specimens were better than those of the FPC-notched specimens, for which all the curves were placed lower than the corresponding EDM notched specimens and were not

as steep, particularly in the early stage of the test. All the curves obtained from the M1 and M2 with EDM-notched specimens, tested in air and CP, showed a rising resistance behaviour, although this was very limited, in terms of J values, for the specimens tested under CP. In the case of the M1 and M2 with FPC-notched specimens, the curves were flat and the rising part of the curve was absent, indicating that, in the presence of a pre-crack, no resistance in terms of cracking initiation could be recorded, as, initiation had already occurred due to presence of the fatigue pre crack. (see Figure 6.20b and Figure 6.21b). It was also observed that, passed the rising resistance behaviour of EDM-notched specimen, the slopes of the curves for the FPC and EDM-notched specimens tested in CP were similar. A rising J R-curve typically implies that ductile tearing plays a role in determining crack extension. This was found in those materials that exhibited a rising R-curve showing a greater proportion of ductile tearing. In such rising curves, the initial part of the curve corresponds to the blunting of the notch and the initiation of cracking.

The Standards offset the initiation of ductile tearing by an amount equal to 0.2 mm, which is assumed to be the size of the blunting of the crack tip, before tearing actually begins. However, in the case of the M1 and M2 specimens tested under CP, the curves show neither equivalent 'blunting', once hydrogen-assisted cracking initiates from the pre-crack, nor that 0.2 mm crack extension seems to be a relevant offset, as any minimal loading might result in crack extension, at the very early stages of testing. Therefore, the use of blunting lines (as described in BS 7448-4 or ISO 12135) for the plotting of resistance curves (or better to say 'crack extension' curves) does not appear to be appropriated here. Figure 6.24 and Figure 6.25 show the fracture morphologies in the M1 specimen tested in air, adjacent to the FPC and EDM notch tips, respectively. Interestingly, brittle areas were observable adjacent to the tips of both notch types, although higher proportions of brittle areas were observable in the specimens with a FPC notch (Figure 6.24). The boundary between the EDM notch and the crack developed during testing was not well-defined (Figure 6.25); some local deformation (tearing and shearing) and multiple secondary cracks developed, before the main crack propagated through the specimen, and a mixed mode of ductile and brittle cracking was identified. Indeed, high local stresses are concentrated at and around the notch tip, which could redistribute and transfer the material's residual hydrogen (i.e. from

fabrication) to those regions. This can lead to HISC cracking, once critical levels of stress and hydrogen are reached [97], [215], [102]. The results could therefore suggest that testing at sufficiently slow displacement rates could enable the internal hydrogen to move around and become concentrated in the stressed/strained areas, resulting in embrittlement of the material via HISC. This is a combined effect of notch geometry and hydrogen-charging environment and was more pronounced in the case of FPC notches as stresses were higher. Similar observations have been reported for SDSSs with U and V- shaped EDM notches [219].

Figure 6.26 and Figure 6.27 show the fracture morphologies in the M1 specimen tested under CP, adjacent to the FPC and EDM notch tips, respectively. High magnification microscopy revealed that the cracking which developed during testing of both materials under CP was consistent with cleavage in the ferrite and shearing/tearing of the austenite, typical of HISC in (S)DSSs [76], [117], [122]. It can be observed that, in hydrogen-assisted crack extension, there is no blunting and the crack developed during testing simply extends directly from the pre-crack. This can, perhaps, explain the low crack growth resistance in the data obtained. In addition, it was apparent that the fracture toughness data only provide information on crack propagation and that the EDM notched specimens did not provide a means of quantifying crack initiation. Thus, the principles developed in Standards for determining R-curves relate to tearing resistance are not relevant when the crack initiates in a way that is not fully ductile, environmental testing in hydrogen charging media. Following those observation, EDM notches were used in the evaluation of the other testing parameters.

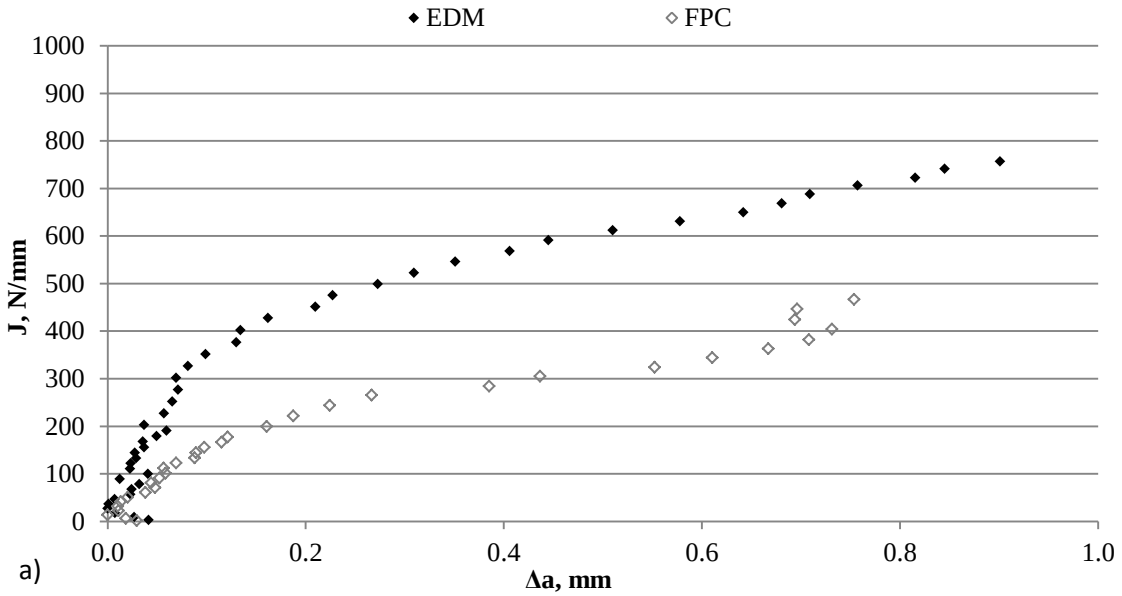

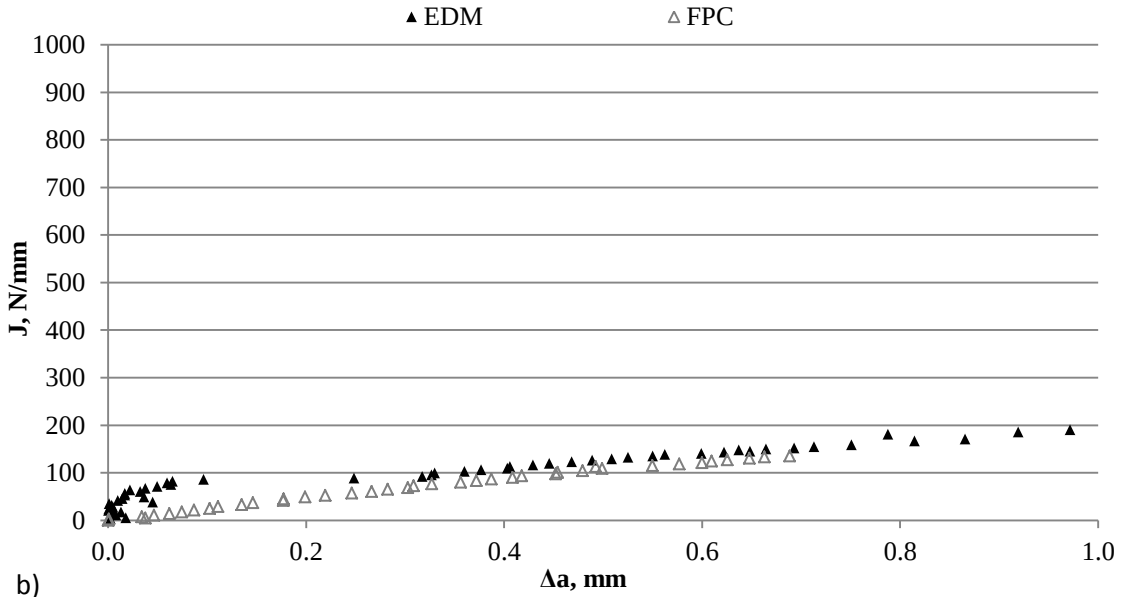

Figure 6.20: Comparison of the J resistance curves for M1 tested at 0.0003 mm.min^{-1} displacement with two notch geometries: EDM and fatigue pre-crack a) in air and b) in CP environment.

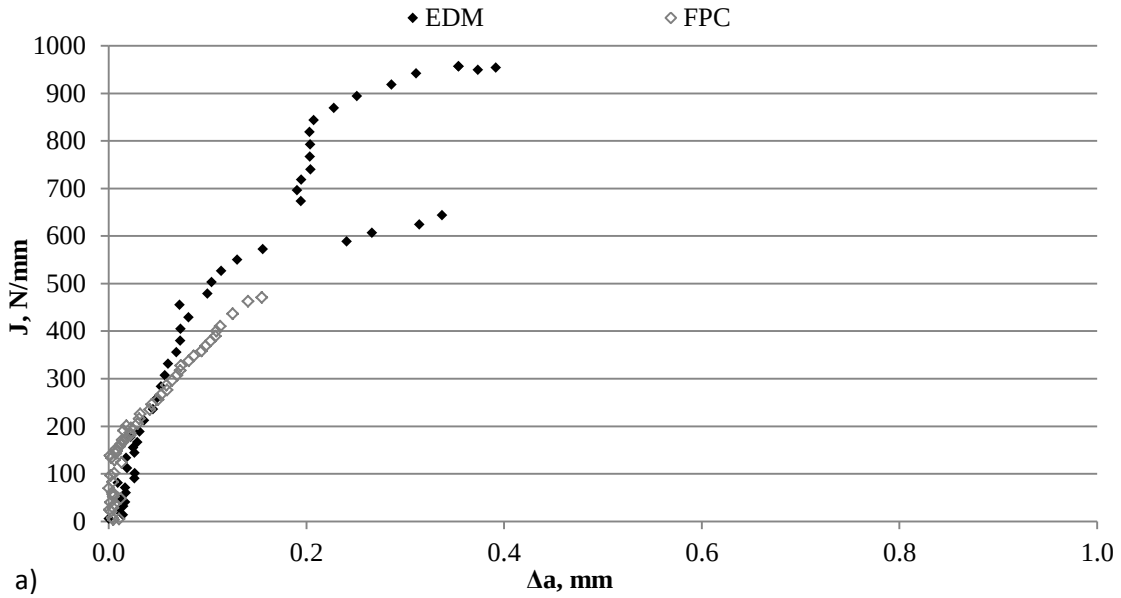

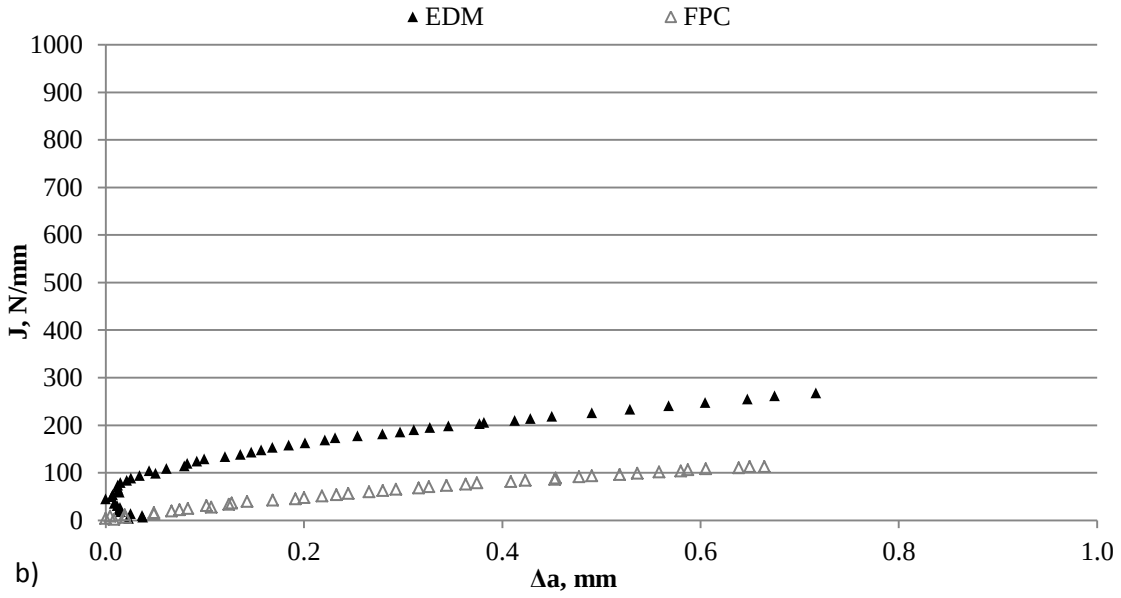

Figure 6.21: Comparison of the J resistance curves for M2 tested at 0.0003 mm.min^{-1} displacement rate with two notch types: EDM and FPC a) in air and b) under CP.

a) Material: M1 Test conditions: Air Displacement rate: 0.0003mm.min^{-1}

b) Material: M2 Test conditions: Air Displacement rate: 0.0003mm.min^{-1}

Figure 6.22 (continued): Fracture faces of a) M1 and b) M2 specimens tested in air. All the samples are EDM notched.

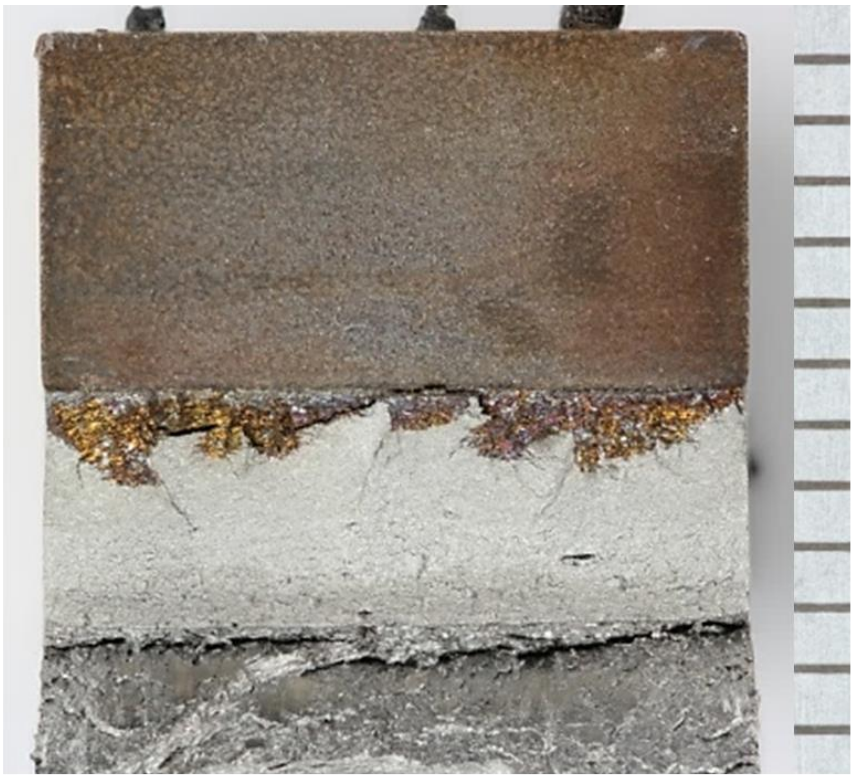

c) Material: M1 Test conditions: CP Displacement rate: $0.0003mm.min^{-1}$

d) Material: M2 Test conditions: CP Displacement rate: $0.0003mm.min^{-1}$

Figure 6.22: Fracture faces of c) M1 and d) M2 specimens tested under CP. All the samples are EDM notched.

a) Material: M1 PC: N/A; T: Air Displacement rate: 0.0003mm.min^{-1}

b) Material: M2 PC: N/A; T: Air Displacement rate: 0.0003mm.min^{-1}

Figure 6.23 (continued): Fracture faces of a) M1 and b) M2 specimens tested in air. All the samples are FPC notched.

c) Material: M1 PC: 72hours; T: CP Displacement rate: 0.0003mm.min^{-1}

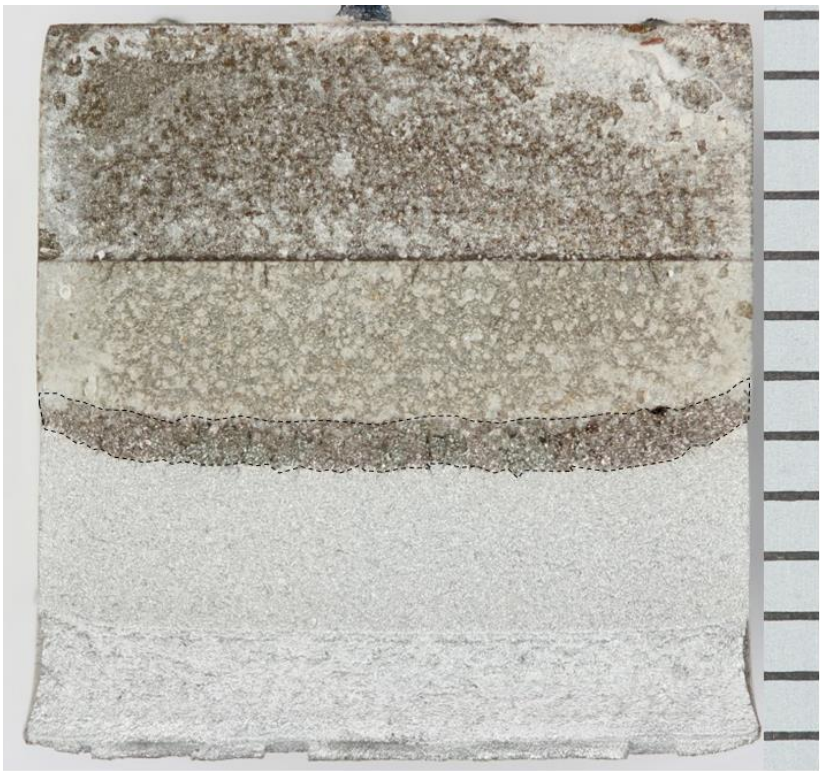

d) Material: M2 PC: 72hours; T: CP Displacement rate: 0.0003mm.min^{-1}

Figure 6.23: Fracture faces of c) M1 and d) M2 specimens tested under CP. All the samples are FPC notched.

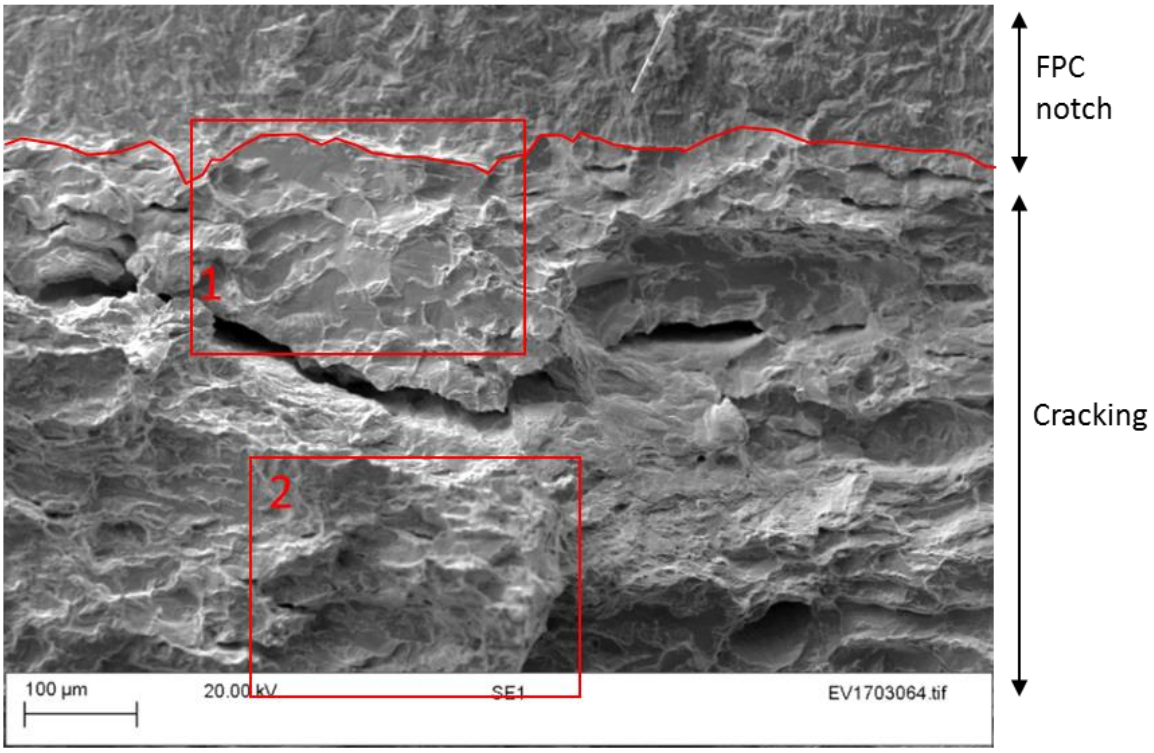

a)

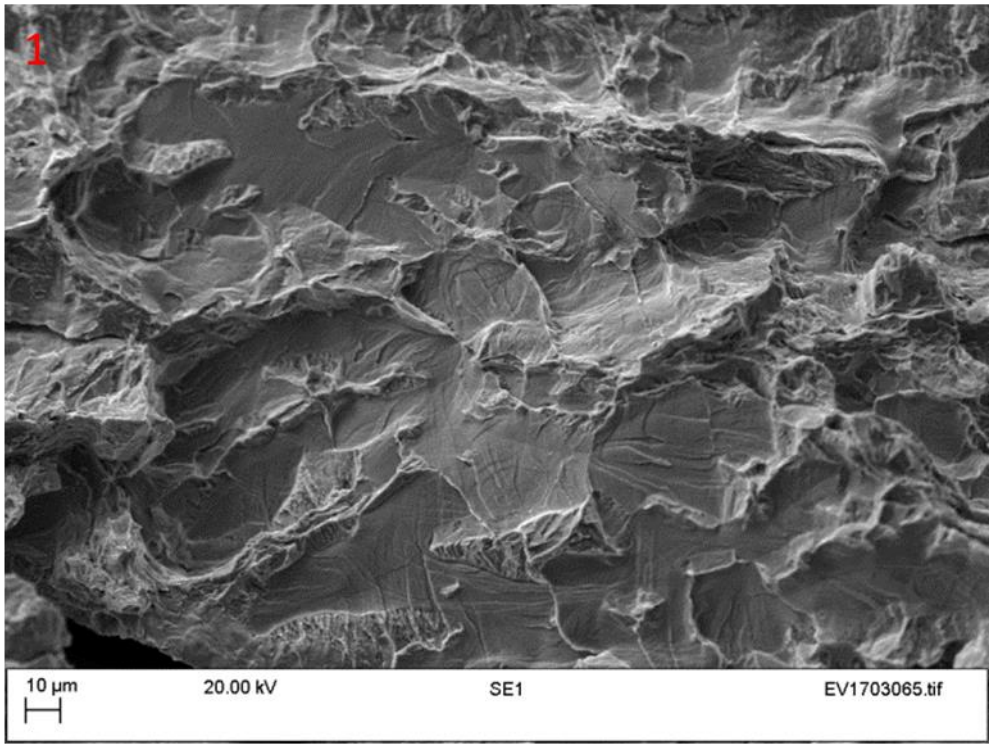

b)

Figure 6.24 (Continued): SEM images of the fracture face of M1 FPC-notched specimen tested in air, a) taken along the transition from the FPC notch to the crack developed during testing b) magnification of an area of a).

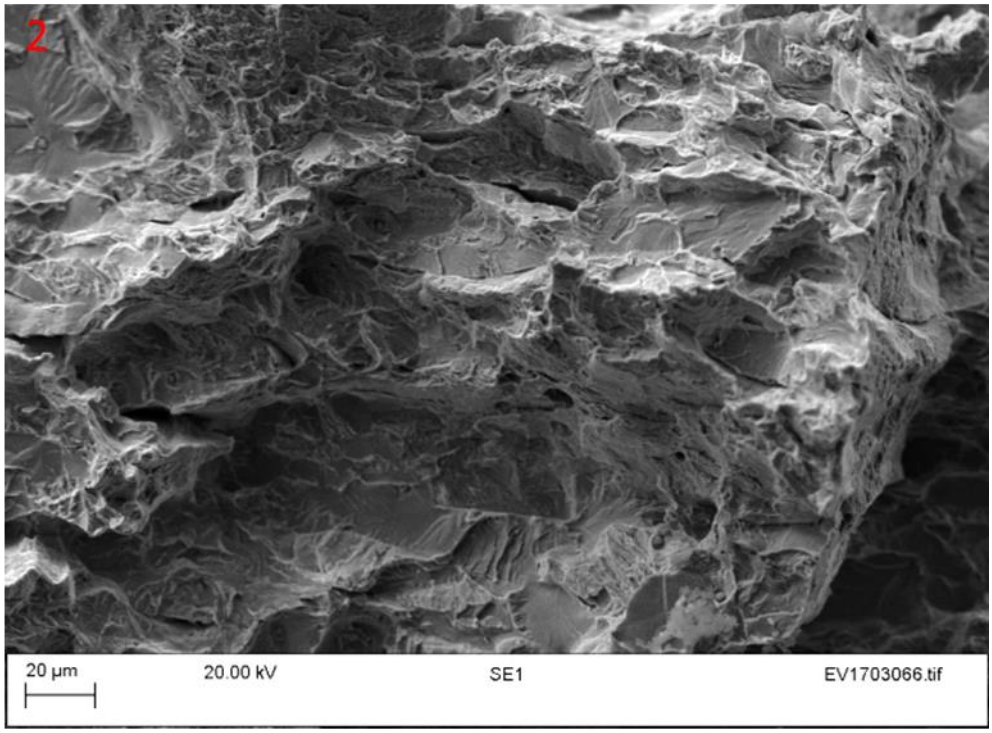

c)

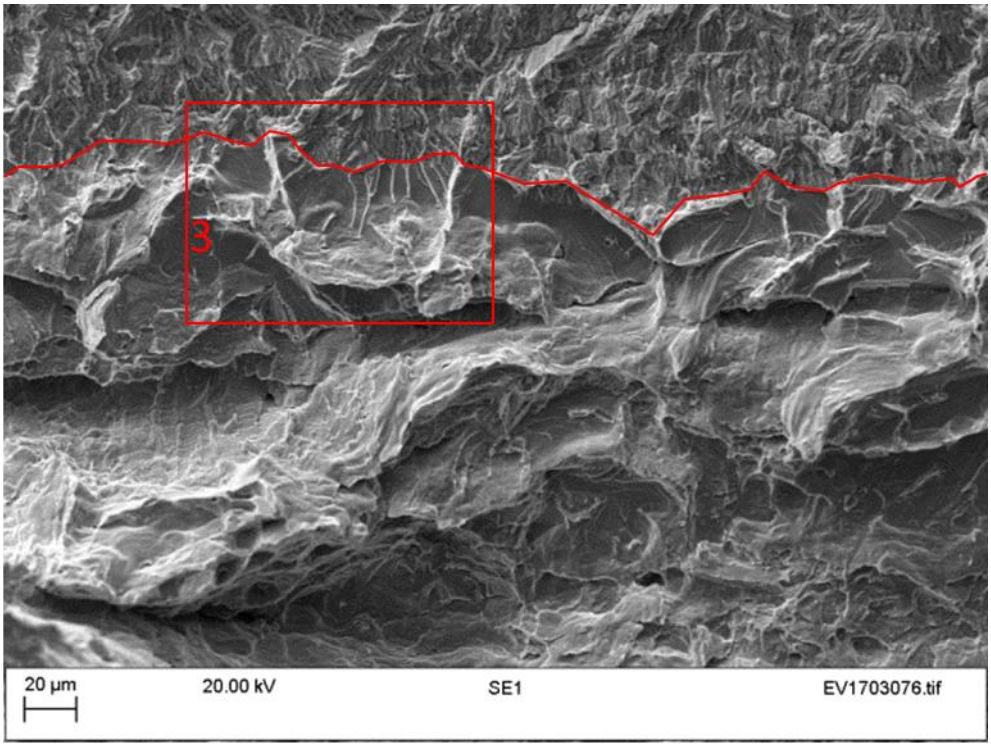

d)

Figure 6.24 (Continued): SEM images of the fracture face of the FPC-notched specimen M1 tested in air, c) magnification from a); d) taken in a different locations along the transition from the FPC notch to the crack developed during testing.

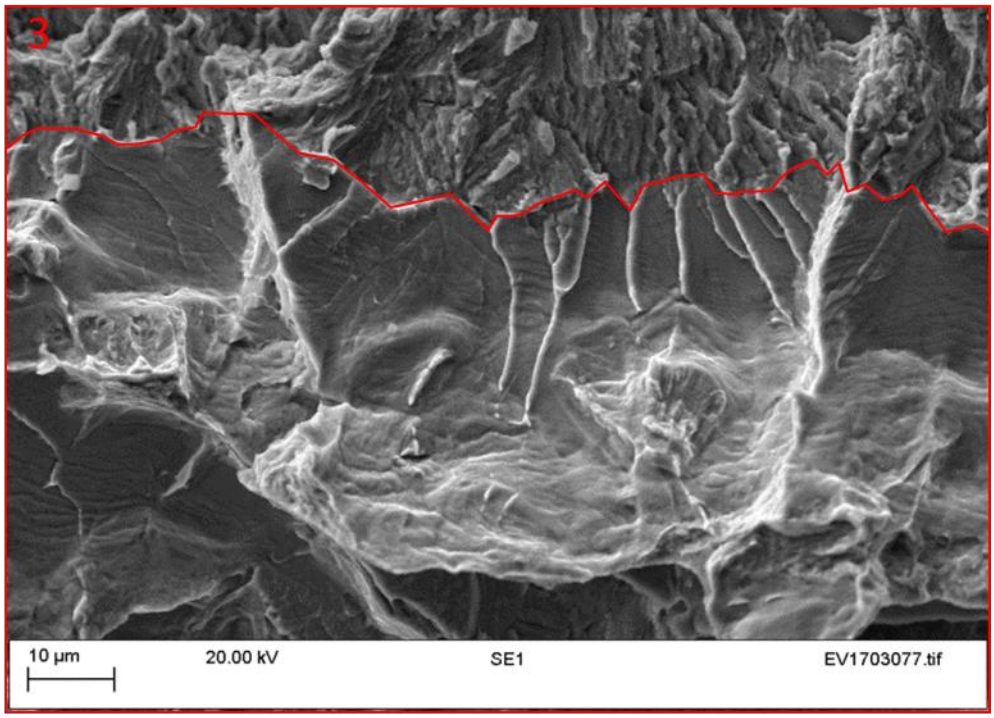

e)

Figure 6.24: SEM images of the fracture face of the FPC-notched specimen M1 tested in air, e) magnification of d).

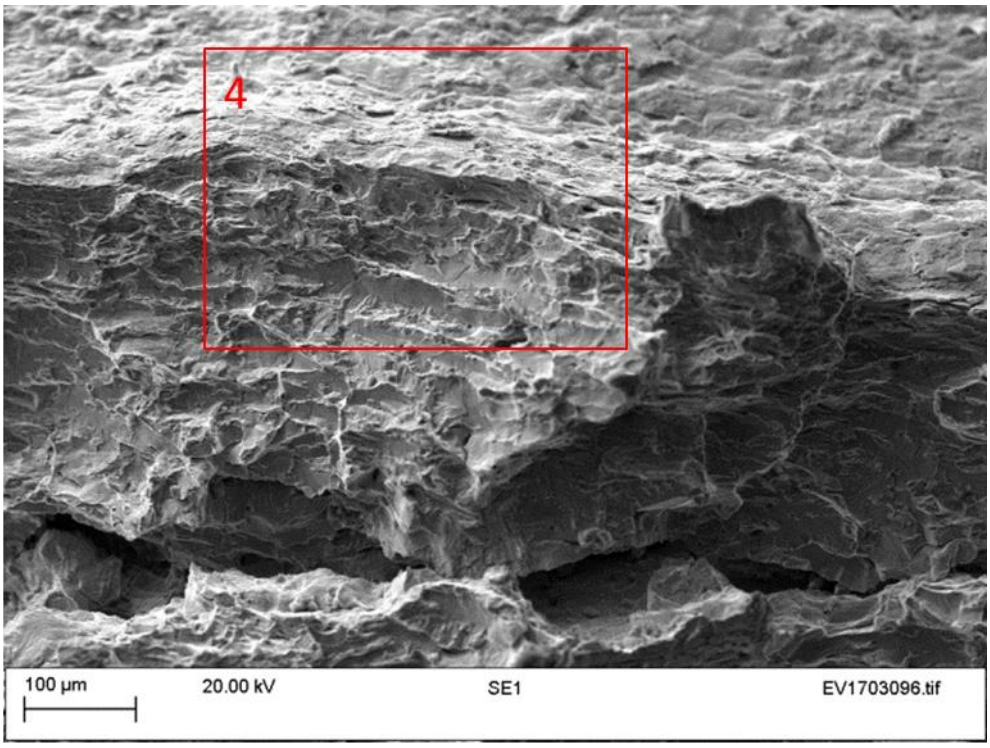

a)

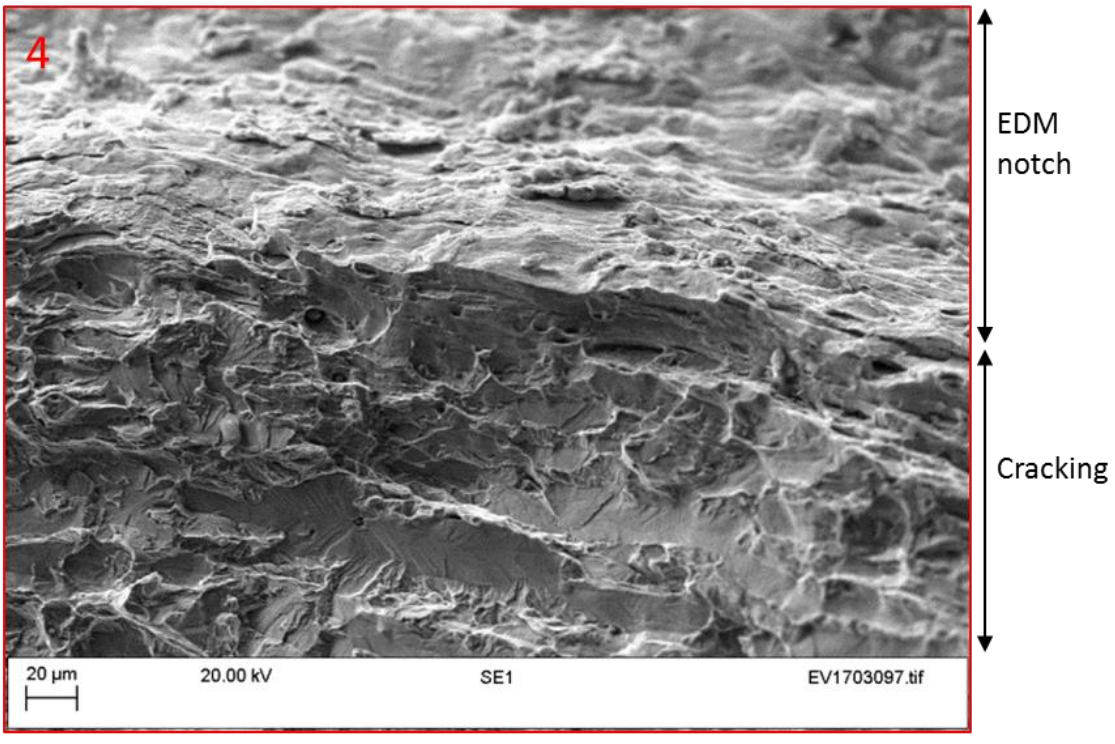

b)

Figure 6.25: a) SEM images of the fracture face of the EDM-notched specimen M1, tested in air, b) is a magnification of a). Cleavage of the ferrite and tearing of the austenite were observed.

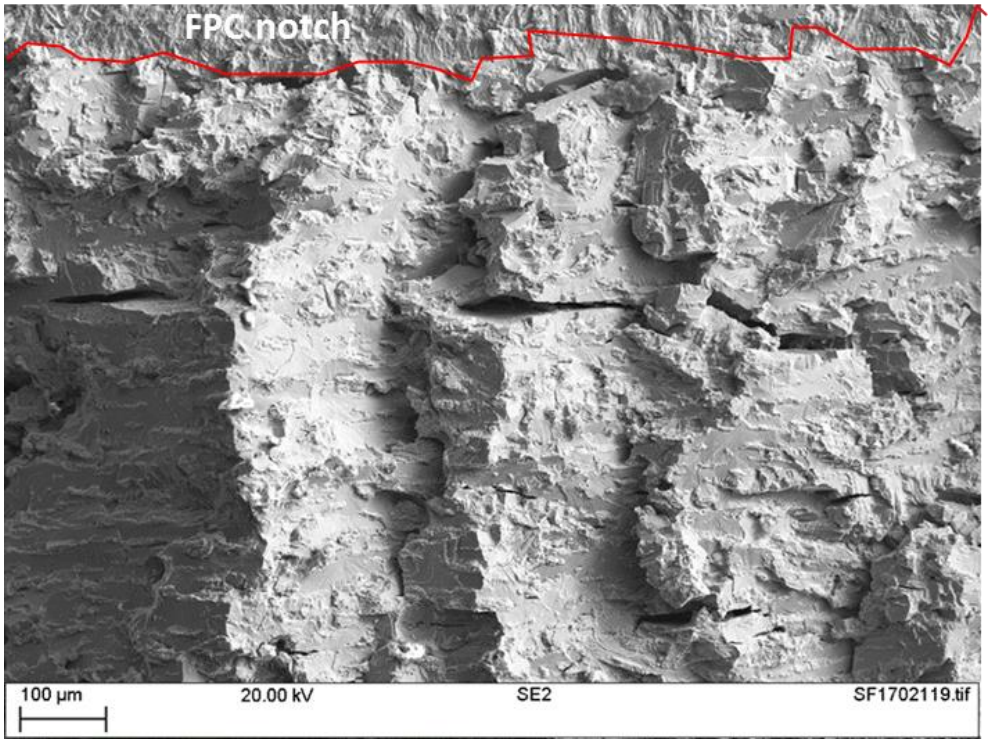

Figure 6.26: SEM micrograph of the crack extension, ahead of the FPC notch in the M1 specimen tested under CP.

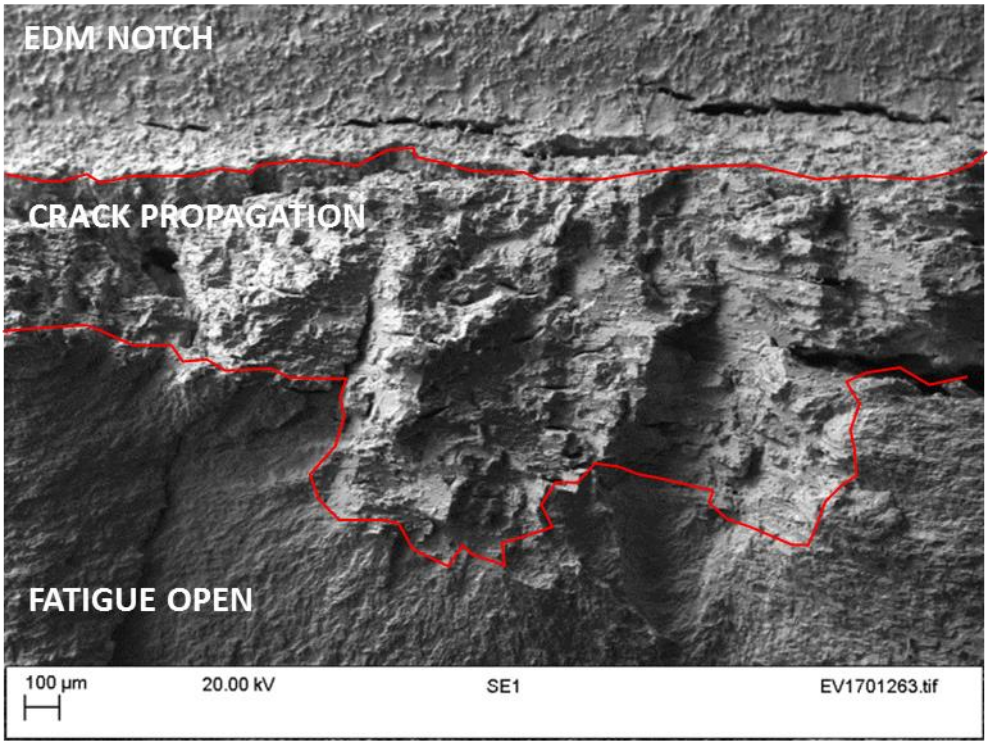

a)

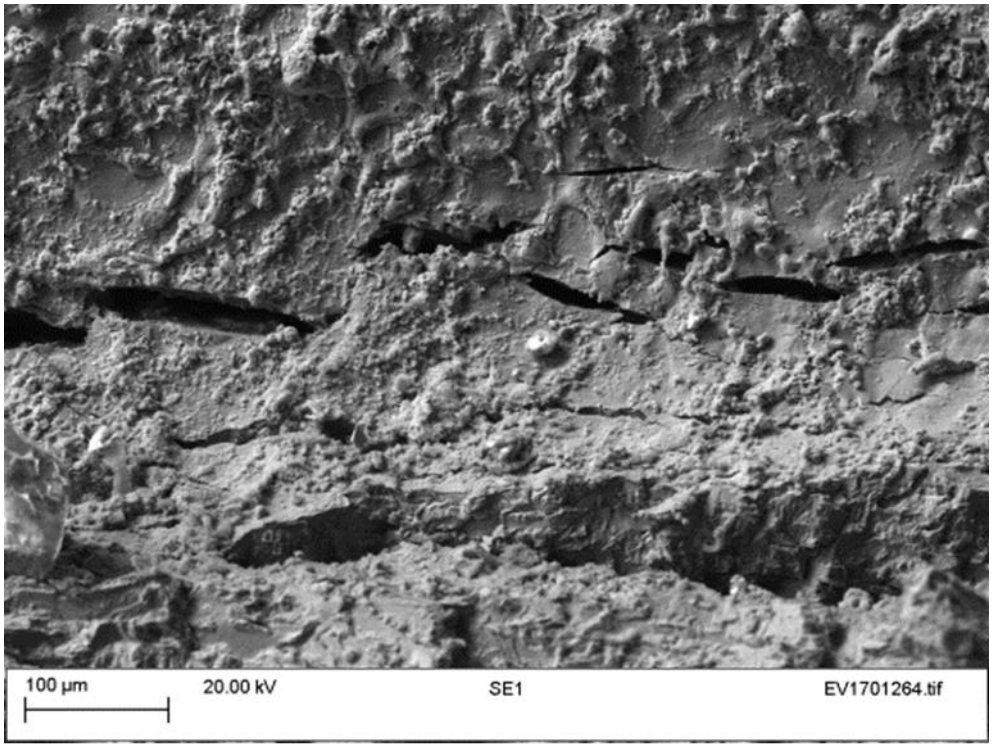

b)

Figure 6.27: SEM micrograph of the fracture face, adjacent to the EDM notch tip, of the M1 specimen tested under CP: a) general view of crack development and b) high magnification images showing multiple cracking across the notch curvature.

Regardless of the notch type used, it was apparent from the results that the interpretation of the data from the early stage of testing is not straight-forward. Moreover, using the approach, specified in some Standards, of assigning a J value at crack initiation, corresponding to 0.2 mm crack extension, does not seem to be relevant here. This is because, as can clearly be inferred by the low, flat curves, HISC initiation values of fracture toughness, even lower than those currently reported at 0.2 mm of crack extension have been experienced with hydrogen-charging environments. This means that once the conditions for HISC initiation are met, a very small load would be required to extend a crack which pre-existed or has already initiated. This highlights the importance of not allowing any crack to be present (from fabrication, installation and commissioning etc., as also stated in DNV RP F112 [79]) or to initiate (ahead of becoming exposed to the environment), and also being able to evaluate resistance to cracking more comprehensively, using method(s) capable of predicting and evaluating conditions required for initiation. Difficulties with obtaining meaningful data from environmental tests and establishing relationships between the observed fracture morphologies of broken specimens and measured toughness values have been reported elsewhere [222]. The difficulties with capturing crack initiation are inherent to test methodologies typically employed which were originally developed for testing ductile materials in air and mainly to provide inputs for ECA.

Whilst it is highly desirable to use such standard fracture toughness test methods (yielding J/CTOD data from fatigue pre-cracked specimens) for determining maximum tolerable flaw sizes in embrittling environments, experience from failure investigations and other environmental testing implies that once a ‘very small’ surface-breaking crack (or a buried flaw which has interacted with hydrogen) is present, the local stress concentration in combination with a locally enhanced hydrogen level can cause the crack to propagate. Thus, the suitability of testing which is employed for conventional fracture assessments, using specimens with a pre-existing crack, i.e. a fatigue pre-crack, is called into question when the requirement is to study and capture crack initiation, which is thought to be a vital aspect of the failures encountered.

One main reason for eliminating the fatigue pre-crack in the test specimens discussed above was to study the effect of notch geometry, and whether the test method sensitivity is sufficient to capture this. Whilst Standard methods such as that used in this

investigation, could serve as a screening method to give a feel for general resistance-to-cracking behaviour of a given material with high susceptibility to hydrogen embrittlement, e.g. (S)DSS, steel-to-nickel dissimilar metal welds (DMWs), etc., further work is required, to develop quantitative test methods which could focus on capturing crack initiation from material's surface rather than a pre-existing crack.

In the light of these results, it is apparent that in the presence of a crack in an embrittled DSS, only a small amount of energy would be required to result in a considerable crack extension. Therefore, one major approach towards assessing environmental cracking could be benefiting from methods such as sustained-load testing, in which it is attempted to determine threshold values (for instance, in terms of cracking driving force) below which no environmental cracking is encountered.

6.3.4 The influence of environment

Following the investigation of specimen notch geometry, specimens with an EDM notch were adopted to study the effects of environment and its relationship with the microstructure, as this would provide further data and insight into the early stage of testing, i.e. crack initiation.

Figure 6.28 compares the crack extension curves obtained for M1 and M2 tested in air and under CP. The general appearance of the fracture faces of the tested specimens, Figure 6.22 c) and d), were shown with the high-magnification SEM micrographs from both materials, revealing the details of cracking under CP, shown in Figure 6.29.

The EDM notched specimens from M1 and M2, showed a very similar behaviour in response to testing in air, up to a Δa of ~ 0.1 mm, as the initial part of their curves almost overlapped. However, their performances were different in terms of crack propagation, i.e. $\Delta a > 0.1$ mm. It was apparent from the air curves and their corresponding fracture surfaces that there was significantly higher resistance to cracking (initiation from an EDM notch) in M2, with a HIPed microstructure, compared to that in M1, with a wrought microstructure.

Fractography of the specimens tested under CP (Figure 6.29) showed a higher degree of cleavage facets and secondary cracking via HISC in M1, compared to that in M2. This qualitative observation was consistent with the test data from testing in air and under

CP, in which M2 showed a better performance in terms of resistance to crack propagation. This is thought to be a twofold effect of the microstructural differences between the two alloys: the coarse, banded microstructure in M1 allows faster hydrogen transport, and also introduces larger, weak, austenite-free paths for brittle, macro-scale, secondary cracking to occur in the notch plane. The superior mechanical properties and resistance to cracking of HIPed microstructures, compared to other DSS microstructures, has been demonstrated in air [223], [224], as well as under CP [105], [104], [129].

Figure 6.30 and Figure 6.31 are macrographs of the side views of the cracks developed in the M1 and M2 specimens, tested in air and in CP. The side views confirmed the ductile behaviour of DSSs tested in air with large deformation observed at the bottom of the EDM notches. For M1, this was characterised by a flattening of the austenite and ferrite and the HIPed material exhibited deformation and elongation of the equiaxed grains close to the notch. In the case of the specimens tested in CP, no deformation was observed but rather secondary cracks perpendicular to the main crack direction. For the specimen extracted from M1, two long secondary cracks were observed propagating through the ferrite phase and parallel to the austenite crack, characteristic of secondary HISC cracking. One of the cracks was located at the EDM notch and the second one was further away from the notch tip. In M2 however, only small secondary cracks were present and homogeneously distributed at the bottom of the EDM notch.

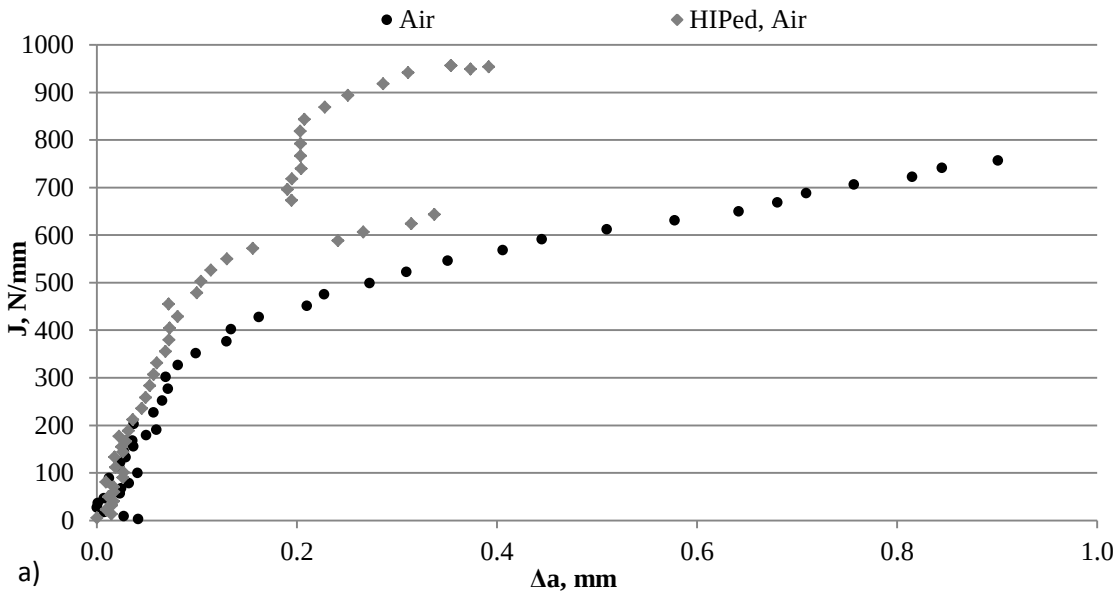

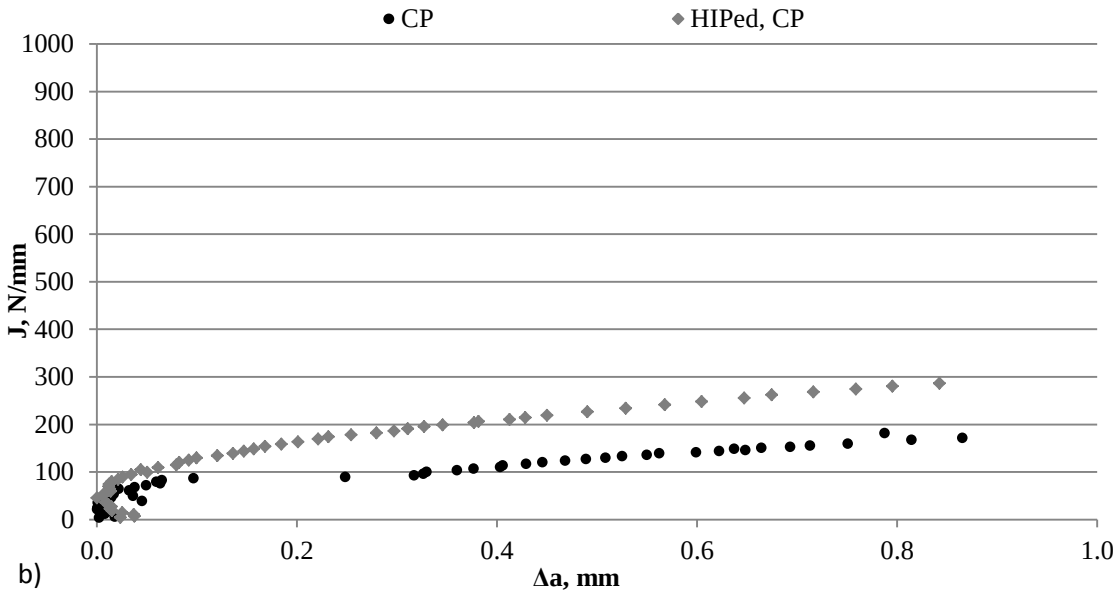

Figure 6.28: Comparison of the J resistance curves in air and in CP environment for a) M1 and b) M2, tested at 0.0003 mm.min^{-1} displacement rate.

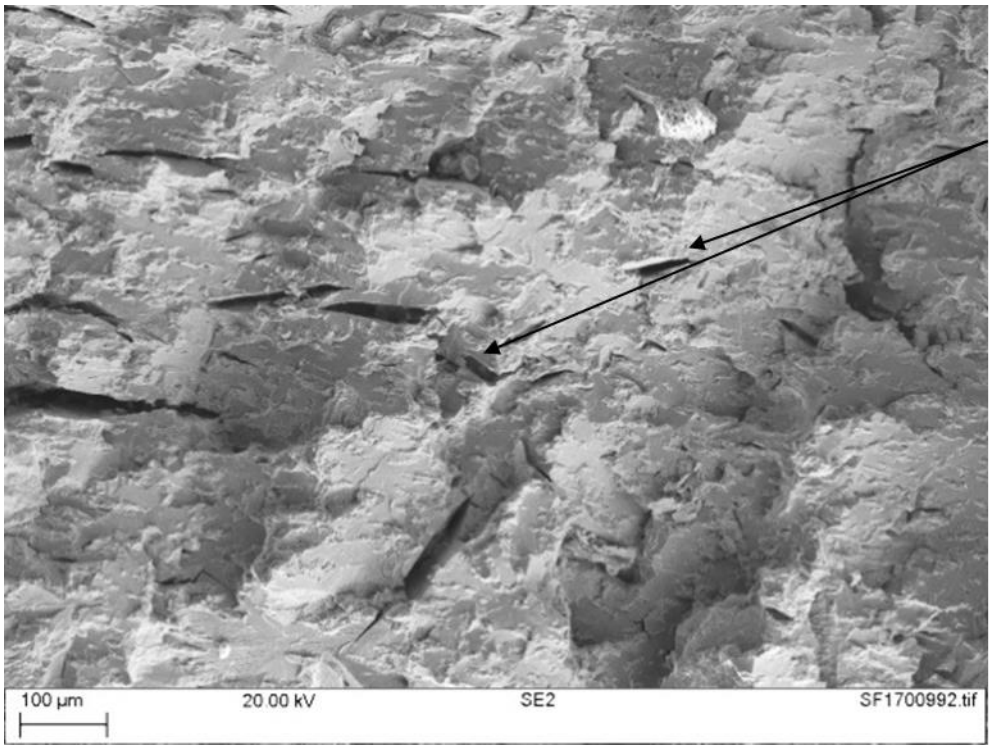

a)

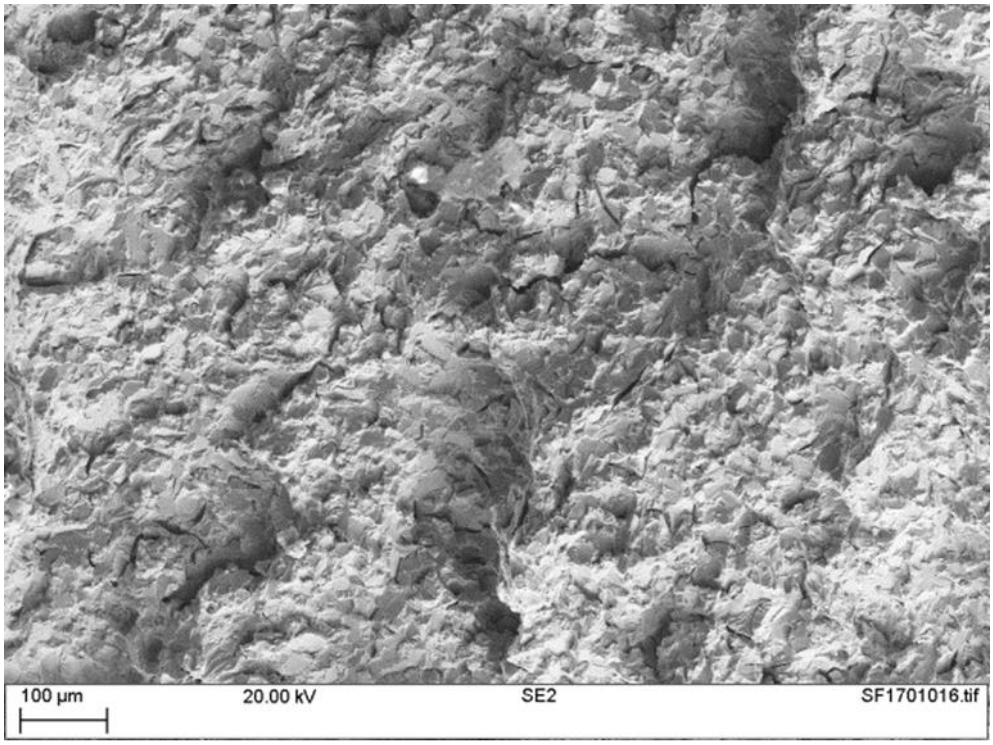

b)

Figure 6.29 (continued): SEM images of fracture faces of a) specimens extracted from M1 and b) specimens extracted from M2 and tested under CP.

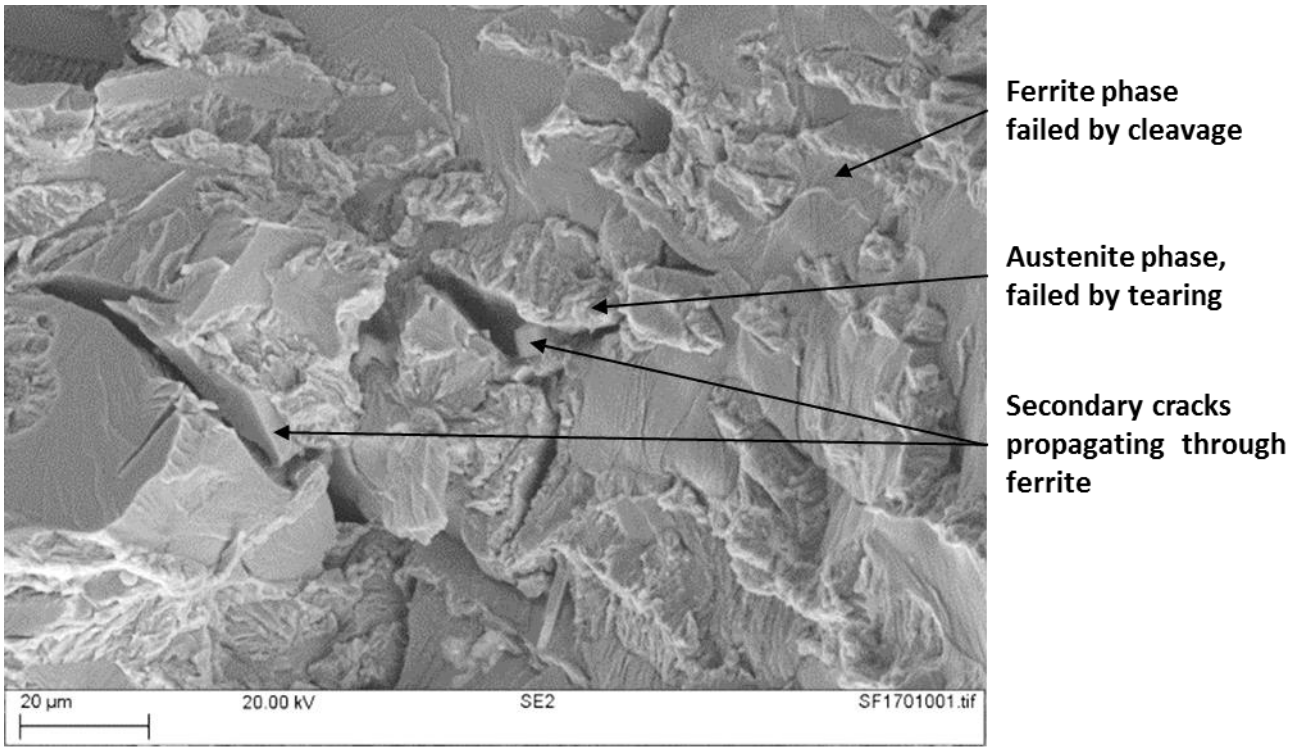

c)

d)

Figure 6.29: SEM images of fracture faces of c) specimens extracted from M1 and d) specimens extracted from M2 and tested under CP.

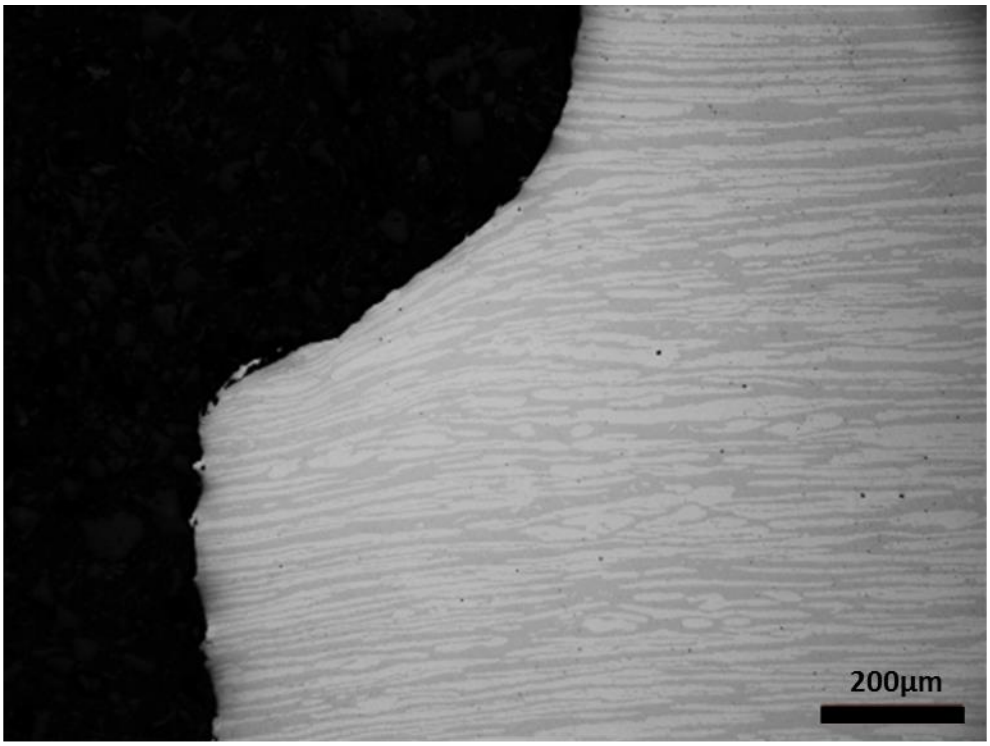

a) Material: M1 Test conditions: Air View: Specimen side

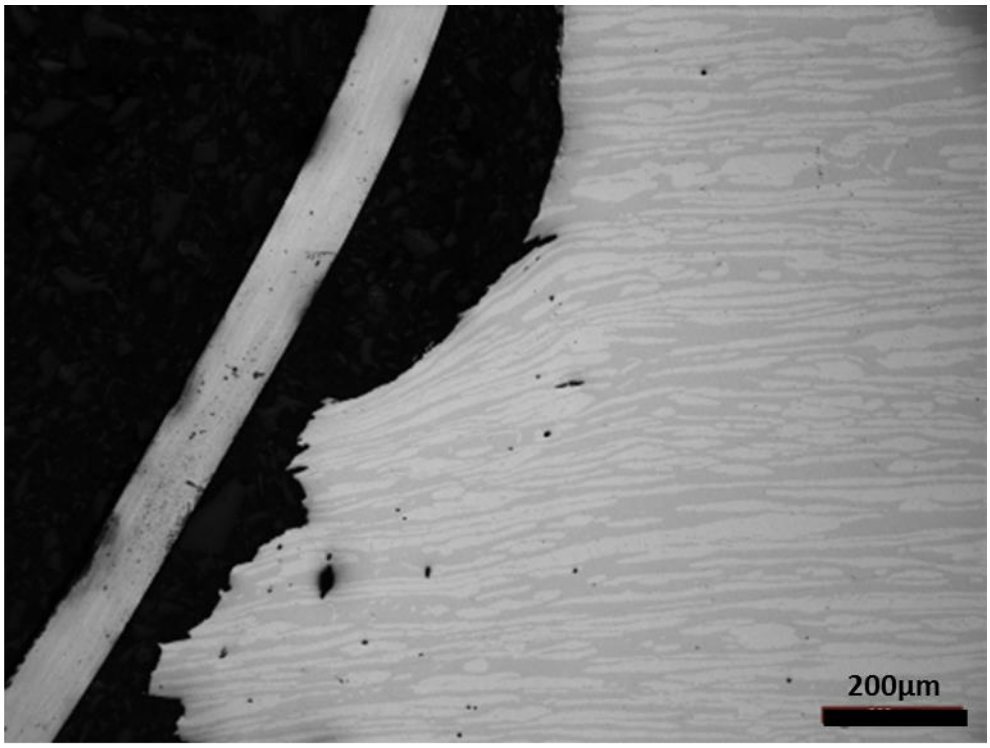

b) Material: M1 Test conditions: Air View: Centre of the specimen

Figure 6.30 (continued): Side views of the a) side and b) centre of the specimen extracted from M1 and tested in air.

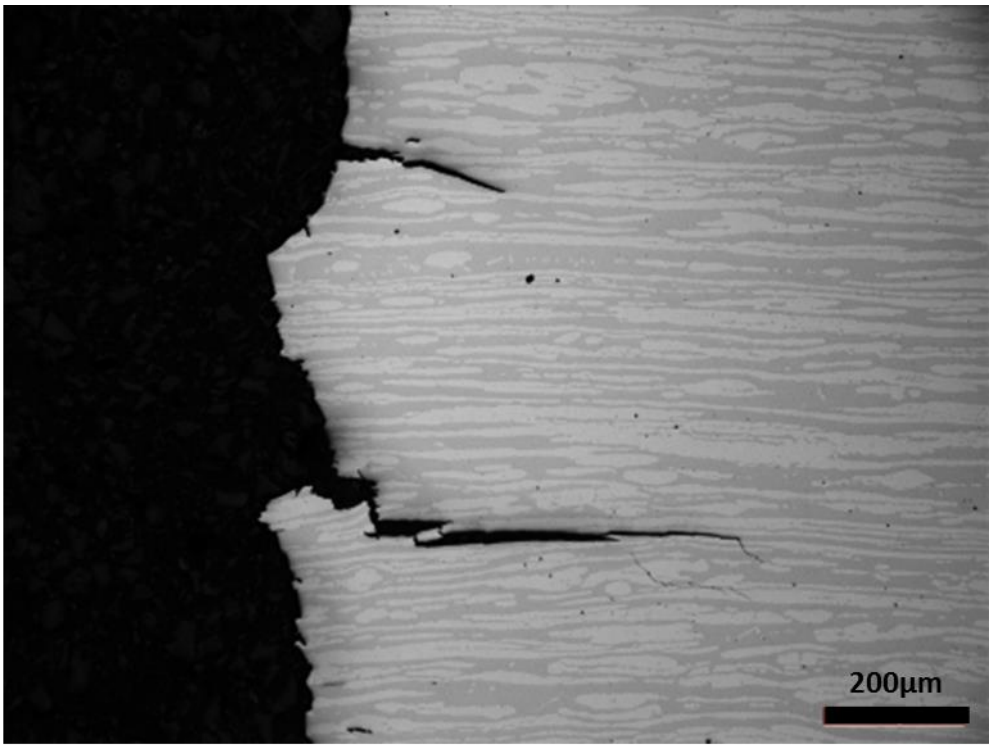

Figure 6.30: Side view of the specimens extracted from M1 and tested c) under CP.

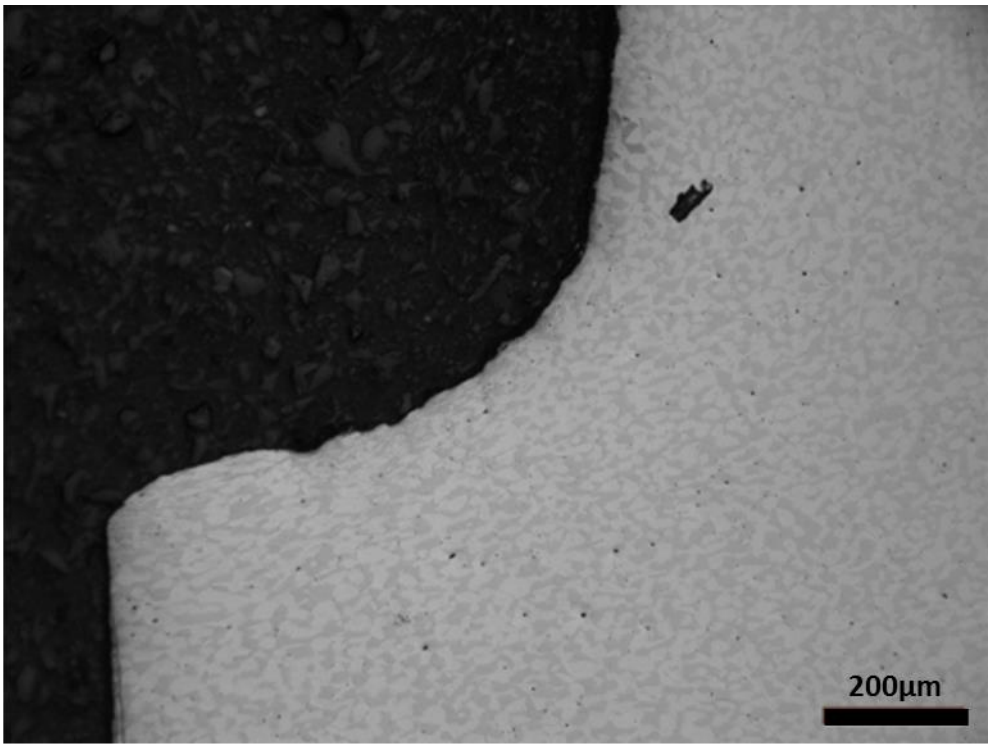

a) Material: M2 Test conditions: Air View: Specimen side

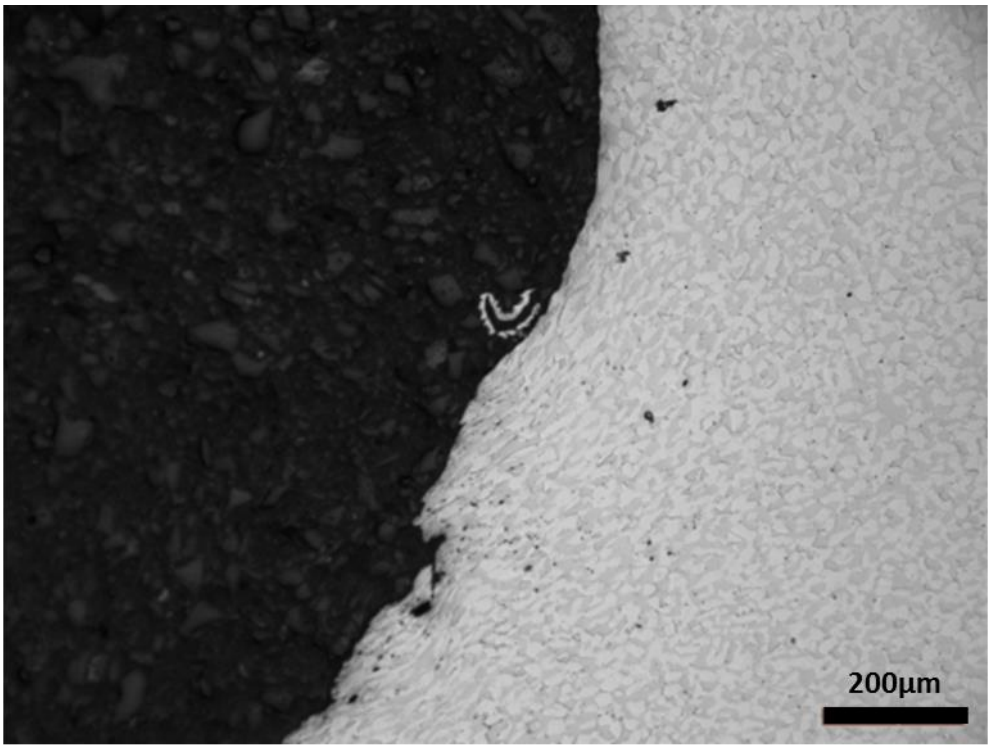

b) Material: M2 Test conditions: Air View: Centre of the specimen

Figure 6.31 (continued): Side views of the a) side and b) centre of the specimen extracted from M2 and tested in air.

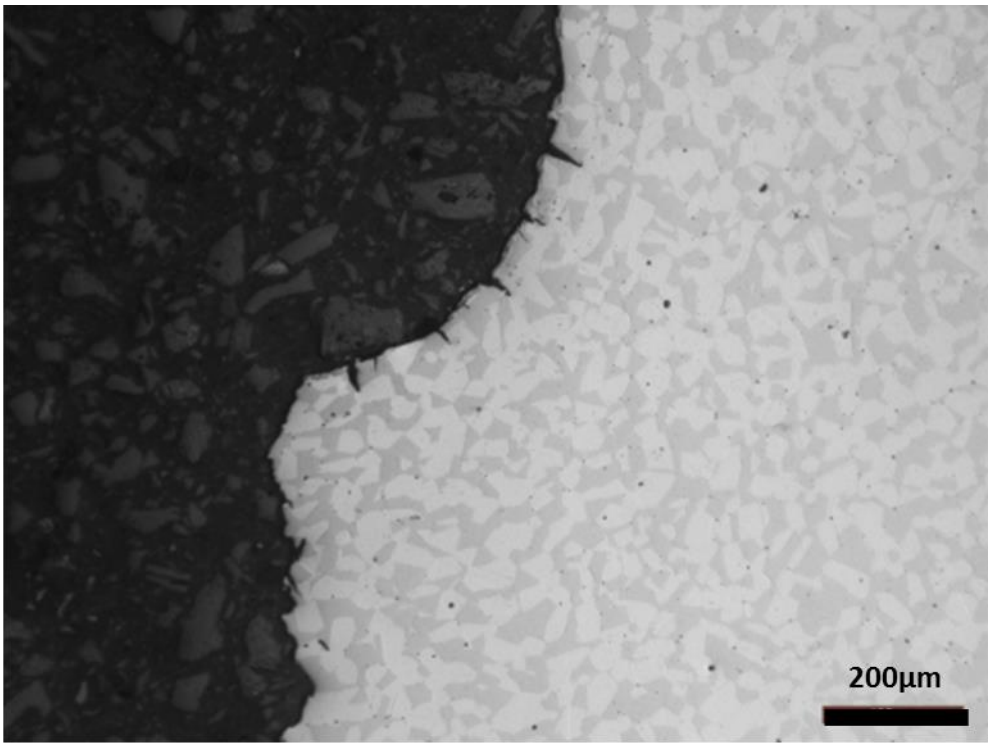

Figure 6.31: Side views of the specimens extracted from M2 and tested c) under CP.

Several studies have established the role of the austenite phase and its spacing (the width of the austenite islands along a given direction, which is often taken to be parallel to the expected cracking direction) in hindering HISC propagation [73], [225], [117], and have attributed the better performance HIPed DSS microstructures due to having a smaller austenite grain size. As a result industrial guidelines [79] put forward an austenite spacing threshold, below which the microstructure would be deemed unsusceptible to HISC.

In the case of the two materials tested and compared here, it was noticed that, despite of the having a austenite spacing/grain size of ~10 µm for both the M1 and M2, along the plan on which cracking occurred by testing, different resistant to cracking behaviours were observed. Unfavourable, secondary cracking through the notch plane, i.e. delamination effect along the ferrite-austenite layers, was much more noticeable in M1, rather than M2. Moreover, this demonstrates that DSSs with similar austenite spacing can exhibit different HISC cracking morphology, depending on the morphology of

microstructure and 'connectivity' of ferrite phase and its role on accelerating hydrogen transport to the crack tip.

This highlights the limitation of two-dimensional material characterisation methods, e.g. merely based on materials' austenite spacing in the TD (as shown in Chapter 3 on material characterisation), on establishing suitable criteria for designing (S)DSS components against HISC.

The fractographic evidences shown Figure 6.23, also revealed a significant difference, with respect to the crack front shape in the M1 and M2 specimens (with a more pronounced effect in the specimens tested under CP, than those tested in air), and regardless of the notch type. As opposed to the uniform crack front developed in M2, the M1 specimen yielded a wavy, uneven crack front. High magnification fractography and mapping the fracture morphologies associated with the two phases, confirmed that this was directly associated with the materials' microstructures and was a function of the size and distribution of ferrite. This is of particular importance, as could lead to further inaccuracy of the measurement of the crack advancement, using the 9-point method which has been specified [162], and could potentially have an influence on the test validity and results.

6.4 Conclusion

An environmental testing programme based on fracture toughness was developed to generate data and compare the resistance-to-HISC of two fundamentally different DSS microstructures and investigate the influence of the testing parameters.

The data generated show that (S)DSSs can be susceptible to hydrogen embrittlement via HISC, even in air, when sufficiently slow displacement rates are applied. It is thought that this could be caused by the residual bulk hydrogen content from alloy manufacturing, which can subsequently be transported to highly stressed/strained regions located adjacent to a crack tip and cause local embrittlement.

DSS SENB specimens tested at slow loading rates, in a simulated seawater environment under cathodic protection, experienced hydrogen embrittlement via HISC, leading to a significant decrease of measured fracture toughness values.

The comparison between the two DSS microstructures demonstrated that the hot isostatically pressed material had a superior resistance to crack growth than the conventional wrought manufactured material. These results together with the fracture morphology and side views of the crack, have showed that austenite spacing:

a) is not thought to be the sole microstructural factor determining the resistance-to-HISC of (S)DSSs;
b) is only relevant to (S)DSSs with a distinct degree of directionality, i.e. wrought products, traditional forgings, etc.

The fraction, connectivity and morphology of the ferrite matrix are thought to be of key importance. Hence, the characterisation of (S)DSS microstructures in three dimensions should be assessed and characterised further to provide a better understanding into the role of microstructure in HISC.

Regarding the testing methodology, a comparison between the acquisition of the resistance curves using the BS7448 – Part 4, ASTM E1820-15a, and ISO 12135 standards was made and the use of the ISO 12135 was consider to be most suitable for the materials investigated here. The application of a slower displacement rate than the one recommended by the standards decreased the cracking resistance of the wrought material, highlighting the non-conservatism of the methodology and the need to define a testing method according to the service conditions in order to qualify a material.

The influence of the notch geometry was also investigated and it was demonstrated that FPC-notched, recommended by the standards, are not thought to be capable of evaluating resistance to cracking of (S)DSSs in hydrogen-charging environments: resistance-to-HISC is deemed to be primarily an initiation phenomenon: in effect, initiation has already taken place and cannot be captured, when FPC-SENB specimens are used.

In comparison, EDM-notched specimens, regardless of the test environment, have yielded higher toughness parameters than FPC-notched specimens. The use of such specimen geometry for unloading compliance tests was a useful method for ranking (S)DSSs in terms of crack growth in the early stage of the test but it did not provide any detailed information on quantifying crack initiation.

6.5 Recommendations and future work

The present results highlighted different paths that should be investigated in order to increase the understanding of HISC in DSSs.

In terms of microstructural features it was assumed that the connectivity of ferrite was responsible for hydrogen transport within DSS microstructures which could not be characterised using conventional 2D techniques. Currently, the most suitable method to map 3D microstructure of DSS is the use of phase contrast micro-tomography using X-ray synchrotron facilities. Specimens extracted from the HIPed and the wrought materials were characterised using Spring-8 facility in Japan, the data is under analysis and a paper on the result should be published in the coming year.

The assumption made on the different hydrogen behaviour within the two microstructures could be confirmed by permeation experiment using a Devanathan and Stachurski electrochemical cell.

Regarding the evaluation of the resistance-to-HISC of DSSs and qualifying those materials, there is a need to developed understanding on the initiation of HISC cracking. Fracture toughness testing has proved to be a powerful tool and hence, those methodologies have to be adapted in order to capture HISC initiation.

It is thought that a methodology involving sustained-load testing with monitoring of the crack advancement could be used to determine threshold values for HISC to initiate

Chapter 7.

SMALL-SCALE HISC TESTING; THE IMPACT AND INTERACTION OF TESTING AND RESIDUAL STRESSES

7.1 Introduction

This chapter investigates the influence of residual stresses induced by welding, and their interactions with stresses developed by HISC testing, on the resistance to HISC of a joint from a subsea component retrieved after 8 years of service. The assessment was carried out using neutron diffraction residual stress measurements and small-scale constant-load tensile testing of round plane-sided specimens, in a simulated seawater solution under cathodic protection. This investigation is the continuation of previous work carried out at TWI, and an attempt to address some unexpected observations made.

A joint programme of evaluating HISC performance of a number of SDSS subsea goosenecks, by TWI and BP was recently completed, with the major findings reported in [226]. As part of this comprehensive testing programme, resistance to HISC of the materials involved was determined, using constant-load tensile testing of a series of small-scale parent and cross-weld specimens, extracted from the upper pipe-to-hub joint of one of the gooseneck subsea components supplied.

The observations showed that the all-hub specimen exhibited an inferior resistance-to-HISC threshold of ~ 85 % of its actual yield strength, compared to the cross-weld and all-pipe specimens with a HISC threshold of $\geq$ ~ 100 % of the hub and pipe actual yield strength, respectively [226]. It could not be explained why the cross-weld

specimen, which encompassed some length of the hub material, did not show any evidence of HISC, when tested well above the hub HISC limit. Similar unexpected results had also been reported in a previous confidential programme of work carried out by TWI, where the superior performance of DSS and SDSS weldments, compared to that in the original parent materials, were observable. General microstructural characterisation of the pipe, hub and weld materials, and the tested specimens, using light and scanning electron microscopy, could not provide any further insight into the surprising observations made in those investigations.

A hypothetical explanation for this surprising behaviour could be the potential influence and interaction of any remaining compressive residual stresses (introduced by welding in the vicinity of a joint due to high local heating followed by rapid cooling [227]) in the small-scale test specimens used for the environmental testing programme. To explore this, the lower end pipe-to-flange joint of another S-shaped subsea components, retrieved from service after 12 years of operation, was investigated. The pipe was made of UNS S32760 SDSS and was connected by a matching girth weld to a UNS S32750 forged SDSS flange. The weld was made using the gas tungsten arc welding (GTAW) process.

The present work reports measurements of the residual stresses in the small-scale tensile specimens extracted from the weld and the parent materials, using the neutron diffraction technique. A discussion on the potential relationship between the HISC testing results and the residual stresses measured, with support from modelling of stress and strain distributions during loading, performed by the TWI's modelling team.

Prior to this study, the assessment of the residual stresses of this intact welded pipe-to-flange joint had been carried out in a different joint programme by TWI and BP [192], where extensive microstructural characterisation of the material was performed, with the results reproduced verbatim, in Chapter 4.

7.2 Experimental methods

7.2.1 Specimens extraction

A total of 12 rounds tensile specimens were extracted. Four specimens were extracted for each part of the component: across the weld and away from the weld in the pipe and flange materials. The specimen geometry is given in Figure 7.1. The average gauge length and diameter of the specimens was calculated from two and five measurements, respectively, using a travelling microscope. In the case of the cross-weld specimens, the weld centre-line was located at mid-length of the tensile gauge length and the samples were taken as close as possible from the cap of the weld, Figure 7.1.

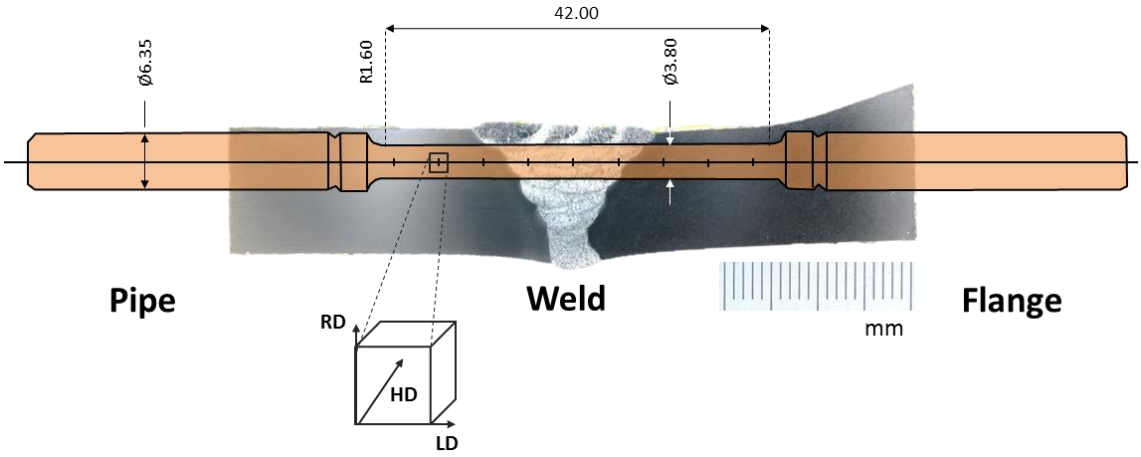

Figure 7.1: Geometry and dimensions (mm) of the tensile specimens with the location of the measurement points along the cross-weld tensile specimen in relation with the component.

7.2.2 Residual strain measurements

7.2.2.1 General methodology

The stress measurements were carried out on Engin-X beamline at ISIS, Rutherford Appleton Laboratory at Harwell, UK. The principle of the technique is presented in Chapter 3. In this experiment, taking into account the size of the specimen's diameter, a gauge volume of 2×2×2 mm was chosen. The instrument allowed the measurement of two strain directions at the time (e.g. radial and hoop). The setup of this configuration is given in Figure 7.2. The samples were then, rotated by 90° in order to perform the third direction measurement (e.g. longitudinal). Before the beginning of the experiment, the

beam was aligned and the instrument was calibrated using a stress-free sample made of powder.

The location of the nine measurement points distribute along the gauge length and equally spaced by 4.2 mm is given in Figure 7.1. From this scheme it can be seen that the two first and last measurement points in a cross-weld specimen fell in the parent materials, the three central measurement points fell in the weld metal, and the last two intermediate ones in the HAZ on the pipe and the flange side, respectively.

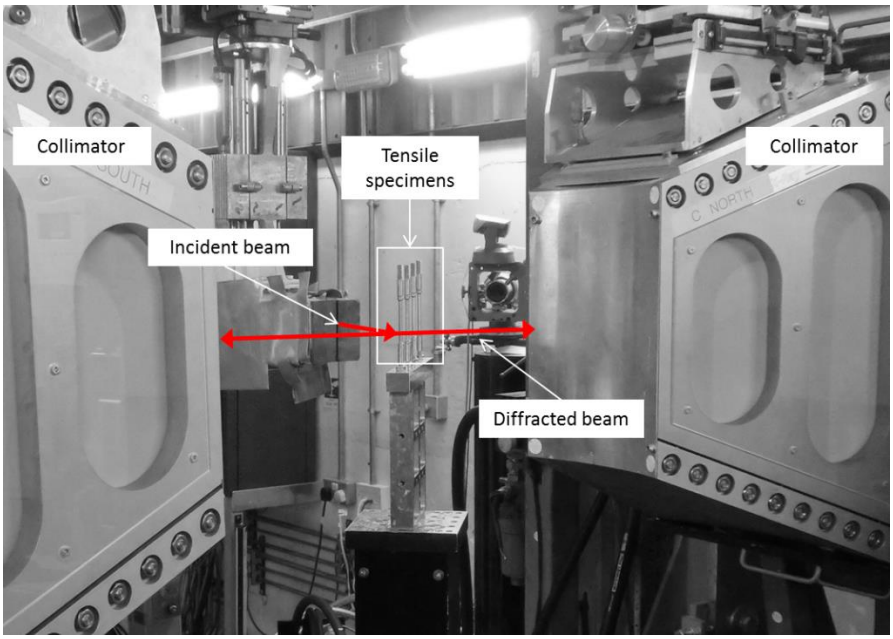

Figure 7.2: Photography of the Engin-X beam line set-up for neutron diffraction measurements in the hoop and radial directions of the tensile specimens.

7.2.2.2 Strain and stress calculation in a two phase alloy

The determination of the lattice parameters from the neutron diffraction time-of-flight spectrums was made by a modified Pawley template [183] allowing the distinction between fcc (austenite) and bcc (ferrite) lattice parameters in the generated time of flight spectrum, Figure 7.3. From those data, the relative strain along the gauge length was calculated for each phases, using the following equations:

$$\varepsilon_{hkl}^{\delta} = \frac{d_{hkl}^{\delta} - d_{hkl}^{\delta,0}}{d_{hkl}^{\delta,0}} \tag{29}$$

$$\varepsilon_{hkl}^{\gamma} = \frac{d_{hkl}^{\gamma} - d_{hkl}^{\gamma,0}}{d_{hkl}^{\gamma,0}} \tag{30}$$

Where, $\varepsilon_{hkl}^{\delta}$ and $\varepsilon_{hkl}^{\gamma}$ are the calculated strains; d_{hkl}^{δ} and d_{hkl}^{γ} are the lattice parameters; and $d_{hkl}^{\delta,0}$ and $d_{hkl}^{\gamma,0}$ are the stress-free lattice parameters in ferrite and austenite respectively. The determination of the stress-free lattice parameters was carried out using three cubes of 3.2×3.2×3.2 mm^3, which is the smallest volume that can accommodate the gauge volume of 2×2×2 mm^3, extracted from the weld and the parent materials.

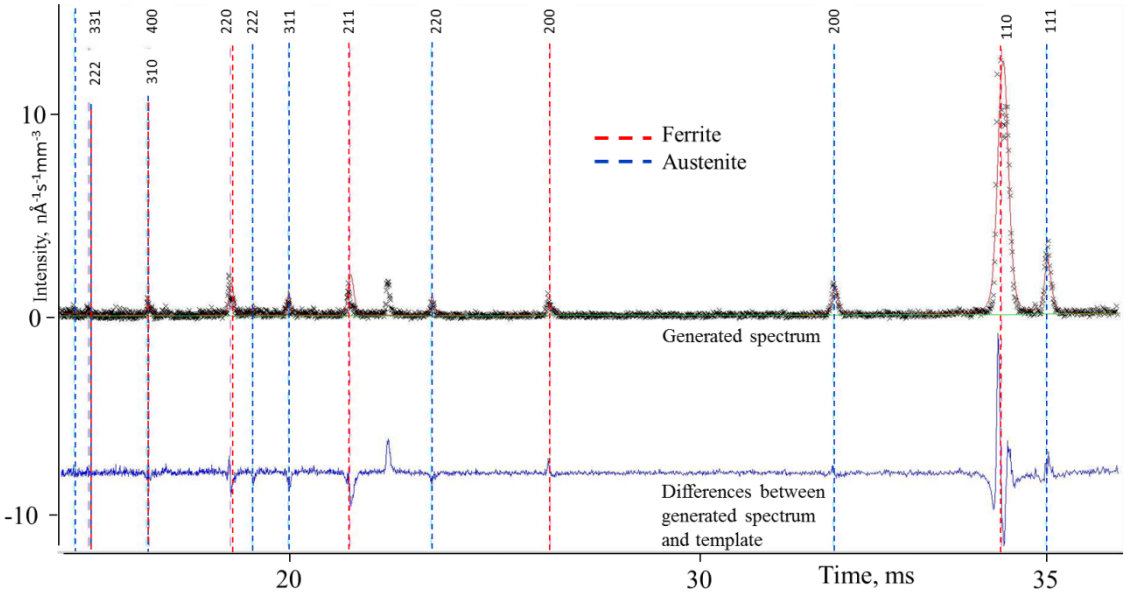

Figure 7.3: Example of a spectrum generated for one measurement point in the longitudinal direction. The magenta peaks are the ones related to the bcc phase and the blue ones are the one from the fcc phase.

The stresses in the three directions were calculated for each phase according to Hooke's law:

$$\sigma_i = \frac{E}{(1+\nu)(1-2\nu)}\left((1-v_f)\varepsilon_i + \nu(\varepsilon_j + \varepsilon_k)\right) \tag{31}$$

Where i,j and k, the three main directions.

The global stress was calculated using the measured ferrite fraction, v_f, given in Chapter 3, the average stresses within the material were calculated with the following formulae:

$$\sigma = \nu_f \sigma_\delta + (1 - \nu_f)\sigma_\gamma \quad (32)$$

The uncertainties, calculated according to the methodology developed in Chapter 3, were added to the resulting graphs.

7.2.3 Small-scale constant–load tensile testing

Constant-load tensile testing under CP was carried out to determine HISC thresholds of the cross-weld specimen and the parent materials. Figure 7.4 is a representation of the constant load set-up. The sample was screwed to the rod at the end of which, a determined load was suspended. The end of the rod was covered with a protective coating, to prevent it from corrosion. The sample was surrounded by PTFE vessels where a Pt counter electrode, a thermocouple and a salt bridge linked to an Ag/AgCl reference electrode were present. Once the sample was set up, a solution of 3.5 % NaCl cooled down to 4°C was circulated within the insulated vessel and potential of -1050 $mV_{Ag/AgCl}$ (-1100 mV_{SCE}) was applied. Those conditions aimed to replicate deep sea water environment. An extensometer was set up parallel to the sample to record its elongation during the test. After 3 days of hydrogen pre-charging, a constant load was applied to the specimen and left for 7 days in these conditions. The first load was 85 %$\sigma_{0.2\ \%}$ for the weld and the flange and 90 % $\sigma_{0.2\ \%}$ for the pipe material. Testing of the weld was performed using 0.2 % proof strength of the flange.

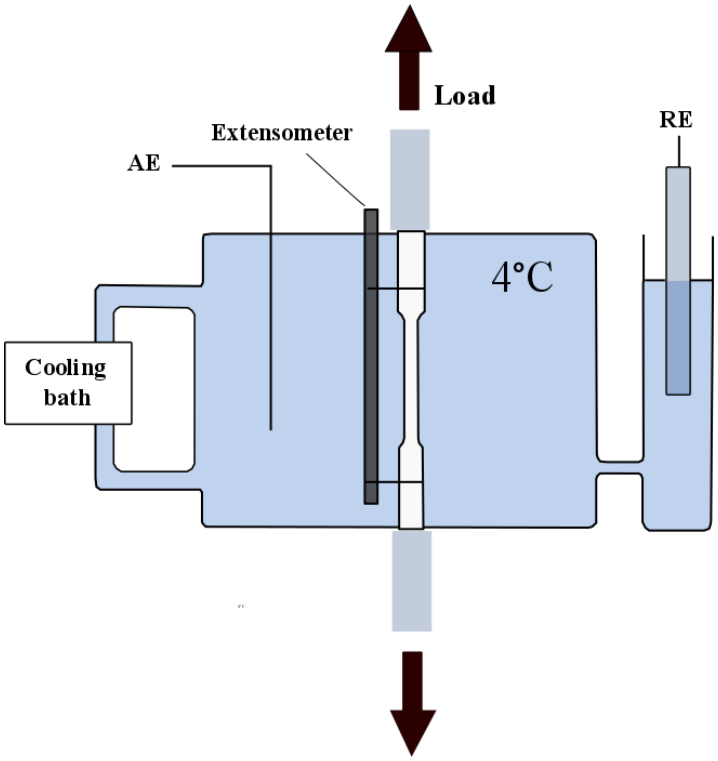

Figure 7.4: Set-up of the constant load test at 4°C in the insulated vessel.

After 10 days, the specimens were unloaded and cleaned in acetone; the average gauge length and diameter of the specimens were measured, following the same methodology described above. From these data, straining of the specimens was calculated in percent. The presence of HISC micro-cracks was first investigated by non-destructive techniques (NDT): liquid penetrant inspection (LPI) and SEM observation of the full circumference of the gauge length. If no micro-cracks were detected the gauge length was extracted and mounted into bakelite, ground to half thickness, metallographically prepared, and electrolitically etched in 40 %KOH solution to be inspected under light microscope. If no crack were detected, a new specimen, extracted from the sample material: pipe, flange or cross-weld, was tested with a load level incrementally higher by 5 %$\sigma_{0.2\ \%}$. This was repeated until cracking was identified or the applied load level exceeded 100 % of the 0.2 % proof stress of the material in question Four cross-weld specimens were used and three for the two parent materials.

7.2.4 Stress/strain distribution and residual stresses across the test specimen during HISC testing

7.2.4.1 Model development

The modelling part was generated and analysed with the commercial finite element analysis software Abaqus from Dassault Systèmes Simulia. A three-dimensional model of the round-bar tensile specimen geometry was generated and meshed densely with linear, hexahedral, reduced integration elements (type C3D8R in Abaqus) with a characteristic element size of 0.25 mm. The finite element mesh is shown in Figure 7.5.

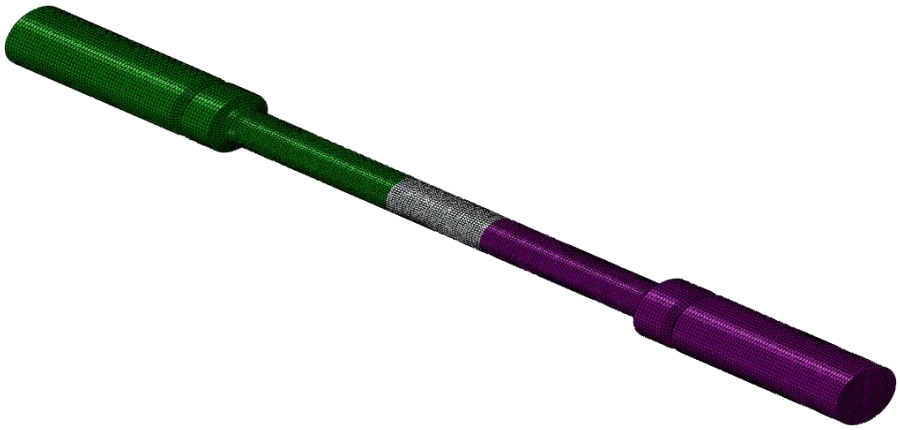

Figure 7.5: Finite element mesh for the round bar tensile models.

Three different models were analysed, with each model representing the different material configurations tested. One model comprised only flange material; one model comprised only pipe material; and the third model represented a cross-weld specimen with flange, weld and pipe metal properties in their respective regions (see Figure 7.5). Representative stress-strain curves for the flange and pipe material at 4°C, reported in Chapter 4, Table 4.9, were sampled at uniformly spaced points and converted to true stress and true plastic strain for the finite element model. In the absence of all weld metal tensile test results, the weld metal was assumed to have a stress-strain curve equal to the average of the flange and pipe metal curves. A rate-independent plasticity model with the von Mises yield criterion and associated flow rule was used to represent the inelastic constitutive behaviour of the material regions.

The analysis of each model comprised two different steps:

1. Introduce the measured residual stresses.
2. Apply an incremental axial displacement, generating a maximum nominal axial strain of 0.2 %.

To introduce the residual stresses as measured from neutron diffraction experiments, the eigenstrain method was used. Details about the specific implementation and background theory for using eigenstrains to reconstruct residual stress fields are described by Salvati et al. [228]. Effectively, the measured residual strains are treated as thermal strains. To do this, anisotropic thermal expansion coefficients were defined to vary spatially with the magnitude of thermal expansion equal to the measured residual strain. This was achieved by using an internal state variable in Abaqus and allowing the fully anisotropic thermal expansion coefficients to depend on three different internal state variables. During the first analysis step, the temperature in the model was increased by one degree. Thermo-elasticity requires that $\varepsilon = \alpha\Delta T$ and therefore by changing the model temperature by unity, the residual strains were automatically enforced. However, it should be noted that as the simulation employed an implicit solver, equilibrium needed to be satisfied and therefore some deviation from the as-measured residual strain field was observed in the model. Nevertheless, the results were sufficiently close for the purposes of this numerical study. The residual stresses induced for the cross-weld specimen are shown in Figure 7.6. Note that the volume averaged residual strains were induced as the simulation was undertaken on the continuum scale. Other residual stress and strain fields were introduced for the flange and pipe measurements with the same level of accuracy.

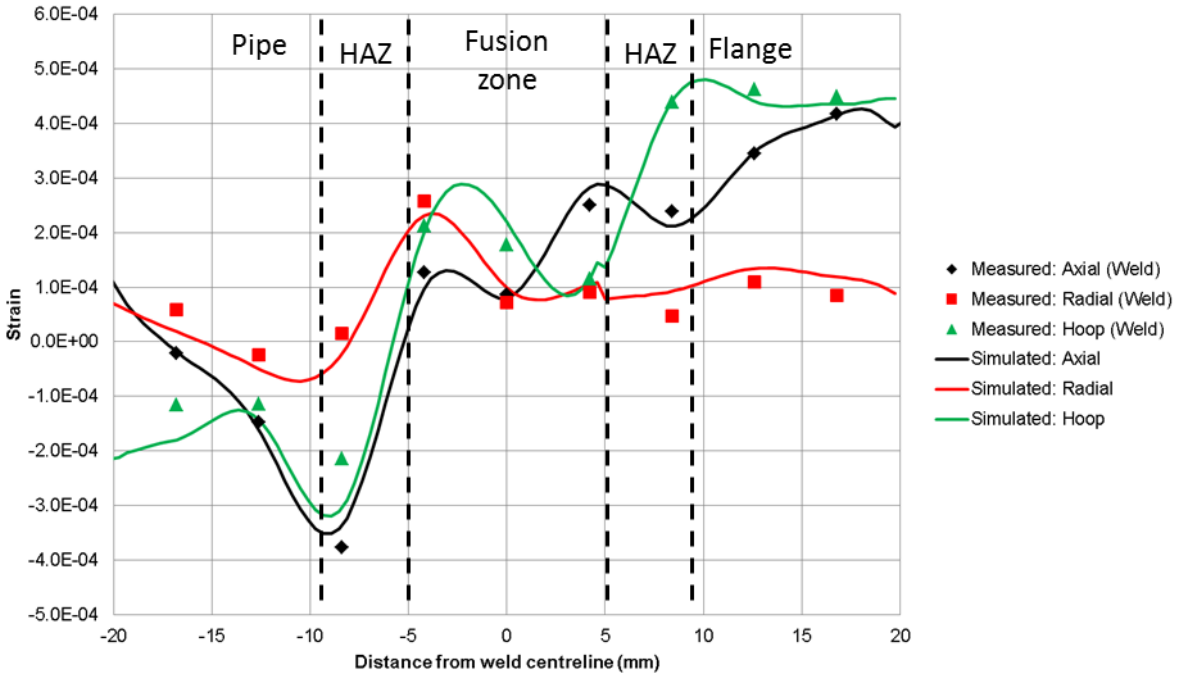

Figure 7.6 Comparison of eigenstrain-induced residual strains with measured residual strains and weighted by volume fraction austenite/ferrite.

Following the introduction of the residual (strain) stress field, an incremental axial displacement was applied to one end of the tensile specimen whilst the other was restrained in the axial direction. The displacement was applied in small increments so that at least the first 5-6 solution increments resulted in only elastic strains being applied.

7.3 Results and Observations

7.3.1 Neutron diffraction measurements

7.3.1.1 Micro-stresses in individual phases

Figure 7.7 showed the measurements of the residual micro-stresses present in austenite and ferrite phases in the three directions. The errors bars are displayed but they are too small to be visualised. The maximum error calculated was 2.6 MPa. Two welds were assessed, showed as plain and dotted line in the Figures, their residual stresses state exhibiting the same trend.

The graphs showed that in all directions the stresses in ferrite and austenite were antisymmetric about the centreline: in the pipe material, ferrite exhibited negative micro stresses and positive micro stresses were observed in the austenite. This trend was inversed in the case of the flange material with positive stresses in the ferrite and negative in the austenite. This could be explained by the different thermomechanical processing history of the pipe and the flange, rolled and cast respectively. As discussed in the literature review, the different thermal expansion coefficients of ferrite and austenite induced residual stresses after solidification and, compressive stresses in the ferrite and tensile stresses in the austenite are expected [229], [230], [231], which is only consistent with the observation of the stress state of the pipe.

The stress state of the weld was more complex: on the pipe side of the weld the ferrite exhibited tensile residual micro stresses and the austenite compressive residual micro stresses. The opposite was observed on the flange side. Welding processes involve high heat input and cooling rates which induced complex stress state in the welds and heat affected zones. The antisymmetric behaviour observed between the two phases was consistent with previous work [192][232].

The maximum and minimal residual stress values were obtained in the weld: 349 MPa was reached in the ferrite phase for the hoop direction and -405 MPa in the austenite in the radial direction. Those values are high considering the 0.2 % offset yield stress of the pipe and the flange, which are 666 MPa and 615 MPa, respectively.

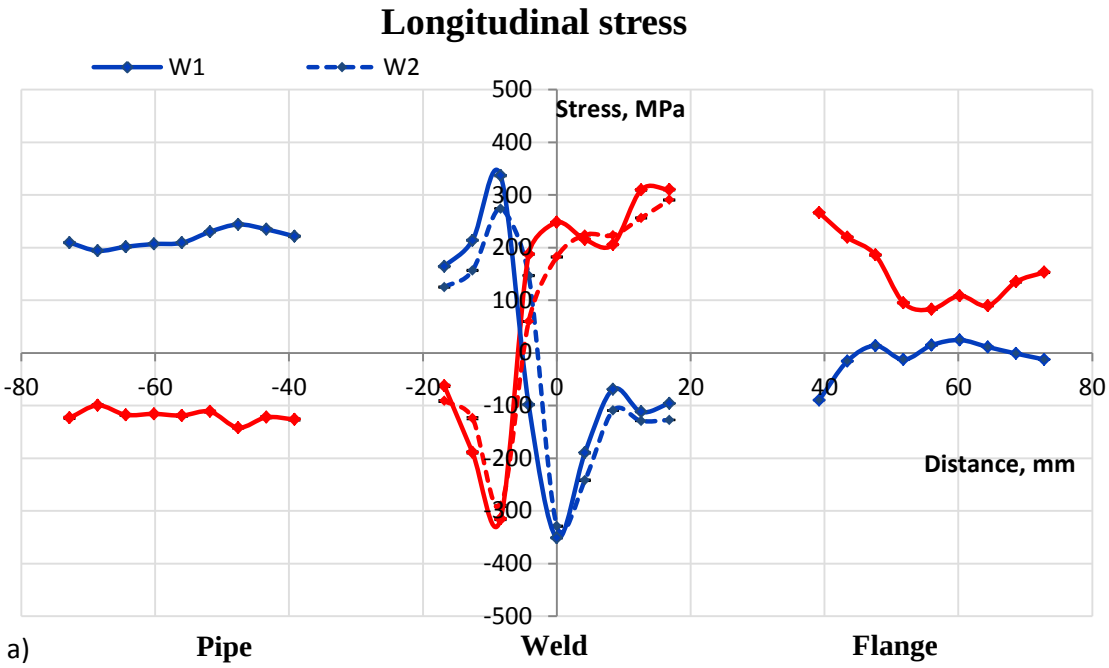

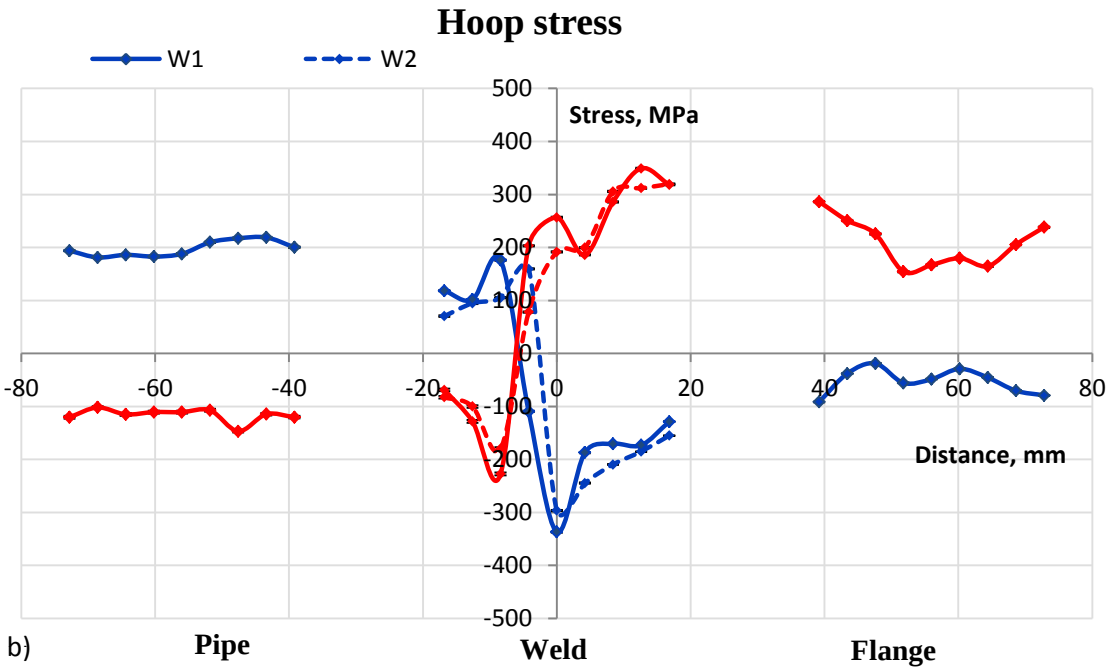

Figure 7.7 (continued): Micro-stresses in ferrite (red line) and austenite (blue line) phases in the a) longitudinal, b) hoop directions.

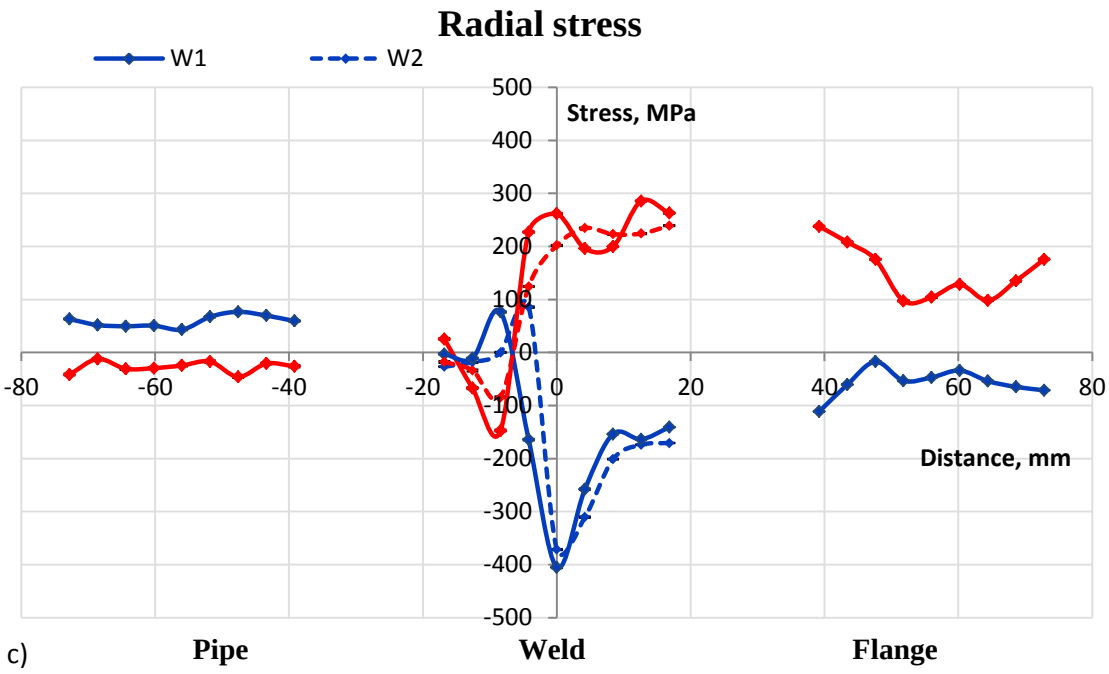

Figure 7.7: Micro-stresses in in ferrite (red line) and austenite (blue line) phases in the c) radial directions.

7.3.1.2 Global stresses

Using the phase fraction measured along the weld and in the parent materials, given in Chapter 4, the average stresses was calculated according to equation 32. The results in the three directions (longitudinal, hoop and radial) for the pipe, flange and cross-weld specimens are given in Figure 7.8. The two welds assessed, showed as plain and dotted line in the figures, both exhibited the same micro stresses trend. In all direction, average residual micro stresses were close to zero in the pipe and positive in the flange material. In the cross-weld specimens the results were more complex: positive micro stresses were visible in the weld and the HAZ on the flange side and negative micro stresses were observed in the HAZ on the pipe side.

The presence of residual stresses as high as 200 MPa inside those small-scale tensile specimen was surprising as it is expected that extracting small-scale specimen from a component results in relieving stresses by the creation of free-surface [184].

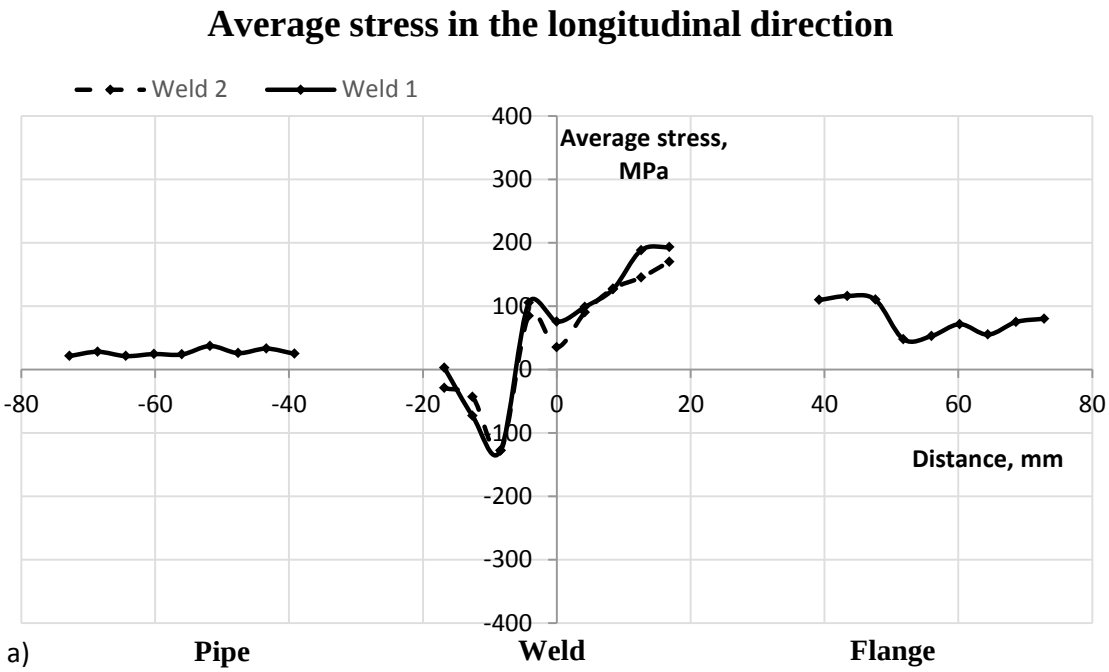

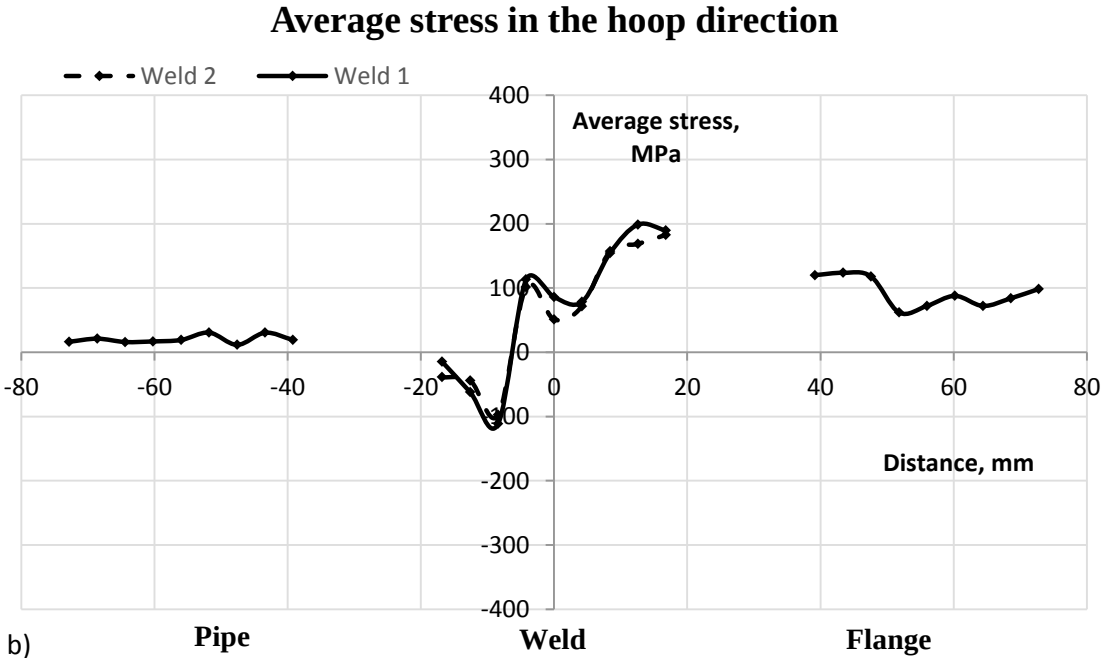

Figure 7.8 (continued): Average micro-stresses in the a) longitudinal, b) hoop directions.

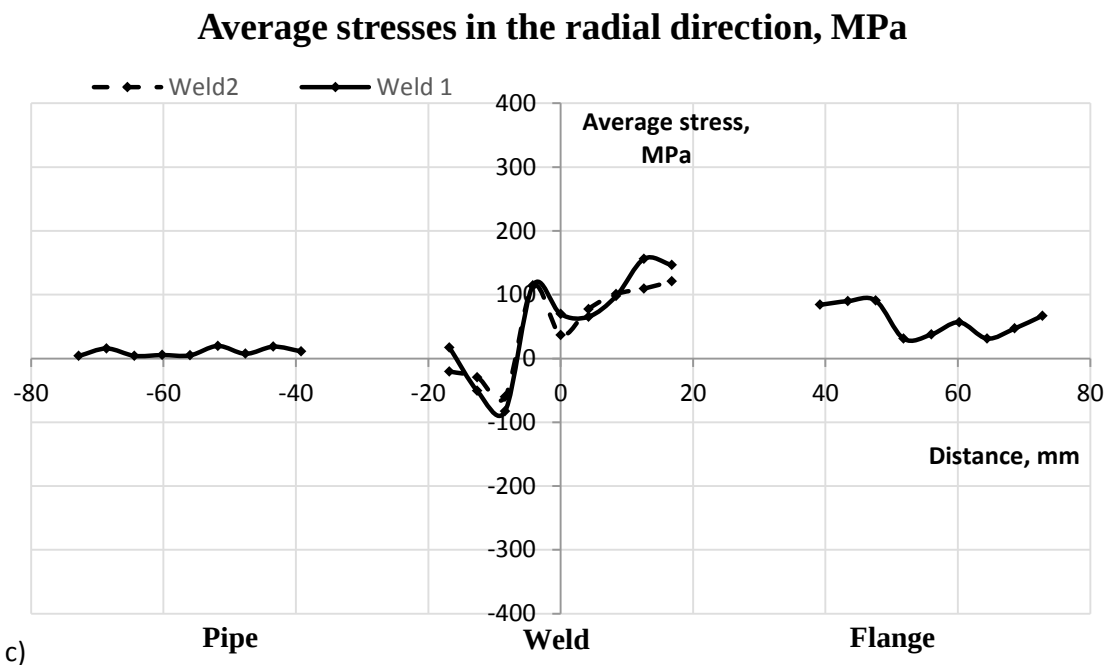

Figure 7.8: Average micro-stresses in the direction c) radial direction.

7.3.2 Environmental constant-load tensile tests

After performing the residual stress measurements, the specimens were testing under constant tensile loads in a hydrogen-charging environment. Table 7.1 records the measurements of the specimen elongation after testing and the results of HISC cracks detection.

The parent materials exhibited similar strains for the same normalised load. The weld metal however, exhibited lower strain results: 0.18 % after loading at 95 %$\sigma_{0.2\ \%}$ for 7 days; compare to 0.93 % and 1.15 % for the flange and the pipe materials respectively. These results indicate the occurrence of LTC during testing: the material exhibited plastic deformation under constant load, even at load levels below the proof stress.

Table 7.1: Constant load parameters testing parameters in the parent material and the cross-weld specimens, strain calculated from the specimen measurements before and after loading and post-test analysis results.

	Specimens designation	Applied load, %σ0.2	Strain, %	HISC cracking detection		
				LPI	SEM microscopy	Light microscopy
Flange	F1	85%	0.29	NCD(*)	NCD	NCD
	F2	90%	0.48	NCD	NCD	NCD
	F3	95%	0.93	Crack detected	Cracks from 10 to 40um length and 1 to 5um wide	
Pipe	P1	90%	0.33	NCD	NCD	NCD
	P2	95%	1.15	NCD	NCD	NCD
	P3	100%	0.94	NCD	NCD	NCD
Weld	W3	85%	0.10	NCD	NCD	NCD
	W4	90%	0.09	Detection of dots at the middle gauge length	NCD	NCD
	W1	95%	0.18	NCD	NCD	NCD
	W2	100%	0.47	NCD	NCD	NCD

(*) NCD: No crack detected

The results of HISC crack detection showed that only the flange material experienced HISC, Figure 7.9. The presence of HISC cracks was detected at 95 $\%\sigma_{0.2\ \%}$. These results were in agreement with the previous observation discussed in the introduction [226].

The microstructural characterisation of the materials showed that the flange exhibited a coarse microstructure compared to the fine microstructure of the pipe. It is well-known that the DSSs with coarse microstructure are more susceptible to HISC failures [76], [77], [109] and hence, this can be an explanation for the inferior HISC performance of the flange compared to the pipe material. However, the superior resistance to HISC of

the cross-weld specimens, which were partly composed of the flange material, could not be explained by the microstructural factors.

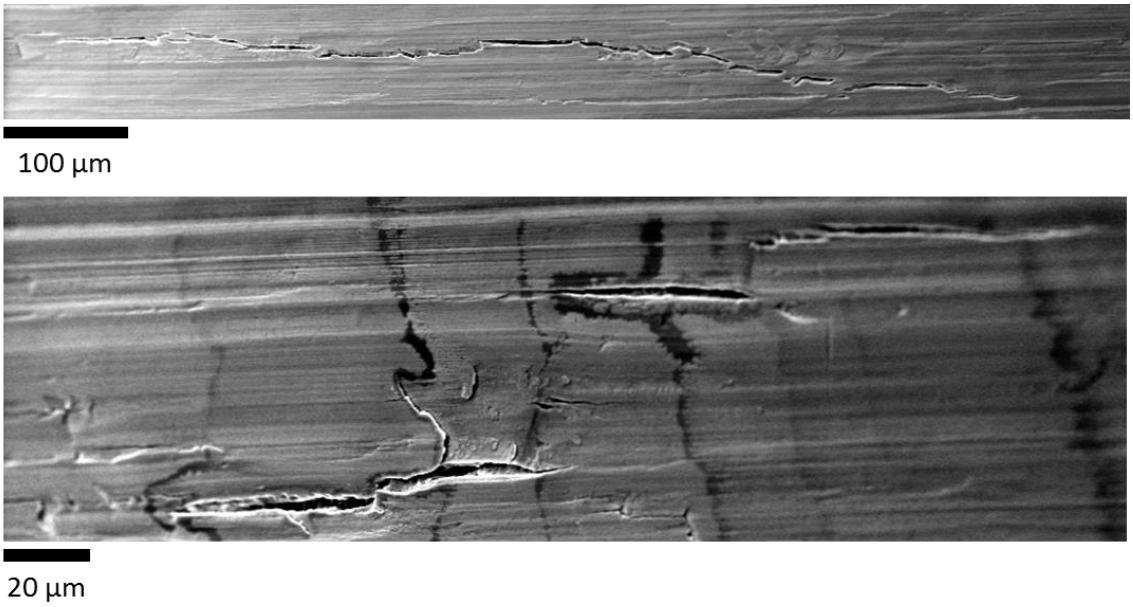

Figure 7.9: SEM images of HISC micro-cracks observed in the specimen extracted from the flange material and loaded to 95%$\sigma_{0.2\%}$.

7.3.3 Modelling results

To support the metallographic examination of unanticipated cracking observed during the constant stress tests, finite element analysis (FEA) was undertaken. The objective of the finite element analyses was to simulate the redistribution of different measured residual stress profiles and determine if the incremental stress fields provided any further insight into the observed cracking.

Each model was developed at different levels of applied strain, i.e. 0.012 % (minute increment applied to allow generation of stresses representing the starting state of stresses), 0.034 %, 0.17 %, 0.47 % and 0.86 %. Figure 7.10 to Figure 7.14 below provide images of the von Mises stress contours, equivalent plastic strain and maximum principal stress (with half of the specimen cut away to reveal the through-thickness distributions). In the case of the cross-weld specimen, the left side corresponds to the pipe and the right side to the flange material. The results indicate that while the level of applied stress (strain) was elastic (i.e. $\leq$ 0.034 %), the residual stresses dominate the stress field compared to the nominal applied stress. However, as the level of applied

strain increases: from 0.17 % to 0.86 % strain, the stresses redistribute due to yielding and a higher load level. As a consequence, the difference in stress field between the three specimens was negligible, with the only differences arising from the different flow (stress-strain) behaviour.

At 0.47 % and 0.86 %, heterogeneities of stress distribution within the cross-weld specimen were observed and the related equivalent plastic strain exhibited higher strain levels on the pipe side of the weld. However, those differences were very low: at 0.47 %, 0.0030 and 0.0021 strain levels were reached in the pipe side and weld, respectively, compared to 0.0012 in the flange.

Another observation was that the Von Mises and maximum principal stresses were higher in the all-flange model than in the other models, at and above an applied strain of 0.86 %. This difference was primarily a result of the flow behaviour of the flange material, but also a consequence, to a small extent, of the initial residual stresses. Therefore, whilst the simulation of global stress state did indicate some motivation for cracking in the flange material compared with the other test pieces, it is not wholly conclusive.

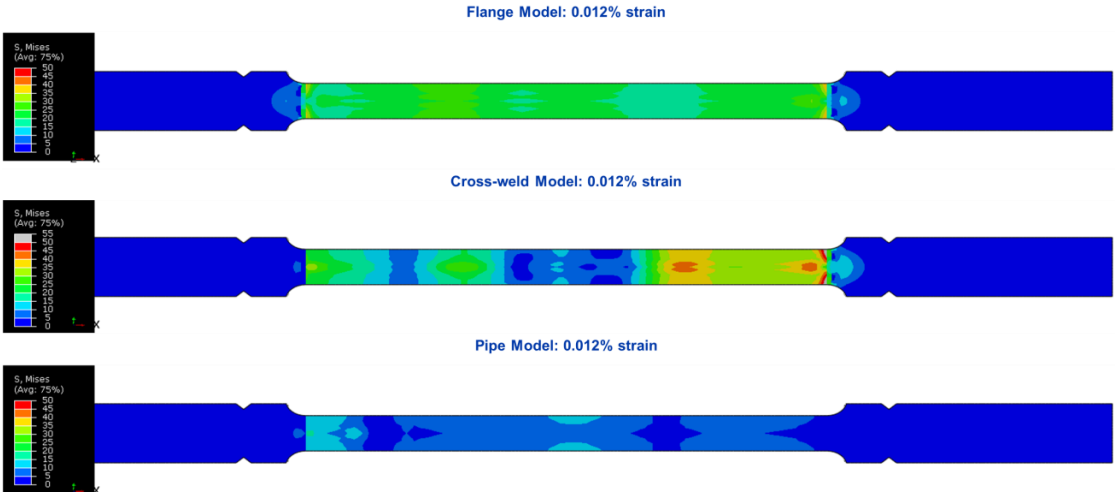

Figure 7.10: Von Mises stress distribution at 0.012 % applied strain. The residual stresses are still dominant compared with the applied stresses.

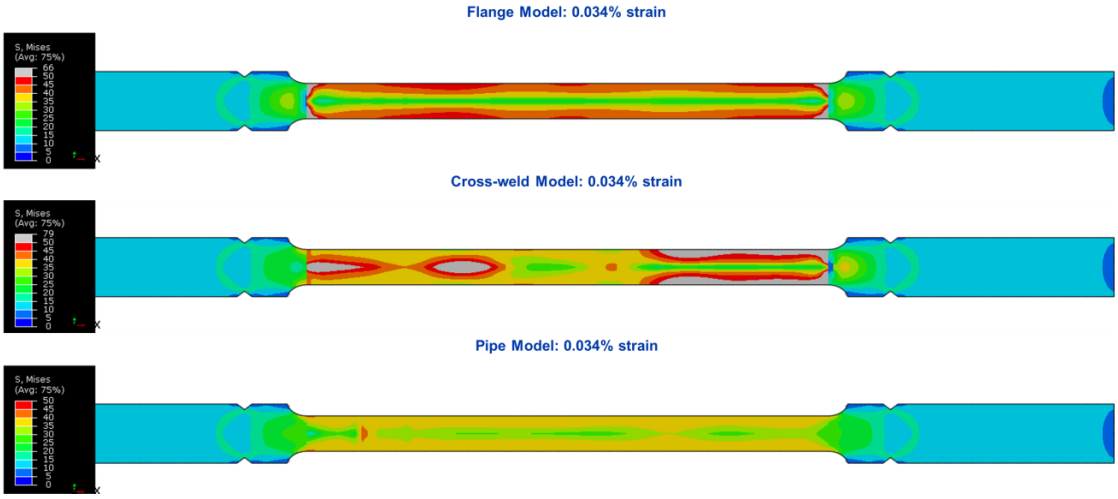

Figure 7.11: Von Mises stress distribution at 0.034 % applied strain. The residual begins to be suppressed and redistributed by the applied stresses.

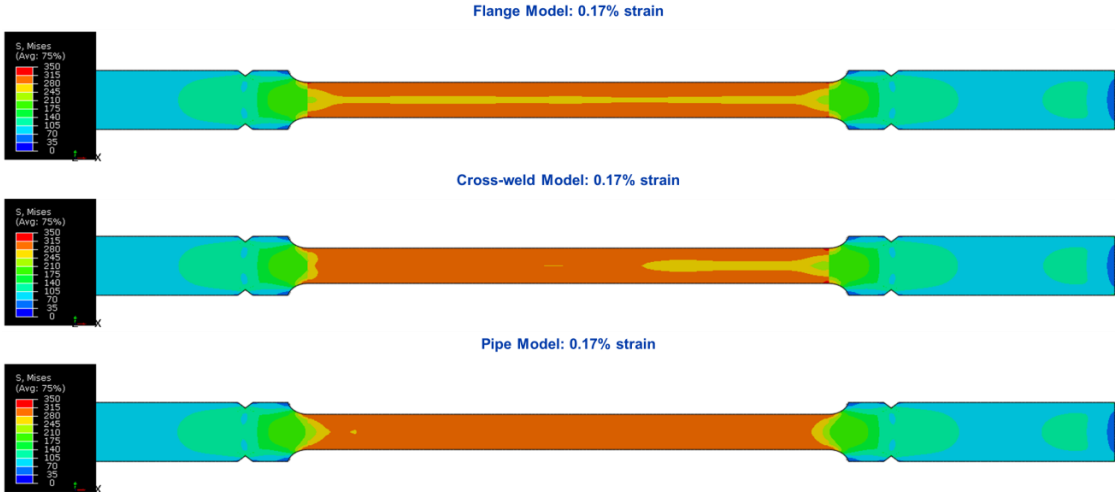

Figure 7.12: Von Mises stress distribution at 0.17 % applied strain. The influence of the residual stresses is almost completely removed at this stage.

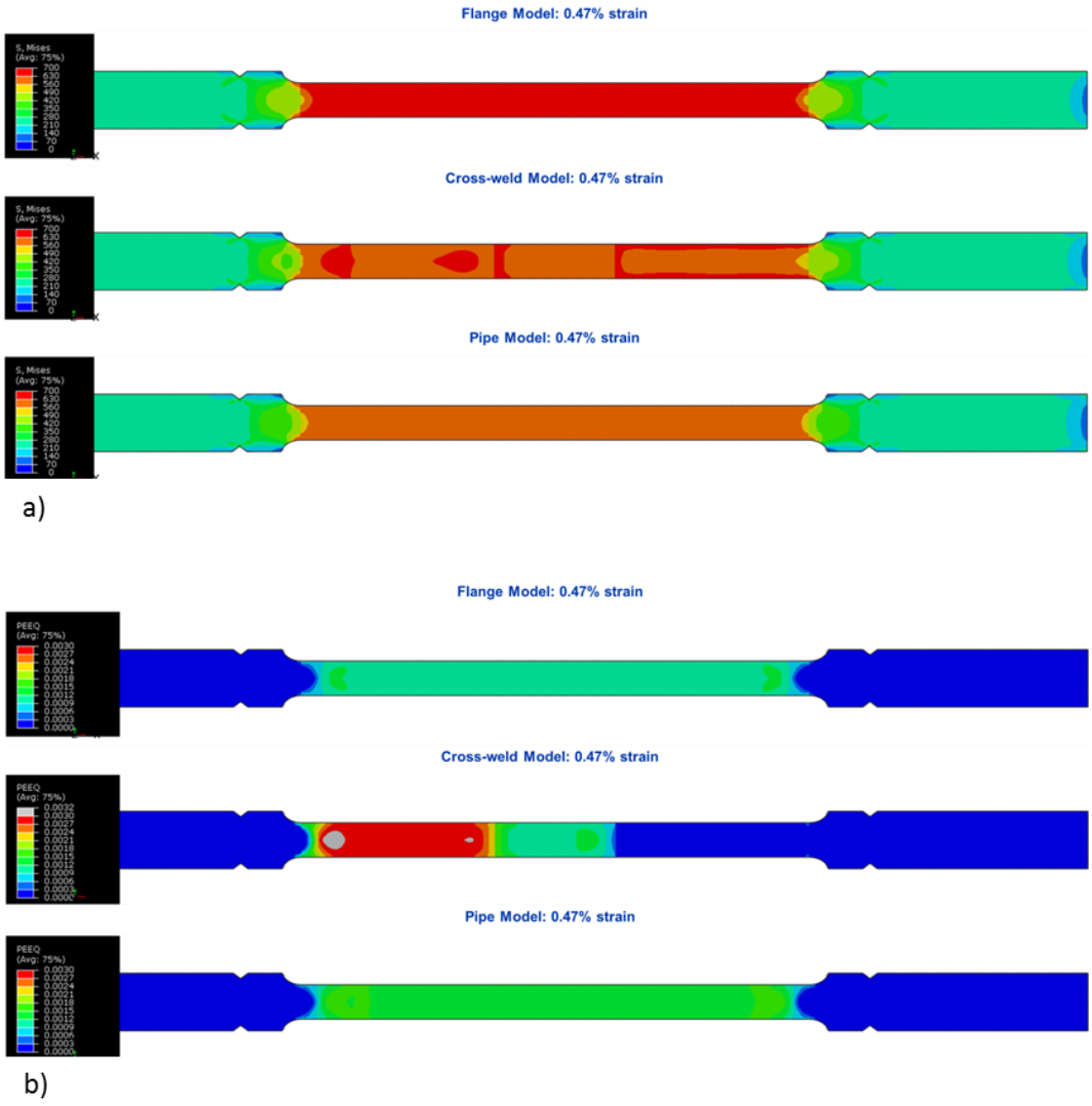

Figure 7.13: a) Von Mises stress distribution at 0.47 % applied strain. At this stage, the influence of the residual stresses is effectively negligible and the only difference between the specimens is the flow behaviour, b) Equivalent plastic strain at 0.47 % applied strain. This contour plot shows the reason for differences in the von Mises stress contour plot in a).

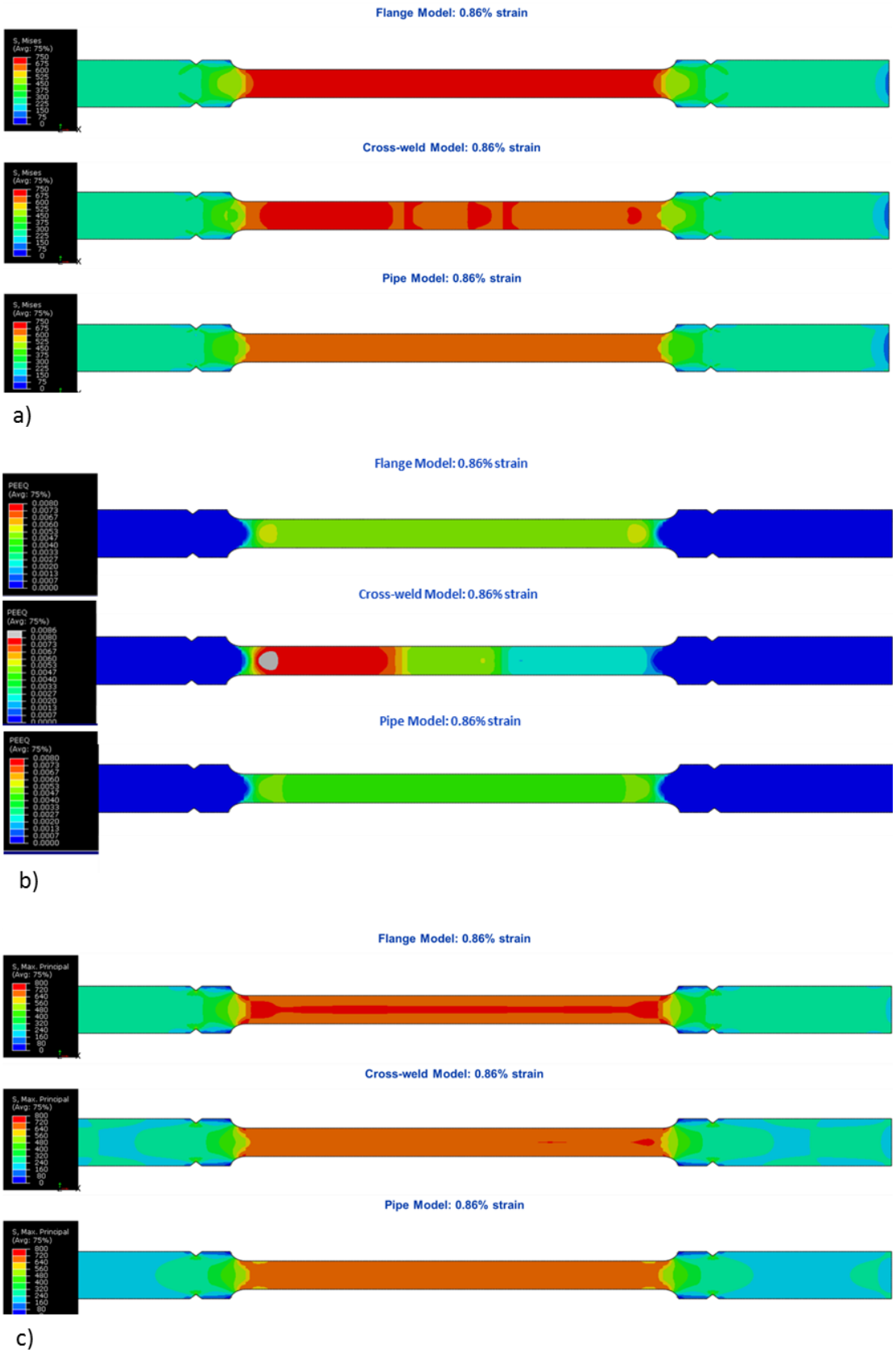

Figure 7.14: a) Von mises stress distribution at 0.86 % applied strain, b) Equivalent plastic strain at 0.86 % applied strain, c) Maximum principal stress distribution at 0.86 % applied strain.

7.4 Discussion

Consistent with the previous observations [226], the cross-weld specimens and the pipe materials exhibited superior performance to HISC than the flange material. The global residual stress-state of the undeformed specimens showed that the specimen extracted from the pipe material was in tension but to a lower level than the specimen extracted from the flange. The cross-weld specimen exhibited tension on the flange side and compression on the pipe side. Once those global stresses were input into the model, the results showed that for low (elastic) levels of applied strain, the residual stresses dominated the overall composite (primary/secondary) stress field. However, once plasticity initiated, significant redistribution of residual stresses occurred such that beyond approximately 0.17 % strain, the influence of the residual stresses could no longer be significantly observed. For lower levels of applied strain, clear influences on the stress state could be observed. However, it was difficult to draw conclusions from the simulation results in light of the observed cracking in the flange test piece.

This model was based on a continuum scale approach: the residual strains included in the model were taken to be the volume averaged contributions of the residual strains measured in the austenite and ferrite phases. The measurements of micro-stresses in individual phases showed that, in all directions (i.e. longitudinal, hoop and radial), ferrite was in tension in the flange specimen and in compression on the pipe specimen, and vice-versa for austenite. In the cross-weld specimen similar trend of tension on the flange side and compression on the pipe side was observed. In this case, the continuum-scale, volume averaged representation of the bulk residual stresses may not capture the correct physics of the stress state at the micro-scale. Indeed, such competing tensile/compressive residual stresses could cause excessive shear stresses along grain boundaries which a continuum scale model does not capture.

Furthermore, investigation of HISC in DSSs has, since a long time, established that ferrite is more susceptible to HISC than austenite [75][108][106]. Hence, localised distribution of tensile stresses in this phase could increase susceptibility to HISC of the flange material. In the case of the cross-weld specimens, the presence of the composite structure of DSSs with different properties, might have resulted in strain localisation within the regions less susceptible to HISC and protect the more susceptible constituents from HISC, specially as the elongation of this specimen was lower than the

elongation of the two parent materials specimens after testing. Further work is required to study the effects of straining, and its micro-mechanisms, across the specimen, at a micro-scale.

7.5 Conclusion

The present work was an attempt to better explain the resistance-to-HISC of cross-weld tensile specimens compare to extract from the parent materials. The assumption assessed here was the influence of the residual stresses remaining in the specimens.

The micro-stresses in ferrite and austenite and the average residual stresses were measured and the actual state of stress and strain during testing was provided by a FEA. Important observations were made from those measurements:

1) Small-scale tensile specimen exhibited remaining high residual stresses;
2) The residual stresses state of austenite and ferrite in this component is antisymmetric about the centreline;
3) The two DSS components assessed exhibited different stress state;

The results of the model taking into account average of ferrite and austenite strains, was not conclusive and did not explain cracking of the higher susceptibility of the flange specimen to HISC.

For future work, it is recommended that a local model including an actual representation of the microstructure is used to determine if these strong local stress variations at the microstructural level may be causing the observed cracking in the flange test piece.

Chapter 8.

SUMMARY AND RECOMMENDATIONS

8.1 Major findings

The present work encompasses a number of research activities studying and addressing some of the most common, and not-fully-elucidated aspects of HISC of (S)DSSs, including the role of microstructure, LTC, usefulness of current fracture-toughness-based test methodologies for the assessment of environmental resistance to cracking of (S)DSSs.

This academic study was carried out in an industrial context, and aimed to not only do provide a better understanding of the fundamentals of, and factors contributing to, this cracking mechanism; but also to generate data and make in-depth observations to improve the existing guidelines for designing with DSSs against HISC.

LTC phenomenon was investigated in the wrought and the HIPed microstructures. It was found that the austenite phase was responsible for the stress accommodation during constant-load testing and hence controlled the DSSs' response in terms of LTC. Furthermore, it was observed that the fundamentally different morphologies of the two phases were responsible for significantly different stress accommodation of the two materials. The homogeneity of the HIPed material compare to the directionality of the wrought material showed that the latter was more prone to strain localisation, which in turn could explain its lower resistance to HISC. Generally, it was concluded that LTC is an inherent response of DSSs to loading, with its extent being a function of DDSs' microstructural parameters, such as the size, fraction, and directionality (and potentially, connectivity) of the phases.

An environmental testing programme based on fracture toughness was pursued to primarily generate data for characterising and comparing the resistance HISC of the two materials and establish a relationship between the alloys' microstructure and their environmental performance. It was soon observed that the test method in terms of the geometry of test specimens, and environmental testing parameters, require further attention, before any meaningful interpretation of the results, particularly with respect to crack initiation, could be carried out. Therefore, certain work was initially performed to develop an understating of the test parameters, and their relevance to assessing DSSs against HISC. The study showed that resistance to initiation is key to resist HISC, and that the current fracture-toughness based testing procedures were not able to capture and quantity HISC initiation.

It was determined that the HIPed material had a superior resistance to crack growth than the conventional wrought manufactured material. The analysis of the fracture morphologies determined that the austenite spacing along the cracking plane, was not the sole microstructural factor determining resistance to HISC of (S)DSSs, and was only relevant to (S)DSSs with a distinct degree of directionality, i.e. wrought products, traditional forgings, etc.

The last part of this work focused on welded pipe-to-flange component. It was an attempt to explain some surprising results obtained in previous work which showed the better resistance to HISC of cross-weld small-scale tensile specimens compared to that of specimens extracted from the parent materials on either sides of the weld. The results of the model taking into account average of ferrite and austenite strains, was not conclusive and did not explained cracking of the higher susceptibility of the flange specimen to HISC.

8.2 Future work

The key findings from this work contributes to a better understanding of HISC mechanism in DSSs and suggests research paths to be pursued in order to improve current design guidelines and raises the need of developing testing methodologies to assess DSSs against HISC.

The investigation of LTC phenomenon and its implication for HISC is suggested to be pursued further through quantifying strain partitioning in DSS microstructures, using larger and finer grids/patterns, in the presence of hydrogen. 3D microstructural analysis of DSSs should be considered, with the quantification of the tortuosity and connectivity of both phases, and linked with the resistance-to-HISC of the material.

As far quantitative evaluation of HISC is concerned, one major approach towards assessing environmental cracking of non-ductile materials could be benefiting from methods such as sustained-load testing, in which it is attempted to determine threshold values (for instance, in terms of cracking driving force) below which no cracking is encountered.

It is also recommended that modelling techniques are used in order to understand stress and strain distribution in the 3D DSS microstructures, the influence of micro-stresses and their implications on hydrogen diffusion and concentration within the microstructure.

REFERENCES

[1] E. Hämäläinen, A. Laitinen, H. Hänninen, Properties of nitrogen alloyed P/PM + HIP DSS, in: Duplex Stainl. Steels ’94, Glasgow, Scotland, 1994.

[2] J.C.S. Bernhardsson, ed., The duplex stainless steels: materials to meet your needs, in: Duplex Stainl. Steels’91, Beaune, Bourgogne, France, 1991: pp. 3–48.

[3] J. Charles, Structure and mechanical properties of duplex stainless steels, in: Duplex Stainl. Steels ’94, Glasgow, Scotland, 1994.

[4] R.N. Gunn, Duplex Stainless Steels: Microstructure, Properties and Applications, Woodhead Publishing, 1997.

[5] Chapter : Duplex Stainless Steels, in: Stainl. Steels An Introd. Their Recent Dev., Bentham Science Publishers, 2012: p. 173.

[6] S. Floreen, H.W. Hayden, The influence of austenite and ferrite on the mechanical properties of two phase stainless steels having microduplex structures, Trans. Quaterly, Am. Soc. Met. 61 (1968) 489–99.

[7] J.-O. Nilsson, Super duplex stainless steels, Mater. Sci. Technol. 8 (1992) 685–700. doi:10.1179/mst.1992.8.8.685.

[8] M. Nystrom, B. Karlsson, J. Wasén, The infuence of prestraining and 475C annealing on the mechanical properties of a duplex stainless steel (SAF 2205), in: Int. Conf. Stainl. Steels, 1991: pp. 738–745.

[9] W. Zheng, D. Hardie, Effect of Structural Orientation on the Susceptibility of Commercial Duplex Stainless Steels to Hydrogen Embrittlement, Corrosion. 47 (1991) 792–799. doi:10.5006/1.3585190.

[10] I. Tamura, Deformation-induced martensitic transformation and transformation-induced plasticity in steels, Met. Sci. 16 (2013) 245–253. doi:10.1179/030634582790427316.

[11] S.S.M. Tavares, J.M. Pardal, M.R. da Silva, C.A.S. de Oliveira, Martensitic transformation induced by cold deformation of lean duplex stainless steel UNS S32304, Mater. Res. 17 (2014) 381–385. doi:10.1590/S1516-14392013005000157.

[12] C.S. Wiesner, Toughness requirements for duplex and super duplex stainless steels, in: Duplex Stainl. Steels 97, 1997: pp. 979–990.

[13] A. Dhooge, E. Deleu, Weldability and fracture behaviour of duplex and superduplex stainless steels., in: Duplex Stainl. Steels ’94, Int. Conf. Vol. 3., Glasgow, Scotland, 1994.

[14] H. Sieurin, Doctoral Thesis: Fracture toughness properties of duplex stainless steels, Stockholm, Sweden, 2006.

[15] O. Kolednik, M. Albrecht, M. Berchthaler, H. Germ, R. Pippan, F. Riemelmoser, J. Stampfl, J. Wei, The fracture resistance of a ferritic-austenitic duplex steel, Acta Mater. 44 (1996) 3307–3319. doi:10.1016/1359-6454(95)00412-2.

[16] M. Faccoli, R. Roberti, Probabilistic fracture toughness of a duplex stainless steel in the transition range, Eng. Fract. Mech. 97 (2013) 207–215. doi:10.1016/j.engfracmech.2012.09.027.

[17] I. Dlouhy, A. Prochikova, V. Kozak, M. Holzmann, Characteristics of fracture behaviour of duplex steels in transition region, in: Mech. Mech. Damage Fail., 1996: pp. 651–656.

[18] E. Deleu, A. Dhooge, Fracture toughness of welded thick walled duplex stainless steels, in: Duplex Stainl. Steels 97, 1997: pp. 387–394.

[19] J. Pilhagen, R. Sandström, Loss of constraint during fracture toughness testing of duplex stainless steels, Eng. Fract. Mech. 99 (2013) 239–250. doi:10.1016/j.engfracmech.2013.01.002.

[20] E. Erauzkin, A.M. Irisarri, Effect of the testing temperature on the fracture toughness of a duplex stainless steel, Scr. Metall. Mater. 25 (1991) 1731–1736.

[21] S. Bernhardsson, The corrosion resistance of duplex stainless steels, in: Duplex Stainl. Steels ’91, Beaune, Bourgogne, France, 1991: pp. 186–210.

[22] R. Francis, Environmental Cracking and Embrittlement of Duplex Stainless Steel, in: Duplex Stainl. Steels ’94, Glasgow, Scotland, 1994.

[23] R. Sriram, D. Tromans, Pitting corrosion of duplex stainless steels, Corros. 1989. (1989) 804–810. doi:10.1108/00035590110365309.

[24] C. Örnek, F. Léonard, S.A. McDonald, A. Prajapati, P.J. Withers, D.L. Engelberg, Time-dependent in situ measurement of atmospheric corrosion rates of duplex stainless steel wires, Npj Mater. Degrad. 2 (2018) 10. doi:10.1038/s41529-018-0030-9.

[25] A. Desestret, R. Oltra, The influence of plastic straining on localized and general corrosion of stainless steels, Corros. Sci. 20 (1980) 799–820. doi:10.1016/0010-938X(80)90059-1.

[26] S. Shimodaira, M. Takano, Y. Takizawa, H. Kamide, Mechanisms of transgranular stress corrosion cracking of duplex and ferritic stainless steels, in: Stress Corros. Crack. Hydrog. Embrittlement Iron Base Alloy., 1973: pp. 1003–1015.

[27] J.W. Flowers, F.H. Beck, M.G. Fontana, Corrosion and age hardening studies of some cast stainless alloys containing ferrite, Corrosion. 19 (1963) 186t 198t.

[28] H.. C.J.R.D. Thomas, Effect of alloying elements on tensile properties of 25-20 weld metal, Weld. J. 25 (1946) 760s–768.

[29] A.L. Schaeffler, Selection of austenitic electrodes for welding dissimilar metals, Weld. J. 26 (1947) 603s–620s.

[30] D. Kotecki, T. Siewert, WRC-1992 constitution diagram for stainless steel weld metals: a modification of the WRC-1988 diagram, Weld. J. (1992) 171–178.

[31] J.C. Lippold, D.J. Koketcki, Welding metallurgy and weldability of Stainless Steels, 2005.

[32] P.D. Southwick, R.W.K. Honeycombe, Decomposition of ferrite to austenite in 26%Cr-5%Ni stainless steel, Met. Sci. 14 (1980) 253–261. doi:10.1179/030634580790426418.

[33] A. Redjaimia, Decomposition of Delta Ferrite in a Fe-22Cr-5Ni-3Mo-0.03C Duplex Stainless Steel. A Morphological and Structural Study, in: Duplex Stainl. Steels ’91, Beaune, Bourgogne, France, 1992: pp. 119–126.

[34] J.C. Lippold, W. Lin, S.D. Brandi, I. Varol, W.A. Baeslack, Heat-affected zone microstructure and properties in commercial duplex stainless steels., in: Duplex Stainl. Steels ’94, Glasgow, Scotland, 1994.

[35] G.L. Leone, H.W. Kerr, The ferrite to austenite transformation in stainless steels, Weld. J. 61 (1982) 13–21. doi:doi:10.1086/652943.

[36] C. Herrera, D. Ponge, D. Raabe, Characterization of the microstructure, crystallographic texture and segregation of an as-cast duplex stainless steel slab, Steel Res. Int. 79 (2008) 10–12. doi:10.2374/SRI08SP014-79-2008-482.

[37] E.F. Monlevade, I.G.S. Falleiros, Orientation relationships associated with austenite formation from ferrite in a coarse-grained duplex stainless steel, Metall. Mater. Trans. A. 37 (2006) 939–949. doi:10.1007/s11661-006-0067-1.

[38] K. Verbeken, L. Barbé, D. Raabe, Evaluation of the Crystallographic Orientation Relationships between FCC and BCC Phases in TRIP Steels, ISIJ Int. 49 (2009) 1601–1609. doi:10.2355/isijinternational.49.1601.

[39] P.D. Southwick, R.W.K. Honeycombe, Precipitation of M 23 C 6 at austenite/ferrite interfaces in duplex stainless steel, Met. Sci. 16 (1982) 475–482. doi:10.1179/msc.1982.16.10.475.

[40] H.D. Solomon, T.M. Devine Jr, Duplex Stainless Steels--A Tale of Two Phases. In Duplex stainless steels, in: ASM (Ed.), Conf. Duplex Stainl. Steels, Ohio, US, 1982: p. 693–756.

[41] K.M. Lee, H.S. Cho, D.C. Choi, Effect of isothermal treatment of SAF 2205 duplex stainless steel on migration of δ/γ interface boundary and growth of austenite, J. Alloys Compd. 285 (1999) 156–161. doi:10.1016/S0925-8388(99)00014-6.

[42] J.Y. Maetz, T. Douillard, S. Cazottes, C. Verdu, X. Kléber, M23C6carbides and Cr2N nitrides in aged duplex stainless steel: A SEM, TEM and FIB tomography investigation, Micron. 84 (2016) 43–53. doi:10.1016/j.micron.2016.01.007.

[43] Y. Ohmori, Y. Maehara, Precipitation of M23C6 and .SIGMA.-phase in .DELTA./.GAMMA. duplex stainless steels., Trans. Iron Steel Inst. Japan. 24 (1984) 60–68. doi:10.2355/isijinternational1966.24.60.

[44] B. Josefsson, J. Nilsson, A. Wilson, Phase transformations in duplex steels and the relation between continuous cooling and isothermal heat treatment, in: Duplex Stainl. Steels'91, Beaune, Bourgogne, France, 1991.

[45] J.O. Nilsson, A. Wilson, Influence of isothermal phase transformations on toughness and pitting corrosion of super duplex stainless steel SAF 2507, Mater. Sci. Technol. (2013).

[46] Y. Maehara, Y. Ohmori, J. Murayama, N. Fujino, T. Kunitake, Effects of alloying elements on σ phase precipitation in δ–γ duplex phase stainless steels, Met. Sci. 17 (1983) 541–548. doi:10.1179/030634583790420457.

[47] R.Y. Wang X.G., Dumortier D., Structural evolution of zeron 100 duplex stainless steel between 550 and 1100^{o}C., in: Duplex Stainl. Steels '91, 1991.

[48] J.O. Nilsson, A. Wilson, Influence of Isothermal Phase-Transformations on Toughness and Pitting Corrosion of Super Duplex Stainless-Steel Saf-2507, Mater. Sci. Technol. 9 (1993) 545–554. doi:10.1179/026708393790172222.

[49] B. Deng, Z. Wang, Y. Jiang, T. Sun, J. Xu, J. Li, Effect of thermal cycles on the corrosion and mechanical properties of UNS S31803 duplex stainless steel, Corros. Sci. 51 (2009) 2969–2975. doi:10.1016/j.corsci.2009.08.015.

[50] S. Kim, Z. Zhang, Y. Furuya, C. Kang, J. Sung, Q. Ni, Y. Watanabe, I. Kim,

Effect of Precipitation of Sigma-Phase and N Addition on the Mechanical Properties in 25Cr–7Ni–4Mo–2W Super Duplex Stainless Steel, Mater. Trans. 46 (2005) 1656–1662. doi:10.2320/matertrans.46.1656.

[51] M. Pohl, O. Storz, T. Glogowski, Effect of intermetallic precipitations on the properties of duplex stainless steel, Mater. Charact. 58 (2007) 65–71. doi:10.1016/j.matchar.2006.03.015.

[52] E. Bettini, U. Kivisäkk, C. Leygraf, J. Pan, Study of corrosion behavior of a 2507 super duplex stainless steel: Influence of quenched-in and isothermal nitrides, Int. J. Electrochem. Sci. 9 (2014) 61–80.

[53] A.J. Ramirez, J.C. Lippold, S.D. Brandi, The relationship between chromium nitride and secondary austenite precipitation in duplex stainless steels, Metall. Mater. Trans. A. 34 (2003) 1575–1597. doi:10.1007/s11661-003-0304-9.

[54] A.J. Ramirez, S.D. Brandi, J.C. Lippold, Secondary austenite and chromium nitride precipitation in simulated heat affected zones of duplex stainless steels, Sci. Technol. Weld. Join. 9 (2004) 301–313. doi:10.1179/136217104225021715.

[55] E. Folkhard, Welding metallurgy of Stainless Steel, 1988. doi:10.1007/978-3-7091-8965-8.

[56] O. Kubaschewski, Iron-Binary Phase Diagrams, Springer, Berlin, Heidelberg, 1982. doi:10.1007/978-3-662-08024-5.

[57] D.R. Anson, R.J. Pomfret, A. Hendry, Castable high nitrogen duplex stainless steels, in: Duplex Stainl. Steels'94, Glasgow, Scotland, 1994.

[58] V.J. Gadjil, E.G. Keim, Scanning Auger microscopy analysis of the nitrogen concentration accross phase boundaries in a high alloy satnless steel, in: Duplex Stainl. Steels '94, 1994.

[59] C.O.A. Olsson, The influence of nitrogen and molybdenum on passive films formed on the austenoferritic stainless steel 2205 studied by AES and XPS, Corros. Sci. 37 (1995) 467–479. doi:10.1016/0010-938X(94)00148-Y.

[60] P. Combrade, J.-P. Audouard, Duplex stainless steels and localized corrosion

resistance, in: Duplex Stainl. Steels ’91, Beaune, Bourgogne, France, 1991: pp. 257–281.

[61] S. Jin, A. Atrens, ESCA-studies of the surface film formed on stainless steels by exposure to 0.1 M NaCl solution at various controlled potentials, Appl. Phys. A. 46 (1988) 51–65. doi:10.1007/BF00615137.

[62] T. Mori, K. Kondo, M. Igarashi, Y. Murata, H. K., Effects of alloying elements on sigma-related phase precipitation in super duplex stainless steels, in: Duplex Stainl. Steels’97, 1997: pp. 915–922.

[63] I. Iturriza, Special steels, in: EPMA Powder Metall. Summer Sch., 2016. doi:10.1038/135741a0.

[64] C. Örnek, D.L. Engelberg, An experimental investigation into strain and stress partitioning of duplex stainless steel using digital image correlation, X-ray diffraction and scanning Kelvin probe force microscopy, J. Strain Anal. Eng. Des. 51 (2016) 207–219. doi:10.1177/0309324716631669.

[65] S. Fréchard, F. Martin, C. Clément, J. Cousty, AFM and EBSD combined studies of plastic deformation in a duplex stainless steel, Mater. Sci. Eng. A. 418 (2006) 312–319. doi:10.1016/j.msea.2005.11.047.

[66] N. Jia, R. Lin Peng, D.W. Brown, B. Clausen, Y.D. Wang, Tensile Deformation Behavior of Duplex Stainless Steel Studied by In-Situ Time-of-Flight Neutron Diffraction, Metall. Mater. Trans. A. 39 (2008) 3134–3140. doi:10.1007/s11661-008-9675-2.

[67] J. Johansson, M. Odén, Load sharing between austenite and ferrite in a duplex stainless steel during cyclic loading, Metall. Mater. Trans. A. 31 (2000) 1557–1570. doi:10.1007/s11661-000-0166-3.

[68] N. Jia, R. Lin Peng, G.C. Chai, S. Johansson, Y.D. Wang, Direct experimental mapping of microscale deformation heterogeneity in duplex stainless steel, Mater. Sci. Eng. A. 491 (2008) 425–433. doi:10.1016/j.msea.2008.02.021.

[69] P.P. Bhattacharjee, M. Zaid, G.D. Sathiaraj, B. Bhadak, Evolution of

microstructure and texture during warm rolling of A duplex steel, Metall. Mater. Trans. A Phys. Metall. Mater. Sci. 45 (2014) 2180–2191. doi:10.1007/s11661-013-2139-3.

[70] G. Byrne, R. Francis, G. Warburton, Hydrogen Induced Stress Cracking (HISC) Resistance and Improvement Methods for Super Duplex Stainless Steels - Paper n.6981, in: Corros. 2016, NACE International, Vancouver, British Columbia, Canada, 2016.

[71] EEMUA 194:2012, Guidelines for materials selection and corrosion control for subsea oil and gas production equipment, in: Engineering Equipment Material Users Association, 2012: p. 175.

[72] B. Wallén, Corrosion of Duplex Stainless Steels in Seawater, in: Duplex Stainl. Steels, World Conf. 5, KCI Publishing, Zutphen, 1997: pp. 59–71.

[73] R. Francis, G. Byrne, G.R. Warburton, Effects of Cathodic Protection on Duplex Stainless Steels in Seawater, Corrosion. (1997) 234–240. doi:10.5006/1.3280465.

[74] W. Zheng, D. Hardie, The effect of hydrogen on the fracture of a commercial duplex stainless steel, Corros. Sci. 32 (1991) 23–36.

[75] J.. Valdez-Vallejo, R.C. Newman, R.P.M. Procter, Cathodic hydrogen embrittlement of a stainless steel, in: Hydrog. Eff. Mater. Behav., 1990: pp. 1003–1012.

[76] T.S. Taylor, T. Pendlington, R. Bird, Foinaven Super Duplex Materials Cracking Investigation, in: Offshore Technol. Conf., Offshore Technology Conference, 1999. doi:10.4043/10965-MS.

[77] S. Huizinga, B. McLoughlin, Failure of a subsea super duplex manifold hub by HISC and implications for design - Paper n.06145, Corros. 2006. (2006) 1–9.

[78] M. Solnørdal, S. Wästberg, G. Heiberg, O. Hauås-Eide, Hydrogen Induced Stress Cracking (HISC) and DNV-RP-F112, Meas. Control. 42 (2009) 145–148. doi:10.1177/002029400904200504.

[79] Design of duplex stainless steel subsea equipment exposed to cathodic

protection, in: Recomm. Pract. DNV-RP-F112, DET NORSKE VERITAS, 2008.

[80] X. An, A. Dobson, I. Probyn, P. Fellow, Super Duplex/Duplex Stainless Steel Umbilical Tube Resistance to HISC, in: 29th Int. Conf. Ocean. Offshore Arct. Eng. Vol. 6, ASME, 2010: pp. 23–31. doi:10.1115/OMAE2010-20137.

[81] R. Kirchheim, A. Pundt, Hydrogen in Metals, Fifth Edit, Elsevier, 2014. doi:10.1016/B978-0-444-53770-6.00025-3.

[82] A. Turnbull, Perspectives on hydrogen uptake, diffusion and trapping, Int. J. Hydrogen Energy. 40 (2015) 16961–16970. doi:10.1016/j.ijhydene.2015.06.147.

[83] P. Olsson, A. Delblanc Bauer, H. Eriksson, Hydrogen embrittlement of duplex grades UNS 32750 and UNS 31803 in connection with cathodic protection in chloride solutions, in: Duplex Stainl. Steels 97 - 5th World Conf., 1997: pp. 607–618.

[84] A. Elhoud, N. Renton, W. Deans, Hydrogen embrittlement enhanced by plastic deformation of super duplex stainless steel, in: Damage Fract. Mech., 2009: pp. 59–67.

[85] A. Turnbull, R.B. Hutchings, Analysis of hydrogen atom transport in a two-phase alloy, Mater. Sci. Eng. A. 177 (1994) 161–171. doi:10.1016/0921-5093(94)90488-X.

[86] A. Turnbull, Gaseous Hydrogen Embrittlement of Materials in Energy Technologies, Woodhead Publishing Limited, 2012. doi:10.1533/9780857095374.1.89.

[87] R. Silverstein, D. Eliezer, Hydrogen trapping mechanism of different duplex stainless steels alloys, J. Alloys Compd. 644 (2015) 280–286. doi:10.1016/j.jallcom.2015.04.176.

[88] R. Johnsen, B. Nyhus, S. Wastberg, G. Lauvstad, New Improved Method for HISC Testing of Stainless Steels - Paper n.07496, Corrosion. (2007).

[89] Tetrahedral Sites, Fac. Eng. Kiel, Ger. (n.d.) 12. https://www.tf.uni-kiel.de/matwis/amat/def_en/kap_1/illustr/t1_3_4.html.

[90] W.. Luu, P.. Liu, J.. Wu, Hydrogen transport and degradation of a commercial duplex stainless steel, Corros. Sci. 44 (2002) 1783–1791. doi:10.1016/S0010-938X(01)00143-3.

[91] E. Owczarek, T. Zakroczymski, Hydrogen transport in a duplex stainless steel, Acta Mater. 48 (2000) 3059–3070. doi:10.1016/S1359-6454(00)00122-1.

[92] Y. Sakamoto, K. Takao, I. Iwanaga, Diffusivity of Hydrogen in a Duplex Stainless Steel, in: Twenty-Ninth Japan Congr. Mater. Res., 1985: pp. 111–116.

[93] M.A. V. Devanathan, Z. Stachurski, The Adsorption and Diffusion of Electrolytic Hydrogen in Palladium, Proc. R. Soc. A Math. Phys. Eng. Sci. 270 (1962) 90–102. doi:10.1098/rspa.1962.0205.

[94] R.B. Hutchings, A. Turnbull, A.T. May, Measurement of hydrogen transport in a duplex stainless steel, Scr. Metall. Mater. 25 (1991) 2657–2662. doi:10.1016/0956-716X(91)90134-M.

[95] A. Turnbull, E. Lembach-Beylegaard, R. Hutchings, Hydrogen transport in SAF 2205 and SAF 2507 duplex stainless steel, in: Hydrog. Transp. Crack. Met., Teddington, UK, 1994: pp. 268–279.

[96] S.-L. Chou, W.-T. Tsai, Effect of grain size on the hydrogen-assisted cracking in duplex stainless steels, Mater. Sci. Eng. A. 270 (1999) 219–224. doi:10.1016/S0921-5093(99)00174-4.

[97] R. Kirchheim, Interaction of hydrogen with external stress fields, Acta Metall. 34 (1986) 37–42. doi:10.1016/0001-6160(86)90229-4.

[98] W. Beck, J.O. Bockris, J. McBreen, L. Nanis, Hydrogen Permeation in Metals as a Function of Stress, Temperature and Dissolved Hydrogen Concentration, 290 (1966) 220–235.

[99] N. Kheradmand, R. Johnsen, J.S. Olsen, A. Barnoush, Effect of hydrogen on the hardness of different phases in super duplex stainless steel, Int. J. Hydrogen Energy. 41 (2016) 704–712. doi:10.1016/j.ijhydene.2015.10.106.

[100] B.R.. DA Silva, D.S. Dos Santos, F. Salvio, Hydrogen embrittlement in super

duplex stainless steel tubes UNS S32750 under mechanical stress, in: Int. Hydrog. Conf., 2012: pp. 245–254.

[101] V. Olden, A. Saai, L. Jemblie, R. Johnsen, FE simulation of hydrogen diffusion in duplex stainless steel, Int. J. Hydrogen Energy. 39 (2014) 1156–1163. doi:10.1016/j.ijhydene.2013.10.101.

[102] V. Olden, C. Thaulow, R. Johnsen, Modelling of hydrogen diffusion and hydrogen induced cracking in supermartensitic and duplex stainless steels, Mater. Des. 29 (2008) 1934–1948. doi:10.1016/j.matdes.2008.04.026.

[103] P. Sofronis, R.M. McMeeking, Numerical analysis of hydrogen transport near a blunting crack tip, J. Mech. Phys. Solids. 37 (1989) 317–350. doi:10.1016/0022-5096(89)90002-1.

[104] G.Ø. Lauvstad, R. Johnsen, M. Bjurström, C.G. Hjorth, B. Nyhus, Improved Resistance Towards Hydrogen Induced Stress Cracking (Hisc) Of Hot Isostatically Pressed (Hip) Duplex Stainless Steels Under Cathodic Protection - Paper n.07497, Corros. 2007. (2007).

[105] G. Lauvstad, R. Johnsen, I. Asbjørnsen, M. Bjurström, C.-G. Hjorth, Resistance Toward Hydrogen-Induced Stress Cracking of Hot Isostatically Pressed Duplex Stainless Steels Under Cathodic Protection, Corrosion. 66 (2010) 115004-115004–13. doi:10.5006/1.3516218.

[106] J.W. Hsu, S.Y. Tsai, H.C. Shih, Hydrogen embrittlement of SAF2205 Duplex stainless steel, in: NACE Int. Corros. 2002, NACE International, 2002: pp. 858–862.

[107] R. Francis, H.S. Campbell, Hydrogen embrittlement tests of piping material, (1986).

[108] Y. Mukai, M. Murata, J. Wang, Analytical evaluation and mechanism of hydrogen embrittlement SCC in duplex stainless steel welds, Weld. Int. 6 (1992) 110–116. doi:10.1080/09507119209548155.

[109] Design of duplex stainless steel subsea equipment exposed to cathodic

protection, in: Recomm. Pract. DNV-RP-F112, DNV-GL, 2017.

[110] A. Scheid, M. Sartori, T. Renck, F.P. dos Santos, M.F. Borges, C.E.F. Kwietniewski, Effect of K-rate and cathodic protection potential on fracture toughness of the super duplex stainless steel UNS S32750, Eng. Fract. Mech. 184 (2017) 296–306. doi:10.1016/j.engfracmech.2017.09.019.

[111] W.J.R. Nisbet, R.H.C. Hartman, G. Handel, Rippled strain rate test for CRA sour service materials selection - Paper n.58, in: Corros. 1997, NACE International, 1997: pp. 1–10.

[112] E. Krempl, An experimental study of room-temperature rate-sensitivity, creep and relaxation of AISI type 304 stainless steel, J. Mech. Phys. Solids. 27 (1979).

[113] R. Francis, The stress relaxation behaviour of zeron 100 bolting, 1997.

[114] U. Kivisäkk, Influence of hydrogen on corrosion and stress induced cracking of stainless steel, Royal Institute of Technology, KTH, 2010.

[115] M. Boniardi, G.M. La Vecchia, R. Roberti, Stress relaxation behaviour in duplex and super duplex stainless steels, in: Duplex Stainl. Steels ’94, Glasgow, Scotland, 1994.

[116] P. Woollin, W. Murphy, Hydrogen Embrittlement Stress Corrosion Cracking of Superduplex Stainless Steel - Paper n.01018, Corros. 2001. (2001).

[117] P. Woollin, A. Gregori, Avoiding Hydrogen Embrittlement Stress Cracking of Ferritic Austenitic Stainless Steels Under Cathodic Protection, in: 23rd Int. Conf. Offshore Mech. Arct. Eng. Vol. 2, ASME, 2004: pp. 777–784. doi:10.1115/OMAE2004-51203.

[118] B.Y. Maehara, Superplasticity Stainless Steels of δ-ferrite / Austenite Duplex Stainless Steels, Trans. ISIJ. 25 (1985). doi:10.2355/tetsutohagane1955.70.15_2168.

[119] M. Sagradi, D. Pulino-Sagradi, R.. Medrano, The effect of the microstructure on the superplasticity of a duplex stainless steel, Acta Mater. 46 (1998) 3857–3862. doi:10.1016/S1359-6454(98)00087-1.

[120] J.L. Song, P.L. Blackwell, Superplastic behaviour of commercial duplex stainless steel SAF 2304, 0836 (2016). doi:10.1179/026708399101505239.

[121] M. Festen, J. Erlings, R.A. Fransz, Low Temperature Creep of Austenitic-Ferritic and Fully Austenitic Stainless Steels and Ferritic Pipeline, in: EICM Proc., 1990: pp. 229–232.

[122] G. Chai, R.L. Peng, S. Johansson, U. Kivisäkk, Hydrogen induced stress cracking in heterogeneous materials, 19th Eur. Conf. Fract. (ECF19), Fract. Mech. Durability, Reliab. Safety, August 26-31 2012, Kazan, Russ. (2012).

[123] S. Lynch, Towards a Consensus On Mechanisms Of Hydrgoen Embrittlement, 2012.

[124] G. Chai, S. Ronneteg, U. Kivisäkk, R.L. Peng, S. Johansson, Mechanisms of Hydrogen Induced Stress Crack Initiation and Propagation in Super Duplex Stainless Steels, Steel Res. Int. 80 (2009) 482–487. doi:10.2374/SRI09SP042.

[125] R. Oltra, C. Bouillot, T. Magnin, Localized hydrogen cracking in the austenitic phase of a duplex stainless steel, Scr. Mater. 35 (1996) 1101–1105. doi:10.1016/1359-6462(96)00293-X.

[126] U. Kivisäkk, Relation of room temperature creep and microhardness to microstructure and HISC, Mater. Sci. Eng. A. 527 (2010) 7684–7688. doi:10.1016/j.msea.2010.08.035.

[127] P.J. Ferreira, I.M. Robertson, H.K. Birnbaum, Hydrogen effects on the interaction between dislocations, Acta Mater. 46 (1998) 1749–1757. doi:10.1016/S1359-6454(97)00349-2.

[128] T. Magnin, Environment Sensitive Fracture Mechanisms, Solid State Phenom. 35–36 (1993) 319–334. doi:10.4028/www.scientific.net/SSP.35-36.319.

[129] T. Cassagne, F. Busschaert, A review on hydrogen embrittlement of duplex stainless steels - Paper n. 05098, NACE Int. Corros. Conf. (2005) 1–26.

[130] K. Nakade, Sigma Phase Precipitation and its Influence on Hydrogen Induced Cracking of Duplex Stainless Steel Base Metal and Weld Metal, Weld. World.

47 (2013) 9–20. doi:10.1007/BF03266396.

[131] H.A. Estupiñan, I. Uribe, P.A. Sundaram, Hydrogen permeation in gamma titanium aluminides, Corros. Sci. 48 (2006) 4216–4222. doi:10.1016/j.corsci.2006.04.010.

[132] R. Francis, D.G. Byrne, G. Warburton, Z.J. Schulz, Advanced Forging Process (AFPTM), Super Duplex Stainless Steel for Increased Low Temperature Impact Toughness and Resistance to Hydrogen Induced Stress Corrosion Cracking (HISCC) Due to Cathodic Protection of API Forgings for Subsea Applications, in: OTC Bras., Offshore Technology Conference, 2013. doi:10.4043/24356-MS.

[133] M. Aursand, L.A. Marken, G. Rørvik, I.M. Kulbotten, Experiences with Hydrogen Induced Stress Cracking of Duplex Stainless Steel Components in Subsea Service with Cathodic Protection - Paper n.2490, in: Corros. 2013, NACE International, Orlando, Florida, US, 2013.

[134] H. Kokawa, E. Tsory, T.H. North, Nitride Precipitation in Duplex Stainless Steel Weld Metal., ISIJ Int. 35 (1995) 1277–1283.

[135] R. Francis, G. Byrne, N. Heath, Experiences with superduplex stainless steel - Paper n.03255, in: Corros. 2003, NACE International, 2003.

[136] G. Byrne, R. Francis, G. Warburton, Variation in mechanical properties and corrosion resistance of different alloys within the generic designation UNS S32760, in: Duplex Am. 2000 Conf., Houston, Texas, US, 2000: pp. 113–126.

[137] A. Bahrami, P. Woollin, Hydrogen Induced Stress Cracking of Duplex Stainless Steel Subsea Components, in: 29th Int. Conf. Ocean. Offshore Arct. Eng. Vol. 6, ASME, 2010: pp. 13–22. doi:10.1115/OMAE2010-20088.

[138] J. Marsh, Influence of Hydrogen Induced Stress Cracking on Subsea Design - Paper n.2787, in: Corros. 2013, Orlando, Florida, US, 2013.

[139] P. Sentance, Hydrogen embrittlement of cold worked duplex stainless steel oilfield tubulars, in: Duplex Stainl. Steels ’91, Beaune, Bourgogne, France, 1991: p. 895 903.

[140] S.S. Chen, T.I. Wu, J.K. Wu, Effects of deformation on hydrogen degradation in a duplex stainless steel, J. Mater. Sci. 39 (2004) 67–71. doi:10.1023/B:JMSC.0000007729.14528.a8.

[141] Y. Huang, A. Nakajima, A. Nishikata, T. Tsuru, Effect of Mechanical Deformation on Permeation of Hydrogen in Iron, ISIJ Int. 43 (2003) 548–554. doi:10.2355/isijinternational.43.548.

[142] A.J. Griffiths, A. Turnbull, Defining the Limits of Application of Duplex Stainless Steel Coupled to Carbon Steel in Oilfield Environments, Corrosion. 57 (2001) 165–174. doi:10.5006/1.3290341.

[143] A. J Griffiths, A. Turnbull, Hydrogen uptake and cracking in 22 Cr duplex stainless steel under galvanic coupling conditions, 1996. doi:10.1108/JSBED-03-2015-0037.

[144] T. Zakroczymski, A. Glowacka, W. Swiatnicki, Effect of hydrogen concentration on the embrittlement of a duplex stainless steel, Corros. Sci. 47 (2005) 1403–1414. doi:10.1016/j.corsci.2004.07.036.

[145] S.Y. Tsai, H.C. Shih, K.P. Yen, Cathodic hydrogen embrittlement of a 22% chromium 5% nickel duplex stainless steel in sulfide containing 3.5 wt% NaCl solution, (1996).

[146] R. Silverstein, O. Sobol, T. Boellinghaus, W. Unger, D. Eliezer, Hydrogen behavior in SAF 2205 duplex stainless steel, J. Alloys Compd. 695 (2017) 2689–2695. doi:10.1016/j.jallcom.2016.11.184.

[147] F. Elshawesh, J.C. Scully, Hydrogen embrittlement of 22-5 duplex stainless steel, Br. Corros. J. 33 (1998) 49–52. doi:10.1179/000705998798483490.

[148] A. Turnbull, A.J.A. Griffiths, T. Reid, P. Dent, Hydrogen Embrittlement of Duplex Stainless Steels - Simulating Service Experience - Paper no. 99148, NACE Int. Corros. Conf. (1999) 148.

[149] J.W. Hsu, S.Y. Tsai, H.C. Shih, Hydrogen Embrittlement of SAF 2205 Duplex Stainless Steel, in: Corrosion, NACE International, 2002.

[150] J.. Hutchinson, Fundamentals of the phenomenological theroy of non-linear fracture mechanics, Trans. ASME. 50 (1983) 1042–1051.

[151] J.R. Rice, A Path Independent Integral and the Approximate Analysis of Strain Concentration by Notches and Cracks, J. Appl. Mech. 35 (1968) 379. doi:10.1115/1.3601206.

[152] A. Bahrami, M. Bourgeon, Anais Cheaitani, Effects of Strain Rate and Microstructure on Fracture Toughness of Duplex Stainless Steels under Hydrogen Charging Conditions - Paper n.49131, in: Proc. 30th Int. Conf. Ocean. Offshore Artic Eng., Rotterdam, The Netherlands, 2011: pp. 93–103. doi:10.1115/OMAE2011-49131.

[153] L.H. Wolfe, C.C. Burnette, Hydrogen embrittlement of cathodically protected subsea bolting alloys, Mater. Perform. 32:7 (1990).

[154] Standard Test Method for Measurement of Hydrogen Embrittlement Threshold in Steel by the Incremental Step Loading Technique, ASTM F1624. 15.03 (2012). doi:10.1520/F1624-12.

[155] ASTM G129 - 00 Standard Practice for Slow Strain Rate Testing to Evaluate the Susceptibility of Metallic Materials to Environmentally Assisted Cracking, (2013).

[156] ISO 7539-7:2005 - Corrosion of metals and alloys -- Stress corrosion testing -- Part 7: Method for slow strain rate testing, 2005.

[157] P.M. Vargas, S. Wastberg, P. Woollin, Stress based design guidelines for hydrogen induced stress cracking (HISC) avoidance in duplex materials, in: ASME 2009 28th Int. Conf. Ocean. Offshore Arct. Eng., 2009. doi:10.1115/OMAE2009-79504.

[158] J. Fonseca, T. Renck, E. Abreu, F.P. Santos, B. Diehl, C.E.F. Kwietniewski, Hydrogen Induced Stress Cracking on Superduplex Stainless Steel Under Cathodic Protection, in: Vol. 5 Mater. Technol. Pet. Technol., ASME, 2014: p. V005T03A031. doi:10.1115/OMAE2014-24251.

[159] V. Olden, C. Thaulow, T. Berstad, E. Ostby, Prediction of hydrogen embrittlement in 25% cr duplex stainless steel based on cohesive zone simulation, in: OMAE 2009, 2009: pp. 1–10.

[160] ASTM Standard E1820-11. Standard Test Method for Measurement of Fracture Toughness, 2011. doi:10.1520/E1820-09.2.

[161] ISO 12135, "Metallic Materials - Unified Method of Test for the Determination of Quasistatic Fracture Toughness", 2014.

[162] BS 7448-4 Fracture mechanic toughnesss tests - Part 4: Method for determination of fracture toughness resistance cured and initiation values for stable crack extension in metalllic materials., 1997.

[163] A.J. Schwartz, M. Kumar, B.L. Adams, D.P. Field, Electron Backscatter Diffraction in Materials Science, 2000. doi:10.1007/s11665-015-1597-8.

[164] A.J. Wilkinson, P.B. Hirsch, Electron diffraction based techniques in scanning electron microscopy of bulk materials, Micron. 28 (1997) 279–308. doi:10.1016/S0968-4328(97)00032-2.

[165] D.J. Dingley, V. Randle, Microtexture determination by electron back-scatter diffraction, J. Mater. Sci. 27 (1992) 4545–4566. doi:10.1007/BF01165988.

[166] V. Randle, O. Engler, Introduction to Texture Analysis: macrotexture, microtexture and orientation mapping, CRC Press, 2014. doi:10.1046/j.1365-2818.2001.00936.x.

[167] T. Maitland, S. Sitzman, EBSD technique and materials characterization, Scanning Microsc. Nanotechnology. Tech. Appl. (2007) 41–76.

[168] W. Peters, WH and Ranson, Digital imaging techniques in experimental stress analysis, Opt. Eng. 21 (1982) 427–431.

[169] J. Quinta Da Fonseca, P.M. Mummery, P.J. Withers, Full-field strain mapping by optical correlation of micrographs acquired during deformation, J. Microsc. 218 (2005) 9–21. doi:10.1111/j.1365-2818.2005.01461.x.

[170] A. El Bartali, V. Aubin, S. Degallaix, Fatigue damage analysis in a duplex stainless steel by digital image correlation technique, Fatigue Fract. Eng. Mater. Struct. 31 (2008) 137–151. doi:10.1111/j.1460-2695.2007.01207.x.

[171] C.C. Tasan, J.P.M. Hoefnagels, M. Diehl, D. Yan, F. Roters, D. Raabe, Strain localization and damage in dual phase steels investigated by coupled in-situ deformation experiments and crystal plasticity simulations, Int. J. Plast. 63 (2014) 198–210. doi:10.1016/j.ijplas.2014.06.004.

[172] F. Di Gioacchino, J. Quinta da Fonseca, An experimental study of the polycrystalline plasticity of austenitic stainless steel, Int. J. Plast. 74 (2015) 92–109. doi:10.1016/j.ijplas.2015.05.012.

[173] Y. Guan, B. Chen, J. Zou, T. Ben Britton, J. Jiang, F.P.E. Dunne, Crystal plasticity modelling and HR-DIC measurement of slip activation and strain localization in single and oligo-crystal Ni alloys under fatigue, Int. J. Plast. 88 (2017) 70–88. doi:10.1016/J.IJPLAS.2016.10.001.

[174] C. Blochwitz, J. Brechbühl, W. Tirschler, Analysis of activated slip systems in fatigue nickel polycrystals using the EBSD-technique in the scanning electron microscope, Mater. Sci. Eng. A. 210 (1996) 42–47. doi:10.1016/0921-5093(95)10076-8.

[175] H. Lin, D.P. Pope, Formation of Slip Traces during Grain Growth of Thin Metal Sheets, Mater. Sci. Forum. 204–206 (1996) 399–404. doi:10.4028/www.scientific.net/MSF.204-206.399.

[176] DoITPoMS - TLP Library Slip in Single Crystals - Slip geometry, (n.d.). https://www.doitpoms.ac.uk/tlplib/slip/slip_geometry.php (accessed August 1, 2018).

[177] D. Rodney, J. Bonneville, Chapter 16: Dislocations, in: Phys. Metall. Fifth Ed., 2014: p. 2963.

[178] M.C. Marinelli, A. El Bartali, J.W. Signorelli, P. Evrard, V. Aubin, I. Alvarez-Armas, S. Degallaix-Moreuil, Activated slip systems and microcrack path in LCF of a duplex stainless steel, Mater. Sci. Eng. A. 509 (2009) 81–88.

doi:10.1016/j.msea.2009.01.012.

[179] T. Zhai, A.J. Wilkinson, J.W. Martin, Crystallographic mechanism for fatigue crack propagation through grain boundaries, Acta Mater. 48 (2000) 4917–4927. doi:10.1016/S1359-6454(00)00214-7.

[180] N.S. Rossini, M. Dassisti, K.Y. Benyounis, A.G. Olabi, Methods of measuring residual stresses in components, Mater. Des. 35 (2012) 572–588. doi:10.1016/j.matdes.2011.08.022.

[181] J.M. Carpenter, Neutron Production, Moderation, and Characterization of Sources, in: Elem. Slow-Neutron Scatt. Basics, Tech. Appl., 2015: pp. 49–86.

[182] A. Fedrigo, F. Grazzi, A. Williams, S. Kabra, M. Zoppi, Phase composition mapping of a 17th century Japanese helmet, J. Anal. At. Spectrom. 30 (2015) 707–712. doi:10.1039/c4ja00390j.

[183] G.S. Pawley, Unit-cell refinement from powder diffraction scans, J. Appl. Crystallogr. 14 (1981) 357–361. doi:10.1107/S0021889881009618.

[184] P.J. Withers, M. Preuss, A. Steuwer, J.W.L. Pang, Methods for obtaining the strain-free lattice parameter when using diffraction to determine residual stress, J. Appl. Crystallogr. 40 (2007) 891–904. doi:10.1107/S0021889807030269.

[185] Development and Applications of Residual Stress Measurements Using Neutron Beams, in: Tech. Reports Ser. n. 477, International Atomic Energy Agency, 2014: pp. 1–176.

[186] S. Salmi, M. Rhode, S. Jüttner, M. Zinke, Hydrogen determination in 22MnB5 steel grade by use of carrier gas hot extraction technique, Weld. World. 59 (2014) 137–144. doi:10.1007/s40194-014-0186-z.

[187] Standard Test Methods for Determining Average Grain Size, 2012. doi:10.1520/E0112-10.1.4.

[188] [JAPIAU], J. Appl. Phys. 42 (n.d.) 4290–4295.

[189] Z. Angew, [ZAPHAX], Physics (College. Park. Md). 60 (n.d.) 245–249.

[190] S. Wrońskia, J. Tarasiuk, B. Bacroix, A. Baczmański, C. Braham, S. Wrońskia, J. Tarasiuk, B. Bacroix, A. Baczmański, C. Braham, Investigation of plastic deformation heterogeneities in duplex steel by EBSD, Mater. Charact. 52–60 (2012). doi:10.1016/j.matchar.2012.07.016.

[191] Standard Test Methods and Definitions for Mechanical Testing of Steel Products 1, Annu. B. ASTM Stand. (2003) 1–54. doi:10.1520/A0370-15.2.

[192] M. Dodge, S.D. Smith, T. London, K. Sotoudeh, R. Morana, S. Kabra, Assessment of Residual Stress and Suitability for Subsea Service of a Welded Superduplex Stainless Steel Flange Joint, Vol. 4 Mater. Technol. (2016) V004T03A027. doi:10.1115/OMAE2016-54004.

[193] P. Woollin, A. Greogory, Avoiding hydrogen embrittlement stress cracking of ferritic austenitic stainless steels under cathodic protection, in: 23rd Int. Conf. Offshore Mech. Artic Eng., Vancouver, British Columbia, Canada, 2004.

[194] C. Fukuoka, K. Morishima, H. Yoshizawa, K. Mino, Misorientation development in grains of tensile strained and crept 2.25%Cr-1%Mo steel, Scr. Mater. 46 (2002) 61–66. doi:10.1016/S1359-6462(01)01197-6.

[195] L.N. Brewer, M.A. Othon, L.M. Young, T.M. Angeliu, Misorientation Mapping for Visualisation of Plastic Strain Via Electron Back-Scattered Diffraction, Microsc. Microanal. 38 (2002) 684–685. doi:10.1017/S1431927606060120.

[196] J.W. Steeds, Dislocation arrangement in copper single crystals as a function of strain, Society. 392 (1966) 15–43. doi:10.1098/rspa.1927.0039.

[197] C.K. Chow, G.R. Brady, V.F. Urbanic, C.E. Coleman, Hydrogen ingress through EDM surfaces of Zr-2.5Nb pressure-tube material, J. Nucl. Mater. 257 (1998) 35–43. doi:10.1016/S0022-3115(98)00436-X.

[198] V.N. Kulkarni, V.K. Jain, A.K. Shukla, Measurement of hydrogen content in electrical discharge machined components, Mach. Sci. Technol. 9 (2005) 289–299. doi:10.1081/MST-200059070.

[199] F. Di Gioacchino, J.Q. Fonseca, Plastic Strain Mapping with Sub-micron

Resolution Using Digital Image Correlation, (2013) 743–754. doi:10.1007/s11340-012-9685-2.

[200] W.A. Scrivens, Y. Luo, M.A. Sutton, S.A. Collette, M.L. Myrick, P. Miney, P.E. Colavita, A.P. Reynolds, X. Li, Development of patterns for digital image correlation measurements at reduced length scales, Exp. Mech. 47 (2007) 63–77. doi:10.1007/s11340-006-5869-y.

[201] U. Kivisakk, Investigation of low temperature creep and relaxation behaviour of stainless steels at stress levels representatve for hydrogen embrittlement, Corros. 2007. (2007) 1–8.

[202] C. Örnek, D.L. Engelberg, Towards understanding the effect of deformation mode on stress corrosion cracking susceptibility of grade 2205 duplex stainless steel, Mater. Sci. Eng. A. 666 (2016) 269–279. doi:10.1016/j.msea.2016.04.062.

[203] V.Y. Gertsman, K. Tangri, A study of grain boundary statistics in 304 and 316L stainless steels, Philos. Mag. A. 64 (1991) 1319–1330. doi:10.1080/01418619108225351.

[204] M.E. Kassner, K.K. Smith, C.S. Campbell, Low-temperature creep in pure metals and alloys, J. Mater. Sci. 50 (2015) 6539–6551. doi:10.1007/s10853-015-9219-2.

[205] L.A. Deibler, Room temperature creep in metals and alloys, (2014).

[206] D. Kujawski, V. Kallianpur, E. Krempl, An experimental study of uniaxial creep, cyclic creep and relaxation of aisi type 304 stainless steel at room temperature, J. Mech. Phys. Solids. 28 (1980) 129–148. doi:10.1016/0022-5096(80)90018-6.

[207] I. Nominc, A.M. Dubois, Creep and Cyclic Tension Behavior of a Type 316 Stainless Steel at Room Temperature, (1982).

[208] T.H. Alden, Strain hardening during low temperature creep of 304 stainless steel, Acta Metall. 35 (1987) 2621–2626. doi:10.1016/0001-6160(87)90261-6.

[209] B. Verhaeghe, Deformation et de rupture d ’un acier thermiquement microstructural study of thermally aged duplex stainless steel, 1996.

[210] W. Zieliński, W. Światnicki, M. Barstch, U. Messerschmidt, Non-uniform distribution of plastic strain in duplex steel during TEM in situ deformation, Mater. Chem. Phys. 81 (2003) 476–479. doi:10.1016/S0254-0584(03)00059-2.

[211] I.. Lin, T.L. Anderson, R. DeWit, M.G. Dawes, Displacements and rotational factors in single edge notched bend specimens, J. Fract. (1982).

[212] W. Shang-Xian, Crack length calculation formula for three point bend specimens, Int. J. Fract. 24 (1984) R33–R38. doi:10.1007/BF00020275.

[213] X. Zhu, J.A. Joyce, Review of fracture toughness (G , K , J , CTOD , CTOA) testing and standardization, (2012). doi:10.1016/j.engfracmech.2012.02.001.

[214] T. Depover, E. Wallaert, K. Verbeken, Fractographic analysis of the role of hydrogen diffusion on the hydrogen embrittlement susceptibility of DP steel, Mater. Sci. Eng. A. 649 (2016) 201–208. doi:10.1016/j.msea.2015.09.124.

[215] R.P. Gangloff, Hydrogen-assisted cracking, Compr. Struct. Integr. (2003) 31–101.

[216] A.H.M. Krom, R.W.J. Koers, A. Bakker, Hydrogen transport near a blunting crack tip, J. Mech. Phys. Solids. 47 (1999) 971–992. doi:10.1016/S0022-5096(98)00064-7.

[217] C.S. Marchi, B.P. Somerday, S.L. Robinson, Permeability, solubility and diffusivity of hydrogen isotopes in stainless steels at high gas pressures, Int. J. Hydrogen Energy. 32 (2007) 100–116. doi:10.1016/j.ijhydene.2006.05.008.

[218] P. Craidy, L. Briottet, D. Santos, Hydrogen–Microstructure–Mechanical properties interactions in super duplex stainless steel components, Int. J. Hydrogen Energy. 40 (2015) 17084–17090. doi:10.1016/j.ijhydene.2015.06.065.

[219] R. Johnsen, B. Nyhus, S. Wästberg, Hydrogen Induced Stress Cracking (HISC) of Stainless Steels Under Cathodic Protection in Seawater: Presentation of a New Test Method, in: Vol. 6 Mater. Technol. C.C. Mei Symp. Wave Mech. Hydrodyn. Offshore Meas. Data Interpret., ASME, 2009: pp. 55–67. doi:10.1115/OMAE2009-79325.

[220] S.-L. Chou, W.-T. Tsai, Hydrogen embrittlement of duplex stainless steel in concentrated sodium chloride solution, Mater. Chem. Phys. 60 (1999) 137–142. doi:10.1016/S0254-0584(99)00077-2.

[221] Q. Liu, A.D. Atrens, Z. Shi, K. Verbeken, A. Atrens, Determination of the hydrogen fugacity during electrolytic charging of steel, Corros. Sci. 87 (2014) 239–258. doi:10.1016/j.corsci.2014.06.033.

[222] S. Roychowdhury, V. Kain, R.C. Prasad, Environmental Effects on the Fracture Toughness of a Duplex Stainless Steel (UNS S31803), CORROSION. 63 (2007) 442–449. doi:10.5006/1.3278397.

[223] E. Hämäläinen, A. Laitinen, H. Hänninen, J. Liimatainen, Mechanical properties of powder metallurgy duplex stainless steels, Mater. Sci. Technol. 13 (1997). doi:10.1179/mst.1997.13.2.103.

[224] H. Hänninen, J. Romu, R. Ilola, J. Tervo, A. Laitinen, Effects of processing and manufacturing of high nitrogen-containing stainless steels on their mechanical, corrosion and wear properties, J. Mater. Process. Technol. 117 (2001) 424–430. doi:10.1016/S0924-0136(01)00804-4.

[225] W.-T. Tsai, S.-L. Chou, Environmentally assisted cracking behavior of duplex stainless steel in concentrated sodium chloride solution, Corros. Sci. 42 (2000) 1741–1762. doi:10.1016/S0010-938X(00)00029-9.

[226] L. Smith, R. Morana, K. Sotoudeh, S. Smith, Validation of DNV RP F112 for Managing Hydrogen Induced Stress Cracking (HISC) in Super Duplex Stainless Steel for Subsea Applications, in: NACE Corros. 2018, 2018: pp. 1–12.

[227] Withers P.J, Bhadeshia H.K.D.H, Residual Stress Part 2 - Nature and Origins, Mater. Sci. Technol. 17 (2001) 366–375.

[228] E. Salvati, A.M. Korsunsky, A simplified FEM eigenstrain residual stress reconstruction for surface treatments in arbitrary 3D geometries, Int. J. Mech. Sci. 138–139 (2018) 457–466. doi:10.1016/j.ijmecsci.2018.02.016.

[229] J. Johansson, M. Odén, X.-H. Zeng, Evolution of the residual stress state in a

duplex stainless steel during loading, Acta Mater. 47 (1999) 2669–2684. doi:10.1016/S1359-6454(99)00149-4.

[230] P. Hedström, T.S. Han, U. Lienert, J. Almer, M. Odén, Load partitioning between single bulk grains in a two-phase duplex stainless steel during tensile loading, Acta Mater. 58 (2010) 734–744. doi:10.1016/j.actamat.2009.09.053.

[231] Y. Wang, Residual Stress Measurement of Centrifugally Cast Duplex Stainless Steel by Neutron Diffraction, J. Soc. Mater. Sci. Japan. 66 (2017) 763–770. doi:10.2472/jsms.66.763.

[232] B. Gideon, L. Ward, D.G. Carr, O. Muransky, Duplex Stainless Steel Welds: Residual Stress Determination, Magnetic Force Microscopy and Susceptibility to Intergranular Corrosion, in: Pentti Karjalainen and Staffan Hertzman (Ed.), 6th Eur. Stainl. Steel Conf. Proc., Helsinki Finland, 2008: pp. 629–636.